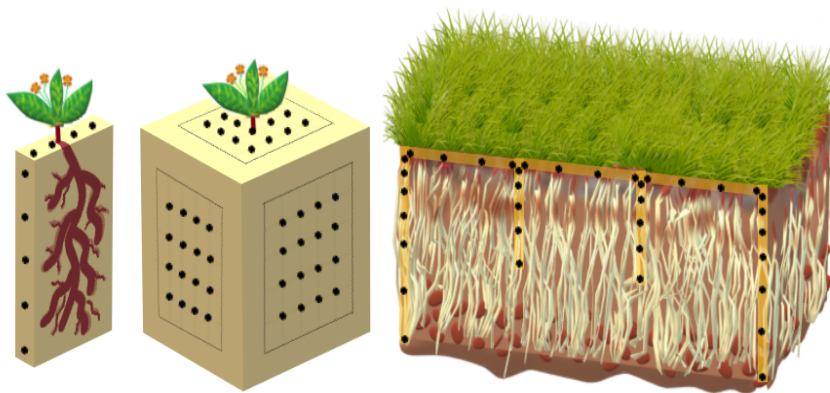


# Investigation of signatures of plant roots from non-invasive geo-electrical measurements



Sathyanarayan Rao

Day Date<sup>th</sup> Month, Year

*Thèse présentée en vue de l'obtention du titre de  
doctorat en sciences de l'ingénieur et technologie*

EARTH AND LIFE INSTITUTE  
UNIVERSITÉ CATHOLIQUE DE LOUVAIN



## **THESIS EXAMINING BOARD**

---

**SUPERVISOR : Prof. Mathieu Javaux**

**CO-SUPERVISOR : Prof. Frédéric Nguyen**

**PRESIDENT OF THE JURY : Prof. Emmanuel Hanert**

**MEMBERS OF THE JURY :**

Prof. Claude Oestges  
Prof. Sarah Garré  
Prof. Andreas Kemna  
Dr. Nimrod Schwartz



## CREDITS

---

The four years of this Ph.D. were funded by the Belgian Fond National de la Recherche Scientifique (FNRS) with a Research Fellow grant.



## ACKNOWLEDGMENTS

---

Firstly, I would like to express my sincere gratitude to my adviser Prof. Mathieu Javaux for his support and guidance that led to the success of this Ph.D. thesis. I thank him for providing good facilities for research and opportunities to attend summer schools and conferences. I especially acknowledge his support and involvement in my thesis during the last few weeks of my Ph.D. This was the time when the entire world was in crisis due to the COVID-19 pandemic and finishing this Ph.D. on time during this pandemic wouldn't have been possible without his support.

Besides my advisor, I would like to thank the supervisors of e-root project, Prof. Frédéric Nguyen of the University of Liège and Prof. Sarah Garré of the Gembloux Agro-Bio Tech (currently at ILVO, Belgium). They provided me great insights and support especially during the early stage of my Ph.D. thesis. It was great to work with them in Liège and Gembloux during which my adviser was Sabbatical at UC Davis. Prof. Sarah Garré arranged for me an office at Gembloux and took the time to take me to the ERT field experiments. It was the first time, I witnessed an ERT experiment in a cropped field and I thank her for this opportunity. Her patience in explaining ERT concepts also deserves mentioning. Special thanks to Solomon Ehsoioke of the University of Liege for allowing me in his lab to conduct experiments on Rapeseed roots and also for providing me the data for root electrical parameterization.

My sincere thanks go to Prof. Andreas Kemna for his support during my stay in Bonn. Discussions with him were very fruitful and it is what led to the work of Chapter 4 of this thesis. I also thank Maximilian Weigand and Shari van Treeck of Bonn University for

their support. I also specially thank Dr. Shiva Pudasaini during my stay at Bonn for his black tea and other friendly discussions.

I appreciate Prof. Adrián Flores Orozco of TU Vienna for helping me in data filtering of ERT acquisition and for his critical review of the work done in Chapter 5. His help was crucial in the removal of outliers and getting meaningful results in Chapters 5 and 6. I also appreciate the help of PyGIMLi team Dr. Thomas Günther and Dr. Carsten Rücker in Gitlab when I was beginning to learn PyGIMLi software. Special thanks go to Dr. Nolwenn Lesparre of Université de Strasbourg and Dr. Florian Wagner of RWTH Aachen for their help in ERT data processing.

I thank Dr. Nimrod Schwartz of the Hebrew University of Jerusalem for his support and introducing me to R-SWMS during the first two months of my thesis. Special thanks go to Félicien Meunier for helping me in R-SWMS and C-root box. I also acknowledge the help of Sébastien François and Benjamin Van der Verren in the field data acquisition. I also thank Axelle Koch and other GERU members for their support.

I also acknowledge the funding agencies: Ph.D. was supported by Fonds de la Recherche Scientifique – FNRS under Grant T.1088.15. The ERT field trial was supported by the Région Wallonne under the project ForDrought D31-1341.

I thank Prof. Emmanuel Hanert and Prof. Claude Oestges for agreeing to serve in thesis examining committee.

I extend my appreciation to Praveen Ranganath of the Indian Institute of Science (Now at Sutherland Global Solutions) for his support in Machine learning related discussions. The K-nearest neighbor classification in Chapter 4 can be attributed to these discussions.

I thank my wife for her support, having enormous patience, and being my close friend for three years in Belgium. She even crossed personal boundaries to help my Ph.D. As an example, I like to acknowledge her help in making illustrative figures for my poster presentations. One of her interesting paintings with Pikachu powering an ERT set-up even won second prize for the best posters' competition at UCL.

I thank my parents for financially supporting me to study a master's degree in the United States that provided me an understanding of western academics. Such an understanding was crucial to succeed in Europe as an academic scholar. I especially thank my mother for her support and motivation. Last but not least, I acknowledge my father. Although he could not do a Ph.D. degree due to personal constraints, he implanted this desire in me long back without which I would not have traveled this far. Finally, I thank Paramātmā who influenced me at a subtle level at the right times that kept me going during the Ph.D.

Sathyanarayan Rao,  
Louvain-la-Neuve,  
Day Date<sup>th</sup> Month, Year

# ABSTRACT

---

Thorough knowledge of root system architecture and functioning is essential for a better understanding of the impact of plants on climate change, for plant phenotyping or for designing more sustainable agro-ecosystems. Recently, electrical imaging of root zone soil has been gaining wide attention among agronomists and soil scientists (Zhao et al. 2019) because of its sensitivity to soil moisture. However, a quantitative understanding of electrical signatures of roots in electrical imaging is still somewhat missing in the scientific literature. For example, it is unclear how roots impact petrophysical relation and if electrical measurements contain geometrical information of root architectures. It is also unclear if the ERT method is sensitive enough to differentiate depletion zones of similar plant types but belonging to different species for phenotyping applications.

The general objective of this Ph.D. thesis is to quantify the direct and indirect impact of plant roots in soil electrical signature. Root affects the soil-plant system directly through its architecture but also indirectly via soil water depletion by uptake.

The first part of the thesis (Chapters 3 and 4) deals with understanding the direct impact of roots in small scale rhizotron and pot via process-based numerical models. We quantify the direct impact of roots while incorporating both direct (root explicit electrical properties) and indirect (root water uptake patterns) in the forward numerical model. To date this is the closest to reality, a numerical model can achieve in understanding electrical signatures of root systems in soils. We also prove that electrical response if measured in magnitude and phase components, magnitude part represents mainly indirect impact (root

water uptake) while the phase part represents mainly direct impact (root architecture) and both magnitude and phase part contain root geometrical information.

The second part of the thesis deals with quantifying the indirect impact of water, i.e., soil water depletion in field-scale ERT experiments. We propose a new methodology where we use a numerical model to interpret field data. The model informed us if the changes we observe in the ERT experiment was due to plants or an artifact. This allowed us to quantify even the slightest changes in water depletion from different plants. Finally, we show that it is possible to phenotype similar plants belonging to different species at field scale using the ERT method.



## **SHORT CONTENTS**

<b>INTRODUCTION AND OBJECTIVES</b>	<b>1</b>
<b>LITERATURE REVIEW AND THEORETICAL BACKGROUND</b>	<b>19</b>
<b>ELECTRICAL SIGNATURE OF ROOTS AT RHIZOTRON AND POT-SCALE</b>	<b>51</b>
<b>ROOT PHENOTYPING AT FIELD-SCALE</b>	<b>115</b>
<b>CONCLUSION AND PERSPECTIVES</b>	<b>171</b>



# TABLE OF CONTENTS

## INTRODUCTION AND OBJECTIVES

---

<b>1</b>	<b>Introduction</b>	<b>5</b>
1.1	Context	5
1.1.1	Importance of studying soil-root interactions	7
1.1.2	Need for efficient root imaging methods	8
1.1.3	Geo-electric methods in soil-root studies	9
1.1.4	Electrical Resistivity/Impedance Tomography	10
1.2	Problem Statement	11
1.2.1	Root influence on petrophysical relation	11
1.2.2	Imaging root systems characteristics	13
1.2.3	Root Phenotyping	14
1.3	Objectives	15
1.4	Outline of the thesis	18

## LITERATURE REVIEW AND THEORETICAL BACKGROUND

---

<b>2</b>	<b>Geophysical monitoring methods for soil-root continuum</b>	<b>23</b>
2.1	Introduction	24
2.2	Theoretical background	25
2.2.1	Lossy dielectrics	25
2.2.2	Conduction and polarization mechanisms in soil-root systems	27

2.3	Measured Electrical properties of Roots	30
2.3.1	Resistive properties of Plant tissues: experimental values	30
2.3.2	Capacitive property of root tissues: experimental characterization	33
2.4	Overview of electrical methods for root system investigation	35
2.4.1	Electrical Resistivity Tomography (ERT)	35
2.4.2	Electrical Impedance Tomography	37
2.5	Petrophysical transfer relations	39
2.5.1	Bare Soil	39
2.5.2	Impact of Vegetation	41
2.6	Soil-root mixing	42
2.7	Need for Explicit modeling of root	44
2.8	Electrical measurements on root segments	45
2.8.1	Introduction	45
2.8.2	Measurement of Electrical DC Resistance	45
2.8.3	Measurement of Polarization Signatures	47
2.9	Summary and Conclusions	49
2.10	Future research perspectives	50

## **ELECTRICAL SIGNATURE OF ROOTS AT RHIZOTRON AND POT-SCALE**

---

### **3 A process-based mechanistic model for electrical conduction in the soil-root continuum 55**

3.1	Introduction	56
3.2	Materials and Methods	58
3.2.1	Soil plant water fluxes	60
3.2.2	Electrical properties of plant root tissues and soils	62

3.2.3	Meshing the root architecture	63
3.2.4	Electrical resistivity forward modeling	66
3.2.5	Apparent and effective electrical conductivities	67
3.2.6	Root electrical signature terms	68
3.2.7	Upscaled electrical properties	69
3.3	Results	70
3.3.1	Electrical conductivity contrasts derived from root water uptake simulations	70
3.3.2	The impact of roots on petrophysical relationships	
72		
3.3.3	Root signatures in ERT forward simulations with point electrodes	75
3.3.4	Root signatures in ERT forward simulations	79
3.4	Model Limitations	83
3.5	Discussion	83
3.6	Conclusion	84
<b>4</b>	<b>Simulation-based investigation of the geometrical information content of the soil-root continuum in geo-electric measurements</b>	<b>87</b>
4.1	Introduction	88
4.2	Materials and Methods	90
4.2.1	Silty Soil Petrophysical Relation	92
4.2.2	Root Electrical properties	93
4.2.3	Root Architecture Simulation	94
4.2.4	Geometrical Indices for Soil-Root System	96
4.2.5	Root water uptake simulation	99
4.2.6	Finite element mesh generation and the finite element model	100
4.2.7	Electrical anisotropic factor	102
4.2.8	The testing discriminatory power of Indices	102

4.3 Results and Discussions	103
4.3.1 Characterization of geometrical and topological differences between root systems	103
4.3.2 Electrical anisotropy signatures of roots	105
4.3.3 The relation between electrical anisotropy and geometrical indices at low frequency	107
4.3.4 Electrical anisotropy phase at high frequency	109
4.3.5 The discriminatory power of electrical anisotropy	
111	
4.4 Conclusion	112

# ROOT PHENOTYPING AT FIELD-SCALE

## 5 Imaging plant responses to water deficit using electrical resistivity tomography 119

5.1	Introduction	120
5.2	Materials and Methods	122
5.2.1	Field Trial Description	122
5.2.2	Field ERT	124
5.2.3	Time Domain Reflectometry (TDR) and Pedophysical Model	127
5.2.4	Numerical Experiments	128
5.2.5	Gaussian fits	130
5.3	Results	131
5.3.1	Synthetic Experiments	133
5.3.2	Using ERT to recover plant-specific depletion zones	136
5.4	Discussion	140
5.5	Appendices	141

## **6 Field phenotyping of grass water uptake under water deficit by ERT**

**149**

6.1	Introduction	150
6.2	Materials and Methods	151
6.2.1	Field Trial Description	151
6.2.2	ERT Acquisition	154
6.2.3	Time Domain Reflectometry	155
6.2.4	Root characteristics measurements	156
6.2.5	Analyses of plant depletion patterns	156
6.3	Results	157
6.3.1	Comparison between soil water content measured by TDR and ERT	157
6.3.2	Water content evolution	158
6.3.3	Depletion depth and root and available water distributions	160
6.4	Summary and Conclusion	166
6.5	Appendices	167

## **CONCLUSION AND PERSPECTIVES**

---

## **7 Conclusions and perspectives**

**175**

7.1	Bulk soil electrical properties vs root electrical properties	177
7.2	Root properties	179
7.3	Perspectives	180

## **GENERAL BIBLIOGRAPHY**

**181**

## LIST OF FIGURES

1.1	Population growth, available land and food production	7
1.2	Impact of vegetation on petrophysical relation	12
1.3	Root mass density versus electrical conductivity	12
1.4	Flowchart of the outline for the thesis chapters	17
2.1	Electrical flow paths in plant cell	29
2.2	Electric double layers in the root surface	30
2.3	Electrical resistivity of plant tissues	32
2.4	Root mass versus electrical capacitance	34
2.5	Linear relation between root mass and electrical capacitance	35
2.6	Schematic of a soil-root continuum with an illustration of SIP and TDIP method	39
2.7	Petrophysical relation of soil and electrical properties of root	41

2.8	Soil-only, root-only and root-soil electrical response	43
2.9	Measuring electrical resistance of root segments	46
2.10	Resistivity of different root species	47
2.11	SIP measuring setup for root segments	48
2.12	SIP signatures of root segments	49
3.1	Flow chart for the simulation of the Virtual Rhizotron drying experiment.	59
3.2	Root architectural evolution shown at different times.	61
3.3	Electrical conductivity of maize root segments	62
3.4	Root properties in finite element mesh	64
3.5	Finite element model of virtual rhizotron	65
3.6	Water saturation distribution for maize root simulation 71	
3.7	Comparing electrical conductivity of maize, sand and loam	72
3.8	Impact of roots on petrophysical relation	74
3.9	Deviation of petrophysical relation due to roots	75
3.10	Root signatures for different ERT simulation schemes in sand	77
3.11	Root signatures for different ERT simulation schemes in loam	78
3.12	Root signature versus root volume	79
3.13	Linear relation between root properties and its electrical signatures	81
3.14	Principal component analysis of different root variables	82
4.1	Methodology for comparing soil-root electrical properties with the geometrical indices of root architecture.	91
4.2	Electrical conductivity of silt soil	92
4.3	Electrical conductivity of different root segments	93
4.4	Root architecture generated in C-Rootbox	95
4.5	Geometrical indices of root system architecture	98

4.6	Root water uptake simulation	99
4.7	Finite element model in pot geometry	101
4.8	Correlation analysis and scatter plot of root geometrical indices	104
4.9	Electrical anisotropy of roots for different root radius	106
4.10	Electrical anisotropy versus geometrical indices at low frequency (10 Hz)	108
4.11	Electrical anisotropy versus geometrical indices at high frequency (10 kHz)	110
4.12	Probability density function of different root indices	111
4.13	K-nearest neighbor classification of root species	112
5.1	Schematic of 2-D ERT imaging in field	123
5.2	Root density and weather condition in the field	124
5.3	Petrophysical characterization of the field soil	128
5.4	Methodology for synthetic experiment and its relation to field experiment	130
5.5	Illustration of Gaussian fits for discriminating plant uptake behavior	131
5.6	ERT inversion results of field data	132
5.7	Simulated evolution of water content	134
5.8	Comparison of simulated forward and ERT inversion of simulated forward data	135
5.9	Quantifying root water uptake in simulated experiment	137
5.10	Quantifying root water uptake in red field experiment	139
5.11	Methodology workflow chart for ERT data processing of field data	143
5.12	Measurement error analysis of ERT raw data	144
5.13	Optimization of the regularization parameter in ERT inversion	146
5.14	Impact of anisotropic regularization on ERT inversion	147

6.1	Picture of the experimental site and ERT setup and description of various plants	152
6.2	Weather condition for water deficit treatment	155
6.3	Root number density for different grass species	156
6.4	Mean soil water content: TDR versus ERT	157
6.5	ERT inverted water content at different times	159
6.6	ERT inverted change of water content and gaussian fits	161
6.7	Comparing statistics of water depletion characteristics using Gaussian fit parameters	164
6.8	Root density, water depletion and available water	165
6.9	Sensitivity of ERT injection scheme	167
7.1	Flowchart for conclusion and perspective of the thesis	
		176

## LIST OF TABLES

5.1	Empirical fits for petrophysical relation	128
5.2	Soil hydraulic properties	148
5.3	Plant parameters used in R-SWMS simulation	148
6.1	Details of plant species in the ERT studies	153
6.2	Tukey HSD statistics for Gaussian fit parameters	163



# LIST OF ABBREVIATIONS

## Chapter 1:

<b>TDR</b>	Time domain reflectometry
<b>GPR</b>	Ground penetrating radar
<b>ERT</b>	Electrical resistivity tomography
<b>EIT</b>	Electrical impedance tomography
<b>EC</b>	Electrical conductivity
<b>DC</b>	Direct current
<b>DCR</b>	DC resistivity imaging
<b>ERI</b>	Electrical resistivity imaging
<b>SWC</b>	Soil water content
<b>RMD</b>	Root mass density
<b>RLD</b>	Root length density

## Chapter 2:

<b>RC</b>	Resistor and capacitor
<b>ICF</b>	Intracellular fluids
<b>ECF</b>	Extracellular fluids
<b>2-D</b>	Two-dimensional
<b>3-D</b>	Three-dimensional
<b>TDIP</b>	Time domain induced polarization
<b>SIP</b>	Spectral induced polarization
<b>RSA</b>	Root system architecture

## Chapter 3:

<b>R-SWMS</b>	Numerical model for modeling root-soil water movement and solute transport
<b>FFEM</b>	Forward finite element mesh
<b>EIDORS</b>	Software used in MATLAB to compute effective properties between plate electrodes

**PC** Principle component

### **Chapter 4:**

**MRI** Magnetic resonance imaging

**C-Rootbox** Software used for generation of root architecture

**ANOVA** Test performed for analysis of variance

**HSD** Honestly significant difference

**pdf** Probability density function

### **Chapter 5:**

**WD** Water deficit

**RND** Root number density

**VGM** Van-Genuchten-Mualem

**ET0** Evapotranspiration

**pyGIMLi** Python Library for Inversion and Modelling in Geophysics

**Gmsh** Software used to mesh 3-D root structures

**2.5-D** 2.5 dimensional

**Kcomp** Compensatory root water uptake conductance

**Krs** Equivalent conductance of the root System

### **Chapter 6:**

**B1 to B4** Four blocks

**A** Alfalfa

**RC** Red clover

**FAO** Food and Agriculture Organization

**RMSE** Root mean square error

**SciPy** Open-source Python library used for scientific computing and technical computing

**1-D** One dimensional

### **Chapter 7:**

**RSA** Root system architecture

# LIST OF SYMBOLS

## Chapter 1:

$\sigma$	Electrical conductivity
$\sigma_{bulk}$	Bulk electrical conductivity of soil
$\rho$	Electrical resistivity
$ \rho $	Frequency averaged resistivity magnitude

## Chapter 2:

$\epsilon$	Relative electrical permittivity
$\epsilon'$	Dielectric term describing the capacitance
$\epsilon''$	Dielectric loss factor describing the dissipation via resistance
$\vec{J}$	Current density inside a medium
$\vec{E}$	Applied harmonic electric field to the material
$\sigma_{dc}$	DC electrical conductivity of the material
$\omega$	Angular frequency of
$\epsilon_0$	Permittivity of free space
$\sigma'$	Ionic DC conduction and frequency dependent conduction via dielectric relaxation
$\sigma''$	Capacitance property of the medium
$ \sigma $	Magnitude describing conduction aspects

of the medium

$\angle\varphi$	Phase describing the polarizing or capacitance aspects of the medium
$Z$	Impedance of a material
$V$	Applied voltage
$I$	Current induced
$r$	Root mass
$\sigma_{bulk}$	Bulk electrical conductivity of soil
$\sigma_w$	Electrical conductivity of the soil fluid
$n$	Porosity of soil
$m \& d$	Fitting parameters for unsaturated soil
$S$	Degree of water saturation
$\sigma_{surface}$	Surface electrical conductivity of the solid phase of the soil
$a, b \& c$	Fitting parameters accounting for surface and fluid conductivities in soil
$\theta$	Volumetric soil water content
$\theta_s$	Saturated water content
$\sigma_{root}$	Electrical conductivity of root segments
$\sigma_{soil}$	Electrical conductivity of soil segments
$\sigma_{mm}$	Effective electrical conductivity predicted by the model for different ranging from -1 to 1
$\alpha$	Mixing model exponent describing the geometry of two phases
$f$	Relative area of to the total area
$(1 - f)$	Relative area of to the total area

### **Chapter 3:**

$\sigma_{bulk-soil}$	Soil bulk electrical conductivity when no roots
$\langle \theta \rangle$	Volume weighted arithmetic mean of water content
$(\sigma_{root} - \sigma_{bulk-soil})$	(C) Contrast between electrical conductivity of root segments and soil bulk electrical conductivity when no roots
$\sigma_{app}$	Apparent conductivities/ synthetic ERT data
$h$	Matrix head
$K$	Isotropic hydraulic conductivity
$Sink$	Sink term for root water uptake
$x, y \& z$	Spatial coordinates
.	Divergence
$\sigma_{bulk-sand}$	Sand bulk electrical conductivity when no roots
$\sigma_{bulk-loam}$	Loam bulk electrical conductivity when no roots
$V_e$	Voltage data
$\vec{J}_e$	Electrical current density
$\Omega$	Region considered in electrical resistivity forward modeling
$d\Omega$	Boundary bounding region
$\phi$	Scalar electric potential
$\nabla$	Gradient operator
$Z_e$	Contact impedance of the voltage measuring electrodes
$\hat{n}$	Unit normal perpendicular to

$\sigma_{app-root}$	Medium having soil and root system
$\sigma_{app-soil}$	Medium having only soil without root segments
$\delta\sigma_{app-rs}$	Relative change in due to the presence of root segments
$N$	Total number of quadrupoles
$\sigma_{eff}$	Effective electrical conductivity
$\sigma_{effZ}$	$\sigma_{eff}$ in vertical direction
$\sigma_{effX}$	$\sigma_{eff}$ in horizontal direction
$\sigma_{eff-root}$	Medium having soil and root system
$\sigma_{eff-soil}$	Medium having only soil considering the roots had the same electrical conductivity as the surrounding soil
$(\sigma_{eff-root} - \sigma_{eff-soil})$	Difference indicating the specific impact of root segments on effective property
$\delta\sigma_{eff-rs}$	Relative change in due to the presence of root segments
$\langle\delta\sigma_{eff-rs}\rangle$	$\delta\sigma_{eff-rs}$ averaged over two perpendicular directions
$\langle\delta\sigma_{app-rs}\rangle$	$\delta\sigma_{app-rs}$ averaged over all the 9742 quadrupoles
$\delta\sigma_{app-rs} - S$	Denotes $\delta\sigma_{app-rs}$ computed for current injection and voltage measurement between electrodes at the surface of rhizotron
$r$	Root radius/ volume
$2r$	Double of r
$3r$	Triple of r
$\langle\sigma_{avg-am}\rangle$	Volume weighted arithmetic mean of

	electrical conductivity within each block
$\langle \sigma_{avg-hm} \rangle$	Volume weighted harmonic mean of electrical conductivity within each block
$V_i$	Volume of i <sup>th</sup> tetrahedron within an average block
$\sigma_i$	Electrical conductivity of i <sup>th</sup> tetrahedron within an average block
$(\delta\sigma_{abmn-rs})$	Relative change in apparent conductivity from root segments compared to soil only
$r$	Pearson correlation coefficient/ root surface area

### Chapter 4:

$\phi$	Soil water content saturation
$a, b \& c$	Fitting parameters along the data
$\sigma_{real}$	Real part of $\sigma$
$\sigma_{imag}$	Imaginary part of $\sigma$
$\sigma_l$	Lower limit of Brachypodium plant
$\sigma_u$	Upper limit of Brassica plant
$AF_e$	Anisotropy based on root system extent
$Z_{extent}$	Vertical growth of root system
$(X_{extent} \& Y_{extent})$	Horizontal growth distance of root system
$SR$	Average slope ratio of root segments
$dx, dy \& dz$	Incremental distance within a root segment in x, y and z directions

$VR$	Root architecture convex hull volume to total volume ratio
$L$	Total length of the root system architecture
$FD$	Fractal dimension
$N$	Number of boxes in box-counting method
$s$	Box size in box-counting method
$FD_x$	Front view of the root architecture
$FD_y$	Lateral view of the root architecture
$FD_z$	Top view of the root architecture
$GAF$	Geometrical anisotropic factor
$\gamma_X, \gamma_Y & \gamma_Z$	Angles between a scan line and root segments in different directions

$\Sigma$	Summation on the number of intersections between scan lines and root segments
$L_X, L_Y & L_Z$	Length of scan lines in X, Y and Z directions
$\xi & \delta\varphi$	Magnitude and phase of plate electrodes' effective anisotropic factor
$\varphi_X & \varphi_Z$	Heterogeneity in electrical conductivity in two principal directions
$drc$	Distance from root collar
$p0$	Test point to compute nearest neighbor points
$p1, p2 & p3$	Nearest neighbor points
$k$	Optimal integer value
$t1$	Represents day 25.2 of root uptake

simulation  
 $t2$  Represents day 31 of root uptake simulation

### **Chapter 5:**

$\mathbf{Ap}, \mathbf{Bt} & \mathbf{C}$	Six different soil horizons
$\hat{\mathbf{d}}$	Data vector or log of measured apparent resistivities from real/numerical experiments
$f(\mathbf{m})$	Gauss-Newton scheme Model
$\phi_d$	Data misfit between the measured $\hat{\mathbf{d}}$ and the data estimated by $f(\mathbf{m})$ down-weighted by $E_{model}$
$\lambda$	Regularization parameter in ERT inversion
$\phi_m$	Model misfit
$\mathbf{m}_0$	Homogeneous starting model vector
$W$	First-order smoothness regularization matrix
$Z_w$	The ratio by which $\lambda$ is reduced for vertical contrast
$\chi^2$	Chi-square value in ERT inversion
$N$	Length of the data vector
$\theta_{TDR}$	Soil water content derived from TDR
$\rho_{TDR}$	Electrical resistivity derived from TDR
$a & b$	Fitting parameters
$\theta_r$	Residual water content
$\sigma_{TDR}$	Electrical conductivity using TDR
$\delta\rho$	2-D time difference of resistivity and

	water content
$\delta\theta$	Water content between t1 and t3
$\mu_{Z,\delta p}, \mu_{Z,\delta\theta}$	Mean parameters represent depth at which depletion is largest
$\sigma_{Z,\delta p}, \sigma_{Z,\delta\theta}$	Extent of the depletion
$\delta p$	Change of log resistivity between t1 and t3
$\sigma_Z$	Depletion zone
$R_n$	Normal resistance
$R_r$	Reciprocal resistance
$FE$	Fractional error
$R_{mean}$	Arithmetic mean of R
$E$	Measurement error in ERT
$E_{model}$	Linear model describing data-error in ERT
$R$	Magnitude of the resistance
$a$	Absolute error in ERT inversion
$b$	Relative error in ERT inversion
$\theta_s$	Saturated water content
$\theta_r$	Residual water content
$(a, n, m & \lambda)$	Shape parameters in Van Genuchten-Mualem equations
$K_s$	Saturated soil hydraulic conductivity
$\theta(t3), \theta(t2) \& \theta(t1)$	2-D distributions of water content at t3, t2 and t1
$\rho(t3), \rho(t2) \& \rho(t1)$	2-D distributions of electrical resistivity at t3, t2 and t1

## Chapter 6:

$Nq_{raw}$  Number of quadrupoles in raw data  
 $Nq_f$  Filtered data as a function of block  
**t1 to t4** Time stamps used for measurements  
*rnd* Root density under drought condition

**Chapter 7:**

----

## PART I

# INTRODUCTION AND OBJECTIVES



In this first section, we introduce the context of thesis, problem statement and objectives.

*Upon this handful of soil our survival  
depends. Husband it and it will grow  
our food, our fuel and our shelter and  
surround us with beauty. Abuse it and  
soil will collapse and die, taking  
humanity with it.*

SANSKRIT TEXT CIRCA 1500 BC





# 1 INTRODUCTION

## 1.1 Context

Crops are the main source of food, fiber, and biofuel and source of economic income for many countries employing a large number of people in the world (Chowdhury 2011). The increasing demand for agricultural products due to population growth and rapid urbanization of the developing countries under changing environments and climate represents an immense challenge for the next decades (Wheeler and Von Braun 2013).

Figure 1.1 shows the relation between world population, arable land, irrigation, and fertilizer usage. We are able to keep up the pace of cereal production with population growth mainly because of mainly three reasons: 1) genetic modification, 2) increased usage of fertilizer, and 3) equipping land with irrigation (Harold 2015).

Currently, we are facing challenges in these three key areas:

1. The green revolution that improved the productivity of rice and wheat was mainly the result of genetic engineering that made plants more responsive to applied fertilizers (Lynch 2007). To define a Genotype, it is a DNA code that genetically defines a plant species. The interaction of several genes and the environment of the plant life leads to physically measurable traits in the plant such as growth rate, yield, root density, leaf counts, biomass, rate of photosynthesis, and adaptation to stress (Costa et al. 2019). Such traits are termed as phenotypes. Current technology allows rapid analysis of genotypes or DNA sequencing in plants but to

understand the impact of a specific genotype, corresponding phenotype data is essential (Yang et al. 2014). However, currently, phenotyping in crops is not as rapid, systematic, and high throughput as genotyping. Only by analysing phenotyping and genotyping data simultaneously, we can completely understand the behavior of a plant. This requires high-throughput phenotyping methods.

2. Although fertilizers have improved food productivity in the past decades, it has limitations. Only 50% of applied nitrogen fertilizers and 5% percent of phosphorous fertilizer are used by the crops (Lynch and Brown 2012) and the unused fertilizer leads to environmental damage and soil degradation (Sekhon 1995).
3. Thirdly, only 23% of arable land in the world is equipped for irrigation and is increasing rapidly (Harold 2015). Today, agriculture accounts for 70% of the usage of freshwater in the world leading to increasing global scarcity of freshwater (Faurès et al. 2002). Further, the agricultural productivity of many countries is climate driven and relies heavily on events like monsoon which has recently become erratic due to global warming (Gadgil and Kumar 2006). Droughts are increasing around the world due to an increase in evapotranspiration in plants due to surface heating caused by human-induced climate change or CO<sub>2</sub> emissions (Trenberth et al. 2014).

Therefore, we urgently need better agricultural practices to improve food security for the growing world population while also conserving soil, water, and biodiversity resources. This requires adopting new agricultural practices that involve finance and policy sectors such as tackling food price volatility (Lipper et al. 2014) to implementation of more sustainable crop input management (irrigation, fertilizers, etc.) and the use of more resilient combinations of plant genotypes.

With arable land and freshwater availability reaching its planetary limits, understanding plant-soil interactions become a very important scientific step to improve agricultural practices (Sposito 2013).

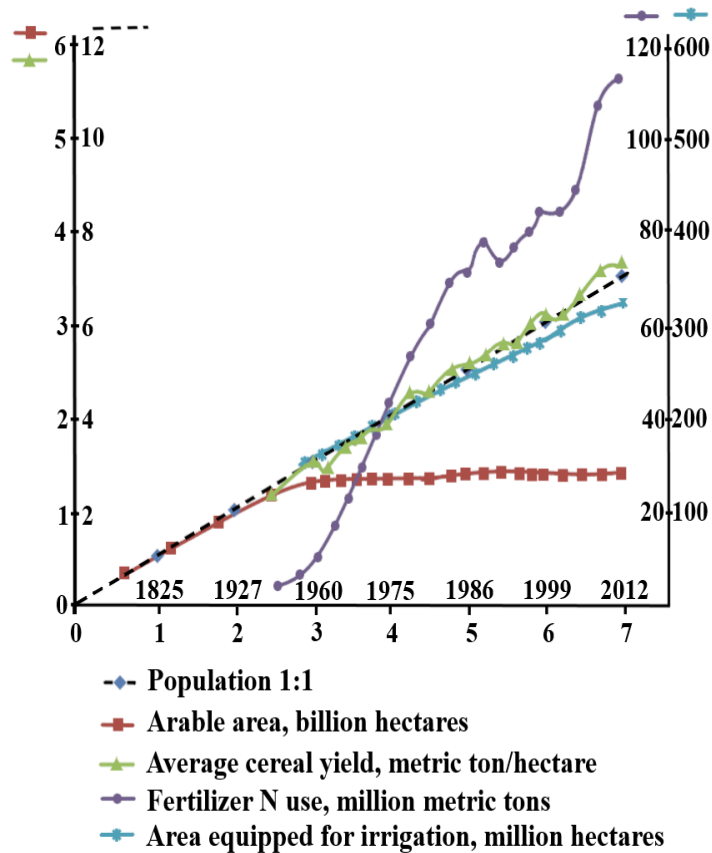


**Figure 1.1:** The relation between world population and arable land, cereal yield, fertilizer use, and irrigated area. The figure is taken from (Harold 2015) who originally adapted it from (Evans et al. 1998).

### *1.1.1 Importance of studying soil-root interactions*

The root system forms the hidden half of a plant's body that provides anchorage to the remaining upper part of the plant and helps plants to absorb water and nutrients from the soil. Root systems have architecturally very complex and variable structures, which develop as a function of their genetic information and their environment.

On the other hand, soil medium is also a complex and heterogeneous system, whose structure, composition, and water and nutrient content vary in space and time. Plants affect soil heterogeneity through many processes such as growth, exudation, microbial activity, and water and nutrient uptake, amongst others. At the interface between soil and root, the rhizosphere is a hotspot of biodiversity and the location of important exchanges between soil and roots.

There is an established link between crop yields and root system performance. Studies have indicated that crop yield or biomass production in maize depended on root system architecture (Lynch 2007; Hammer et al. 2009). For example, (Wasson et al. 2012) demonstrated that wheat genotypes with a denser root system in deeper soil layers produce higher yields. In addition, studies find that shallow root growth is efficient in acquiring nutrients like phosphorous where water scarcity is not a problem while deep vertical root growth is an important subject to water deficit (Lynch and Brown 2008).

Desired genotype characteristics such as drought tolerance can be achieved by engineering a deeper root system by cloning or other crop breeding methods (Uga et al. 2013). However, a large root system also means higher metabolic costs for root growth (Lynch 2015), which can sometimes reduce yield (above-ground biomass) as observed in Maize under drought (Bruce et al. 2002). Therefore, it has been shown that the

efficiency of a certain genotype critically depends on other root system characteristics (or traits or phenes). (Leitner et al. 2014) for instance, it showed that root hydraulic conductance could improve water uptake efficiency more than deep roots under certain environments.

Monitoring evolution of root biomass, root architecture, and root water uptake dynamics in cropped fields under varying climatic conditions is critical information needed to understand drought tolerance, optimization of irrigation strategies, root phenotyping, plant breeding and to develop reliable plant-soil models. However, such monitoring is still a challenging task due to the opaque nature of soil (Cairns et al. 2012).

Hence, in the context of understanding soil-plant interactions, we need efficient measurement techniques to monitor root growth, root activity, and soil water fluxes.

### *1.1.2 Need for efficient root imaging methods*

Traditional methods used to investigate soil-root zone includes soil excavation and rhizotubes, which are inherently intrusive interferes with the natural state of the system. Rhizotubes allow visualizing root arrival rates at a given depth (Cai et al. 2016) but can hardly be installed in very large fields and provide only a partial view of the system. Large containers are also tested (Svane et al. 2019) but cannot represent the natural soil heterogeneity.

Other minimally invasive techniques include the use of point sensors such as time domain reflectometry (TDR) probes, electrical conductivity sensors ( $\sigma$ ), soil tensiometers, capacitance probes that measure variables of interests such as soil moisture and soil water potential at discrete locations.

Smart irrigation systems currently make use of signal inputs from soil moisture and evapotranspiration sensors to manage the irrigation sprinklers (McCready et al. 2009). These systems either use point sensors mounted on the surface of the soil (Iggulden et al. 1989) or network of sensors (Morais et al. 2005). However, they do not accurately capture the temporal and spatial variability of root-zone. It is very important to include the complexity of soil-root moisture patterns in these smart irrigation systems if it has to be accurate and robust enough.

On the other hand, remote sensing-based approaches that make use of satellite imaging to measure variables such as soil water content over a large area of tens of km lack the resolution at plant scale. Techniques that offer high-resolution spatial and temporal variability such as light transmission imaging needs specialized soil medium and transparent rhizotron (Garrigues et al. 2006) and hence cannot be applied in natural soil conditions.

### *1.1.3 Geo-electric methods in soil-root studies*

Geophysical methods offer the ability to infer properties and structures of the pedosphere as well as flow and transport processes at various spatial scales ranging from the single root to the field scale (Cimpoiașu et al. 2020). Geophysical properties can be related to soil state variables (e.g. soil moisture, salt concentration), soil properties (e.g. clay content, cation exchange capacity), and root properties (e.g. root mass, root surface area) (Vanderborght et al. 2013). The application of geophysical techniques in an agricultural context to study how agricultural production is affected by environmental variables (e.g. water availability, salinity) and agricultural management (e.g. impact of fertilizer and irrigation application) as well as to study fundamental soil-root interactions is now referred to as

agrogeophysics (Vereecken et al. 2006; Allred et al. 2008).

Various applications of geophysical methods in agriculture are reported in the literature ranging from mapping of compaction or determination of plow-pan depth (Besson et al. 2004; Lu et al. 2004) to irrigation efficiency monitoring (Tresoldi et al. 2019). Soil mapping for precision agriculture and crop modeling has been realized using on-the-go electrical resistivity tomography (Andrenelli et al. 2013) and Ground-penetrating radar (Huisman et al. 2002).

These methods are continuously evolving from the past few decades to monitor partially the soil-root systems and their functioning, which include: ground penetrating radar (GPR), electrical resistivity tomography (ERT), electrical impedance tomography (EIT), time-domain reflectometry (TDR), electrical capacitance tomography and amongst others, each method offering its advantages and disadvantages. They offer promising features and rely on the fact that the electrical properties such as electrical resistivity/impedance and dielectric permittivity are very sensitive to hydrological parameters of interest such as soil water content (Michot et al. 2003) and solute concentration (Kemna et al. 2002). For example, the electrical conductivity (EC) map of soil obtained from geo-electric methods in a cropped field is sometimes used as a proxy to measure crop yields (Grasso et al. 2009). Among the geo-electrical methods discussed above, ERT/EIT method offers several advantages such as being cost-effective and easier to install in fields and is the method of interest in this thesis.

#### *1.1.4 Electrical Resistivity/Impedance Tomography*

Electrical resistivity tomography (ERT), also called DC resistivity imaging (DCR) or Electrical Resistivity Imaging (ERI), determines the distribution of electrical

resistivity in the subsurface by performing a set of resistance measurements on the ground surface and/or in boreholes. Electrical Impedance Tomography (EIT) is similar to ERT in terms of set-up and measurement but using a frequency-dependent current injection and inverting both the real and complex parts of the impedance at different frequencies.

In the context of monitoring soil water content, ERT has been widely applied in field-scale (Beff et al. 2013; Garré et al. 2011; Michot et al. 2003, 2016; Whalley et al. 2017; Zhou et al. 2001). Michot et al. (2003) studied the soil water content (SWC) in irrigated maize cropland using ERT and showed that the changes in SWC had an effect on measured electrical conductivity data and Beff et al. (2013) used TDR and ERT to quantitatively measure soil water distribution in a maize field and found that both of these techniques yield a similar result. More recently, ERT-estimated water content was used for phenotyping root systems at field scale (Whalley et al. 2017). The authors monitored changes in  $\sigma$  of the soil root zone in drying conditions at different soil depths, which acted as a proxy for root activity.

Other studies used ERT or EIT related techniques to image root biomass or root structures. Zenone et al. (2008) used ERT and GPR in conjunction to detect poplar roots and pine roots and found that ERT is capable of detecting tree roots independent of the root directional orientation whereas GPR could detect only roots that are perpendicular to radar profile. They suggested that the combination of these methods (GPR and ERT) could more accurately predict root biomass non-invasively. Amato et al. (2008) used resistivity imaging to map root biomass and showed a high correlation between measured resistivity and root mass density. In the work of Weigand and Kemna (2017), the spectral signatures of complex  $\sigma$  of rapeseed roots grown in Rhizotron were investigated using EIT. They found that the presence of roots in soil significantly

altered the complex  $\sigma$  spectra and thus suggesting the possible use of EIT in root imaging. The electrical polarization property of roots was investigated in the context of the imaging root system (Mary et al. 2016, 2017). However, using EIT, they could detect only the shallow roots and not the roots located deeper in the soil. In addition, there existed some anomalies in electrical phase distribution, which they could not explain. More recently, Mary et al. (2018) found that by injecting electric current directly into the stem as opposed to the soil, some information about the root architecture could be inferred.

## 1.2 Problem Statement

### 1.2.1 Root influence on petrophysical relation

The performance of several smart agricultural systems depends on the accuracy of estimated soil water content. Precise and accurate measurements of SWC are also important to understand physiological processes, control automated irrigation systems, and develop new crop models for better crop management (Jones 2006). Despite the success in using geo-electric methods such as ERT and EIT in estimating soil water content in agricultural field (Samouëlian et al. 2005; Srayeddin and Doussan 2009; Garré et al. 2011; Beff et al. 2013; Michot et al. 2016), the possibility of root segments contaminating ERT measurements remains mostly unexplored.

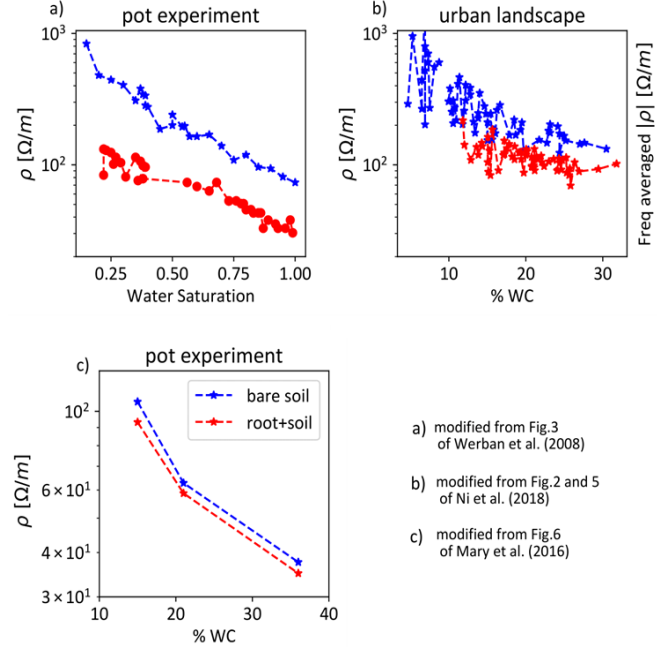
The petrophysical relation is commonly the relation between the bulk electrical conductivity of the soil medium and the soil water content. To transform the bulk electrical conductivity of soil obtained by geophysical measurements (André et al. 2012; Zenone et al. 2008) into soil water content, we use functions

called petrophysical models. These models relate  $\sigma_{bulk}$  with other properties of soil as the soil water content (see section 2.5.1).

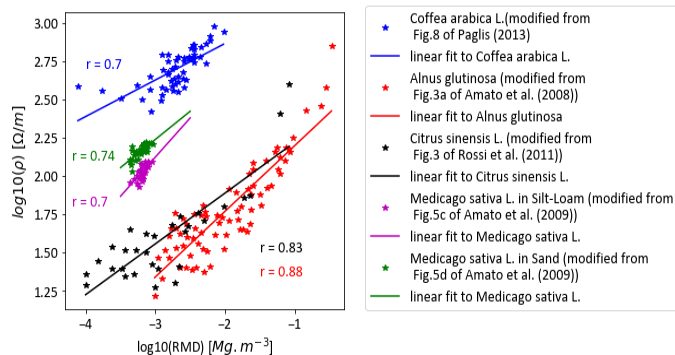
The bulk electrical conductivity of soil, here onwards denoted by  $\sigma_{bulk}$ , depends on several factors, which include the porosity of soil particles, the electrical conductivity of soil liquid phase, temperature, soil compaction or bulk density, organic carbon content, and soil water content (Corwin and Lesch 2005). Also, the presence of roots affects the bulk electrical conductivity of the soil (Werban et al. 2008; Ni et al. 2018). Yet, in some lysimeter experiments, we see that petrophysical function is time-invariant, despite ongoing root growth (Garré et al. 2011). Beff et al. (2013) could not see the impact of roots in terms of petrophysical relations for Maize species as opposed to Werban et al. (2008). Thus, it is not clear how vegetation affects petrophysical relations. In some studies, the presence of roots tends to decrease the electrical resistivity in the petrophysical curve (Werban et al. 2008; Mary et al. 2016; Ni et al. 2018) while others observed an increasing trend between ERT derived electrical resistivity and root biomass as shown in Figure 1.2 (Amato et al. 2008, 2009; Rossi et al. 2011; Paglis 2013). This increasing trend could be due to increased root water uptake in root dense regions resulting in drying up of the soil and thus increasing the electrical resistivity. Hence, along with root-specific electrical property, the indirect impact of roots such as root water uptake and solute uptake also affects soil electrical property and petrophysical relations.

Figure 1.1 shows different petrophysical relations in vegetated soils with different root density and scales. Michot et al. (2016) also observed different petrophysical relation for rooted and bare soil (although we did not show their data in Fig. 1.1). Werban et al. (2008) in their concluding remarks, suggests that using Archie's law with only three phases

(sand particle, water, and air) is not suitable for the root zone, which requires a fourth phase (root segments).



**Figure 1.2:** a) Electrical resistivity ( $\rho$ ) versus water saturation from Figure 3 of Werban et al. (2008). b) Electrical resistivity ( $\rho$ ) versus percentage volumetric water content (WC) from Figure 2 and Figure 5 of Ni et al. (2018). c) Frequency Averaged resistivity magnitude ( $|\rho|$ ) as a function of percentage volumetric water content.



**Figure 1.3:** Root mass density (RMD) versus electrical resistivity ( $\rho$ ) of various plant/tree species from different

works of literature as described in the legend. Digitization of pictorial data done using WebPlotDigitizer (Rohatgi 2011).

### *1.2.2 Imaging root systems characteristics*

How roots invade the soil and react to soil water spatial distribution, how the root hydraulic properties are distributed between root orders and as a function of age is plant genotype characteristics that can be targeted by breeders to optimize plant performances under adverse conditions.

However, the ability to easily, accurately, and extensively characterize root phenotypes even at pot scale is a major challenge in the field of root biology (Meister et al. 2014). There are various bottlenecks in the root phenotyping procedure (Atkinson et al. 2019). One such bottleneck is high throughput imaging or phenotyping techniques available for root systems (Atkinson et al. 2019). While there are many studies focusing on high-throughput imaging of the above-ground part (Fahlgren et al. 2015; Bai et al. 2016; Singh et al. 2016), the studies on root systems are relatively limited.

Geo-physical techniques such as the electrical resistivity tomography (ERT) and Electrical Impedance Tomography (in principle similar to ERT) offer promising features such as being cost-effective and high throughput. Although there are few recent studies in using these geophysical techniques for non-invasive root phenotyping, it is not yet clear that if electrical properties of a soil-root domain that can be measured from Geophysical techniques contains information on root architectural parameters such as its extent and length (Whalley et al. 2017; Corona-Lopez et al. 2019; Peruzzo et al. 2020).

The strength of electrical signatures from roots in geophysical methods depends on electrical

conductivity contrast between soil matrix and root segments. Investigating the effect of roots on electrical conductivity is however difficult as pointed out by Rossi et al. (2011) due to complex soil-root interaction. For example, in the study of Zenone et al. (2008), poplar roots could be discriminated in loam but pine roots could not be discriminated in the sand. Rossi et al. (2011) could correlate bulk electrical conductivity with root mass density (RMD) but not with root length density (RLD) for orchard roots. They could relate bulk electrical conductivity with root mass density only for a certain range of conductivities but not for all the range. Further, it is also not clear how the root architecture or root segment connectivity and its geometrical properties such as root volume, root surface area, and root radius play a role in affecting electric current flow. Mary et al. (2016) conclude that success in accurately imaging root systems using EIT is limited by incomplete understandings of how soil-root interaction such as root water uptake influences the EIT measurements.

Al Hagrey and Petersen (2011) studied the impact of roots on ERT imaging by using an adaptive root growth numerical model (Wilderotter 2003), but however, they ignored the inherent heterogeneity of electrical conductivity that can exist within a soil-root continuum. They assumed that electrical conductivity for conductive root to be 0.05 S/m, resistive root to be 0.002 S/m, which were contained in a homogeneous soil with the conductivity of 0.01 S/m. While homogeneous simplifications may explain certain experimental aspects, such a simplified model cannot quantify the impact of roots hidden in ERT measurements. As mentioned earlier, we should examine/include heterogeneity or variability of sub-surface properties along with root electrical properties into the model for such purposes. Unfortunately, there are no detailed numerical studies aiming to understand the root impact on bulk electrical properties or ERT measurements, which includes the

complexity of real-world variabilities such as plant transpiration, root water uptake, and electrical conductivity heterogeneity, despite increasing usage of ERT in agronomy.

Such a numerical study would advance our understanding to develop a petrophysical correction term for root impact in ERT measurements. Understanding of electrical current flow in the soil-root system would also help us in the context of non-invasive imaging of root systems via ERT method.

### *1.2.3 Root Phenotyping*

Currently, root phenotyping is typically performed on young plants grown aeroponics, or in small containers filled with non-natural substrates. Their ability to deal with the heterogeneous environment is therefore impossible to assess. Recognizing the limiting interest of root phenotyping in pots (Passioura 2002), Passioura (2012) suggested that field phenotyping is needed to ensure that plant genotypes are able to deal with the natural temporal and spatial variability of the environment.

High-resolution root-zone soil moisture monitoring using ERT can reveal the differences in water depletion of different genotypes and species under varying climatic conditions. For example, ERT imaging conducted on a transition zone from forest to grassland showed that soil moisture dynamics at different seasons were significantly different for forest and grassland (Jayawickreme et al. 2008). Garré et al. (2013) showed that in an inter-cropped field, the ERT method could distinguish the depth of soil water depletion for different plant species and also differentiate fertilized and unfertilized treatments. Although there are very few field-scale studies using ERT/EIT to phenotype roots, additional experiments at different conditions and environments are needed to establish Geo-electrical methods as a reliable phenotyping tool.

## 1.3 Objectives

The general objective of this Ph.D. thesis is to quantify the direct and indirect impact of plant roots in soil electrical signature. Root affects the soil-plant system directly through its architecture but also indirectly via soil water depletion by uptake. Two main questions will be tackled in this Ph.D.: (1) how do roots impact pedometrical relations and (2) is it possible to determine root system properties with Geo-electrical measurements such as ERT.

The general objective will be addressed through 4 sub-objectives (see flowchart in Fig. 1.3):

- 1. Reviewing the electrical properties of soil-root continuum and state of the art Geophysical methods:**

Some studies have speculated that electrical conductivity contrast between soil matrix and root segments determines the ability of root segments to affect electrical measurements (Rossi et al. 2011; Vanderborght et al. 2013). Hence, our first objective is to review the electrical properties (including polarization) of root segments and soil matrix. This will allow us to draw a conclusion on conditions under which root segments and soil traits could be discriminated via state-of-the-art geophysical methods.

- 2. Process-based virtual rhizotron experiments to investigate the impact of roots on ERT derived soil water content and petrophysical relations:**

The second objective of this thesis is to investigate how a transpiring, growing single plant might affect

the ERT estimate of soil water content and petrophysical relation. For achieving this objective, we chose to work with a rhizotron geometry, which is a thin container (typically around 1 cm x 50 cm x 50 cm), filled up with a growing substrate in which plant roots develop. An electrically isolated soil-root system of a rhizotron offers simplicity yet elegant environment to understand the impact of roots on ERT derived water content. We hypothesize that the electrical conductivity contrast between the plant root system and the soil surrounding the roots (impacted by root, soil properties, and plant hydraulic boundary conditions) together with the number of roots will affect the ERT measurements and therefore ERT-derived quantities. Quantification of root impact will be then investigated with the help of development of a coupled numerical model that can stimulate root growth and development (including changes of root electrical properties with aging), water flow in soil and root systems, as well as electrical transfer in the soil-root continuum in a rhizotron geometry.

**3. Relating structural properties of a root system to effective electrical properties of a soil-root continuum:**

We hypothesize that electrical measurements in the soil root continuum contain information on root system topology and/or architecture. We base our hypothesis on the fact that the root system having different electrical and hydraulic properties than soil, should affect effective electrical properties of a soil-root continuum in a systematic way either by its direct presence or via indirect water uptake that is somehow related to root architecture. Here, we investigate whether the electrical properties of the soil-root system have any relation to root system geometrical features and to what extent. This

assessment will answer the question: can we use electrical measurements to phenotype root systems in agricultural fields and under what conditions? To do so, developing different indices characterizing the geometry of the root system network and electrical properties of the soil-root continuum and testing the relationship between them using numerical modeling will be the third objective of this thesis.

#### **4. Phenotyping root systems at field scale using ERT**

Crop yields might be dramatically affected by drought stress. It is therefore important to understand how different plants react to a limited amount of soil water and high evaporative demand. Non-invasive phenotyping methods are essential to identify drought-tolerant plants. We hypothesize that under drought conditions, Electrical Resistivity Tomography (ERT) should be able to quantify and distinguish the plants in terms of depth and quantity of root water uptake and thus be used for root phenotyping. Therefore, the objective of this chapter is to test the ability of ERT in the field to acquire information on root water uptake by different forbs and grass species. In particular, we are interested in understanding root water uptake under drought stress.

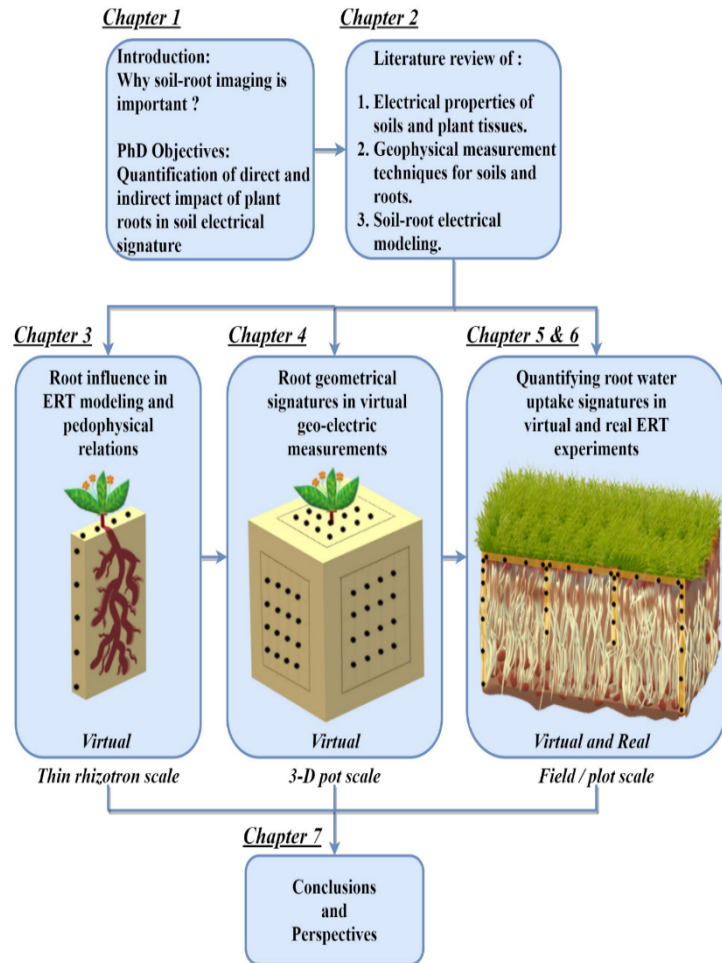


**Figure 1.4:** Flowchart of the outline for the thesis chapters

## 1.4 Outline of the thesis

The structure of the remaining part of this thesis into different chapters is as follows:

- **Chapter 2** discusses the electrical properties of the soil-root continuum. To measure root electrical properties, we designed specific experiments on real plants. In addition, we also provide a review of various petrophysical relations from literature used to convert electrical resistivity to soil water content for water content estimation purposes. We also describe the measurement procedure adopted to characterize the electrical properties of the root segment. The measured quantities are then used to parameterize the process-based model described in chapter 3.
- **Chapter 3** presents the results of the process-based rhizotron model. We simulate virtual ERT experiments and assess the influence of root segments in a thin rhizotron geometry.
- **Chapter 4** explores the possibility to use electrical measurements for deducing root architectural features and thus for pot-scale phenotyping. Here, we extend the process based rhizotron model to different plant species having varying root architectures and examine the relation between the geometry of root network and electrical properties.
- **Chapters 5 and 6** deal with actual ERT experiments on multi-species grassland. We discuss the filtering process and data handling involved in ERT inversion. Then we examine the root phenotyping information contained in the electrical resistivity information derived from ERT measurements.
- **Chapter 7** concludes this thesis with remarks and future perspectives.



## PART II

# LITERATURE REVIEW AND THEORETICAL BACKGROUND



This section will present the literature review of electrical properties of roots, soils and geo-physical methods used for soil root imaging.

*Yathā vṛkṣo vanaspatistathaiva puruṣo amṛṣā  
Tasya lomāni parṇāni tvagasyotpāṭikā bahiḥ  
Tvaca evāsyā rudhiram prasyandi tvaca utpaṭah  
Tasmāttadātṛṇṇātpraiti raso vṛkṣādivāhatāt  
Māṃsānyasya śakarāṇi kināṭam srāva tatsthiram  
Asthīnyantarato dārūṇi majjā majjopamā kṛtā  
Bṛhadāraṇyakopniṣad*

Meaning: A tree is similar to a man.  
His hairs are its leaves, his skin its outer bark.  
Just like blood flows in man, sap flows in bark.  
Just like blood flows out from an injury,  
sap flows out from a tree that is hit.  
His flesh is its inner bark.  
His ligaments are its innermost layer of the bark.  
His bones, which lie within ligaments,  
are its wood and his bone marrow being similar  
to its pith.

Brihadaranyaka Upanishad





## **2 GEOPHYSICAL MONITORING METHODS FOR SOIL-ROOT CONTINUUM**

Chapter adapted from:

Ehosioke, S., F. Nguyen, S. Rao, T. Kremer, E. Placencia-Gomez, J.A. Huisman, M. Javaux, and S. Garré, Sensing the electrical properties of roots; a review, Vadose Zone Journal, Submitted 2020.

---

### **ABSTRACT**

Thorough knowledge of root system architecture and functioning is essential for a better understanding of the impact of plants on climate change, for plant phenotyping or for designing more sustainable agro-ecosystems. Its characterization is challenging due to its inaccessibility, the heterogeneity of the pedosphere, and the complex biogeochemical processes in the root zone. Electrical methods address some of these limitations by inferring properties and structures of the pedosphere as well as flow and transport processes non-invasively at various spatial scales. In this review paper, we highlight the applications of low-frequency electrical geophysical methods to root biomass investigation reported by plant, soil, and geophysical scientific communities.

Conduction and polarization processes occur in and around roots, but the mechanisms responsible for this

behavior are not yet fully understood. Measurements of different communities' target either resistance, capacitance or impedance of the soil-plant continuum at scales ranging from the root segment to the field. Combining knowledge of both in-phase and out-of-phase electrical properties at a range of frequencies (length scales) offers opportunities to separate signatures from soil and root and identify key processes in the equivalent electrical circuit of the soil-plant continuum.

Future research should be focused on developing and parameterizing equivalent circuit models for the soil-plant continuum under study, so that the contribution of different components to the in- and out-of-phase electrical properties can be quantified and used as diagnostic or imaging tools. Further, development of mechanistic soil-root models can be used as a calibration model for circuit models and they can also help us in understanding the effect of the multiple scale levels involved in the underlying processes.

## 1.1 Introduction

Understanding root zone processes is crucial for sustainable agriculture and food production. Traditional methods of soil and root investigation provide insights into the structure, composition, and variability in the subsurface. However, they have clear limitations in terms of temporal and spatial resolution mainly caused by the spatial heterogeneity of the root zone and its dynamics. Root growth, plant water, and nutrient uptake, and transient boundary water fluxes create highly heterogeneous and dynamic patterns in root and soil properties that can be difficult to capture, even with a high-density network of point sensors (Jayawickreme et al. 2014).

One of the key opportunities in agrogeophysics is the non-invasive investigation of root biomass (Amato et al. 2009). Due to the vital role root biomass and architecture play in plant breeding, drought tolerance, and carbon sequestration, measurements of root extent and distribution are necessary for proper understanding and modeling of plant growth, root water uptake, and the carbon balance of agricultural systems.

Root biomass and soil water content are the two primary drivers of sub-surface electrical properties that can influence Geophysical measurements (Amato et al. 2008). Other secondary drivers include soil salinity, soil temperature, soil bulk density, soil porosity, and soil texture (Friedman 2005), and soil microbes in the rhizosphere (Yan and Marschner 2012). Often these drivers are interconnected. For instance, root growth can modify soil porosity and bulk density while canopy shade can reduce soil temperature thereby affecting measured electrical properties (Ni et al. 2018).

Discrimination of root segments from soil medium using the Geophysical method primarily depends on electrical conductivity (EC) and polarization contrast between root segments, rhizosphere, and soil medium. Since this EC/polarization contrast further depends on the type of root and soil conditions, it is important to know, in prior, what can be the expected influence of roots on ERT/EIT measurements. It must be noted that neither the soil electrical conductivity nor the root electrical conductivity are material constants but instead depend on several other factors as described in the following sections of this chapter.

The aim of this chapter is to provide a background for the thesis. In particular, we examine the ERT and EIT methods. The chapter is organized as follows: After a brief introduction to electrical conduction and polarization in plants and soils, we will describe the different measurement techniques and highlight their potentials and limitations. We will also discuss the widely used petrophysical transfer functions used to

estimate soil water content from ERT/EIT measurements. Then we differentiate vegetated soil from bare soil in terms of petrophysical models and finally compare the regimes of soil-root electrical property contrasts under which we can extract the information about roots via ERT or EIT method. Finally, we will discuss future perspectives and identify knowledge gaps for this active field of research.

## 1.2 Theoretical background

Early works of Dvořák et al. (1981) showed that plant tissues behave like a Resistor and Capacitor (RC) circuit. Using the current decay curve, they could characterize the electrical properties of leaf tissues of following plant species: *Zea mays*, *Dactylis glomerata*, and *Phalangium comosum*. They suggested that resistance of plant tissues depends on spatial arrangements of cells and different ionic pathways within the plant tissue while cytoplasmatic membranes behaved like a capacitor. The current decay curve that the authors observed differed for different species suggesting the role of cellular structures of plant tissues (Dvořák et al. 1981).

Numerous studies have used electrical properties of plant tissues such as electric potential, resistance, and capacitance to investigate different aspects of physiology such as root growth rate, root system size, phloem thickness and width, wood decay, fungal infections, tree vigor and moisture content (Gora and Yanoviak 2014).

We discuss both direct current (DC) resistive properties of plant tissues that are relevant to ERT monitoring and polarizing/capacitance aspects that are relevant to EIT.

### 1.2.1 Lossy dielectrics

Because plant tissues and soil materials belong to the class of lossy dielectrics meaning they have finite electrical conductivity yet exhibits dielectric behavior. The conduction in the soil-root system is mainly ionic in nature, where both anions and cations contribute to the conduction and polarization phenomena. We will first present here some of the basic theory/nomenclature used in lossy dielectrics.

Lossy dielectrics are in-between perfect conductors like metals (pure resistors) and perfect dielectrics (pure capacitors). They behave like leaky capacitors that dissipates stored electrical charges into heat. We can express the relative electrical permittivity of such a lossy dielectric medium as:

$$\epsilon = \epsilon' - i\epsilon'' \quad (2.1)$$

where,  $\epsilon'$  is the dielectric term describing the capacitance, and  $\epsilon''$  is the dielectric loss factor describing the dissipation via resistance. The current density inside such a medium consists of DC and displacement parts given by (Kuang and Nelson 1998):

$$\vec{J} = \sigma_{dc} \vec{E} + \epsilon_0 \epsilon' \frac{\partial \vec{E}}{\partial t} = \sigma_{dc} \vec{E} + i\omega \epsilon_0 \epsilon'' \vec{E} \quad (2.2)$$

where,  $\vec{E}$  is the applied harmonic electric field to the material,  $\sigma_{dc}$  is the DC electrical conductivity of the material,  $\omega$  the angular frequency of  $\vec{E}$ , and  $\epsilon_0$  the permittivity of free space.

Substituting (2.1) in (2.2), we get:

$$\begin{aligned}
\vec{J} &= \sigma_{dc} \vec{E} + i\omega\epsilon_0 (\epsilon' - i\epsilon'') \vec{E} \\
&= \sigma_{dc} \vec{E} + i\omega\epsilon_0 \epsilon' \vec{E} + \omega\epsilon_0 \epsilon'' \vec{E} \\
&= (\sigma_{dc} + \omega\epsilon_0 \epsilon'') \vec{E} + i\omega\epsilon_0 \epsilon' \vec{E} \\
&= (\sigma_{dc} + \omega\epsilon_0 \epsilon'') \vec{E} + i\omega\epsilon_0 \epsilon' \vec{E}
\end{aligned}
\tag{2.3}$$

From (2.3), we can entirely express the transfer function relating  $\vec{J}$  and  $\vec{E}$  in terms of complex conductivity:

$$\vec{J} = (\sigma' + i\sigma'') \vec{E}
\tag{2.4}$$

where,  $\sigma' = \sigma_{dc} + \omega\epsilon_0 \epsilon''$  represents ionic DC conduction and frequency-dependent conduction via dielectric relaxation,  $\sigma'' = \omega\epsilon_0 \epsilon'$  represents the capacitance property of the medium.

We can describe the electrical property of a soil-root continuum entirely by  $\sigma'$  and  $\sigma''$ . Alternatively, we can also use magnitude ( $|\sigma|$ ) and phase ( $\angle\varphi$ ) notation or its inverse resistivity ( $\rho$ ) to describe the medium property:

$$\sigma' + i\sigma'' = |\sigma| \angle\varphi
\tag{2.5}$$

$$\rho = \frac{1}{|\sigma|} \angle\varphi
\tag{2.6}$$

In magnitude and phase rotation, the magnitude part describes the conduction aspect while the phase part (measured in radians) describes the polarizing or capacitance aspects of the medium.

Normally the measured electrical quantity is the impedance of a material ( $Z$ ) which is defined as the

ratio of applied voltage ( $V$ ) to the current induced ( $I$ ) within the material:

$$Z = \frac{V}{I} \quad (2.7)$$

The impedance ( $Z$ ) is dependent on the size, shape, and cross-section of the material that is being tested. However, resistivity or conductivity (Eqs. 2.5 and 2.6) is a material intrinsic property that is the size or shape independent.

### 1.2.2 *Conduction and polarization mechanisms in soil-root systems*

Electricity can flow in the soil through three pathways: the first one consists in a solid phase made up of particles with varying chemical composition, size, shape and organic content; a second pathway is the mode of the pore liquid phase composed mainly of soil water and solute and, the last pathway is the gaseous phase consisting of atmospheric gases. In vegetated soils, we have a fourth pathway: root segments and rhizosphere (See Fig. 2.1).

#### *Conduction Mechanism*

Soils conduct electricity mostly through electrolytes or ions that are present in the soil liquid phase and at the surface of soil particles. Rhoades et al. (1989) pointed out the three different conduction paths for electric current in unvegetated soils: a) conduction through entirely liquid phase of the soil, b) ionic conduction along the surface or through the volume of two solid soil particle in contact and c) conduction through both solid and liquid phase of the soil. Rhoades developed a model explaining the specific conductivity of soil represented by the above three conductance paths. However, in vegetated soils, an additional path could exist, i.e. electrical conductance via root segments, owing to roots distinct electrical properties as discussed

in the previous section. In fact, electrical conduction via root segments was observed in an experimental study (Aubrecht et al. 2006). Further, the current pathways in the root segment also depend on axial and radial conductivity and internal root structures such as xylem, cortex, and stele (Anderson and Higinbotham 1976; Peruzzo et al. 2020). When the axial conductivity of root segments is higher than the radial conductivity of the root segment, the current flowing inside the root segments tends to flow in xylem along with the root architecture without leaking into the soil for a considerable distance (Peruzzo et al. 2020). On the other hand, if the radial conductivity is higher than the axial conductivity, any electric current inside root segments quickly leaks into the surrounding soil medium.

### *Polarization Mechanism*

Roots are the primary source of polarization in the soil-root system (Weigand and Kemna 2017). Roots are made up of cells that contain organelles and intracellular fluids (ICF), together called the cytoplasm (see Fig. 2.1-a). In-plant cells, these cell components are enveloped by cell membranes and walls. This network is called the symplast. Between cells, there are extracellular spaces, also filled by a liquid, called the extracellular fluid (ECF). The network of water-filled cell walls and ECF is also called the apoplast (Raven et al. 2005). The apoplastic and symplastic pathways are both responsible for the transport of water and nutrients in the plant and therefore play an important role in electrical current flow. Current conduction depends on the resistance of the apoplast and extracellular fluid whereas all membranes and walls play an important role in the storage of electrical charges (polarization). Conduction is assessed by measuring resistance and then calculating resistivity or conductivity, while

polarization is assessed by measuring the capacitance of the biological tissue. Both conduction and polarization can also be assessed simultaneously by measuring the electrical impedance of biological tissue and then calculating the complex resistivity. The real part of the complex resistivity gives information about its conduction properties while the imaginary part gives information about its polarization properties.

The cell membrane is made up of a protein-lipid-protein layer (see Fig. 2.1-a). Polarization occurs in plant tissues because this protein-lipid-protein layer forms a selective barrier to specific ions, resulting in a charge accumulation at the interface. The polarization strength depends on the frequency of the alternating electric field, ionic concentration, water content, tissue composition, and health or structural heterogeneity (Bera et al. 2016). Polarization is assumed to occur at three frequency ranges: the  $\alpha$ -,  $\beta$ -, and  $\gamma$ -range (Schwan 1992).

Current flow pathways in plant tissues depend on the frequency of the applied electrical field. At low frequencies, the capacitance effect of the cell membranes is so high that it does not allow the current passage, and instead the current passes through the apoplast (see Fig. 2.1-b). In this case, the total impedance will be mainly determined by the resistance of the extracellular fluid (Repo et al. 2012; Bera et al. 2016). As the frequency increases, the capacitance of the cell membranes reduces, and the cell membranes become increasingly more conductive. They then allow current flow through the entire cell (see Fig. 2.1-c) such that the total impedance will be a resulting combination of that of the intracellular and the extracellular fluid (Repo et al. 2012; Bera et al. 2016).

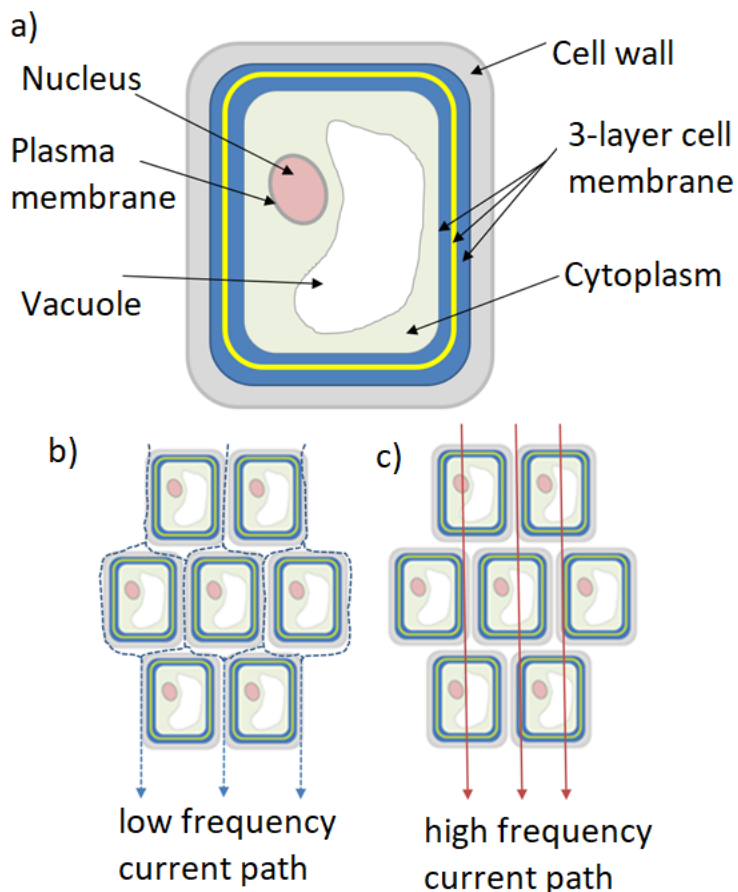


**Figure 2.1:** Schematic illustration of a) plant cell, showing the organelles, the cell wall, and the 3-layer (protein-lipid-protein) cell membrane. The frequency-dependent current paths through plant tissues, showing b) low-frequency current path and c) high frequency

In addition, both root surface and soil particles (containing clay) have negatively charged surface, onto which a thin firm film of positive ions always surrounds. It is termed as a stern double layer. Outside the stern double layer, we have another diffusive layer of negative ions loosely held by the stern layer and

easily influenced by an external electrical field, soil water fluxes, and other dynamics. Relaxation of diffusive double layers present in the soils and plant root surfaces and interfaces occurs at the  $\alpha$ -polarization range (Kemna 2000). These double layers are thin layers of opposite charges with both fixed and diffusive layers. The diffusive layer also affects the ion conduction across the soil-root medium by setting them into relaxation mode. When ions flow across charged soil or root surfaces (double layer), they form ionic gradients due to charge accumulation and redistribution process and thus store electrical charge similar to a capacitor. This capacitive behavior gives rise to the observable polarization response in induced polarization methods (Kemna 2000).

Movement of ions across cell walls within the root, from soils to root and vice versa can cause ionic gradients that make plant root surfaces acquire a net negative charge in soils (Kinraide et al. 1992). The interaction of negatively charged root surface with the surrounding ions present in the soil forms an electric double layer (Li et al. 2015). In an electric double layer, the electric potential exponentially drops from the highest absolute value (ignoring the negative polarity) at the surface of the root to its lowest absolute value away from the root (Fig. 2.2). According to Li et al. (2015), studying electric double layers in root surfaces is important as they influence the nutrient uptake process.

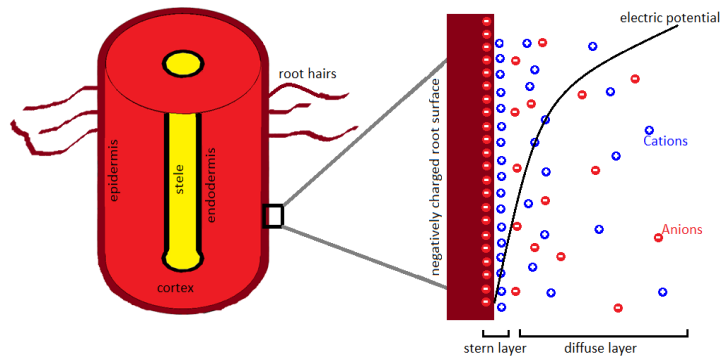


**Figure 2.2:** Schematic of the double-layer structure in the root surface. Figure adapted from Li et al. (2015).

## 1.3 Measured Electrical properties of Roots

### 1.3.1 Resistive properties of Plant tissues: experimental values

The electrical resistivity of plant tissues including roots depends on several variables such as water channel pathways inside the plant tissue, ionic concentration, ambient temperature, ion mobility, measuring voltage, and water content of the plant cells (Fensom 1966; Glerum 1969; Aubrecht et al. 2006). Therefore, electrical resistivity in plant tissues is not material constant and influenced by many factors described above (Aubrecht et al. 2006).

The aqueous solution inside plant cells consists of various solutes that influence the electric current flow depending on the type of solute. For example, solute such as sucrose tends to increase the electrical resistance while ions such as potassium tend to decrease the electrical resistance (Stout 1988). Similar to water flow in plant tissues, electrical current in tissue can choose either apoplastic or symplastic paths or both. These paths have different electrical resistivity

(Anderson and Higinbotham 1976). The passage of DC in plant tissue is mainly apoplastic (Aubrecht et al. 2006) and studies conducted on Maize leaf tissue show that the apoplastic path has the lowest degree of anisotropy in electrical resistance (Ksenzhek et al. 2004).

Further, different types of tissue have different electrical resistivity spanning a very broad range as shown in Figure 2.3 (Dainty and Hope 1959; Fensom 1960; Wilner 1964; Fensom et al. 1965; Hayden et al. 1969; Anderson and Higinbotham 1976; Kulkarni et al. 1981; Repo and Zhang 1993; Cao et al. 2010; Mancuso 2011; Gora and Yanoviak 2014; Ehosioke et al. 2018). Electrical resistivity of root tissues from various works of literature, which range at least two orders of magnitude. Plant cells/root tissues have lower resistivity while fiber/stem tissues seem to have higher resistivity (Fig. 2.1). Some plant tissues like roots are highly anisotropic (Anderson and Higinbotham 1976; Behrens and Gradmann 1985). On the other hand, tissues such as leaves are less electrically anisotropic (Ksenzhek et al. 2004).

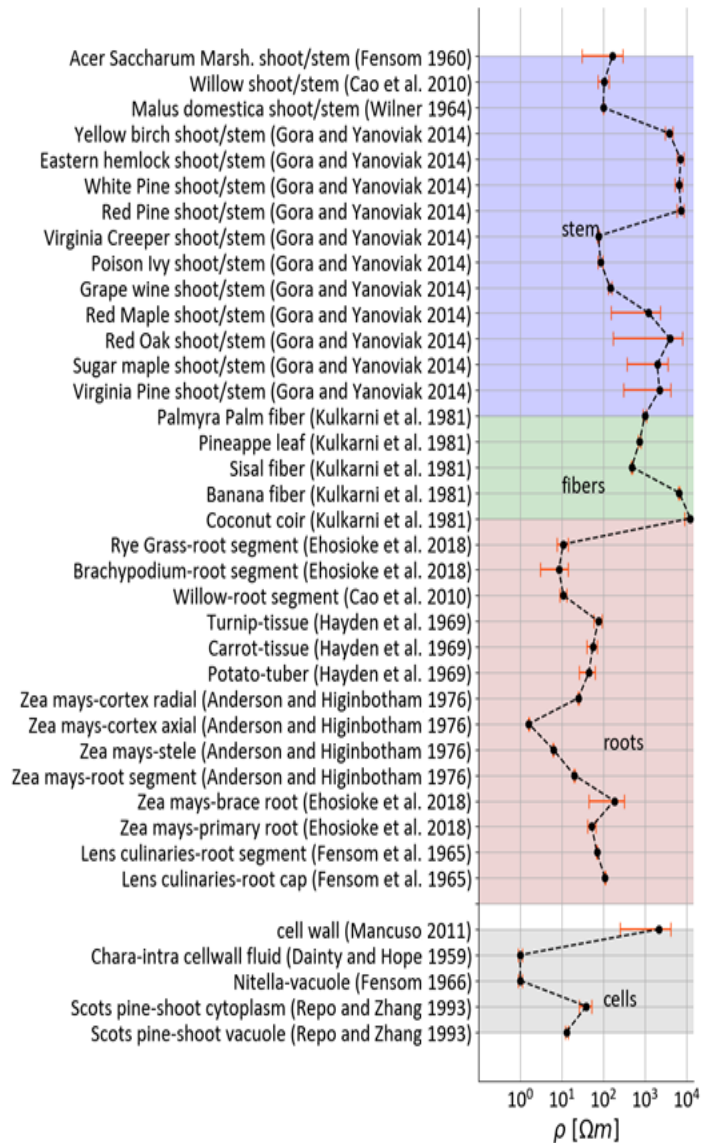


**Figure 2.3:** Electrical resistivity of plant tissues reported in various literature. The color code represents a different type of tissue: root (brown), cells(grey), fibers(green), and stem (blue). The error bar represents the variations within a tissue.

We mention some studies below that used electrical resistance as a parameter to characterize root segments:

- Ginsburg and Lties (1973) studied electrical properties of maize root in a bathing potassium chloride solution by separating roots into stele and cortex structures. They showed that varying the concentration of the bathing medium, the root resistance remained approximately unaffected, but the stele resistance showed variations implying the higher sensitiveness or leakiness of stele layer to the surrounding medium. Thus, maize root behaves electrically like a leaky conducting cable. They also show that xylem has higher electrical resistance than the rest of the root. This suggests that the root structure is anisotropic in its electrical property due to stele and cortex structures.
- Anderson et al. (1976) found that older maize root segments are more electrically conductive than younger roots. They performed studies on excised root segments and confirmed the electric anisotropy of root structure by showing that the outer layer of the root segment (cortex) has very low electrical resistance ( $\sim 50$  k $\Omega$ ) in the radial direction when compared to the axial direction ( $\sim 600$  k $\Omega$ ). By treating cortex and stele as concentric parallel conductors, the reported resistances, when converted into conductivity is of the order:  $\sigma_{root} \sim 0.05$  S/m.
- Repo et al. (2005) studied the electrical impedance of willow roots in hydroponics and could detect its growth based on impedance measurement.
- Cao et al. (2010) reported that the electrical resistance of willow roots grown in hydroponics relates to root physical properties such as surface area, number of lateral roots, and root length.
- Electrical impedance measurements are also used to estimate active root surfaces believed to be the zones of water uptake or nutrient uptake processes (Aubrecht et al. 2006; Urban et al. 2011). Their active root surfaces are also assumed to be the

zones where electrical transfer takes place between soils and roots (Aubrecht et al. 2006).

### *1.3.2 Capacitive property of root tissues: experimental characterization*

The interior of a plant cell such as vacuole and protoplasmic fluids is highly conductive with an electrical resistivity of one to a few tens of Ohmmeter (Dainty and Hope 1959; Fensom 1966). On the other hand, the electrical resistivity of the cell wall that surrounds these cells are two to three orders higher than the cell interiors (Mancuso 2011). Highly conducting materials separated by insulating material makes a plant tissue an electrical capacitor. Because of high capacitances involved, root segments polarize much stronger compared to soils in the presence of induced electric field (Vanderborght et al. 2013). It has been long known that vacuole or protoplasmic size is dependent on age (Stiles 1994) and hence it is not surprising that experiments observe age dependency of electrical capacitances. For example, Dalton (1995) studied electrical capacitance of tomato plants in nutrient solution and observed high correlation to root mass ( $r \sim 0.77$ ). The author showed that root capacitance increased with the age of the root.

Similar to electrical resistivity, many studies have found a positive correlation between root mass [gram] and electrical capacitance of roots [Nano Farads]. Figure 2.4 summarizes the relation between root capacitance and root mass from various literature.

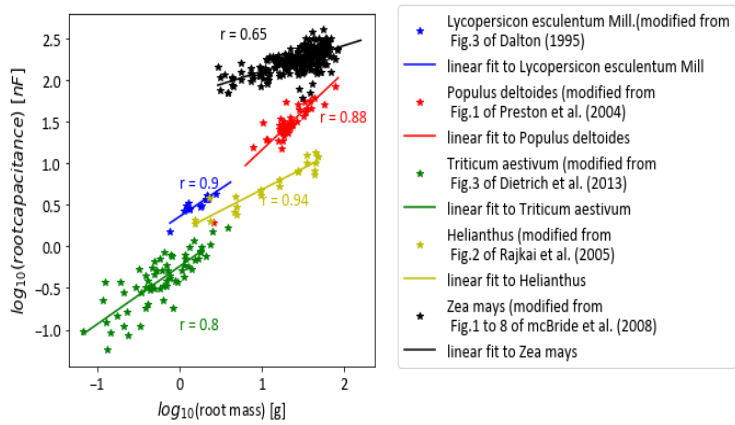


**Figure 2.4:** Log10 of Root mass [g] versus Log10 of the electrical capacitance of roots [nF] of various plant/tree species from different works of literature as described in the legend. Digitization of pictorial data done using WebPlotDigitizer (Rohatgi 2011).

Studies show that the observed capacitance depends on the surface area of roots as well as the content of the cells present inside the root tissues (Chloupek 1972, 1977). For example, some species show better correlation while others show poor correlation between capacitance and root mass as shown in Figure 2.5. Hence, the anatomy of cells, which differs in each species, might also play a role in affecting their macroscopic measured electrical capacitances.

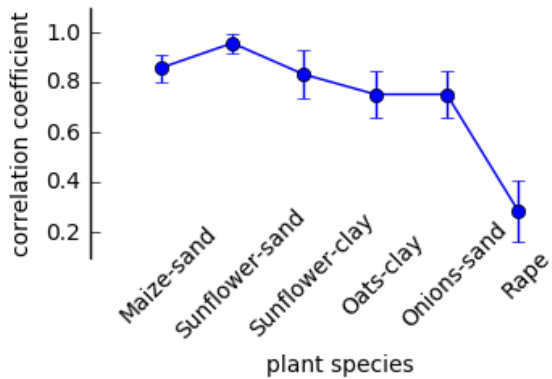


**Figure 2.5:** Correlation coefficient between the fresh weight of roots [g] and electric capacitance of roots [pF] for different species and substrate. The figure made from data given in “Table 1: Correlation and regression coefficients of electric capacitance and capacitance and other root parameters (Chloupek 1972)”.

## 1.4 Overview of electrical methods for root system investigation

### 1.4.1 Electrical Resistivity Tomography (ERT)

ERT, also called DC resistivity imaging or Electrical Resistivity Imaging, determines the distribution of electrical resistivity in the subsurface by performing a set of resistance measurements on the ground surface and/or in boreholes. Measurements are performed by injecting current via two electrodes and measuring the resulting voltage difference at two other electrodes and this in various combinations of current and potential electrodes along a transect or grid. To determine the resistivity of the subsurface, a geophysical inversion of the measured resistances must be performed. The obtained resistivity distribution models are typically presented as tomograms. Since the inverse problem is ill-posed, the obtained resistivity model is non-unique

and typically represents a smoothed representation of the actual resistivity distribution.

ERT is often used for root system investigation because of its high 2-D or 3-D spatial coverage, acquisition speed, minimally invasive nature, and cost-effectiveness. The application of ERT for root studies can be classified into direct and indirect methods. The direct approach focusses on root biomass estimation, while the indirect application investigates physiological processes such as water and nutrient uptake by the root system.

Some ERT studies on cropped soil have demonstrated its ability to obtain information on root mass density from sub-surface electrical resistivity variations (Amato et al. 2008, 2009; Robinson et al. 2012; Rossi et al. 2011; Zenone et al. 2008). For example, studies in *Alnus glutinosa* tree roots show that root mass density (RMD) correlated with ERT derived  $\sigma_{bulk}$  for resistive lignified roots (Amato et al. 2008). Even for smaller herbaceous plants, where there is low root density and roots are finer as compared to a tree, there can still exist a correlation between RMD and  $\sigma_{bulk}$  (Amato et al. 2009). The influence of finer roots on  $\sigma_{bulk}$  as observed by Amato et al. (2009) is due to the fact that finer root segments and their exudates can potentially act as an additional electrically conducting path thereby affecting ERT measurements (Vanderborght et al. 2013). Satriani et al. (2010) was able to distinguish older woody roots and finer younger roots in peach species from ERT obtained images at laboratory conditions (homogeneous soil). Similarly, Jayawickreme et al. (2008) distinguished contrasting vegetation (forest and grassland) effects on root water uptake from ERT images showing the usefulness of this method at field conditions.

Despite the success described above, imaging individual roots via ERT, especially in field conditions,

is a difficult task due to inherent ambiguity resulting from low contrast in electrical resistivity between soils and roots (Urban et al. 2011). As pointed out by Amato et al. (2008), finer conductive root within a soil matrix is difficult to image as compared to woody roots as the contrast between finer roots and soil in terms of electrical resistivity is poor. Sometimes, the electrical resistivity of root and soil may even overlap leading to the indistinguishability of root from soil (Mary et al. 2016).

Bulk soil resistivity is highly influenced by soil moisture content, porosity, mineralogy, temperature, and salinity level and only to a lesser extent by roots. The contrast between roots and soil depends highly on soil type and saturation state (Rao et al. 2019) and is, therefore, varying over time. Besides, fine roots actively take up water & nutrients and release different exudates. These processes affect resistivity at several temporal scales: daily (night vs day, sunny vs cloudy days) to seasonal (growth period vs winter or drought season) (Mary et al. 2018). Overall, ERT lacks sensitivity to root properties due to a lack of contrast between bulk soil and root electrical resistivity and the relatively low volume of a fraction of roots. Using resistivity as a predictor for root biomass without taking these factors into account is therefore highly uncertain to our opinion.

The indirect application of ERT for root studies is based on its high sensitivity to the water content in the root zone, especially when monitoring root systems using ERT (Garré et al. 2012; Michot et al. 2003). Roots modify hydraulic conductivity and porosity of soils thereby indirectly affecting its electrical properties (Ni et al. 2018). Some studies show that rooted soil differs from bare soil in terms of its petrophysical function (Werban et al. 2008). While other studies did not observe the impact of roots on the petrophysical function of soil (Beff et al. 2013). The presence of root segments can cause a significant error or negligible

error in the water content estimates depending on soil type (Rao et al. 2019). For detailed information and recent advances in the ERT method in the agronomical context, the reader is referred to the review of Mancuso (2011) and Vanderborght et al. (2013).

From the above studies, it can be understood that it is difficult to distinguish the influence of roots on the bulk electrical resistivity distribution variations in space or time from that of system properties (soil texture, porosity, stone fraction, mineralogy) and state variables (soil temperature, fluid conductivity, soil moisture). Although ERT is more sensitive to the moisture and salinity changes near the roots, the influence of their biomass is still present and adds time-dependent uncertainty to the quantification of the studied processes.

#### *1.4.2 Electrical Impedance Tomography*

Electrical Impedance Tomography (EIT) is similar to ERT in terms of set-up and measurement but measures the electrical capacitive response or chargeability of the sub-surface in addition to resistivity either using time-domain EIT approach or using frequency domain EIT approach. Accordingly, Time Domain Induced Polarization (TDIP) is the term used for time-domain EIT while Spectral Induced Polarization (SIP) is the term used for frequency-domain EIT.

In TDIP, the sub-surface is excited with a step signal and the time decay of the voltage response is measured. The decay rate of the voltage response contains information on polarizability or capacitive response of the sub-surface (Binley and Kemna 2005). In SIP, we apply a continuous time-harmonic alternating current of a given frequency to the sub-surface and the resulting response is measured. The phase difference between response and source signal contains information on polarizability or the capacitive response of the soil-root continuum (Mary et al. 2017). We

illustrate of time domain and frequency domain approaches in Figure 2.6.

Weigand and Kemna (2017) investigated the suitability of multi-frequency EIT to characterize and monitor plant root systems in a laboratory rhizotron experiment. They monitored the Spatio-temporal distribution of the complex electrical resistivity of the root system of an oilseed plant (*Brassica napus*) in a water-filled rhizotron under nutrient deprivation using EIT. Total polarization parameters recovered from the multi-frequency EIT results showed a low-frequency polarization response of the root system, which enabled a successful delineation of the spatial extension of the root system. The magnitude of the overall polarization response decreased along with the physiological decay of the root system due to nutrient deprivation. The length scales (i.e. frequencies) at which polarization processes were occurring did also change due to prolonged nutrient deficiency.

Some authors speculate that SIP and TDIP methods are better suited than ERT alone in imaging roots due to higher contrast between root segments and soil medium in terms of electrical polarizability or capacitance as compared to contrast in electrical resistivity alone (Mary et al. 2016, 2017; Vanderborght et al. 2013; Weigand and Kemna 2017).

Mary et al. (2016) investigated the suitability of EIT for mapping tree roots in dikes, they concluded that EIT is useful to interpret anomalies produced by woody roots. A similar study by Mary et al. (2017) used EIT to map roots embedded in the soil (field study) and observed that the maximum phase contrast between root and soil was found at a frequency of 1 Hz and noticed anisotropy in the polarization process such that the polarization signal was strongest when the current line was aligned to the root. They found that root water uptake induced soil dryness increased the electrical polarization signatures of the root at shallow depths (~20cm) in loamy soils. However, at deeper depths

(~70cm) the chargeability did not correspond to root density. In addition, the observed polarization signature depended strongly on soil water content level, rainfall, and root water uptake. Soil polarization sometimes masked the root polarization response suggesting the important role played by soil-root polarization contrasts (Mary et al. 2016). Even concerning polarization, roots can have low contrast as compared to soil depending on the frequency of measurement and the direction of measurement protocol. For example, Mary et al. (2017) found that the chargeability of root/soil ratio to be as low as 1.5 at 1.4 Hz and higher frequencies soil effect dominated. They could also maximize the polarization signatures of roots by having measurement current lines in parallel with the root orientation. Also, they observed some phase anomalies in the region of no root presence (Mary et al. 2017). EIT is very promising for root system investigation, however, some challenges need to be addressed in its application to explore its full potential.

The challenges in the use of EIT includes: (a) difficulty in obtaining high-quality data due to noise and electrode polarization (b) forward modeling errors resulting from imprecise electrode locations, inaccurate discretization etc. (Zhao et al. 2019) (c) complex resistivity inversion is still basic and thus should be improved e.g. related errors on inversions could be addressed by the use of data weighting or filtering (Binley 2015; Adler and Boyle 2017).

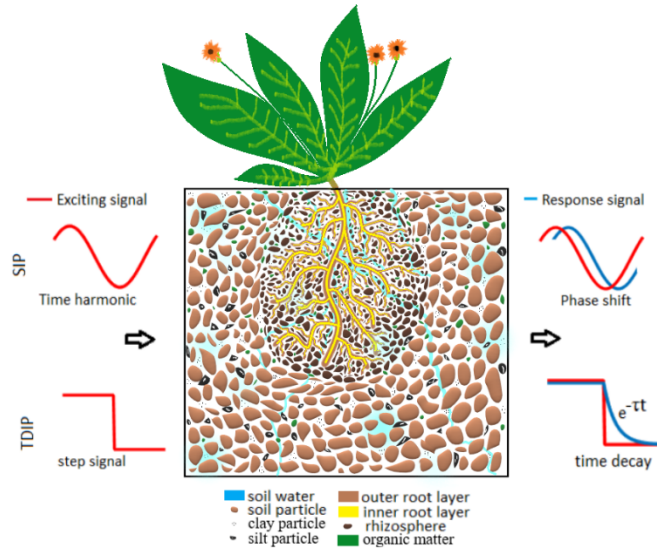


**Figure 2.6:** Schematic of a soil-root continuum with an illustration of SIP and TDIP method.

## 1.5 Petrophysical transfer relations

### 1.5.1 Bare Soil

Archie formulated the first commonly used petrophysical empirical relation better known as Archie's law (Archie 1942). This empirical relation relating soil water content, denoted by  $\theta$  and  $\sigma_{bulk}$  for unsaturated soil is given by Equation 2.7, where the fitting parameters ( $m$  and  $d$ ) vary for different types of soil (Friedman 2005; Vanderborght et al. 2013):

$$\sigma_{bulk} = \sigma_w n^m S^d \quad (2.7)$$

where  $S$  is the degree of water saturation ( $S = \frac{\theta}{n}$ ),  $\theta$  is the volumetric water content,  $n$  the porosity of soil (assumed to be equal to saturated water content:  $\theta_s$ ),

$\sigma_{bulk}$  the bulk electrical conductivity of the soil medium,  $\sigma_w$  the conductivity of the soil fluid phase.

According to Equation 2.7, soil can conduct electricity only when it is wet, and its solution is conductive. Thus, the soil becomes a perfect insulator if it is completely dry. Hill and Milburn (1956) showed that for clayey soils, Archie's law needs additional terms to explain measured data. Waxman and Smits (1968) modified Archie's law by adding a surface conductivity term (Friedman 2005):

$$\sigma_{bulk} = \sigma_w n^m S^d + S^{d-1} \sigma_{surface} \quad (2.8)$$

where,  $\sigma_{surface}$  is the surface electrical conductivity of the solid phase of the soil (clay content) which is dependent on mineral content, porosity, water content, and electric conductivity of soil fluidic phase (Vanderborght et al. 2013). In some cases, clay content dominates the petrophysical relation as compared to soil water content. For example, Sudduth et al. (2005) found that apparent electrical conductivity measured using soil sensors correlates better with a clay content of the soil than soil water content. Hence, the petrophysical model needs site-specific calibration to fit the observed data.

Some authors have used simplified Waxman-Smit model in their fieldwork (Beff et al. 2013; Garré et al. 2013a; Chen et al. 2019):

$$\sigma_{bulk} = a\theta^c + b \quad (2.9)$$

where  $a [S m^{-1}]$ ,  $b [S m^{-1}]$  and  $c (-)$  are the fitting parameter accounting for surface and fluid conductivities in soil. Some studies also found that by taking the exponential of Equation 2.9, a better fit

could be achieved for electrical resistivity ( $\rho = \frac{1}{\sigma_{bulk}}$ )  
 (Ackerson 2013) :

$$\rho = \exp(a\theta^c + b) \quad (2.10)$$

In Figure 2.7, we compare the electrical resistivity ( $\rho = \frac{1}{\sigma_{bulk}}$ ) versus soil water content ( $\theta$ ) from the experiments of Wunderlich et al. (2013) and Al Hagrey et al. (2007) along with the range of root electrical resistivity values. Hence, at lower water content ( $<= 0.15$ ), the root system represents a more conductive medium than soil. We should observe root signatures in terms of both resistivity measurement and polarization measurements at these water contents. An experimental study by Mary et al. (2016) confirms this conclusion. They observed that the polarization signature of roots was detectable only when root water uptake leads to drier soil, while anomalies were present at higher water contents.

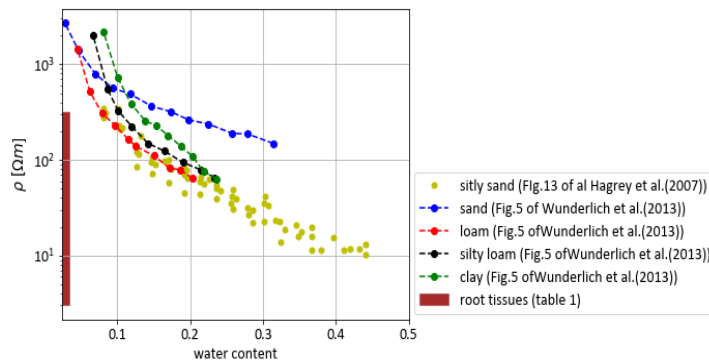


**Figure 2.7:** Petrophysical experimental data for different types of soils from works of literature as described in the legend. We show the Root electrical resistivity from table 1 as a brown patch to the left illustrating the resistivity contrast between root and soil medium. Digitization of pictorial data done using WebPlotDigitizer (Rohatgi 2011).

### *1.5.2 Impact of Vegetation*

Soil colonization by roots can affect soil hydraulic conductivity (Rasse et al. 2000; Kodešová et al. 2006), soil bulk density (Young 1998), and soil porosity (Bodner et al. 2014). The electrical conductivity of soil, in turn, depends on these soil properties (Friedman 2005). Also, swelling and shrinking of roots cause air gaps that are spatially and temporally changing in-between soil and root (Carminati et al. 2009). Root movements and their decay also create macropores in the soil (Holtham et al. 2007). Air gaps and macropores due to roots make soil electrical measurements anisotropic. Further, in the regions where the root is in contact with soil, known as root surface absorption area, root segments serve as an additional path for the electrical current to flow within it (Aubrecht et al. 2006; Urban et al. 2011). The root tissues have distinct electrical properties (see next section). Hence, it is not surprising that rooted soils can behave quite differently as compared to bare soils in terms of electrical response.

Here we compare three different experiments from different studies to illustrate the impact of vegetation:

- *Experiment 1:* Werban et al. (2008) conducted a pot experiment (30 cm radius, 50cm height) with Lupine roots in sandy soil and provided the electrical resistivity versus water content for bare and rooted soil in Figure 3 of their paper. The digitized data from this figure is shown here in Figure 2.6-a. The pot experiment consisted of a pre-grown fully developed Lupine root system. In Figure 1.1-a, we saw that root decreases the electrical resistivity of soil.
- *Experiment 2:* Ni et al. (2018) conducted a field experiment in a region covered with roots of the Chinese Banyan tree and Bermuda grass as well as in the region of bare soil. They provided the water

content as a function of time in Figure 6 and electrical conductivity data as a function of time in Figure 5 of their paper. We extracted the data and converted it into resistivity versus water content plot (Fig. 1.1-b). Interestingly, we observe the decrease in electrical resistivity due to roots similar to the work of Werban et al. (2008).

- *Experiment 3:* Mary et al. (2016) conducted a pot experiment (length: 37 cm, height: 28 cm) with an excised Poplar root of diameter 4 cm and length 20 cm buried within the container. They compared electrical conductivity as a function of frequency for bare soil and rooted soil at three different water content levels in Figure 6 of their paper. We first extracted the data from this figure, averaged the electrical conductivity with frequency axis, and then converted it into electrical resistivity. Figure 1.1-c showed the extracted data as a function of reported water content levels. Although the impact of roots was smaller, the trend of decreasing resistivity due to roots was evident.

## 1.6 Soil-root mixing

Figure 2.8 illustrates the electrical mixing of soil and root components in vegetated soils. In the study of Rajkai et al. (2005), the shape of rooted soil spectrum is similar to root specific spectra while its magnitude is in-between root only and soil only spectra's (Figs. 2.8-a and 2.8-b). They used sunflower species grown in a sandy medium with a soil water content of around 25%.

On the other hand, the shape of phase spectra for silty soil with poplar root looks similar to soil-only spectra and its magnitude is in-between root-only and soil-only (Fig. 2.8-c). We must note that the conditions of Mary et al. (2017) were different from Rajkai et al. (2005).

Mary et al. (2017) used poplar root in silty soil with a soil water content around 10%, which is significantly lower than the water content of Rajkai et al. (2005). Also, the species and volumes of roots in the two studies were different. However, we see a general trend of roots affecting the soil-root continuum in terms of SIP spectra.

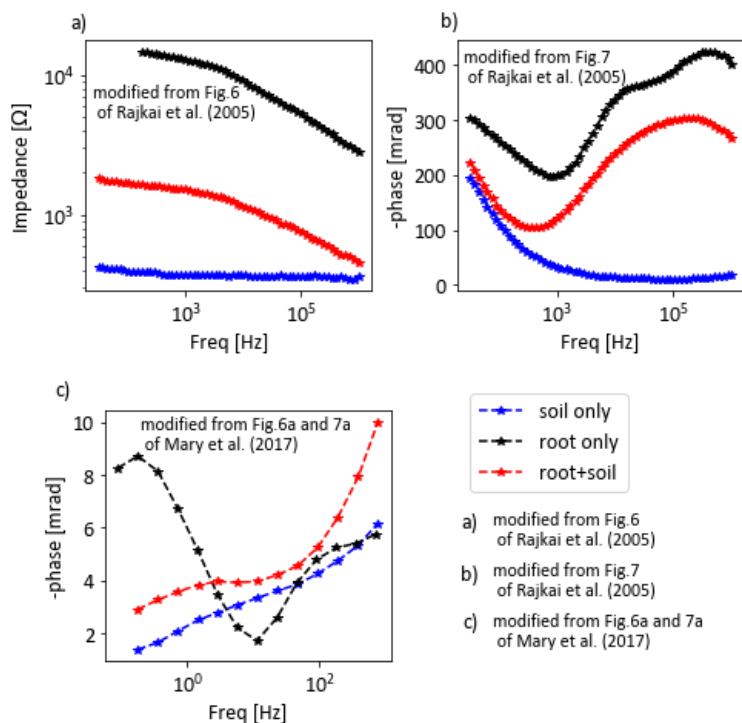


**Figure 2.8:** Comparison of soil only, root only, and root-soil combined data. a) Electrical impedance spectrum of sunflower roots from Figure 6 of Rajkai et al. (2005). b) Phase spectrum of sunflower species from Figure 7 of Rajkai et al. (2005). c) Phase spectrum of poplar species from Figures 6-a and 7-a of Mary et al. (2017). Digitization of pictorial data done using WebPlotDigitizer (Rohatgi 2011).

The two medium, soil and root mix electrically to give a single soil-root continuum response. To separate the soil and root components, understanding of individual soil/root response and their geometrical connection is

essential. Roots represent complex architecture embedded in the soil matrix. Neither root nor soil has simple geometry to determine the electrical mixing behavior analytically calling for a numerical model.

However, assuming root and soil to be two phases homogeneous distribution of electrical conductivities,  $\sigma_{root}$  and  $\sigma_{soil}$ , we can characterize such a simplified system analytically by power averaging mixing model (Winchen et al. 2009):

$$\sigma_{mm}(\alpha) = \left[ f(\sigma_{root})^\alpha + (1 - f)(\sigma_{soil})^\alpha \right]^{1/\alpha} \quad (2.11)$$

where,  $\alpha$  = Mixing model exponent describing the geometry of two phases,  $f$  is the relative area of  $\sigma_{root}$  to the total area and  $(1 - f)$  is the relative area of  $\sigma_{soil}$  to the total area. The  $\sigma_{mm}$  in Eq. (11) is the effective electrical conductivity predicted by the power-law mixing model for different  $\alpha$  ranging from -1 to 1. If the two-phase component is perfectly in series connection, then  $\alpha = -1$  and for perfectly parallel connection,  $\alpha = 1$ . In reality, the soil-root system represents a mixture of series and parallel connection, and hence,  $\alpha$  captures this complex connectivity information.

## 1.7 Need for Explicit modeling of root

Equivalent electrical circuit models are essential to interpret contributions of different processes in the soil-plant continuum governing electrical conduction and polarization during plant- or field-scale measurements. The use of multiple frequencies/broadband allows the determination of length scales, which is essential for the development of electrical circuit models. Small-scale measurements

such as Resistance and polarization measurement on root segments (with or without the plant still connected) are important to validate these electrical circuit models and determine the contribution of individual components on the behavior of the full root architecture in the soil. Recent studies show low-frequency polarization of root systems probably originating from polarization at various double layers, be it at cell membranes, or larger ion-selective structures such as the Caspary strip or the root surface. This is not only important to study roots, but also to study soil moisture and solute transport dynamics about plant growth since the contribution of the presence of roots to the measured electrical signal is now typically neglected.

Dalton (1995) developed the first equivalent electrical network model comprising of resistor-capacitor components that could represent the electrical response of a root system architecture. According to the author, the root capacitance was an indirect measure of the active zone of the root surface area that exchanges ions and water with the surrounding soil.

A similar lumped circuit based impedance model of the root system was later developed by Ozier-Lafontaine and Bajazet (2005). In their model, the soil was a pure resistor, while the soil-root interface and root-stem continuum comprised of parallel resistor-capacitor components. However, they could not strictly relate soil-root interface processes to the lumped circuit parameters. Earlier, Repo and Zhang (1993) showed that a distributed model with reduced circuit components (resistors and capacitors) of Zhang and Willison (1993) fits the impedance of plant tissues better than lumped circuit model. Even with the distributed model, they could fit only the bark layer but not the wood. They observed large variations among different samples due to physiological differences. To quantify the electrical response of roots in soils, a widely used circuit model is inadequate in capturing

the complex geometry of root architecture and its electrical connection to the soil matrix for the following reason: First, there are few parameters in circuit model to fit large variations of electrical response observed in soil-root medium leading to non-uniqueness of solution. That is, more than one circuit parameters can explain the observed response. Second, the electrical circuit assumes components to be connected in series or parallel but in reality, root structures are complex and are connected to soil neither in series nor parallel fashion.

Thus, explicit modeling of root structures becomes important (where circuit model fails) to understand the electric response of roots in soils.

## 1.8 Electrical measurements on root segments

To get insight on root electrical properties and to parametrize the process-based model that we develop in the next chapter, we describe the experimental setup and some of the results of Ehosioke et al. (2018) which is a part of the Ph.D. thesis of Solomon Ehosioke who is also our collaborator and part of an e-root project that funded this Ph.D. thesis (Ehosioke et al. 2018).

### 1.8.1 Introduction

We examined four different species for their electrical properties: a) Maize (*Zea Mays*), b) Ray Grass (*Lolium Perenne*), c) Brachypode (*Brachypodium distachyon*) and d) Rapeseed (*Brassica napus*) for their electrical properties. The different root species considered here have varying morphology. Maize, Brachypodium, and Ray grass are classified as monocot roots. In monocot roots, the root segments are spatially spread into complex networks and all the segments (primary and secondary) participate equally

in water and nutrient uptake process. Ray grass has a fibrous root system that has numerous branches and very fine root segments inside the soil. In addition to primary roots, maize has an aerial root system, where the root develops above the soil and then penetrates the soil to form fibrous root architecture. Brachypodium is architecturally simpler compared to Maize and Ray grass in terms of root architecture. Rapeseed develops a deep taproot and a near-surface fibrous root system.

### 1.8.2 Measurement of Electrical DC Resistance

The electrical resistance of root segments was measured using a digital multimeter (Fluke 289) and was converted into electrical conductivity ( $\sigma_{root}$ ) by approximating the root segment as a cylindrical geometry similar to Cao et al. (2010). All species (except Rapeseed) were considered in this experiment. The measurement direction of root segments in Cao et al. (2010) is from root apex towards root collar while it is opposite in the case of our experiment (Ehosioke et al. 2018). The segment length between the two-measuring electrode was 2cm. In Figure 2.9, we show the measurement set-up used to measure  $\sigma_{root}$  for root segments. To improve the electrical contact between root segments and measuring electrodes, conductivity gel (Rodisonic, from Pannoc Nv/SA Belgium) was used.

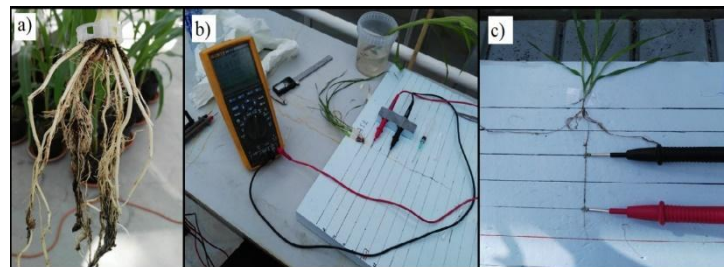


**Figure 2.9:** a) Uprooted maize roots washed with distilled water, b) Experimental set-up for measuring the electrical resistance of intact root segments using Fluke 289

multimeter, and c) close-up view of electrodes and intact root segment.

Cao et al. (2010) measured resistivity of willow root segments to be in the range of 8.9 to 13  $\Omega\text{.m}$  with a mean value of 10.5  $\Omega\text{.m}$ . They find that the root segments have lower resistivity compared to that of the stem segments whose range was between 73.9 to 134.8  $\Omega\text{.m}$ . From Figure 2.10, we see that the resistivity of willow root, ray grass, and brachiopods are approximately in the same range (3 to 20 Ohm m) while the maize root has slightly higher resistivity and the brace roots of maize show the highest resistivity. For maize, we observe a gradual decrease in electrical resistivity of intact maize root segments as the segment distance from root collar increased. The trend is different in primary and brace roots, where the brace root resistivity decreases much more rapidly with increasing distance of the segment from the root collar compared to primary root segments.

The electrical resistivity of roots also varies concerning the root cross-sectional area. Our measurements indicate that thinner roots have lower electrical resistivity as compared to thicker roots (Fig. 2.9-b). This could be due to the higher water content of younger roots. Since we measured intact root segments, the surface electrical resistivity of endodermis and contact resistance of stele and cortex layers of the root are accounted for in the measurements. The thicker outer layer (cortex) of the root is electrically more insulating than water-rich younger roots or inner part (stele) as seen in early studies of Anderson et al. (1976). However, our measurements represent the combined resistivity of cortex and stele in an intact form.

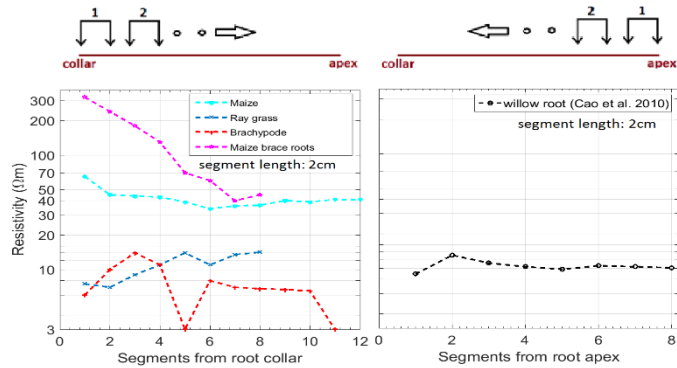


**Figure 2.10:** a) Resistivity of different root species Maize (primary roots), Maize brace root, Brachypode, Ray grass, and b) willow root (data taken from Cao et al. 2010).

Age-dependent electrical resistivity variations within a given species were earlier studied in poplar roots (Zenone et al. 2008). Figure 2.10 shows that within the same species (Maize), in addition to age, different types of roots (brace and primary roots) can have different electrical properties.

### 1.8.3 Measurement of Polarization Signatures

The impedance was measured at different frequencies ranging from 1 to 45 kHz using the measurement set up of Zimmermann et al. (2008) shown in Figure 2.11. In addition to Maize (*Zea Mays*), Ray Grass (*Lolium Perenne*), Brachypode (*Brachypodium distachyon*), we included an additional species: oilseed (*Brassica napus*). It consisted of a signal generator and a 4-electrode setup for measuring impedances at different frequencies. The custom-made root holder with electrodes (Fig. 2.11-c) was 3-D printed at the Institute of Bio- and Geosciences, Forschungszentrum Jülich GmbH. We placed conductivity gel in-between root segments and electrodes for good contact. We then corrected the measured impedances for the effect of conductivity gel to obtain the root only electrical

properties. Measured impedances were then converted to electrical conductivity and phase (or complex conductivity) using the measured radius of root segments, assuming cylindrical root geometry as described in Cao et al. (2010). We used a digital caliper to measure the radius of root segments accurately. We repeated the measurements for four replicates within a given species for a statistical average.

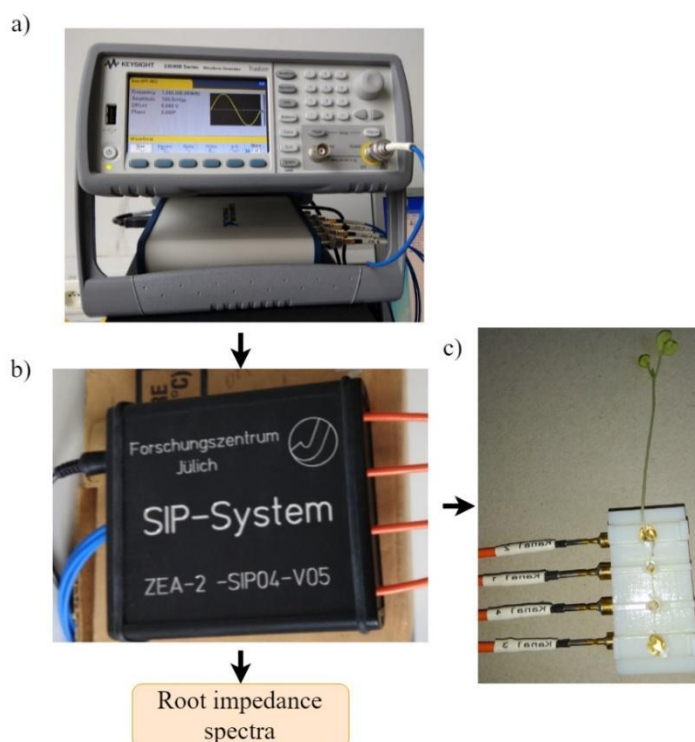


**Figure 2.11:** Block diagram of SIP measuring system with its main components: a) signal generator, b) SIP 4-electrode system and c) root segment holder with electrodes.

Figure 2.12 depicts the measured SIP response of different root species using the setup of Figure 2.11. We chose four different species (Fig. 2.12) and at the time of measurement, they were four-week-old samplings from the date of sowing. The magnitude response of the electrical conductivity of different

species followed a similar trend, that is, they tend to increase with increasing frequency. The ranges of electrical conductivity in magnitude are species-specific with oilseed roots being highly conductive and *Brachypodium* being the least conductive among the species compared (Fig. 2.12-a). We can attribute these differences in magnitude response to anatomy, ionic, and water content of the root segments. On the other hand, we can distinguish different species in phase only above 100 Hz, below which all species have approximately the same response (Figure 2.12-b).

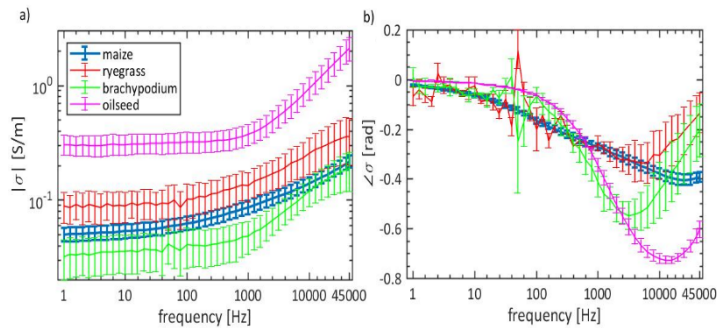


**Figure 2.12:** Spectral Induced Polarization signature of four-week-old root segments (Spectra of electrical conductivity): a) magnitude and b) phase. The error bar represents the standard deviation of four different replicates within each species.

## 1.9 Summary and Conclusions

Both plant scientists and hydrogeologists use/see potential in electrical methods to characterize the root system of plants. Measurements show correlations of electrical properties with root biomass and/or root activity, confirming that roots can behave like resistors and capacitors such that both conduction and polarization occurs when roots are present. Although initial studies focused on resistance and capacitance

measurements used to study conduction and chargeability in roots separately, the most potential lies in measurements focussing on impedance. This is because it allows both the resistance and the chargeability to be quantified, giving information on different properties of the root zone simultaneously. The resistance of bulk soil with roots is still mostly connected to soil moisture dynamics and is best used to study roots indirectly (looking at water depletion patterns they cause). Chargeability is related to the anatomy of the tissue and cell structure (e.g. cell membranes properties) and fluid content properties, and plant physiological state.

In this chapter, we provided the context under which understanding the electrical properties of the soil-root continuum is relevant to ERT and EIT methods. The electrical properties of the soil-root medium are not material constants but depend on several other properties. Soil-root electrical contrast needs to be high enough to have a detectable root signature for root imaging applications using ERT/EIT. Our review suggests that how complex this contrast can be. Though roots possess stronger polarization response, at higher soil water content, they become unobservable due to soil dominance (Mary et al. 2016). Figure 2.6 suggests that lower water content in soil should make electric current to take root segments as a flowing path and hence ideal for root imaging with the EIT method.

From the measurement of root segments described in the previous section, we can conclude the following:

- a) The electrical resistance of a root segment is species, age, and root type-dependent (Fig. 2.9).
- b) Compared to soils and earth materials, whose polarization range from 0 to 20 milliradians (Vanhala and Soininen 1995; Vanderborght et al. 2013), we can see that the root segment exhibits a very large polarization signature (0.2 to 0.6 radians).

- c) We have parameterized the effective electrical properties of root segments which can be used to model soil-root electrical response at root architectural scale.

## 1.10 Future research perspectives

More studies are needed to link root physiology and electrical properties (conduction and polarization) of roots at different scales. Equivalent circuit models are used to derive effective properties to explain electrical polarization in roots at the macroscopic scale in bulk soil or water. Nevertheless, data obtained at the root segment scale are necessary to validate phenomena underlying conduction and polarization occurring at the root segment and root architecture scale and establish the models summarizing these phenomena.

Due to the complexity of the root system architecture (RSA) embedded in the soil matrix, upscaling electrical properties measured at root segment scale to plant scale or to field scale is a challenging task (Mary et al. 2016; Weigand and Kemna 2017). Process-based multi-scale numerical modeling of a soil root continuum can thus pave a way for our understanding of the upscaling mechanism as we move from segment to plant and to field scale. A recent detailed numerical study at plant scale shows that roots indeed affect ERT measurements and the effective EC (Rao et al. 2018). However, explicitly representing root architecture (as in their study) in the computational domain demands a very high spatial resolution in the numerical grid, thus increasing computational time and memory

consumption. Further research on numerical approaches for such mechanistic models and the effect of the multiple scale levels involved in the underlying processes on the macroscopic properties is required.



## PART III

# ELECTRICAL SIGNATURE OF ROOTS AT RHIZOTRON AND POT-SCALE



The third part of the thesis presents results from a coupled electrical and water flow model and the analysis of root signatures in geo-electric measurements.

*Vṛkṣo raksati rakṣitā:*

Meaning: You protect the trees and the trees will protect you/ save the trees, they will save the world

Sanskrit Quote





# **3 A PROCESS-BASED MECHANISTIC MODEL FOR ELECTRICAL CONDUCTION IN THE SOIL-ROOT CONTINUUM**

Chapter adapted from:

Rao S, Meunier F, Ehosioke S, Lesparre N, Kemna A, Nguyen F, Garré S, Javaux M. Impact of Maize Roots on Soil–Root Electrical Conductivity: A Simulation Study. Vadose Zone Journal. 2019 Oct 1;18(1).

---

## **ABSTRACT**

Electrical Resistivity Tomography (ERT) has become an important tool to study root-zone soil water fluxes in field conditions. ERT results translate to water content via empirical petrophysical relations, usually ignoring the impact of roots. However, studies in the literature show that roots in soils could play a non-negligible role in bulk electrical conductivity of the soil-root continuum. Yet, we do not completely understand the impact of root segments on ERT measurements.

In this numerical study, we coupled an electrical model with a plant-soil water flow model to investigate the impact of root on virtual ERT measurements. The coupled model can simulate root growth and development, water flow in soil and root systems, as

well as electrical transfer in the soil-root continuum in 3-D.

ERT forward modeling in 3-D illustrates that in rooted soils shows that for every 1% increase in root to sand volume ratio, there can be 4 % increase in uncertainty of effective electrical conductivity, computed using the model, caused due to the presence of root segments while such uncertainty in loam medium is 0.2%. Further, this uncertainty is three times higher (13% in the sand and 0.7% in loam) in apparent conductivity computed using point electrodes. Further, the influence of root segments on ERT measurements depends on the root surface area ( $r \sim 0.6$ ) and electrical conductivity contrast between root and soil ( $r \sim 0.9$ ) as revealed by correlation analysis. We find that the water uptake process dominates the effective electrical properties. This study is important in the context of accurate water content prediction for automated irrigation systems in sandy type soil.

## 2.1 Introduction

Understanding root water uptake and associated nutrients are critical for crop management (e.g. Gregory et al. 2005) but remain a challenging task due to the inherent difficulty to collect observations in soils (e.g. De Dorlodot et al. 2007). Geophysical monitoring of root-zone soil moisture has received growing interest in the past decades to tackle this challenge. One such method is Electrical Resistivity Tomography (ERT), which aims at retrieving the 2-D or 3-D distribution of the electrical conductivity ( $\sigma$ ) or its inverse (electrical resistivity) in the soil from electric resistance measurements at discrete electrode locations. The  $\sigma$  is then related to the property or state variable of interest - for instance, the soil water content,  $\theta$ , the porosity, the electrical conductivity of the soil fluid ( $\sigma_w$

), the temperature or the mineral composition (Friedman 2005) - through a proper petrophysical relationship, e.g. quantifying  $\sigma$  as a function of  $\theta$ . In cropped fields, ERT has been increasingly used for monitoring soil water content (Michot et al. 2003; Srayeddin and Doussan 2009; Beff et al. 2013; Garré et al. 2013b; De Carlo et al. 2015; Brillante et al. 2016; Vanella et al. 2018). More recently, ERT-estimated water content was used for phenotyping root systems at field scale (Whalley et al. 2017). The authors monitored changes in  $\sigma$  of the soil root zone in drying conditions at different soil depths, which acted as a proxy for root activity. However, the bulk electrical conductivity of a vegetated soil potentially containing roots, denoted by  $\sigma_{bulk}$ , not only depends on  $\theta$ , but also on roots and their impact on soil structure. In some field experiments, different petrophysical relations for soils with and without roots have been observed (Werban et al. 2008; Michot et al. 2016; Ni et al. 2018). However, in lysimeter experiments, studies show petrophysical function was time invariant despite ongoing root growth (Garré et al. 2011). The Figure 2.8 highlights that the contrast between  $\sigma_{root}$  and  $\sigma_{bulk-soil}$  is a function of plant species, in addition to the soil bulk properties or state variables and indicates that roots could have a measurable but variable impact on ERT measurements.

For a given species,  $\sigma_{root}$  is generally a function of root anatomy, which can be related to root age, root order, or root diameter. In their study, Anderson and Higinbotham (1976), found that older maize root segments are electrically more conductive than younger roots. Their study was performed on excised root segments. They showed that the outer layer of the root segment (cortex) has very low electrical resistance ( $\sim 50$  k $\Omega$ ) in the radial direction when compared to the axial direction ( $\sim 600$  k $\Omega$ ). By treating cortex and stele as concentric parallel conductors, the reported resistances,

when converted into conductivities are of the order  $\sigma_{root} \sim 0.05$  S/m. However, the electrical behavior of intact root segments embedded in the soil might be different as compared to excised segments. Another study by Cao et al. (2010) reported that the root electrical resistance could be related to root properties such as surface area, number of lateral roots and root length. Studies on poplar roots show that  $\sigma_{bulk}$  of the soil-root medium may increase or decrease with the increase in root mass density depending on the age of the plant (Al Hagrey 2007; Zenone et al. 2008). Also, some studies found a correlation between root length/mass density and electrical resistivity obtained from ERT (Amato et al. 2009; Rossi et al. 2011). Along with root geometrical properties such as root length/surface/mass densities, the electrical contrast between root and soil also plays a role in influencing ERT results. However, it is not clear that how much proportion of electrical signature of root present in the ERT measurements can be attributed to each of these root parameters such as electrical contrast, root length/surface/volume densities.

Beyond the impact of the electrical conductivity of root tissues, root-related processes like water uptake, exudation or solute uptake will also affect the electrical properties of the rhizosphere, i.e. the soil zone close to root segments, thereby affecting the  $\sigma_{root} - \sigma_{bulk-soil}$  contrast. Recent ERT experiments on orange orchard fields suggest that ERT results are more sensitive to root water uptake patterns (Vanella et al. 2018) than to the resistive lignified roots. Performing such experiments is however costly and time-consuming and is difficult to reproduce for various species and soil types, hence the need for modeling. Al Hagrey and Petersen (2011) previously studied the impact of roots on ERT imaging by using a root growth model (Wilderotter 2003) but ignored the inherent heterogeneity of  $\sigma_{root}$  and  $\sigma_{bulk-soil}$ . To understand the

effect of root system connectivity and their impact on  $\sigma_{bulk}$ , a model where roots are explicitly represented and functional is needed. Explicit root representation using an unstructured finite element mesh has been studied for water and nutrient uptake processes (Wilderotter 2003; Tournier et al. 2015). Here we extend it to ERT forward and inverse problem coupled to a plant-soil water flow model and a realistic complex root system architecture.

The objective of this chapter is to investigate the direct (presence of root segments) and indirect (root water uptake) impacts of plant roots on the effective soil-plant electrical conductivity. Specifically, we wanted to quantify the effect of soil-root contrast, plant growth, and root water uptake on the petrophysical relations.

To achieve this, we developed a coupled electrical-hydraulic soil-plant model and applied it to generate virtual rhizotron experiments. A rhizotron is a thin container (typically around 2 cm x 20 cm x 40 cm) filled up with a growing substrate in which plant roots develop, which allows the observation of the root system architecture evolution and sometimes of the substrate water content (Garrigues et al. 2006) (Ahmed et al. 2018) and can thus be used to investigate how soil heterogeneity affects root growth and uptake (e.g. Bauke et al. 2017). In this study, the soil-root system is first modeled with a fine spatial resolution for the roots using a 3-D unstructured mesh for the ERT forward simulation. The virtual environment allows us to account for root architecture, soil water redistribution, soil heterogeneity, root-specific electrical property along with root growth, and transient transpiration.

## 2.2 Materials and Methods

Our virtual experiment consists of monitoring with ERT the changes of electrical conductivity of a transpiring Maize plant growing in a thin rhizotron for 21 days. Root growth, root maturation, and root water uptake generate changes in the soil water and electrical conductivity field distributions, which will affect ERT measurements. Figure 3.1 summarizes the various steps described below in a flowchart. First, a simulation of root water uptake and root growth of a maize plant in a rhizotron is run with a soil-plant water flow model (R-SWMS, Javaux et al. 2008), which generates maps of soil water distribution ( $\theta$ ) and root architecture evolution. Then these distributions are transformed into detailed electrical conductivity ( $\sigma$ ) maps through pedo-physical relations. Third, these distributions are used to simulate a virtual ERT measurement to get apparent conductivities ( $\sigma_{app}$ ) or synthetic ERT data. Fourth, the synthetic ERT data is inverted to assess the impact of roots in ERT inversions.

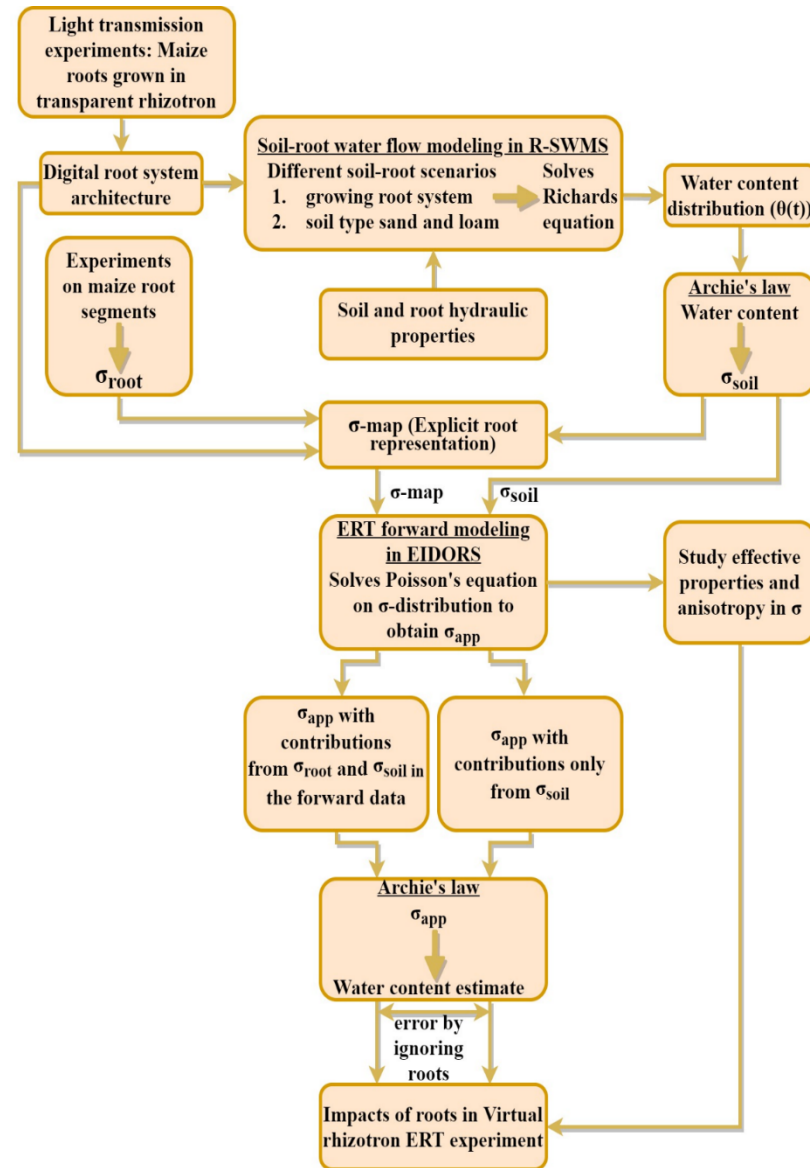


**Figure 3.1:** Flow chart for the simulation of the Virtual Rhizotron drying experiment.

### 2.2.1 Soil plant water fluxes

The 2-D root architecture (see Fig. 3.2) was extracted from real experiments on a rhizotron with a 21-day old Maize using the root image analyzing tool smart root (Lobet et al. 2011). We used one root system between 5 and 21-d old for our simulations. Since the root growth was monitored every day, ages were easily assigned to each root segment. In these experiments, rhizotrons were weighted daily, thereby allowing one to estimate averaged transpiration rates.

The size of the rhizotrons were 22 cm x 2 cm x 42 cm (the corresponding reference axes are -11 cm  $\leq$  x  $\leq$  11 cm, -1 cm  $\leq$  y  $\leq$  1 cm, -40 cm  $\leq$  z  $\leq$  2 cm). We considered two soil types: sandy and loamy with hydraulic properties represented by Mualem-van Genuchten equations (van Genuchten 1980). Hydraulic parameters for both soils are from (Carsel and Parrish 1988).

The soil-plant water flow model R-SWMS (Javaux et al. 2008) was used to estimate the evolution of root water uptake, soil water flux, and soil water content distributions in the rhizotrons. R-SWMS uses the finite element method on a regular uniform grid to solve Richards equation to simulate three-dimensional water flow in the soil:

$$\frac{\partial \theta}{\partial t} = \frac{\partial}{\partial x} \cdot \left( K \frac{\partial h}{\partial x} \right) + \frac{\partial}{\partial y} \cdot \left( K \frac{\partial h}{\partial y} \right) + \frac{\partial}{\partial z} \cdot \left( K \frac{\partial(h+z)}{\partial z} \right) - Sink \quad (3.1)$$

where  $\theta$  is the volumetric soil water content [ $\text{cm}^3 \text{ cm}^{-3}$ ],  $h$  the matrix head [cm],  $K$  the isotropic hydraulic conductivity [ $\text{cm d}^{-1}$ ],  $Sink$  is a sink term for root water uptake [ $\text{cm}^3 \text{ cm}^{-3} \text{ day}^{-1}$ ], and  $x, y$ , and  $z$  are the spatial coordinates and the dot represents divergence. The Sink term is estimated based on a weighted averaged of the uptake fluxes in each soil voxel.

The water fluxes in and towards the roots are calculated with a finite difference method in the root system network based on soil and root water potential distributions and transpiration rate. The transpiration rate increased with root growth. Each root segment is characterized by its radial and axial hydraulic properties, which evolve with the root segment age. Experimentally measured maize root hydraulic conductivities were used in the R-SWMS model, in which they are age and type-dependent (Doussan et al. 2006; Couvreur et al. 2012). The total root length per unit volume in the R-SWMS simulation was 0.06, 0.22, 0.66, 1.1, and 1.61 cm/cm<sup>3</sup> at day 5, 10, 15, 18 and 21, respectively. In the typical field, mature root density reaches values of 1cm/cm<sup>3</sup>, especially in the topsoil (Gao et al. 2010).

Root growth was simulated by updating the root system architecture at each time step between the beginning (day 5) and the end (day 21) of the simulation. The same architecture evolution was used for sand and loam. We imposed a sinusoidal day/night transpiration as root boundary condition with daily transpiration progressively increasing between the beginning (day 5, 5 cm<sup>3</sup>) and the end of the simulation (day 24, 30 cm<sup>3</sup>), which corresponds to transpiration rates experimentally observed in greenhouse experiments for similar plant size (Lobet et al. 2011).

The initial soil condition was a hydrostatic equilibrium with a saturated soil at the bottom of the rhizotron (corresponding to experimental conditions) and root water uptake was the only source/sink term that allowed the total water content to change.

We ignored root exudation and assumed that solute uptake was proportional to soil solute concentration (i.e. passive uptake (Hopmans and Bristow 2002), allowing us to assume a uniform solute concentration distribution.

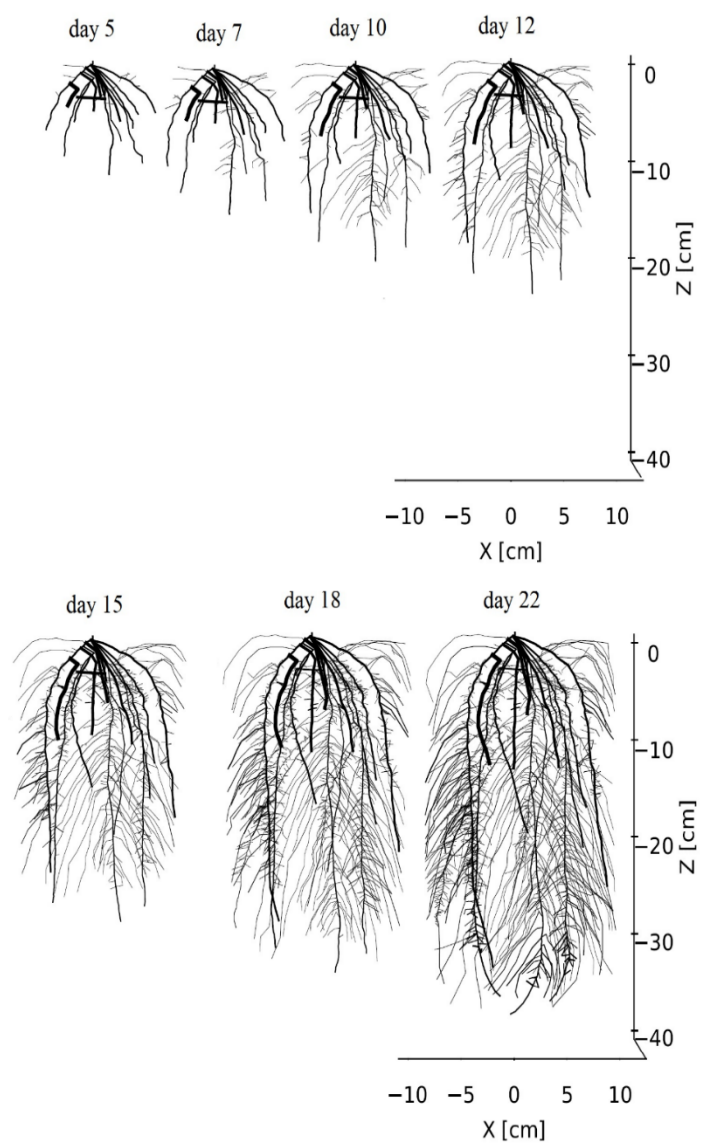


**Figure 3.2:** Root architectural evolution shown at different times.

### 2.2.2 Electrical properties of plant root tissues and soils

We used the measured electrical properties of Maize roots as described in Chapter 3. We used the variations of  $\sigma_{root}$  as a function of segment distance from the root collar (see Fig. 3.3). The digital maize roots in our simulation are around three weeks old while the brace roots develop only after several weeks in a real maize plant; hence, the brace root data are not included in our model. Figure 3.3 shows the experimental data of  $\sigma_{root}$  as a function of the root age for the maize plant. We observe a gradual increase in  $\sigma_{root}$  of intact maize root segments, as the segment distance from root collar increased. The black solid curve of Figure 3.3 represents the root electrical property incorporated in our virtual rhizotron simulations:  $0.0154 < \sigma_{root} < 0.03$  [S/m]. The polynomial fit in Figure 3.3 is given by:

$$\sigma_{root} = -5.5 * 10^{-5}(drc^2) + 0.0018drc + 0.0137 \quad (3.2)$$

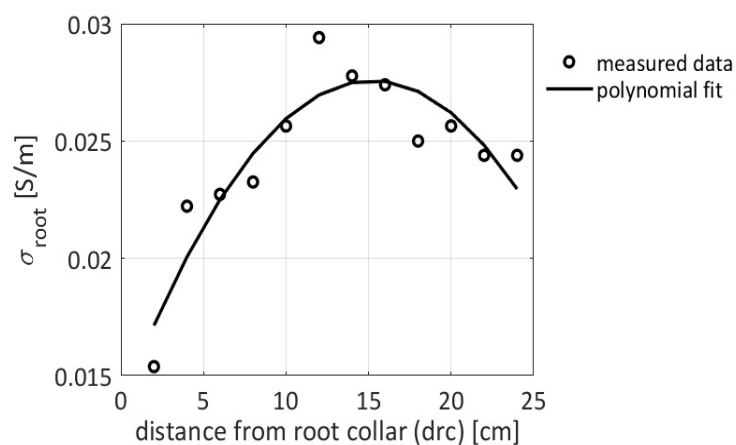


**Figure 3.3:** Measurement data on Maize roots:  $\sigma_{root}$  vs distance from the root collar. The quadratic fit is shown as a solid line while measurement data is represented at discrete locations as circles (primary root).

To transform soil water content maps into electrical conductivity maps, we used Equation 2.8. Sand typically has very low surface conductivity ( $\sim 10^{-5} \text{ S/m}$ ) while for loam, we assume  $\sigma_{surface}$  to be 0.015 S/m (Brovelli and Cassiani 2011). For Archie's fitting parameters, we use the typical values  $d = 2$  and  $m = 1.3$  (e.g. Werban et al. 2008).  $\sigma_{bulk-soil}$ , in the rhizotron also depends on the electrical conductivity of the nutrient solution ( $\sigma_w$ ) used to grow plants. We assumed  $\sigma_w$  to be 0.2 S/m and chose  $n$  as 0.35 (sand) and 0.435 (loam) to be in the same range as the other observed petrophysical models (Fig. 2.6). In the following sections, we will refer to  $\sigma_{bulk-soil}$  as the soil bulk electrical conductivity (with  $\sigma_{bulk-loam}$  and  $\sigma_{bulk-sand}$  to the specific soil types) when no roots are present and  $\sigma_{bulk}$  will be used for studies or datasets where both roots and soil are present.

Note that extremely low value of conductivity in the sand ( $\sim 5 \times 10^{-9} \text{ S/m}$ ) can arise and would need additional mesh refinement in the finite element mesh in regions where there are large conductivity gradients to obtain an accurate result. To avoid that and to maintain accuracy, we set a limit of 0.0001 S/m as the lowest possible conductivity value.

### 2.2.3 Meshing the root architecture

For the electrical simulation, we generated finite element meshes for the specific root geometry. In the

finite element mesh, either a  $\sigma_{root}$  or  $\sigma_{bulk-soil}(\theta)$  value is assigned to each element (tetrahedron). The maize primary roots in our simulation have a mean radius ( $r \sim 0.025$  cm) which is small compared to the dimensions of rhizotron (20 x 1 x 42 cm), requiring a very high spatial resolution for roots in the forward finite element mesh (FFEM).

To generate a 3-D root resolved mesh with high spatial resolution but manageable computational load, we needed to simplify the root system. First, we removed extremely fine root hairs and root branches that were below 0.01 cm in radius assuming that such roots have a negligible effect on the voltage measurements. Also, nearly parallel secondary root-branches with the distance between them less than 2 times the root radius were combined and treated as a single branch. This procedure reduces the total root length in the finite element mesh as compared to the real plant. Hence to preserve the root volume (which we assume to be the most important factor at this stage) in the finite element mesh with the actual measurements, we had to increase the mean radius of root segments in the finite element mesh. Also, we discretize the root segment radius in the finite element mesh into two possible values, where all primary roots have one radius, while all secondary roots have half the radius of primary roots while in reality, each segment had unique radii. The above-mentioned simplification only affects the electrical forward model (roots are explicit 3-D structures in electrical mesh) and not the water flow model (roots are treated as a network having no volume in the water flow grid), where we used digitized root having identical features (radii and no. of segments) as in the rhizotron experiments.

We compare the time evolution of root volume, total root length, and mean root radius in the finite element mesh with the actual plant in Figure 3.4. The root volume in the finite element mesh matches with the real plant (Fig. 3.4-a). The total root length in the finite

element mesh matches the measurements only at a younger age (Fig. 3.4-b). At later ages, we lose around 50% of root length due to root simplification procedure. The simplified root architecture represents segments with a mean radius as shown in Figure 3.4-c.

The finite element model of the simplified root architecture at age 5 is shown in Figure 3.5. The 3-D finite element mesh in Figure 3.5-b was generated from the simplified root architecture using Gmsh software (Geuzaine and Remacle 2009). Figures 3.5-a, 3.5-b represent the simplified architecture at age 5 while Figure 3.2 represents the original architecture from a real plant at different times. Comparing these two figures at age 5, we see that the overall skeleton of the root system and its volume is preserved while its radii were modified to meet the computational speed. We assumed that root mass density (or root volume) plays a bigger role than root length density in affecting the electrical current flow and hence we prioritized preserving the root volume and to some extent the architecture rather than preserving the actual root length and radius, which were modified in the mesh due to merging of nearby segments. Also, preserving root radius and root length requires a very refined grid and hence computationally intensive.

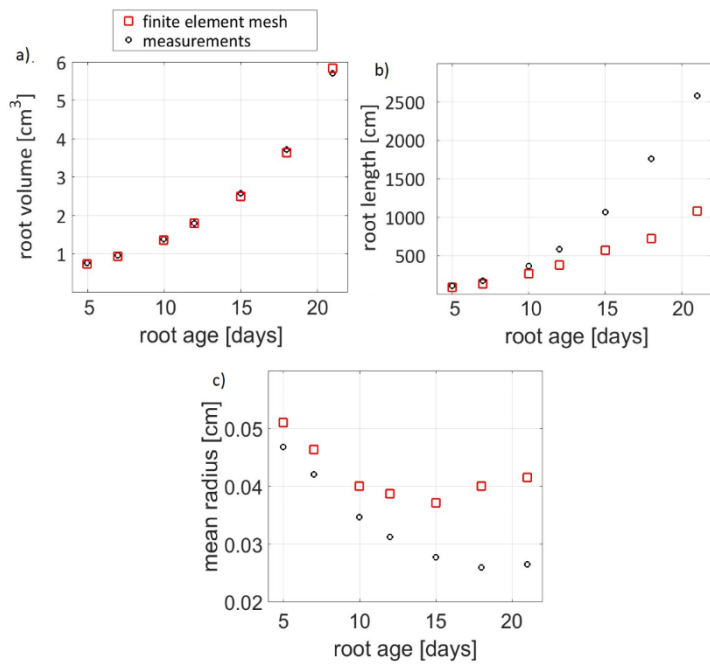


**Figure 3.4:** a) root volume vs root age as simulated in the finite element mesh (red squares) or light transmission image (black circles), b) root length vs root age as simulated in the finite element mesh (red squares) or measurements (black circles), and c) mean r

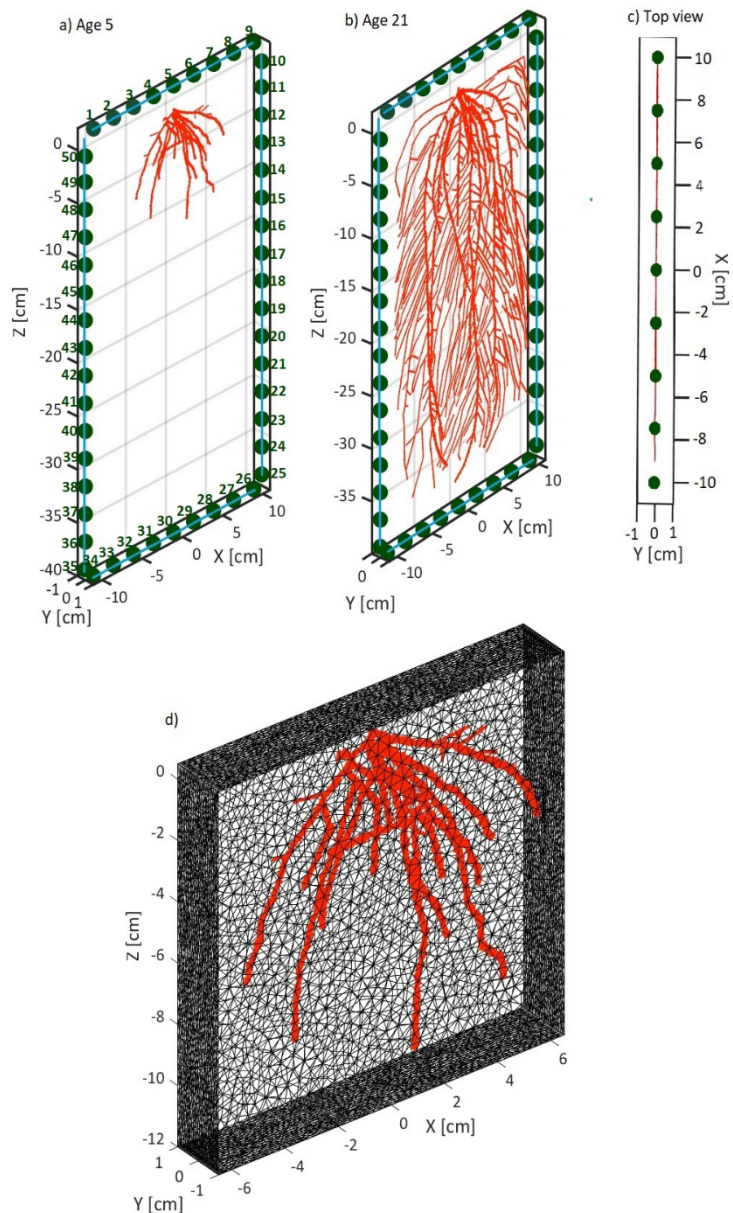


**Figure 3.5:** Finite element model of virtual rhizotron (with mesh hidden) at a) age 5, b) age 21 and c) Top view. The root tetrahedrons are shown in red while green dots represent the point electrode locations and the blue line connecting green dots represents the line electrodes and d) A section of forwarding finite element mesh at age 5.

### 2.2.4 Electrical resistivity forward modeling

We used the finite-element based software EIDORS (Adler and Lionheart 2006) to solve the ERT forward problem for the generated finite element meshes. The ERT forward problem solves for the resulting voltages of an electric current of density,  $\vec{J}_e$ , injected into a medium of electrical conductivity ( $\sigma$ ) given the proper boundary conditions. The equations governing the physics of electrical resistivity forward modeling is derived from Maxwell's equations for a DC. Consider a region,  $\Omega$  bounded by its boundary,  $d\Omega$ . The electric field  $\vec{E}$  in  $\Omega$  is related to the scalar electric potential  $\phi$  through the gradient operation,  $\vec{E} = -\nabla\phi$ . Applying the conservation of electric charge for a source free region,  $\nabla \cdot \vec{J}_e = 0$ , and Ohm's law,  $\vec{J}_e = \sigma \vec{E}$ , we obtain the governing equation for ERT inside the medium (also known as Laplace equation):

$$\nabla \cdot (\sigma \nabla \phi) = 0 \quad (3.3)$$

The injected current density  $\vec{J}_e$  is specified by the Neumann boundary conditions at the current injecting electrode locations usually located in  $d\Omega$ :

$$\hat{\sigma} \nabla \phi \cdot \hat{n} = \sigma \frac{\partial \phi}{\partial n} = \left\{ \begin{array}{l} \vec{J}_e \text{ on current injecting electrode} \\ -\vec{J}_e \text{ on sink electrode 0, else where} \end{array} \right\} \quad (3.4)$$

The voltage measuring electrodes dictate the Dirichlet boundary conditions:

$$\phi + Z_e |\vec{J}_e| = V_e \quad (3.5)$$

where,  $Z_e$  is the contact impedance of the voltage measuring electrodes (assumed to be 0.01 Ohms in this work),  $\vec{J}_e$  is the current density given by  $\vec{J}_e = \sigma \frac{\partial \phi}{\partial \hat{n}}$  and  $V_e$  is the voltage measured in volts,  $\hat{n}$  is the unit normal perpendicular to  $d\Omega$ . Equations 3.3 to 3.5 are the governing equations for the ERT forward problem.

The electrical resistivity forward problem seeks voltage or apparent conductivity data by numerically solving Equations (3.3 - 3.5) for a known electrical conductivity distribution. The voltage data ( $V_e$ ) can be converted to apparent conductivity data, i.e. that of an equivalent homogeneous medium ( $\sigma_{app}$ ), with an appropriate geometric factor of the electrodes. The  $\sigma_{app}$  now becomes a crude measure of actual electrical conductivity distribution; that we had in the forward problem. In ERT inverse problems, we aim at reconstructing an estimate of the electrical conductivity distribution within the soil-root domain from  $\sigma_{app}$  or  $V_e$

The 3-D electrical conduction model for the rhizotron (same as the water uptake model in R-SWMS) had overall dimension:  $-11 < x < 11$  cm,  $-1 < y < 1$  cm,  $-40 < z < 2$  cm. For scaling comparison between 3-D and 2-D, the electrical simulation was repeated in 2-D ( $Y = 0$ ) having a similar dimension as 3-D in  $x$  and  $z$  axes.

### 2.2.5 Apparent and effective electrical conductivities

A point electrode model (Hanke et al. 2011) with a total number of 50 electrodes and different measurement schemes are used to compute the forward response (Fig. 3.5-a). All the electrodes are located at the boundary of the computational domain with a similar set-up to the one in Weigand and Kemna (2017). In the finite element mesh, either a  $\sigma_{root}$  or

$\sigma_{bulk-soil}(\theta)$  value is assigned to each element (tetrahedron).

To compute the apparent conductivity from the voltages, we first run forward calculation for the medium with homogeneous conductivity ( $\sigma = 1$  S/m), on the same mesh as the soil-root medium and obtain the numerical geometric factors for the given electrode configuration. The numerical geometric factors here is nothing but the ratio of injected current to the measured voltage. These numerical geometric factors obtained for the homogenous medium ( $\sigma = 1$  S/m) is then used to convert the voltages into apparent conductivity ( $\sigma_{app}$ ) for the given virtual data.

We computed apparent conductivity data set for two scenarios: 1) medium having soil and root system included ( $\sigma_{app-root}$ ) and 2) medium having only the soil ( $\sigma_{app-soil}$ ). The second scenario where the data without considering root segments ( $\sigma_{app-soil}$ ) were realized by obtaining the forward data on the soil water content map (converted to electrical conductivity) only, without considering the root electrical properties. The difference in  $\sigma_{app-root}$  and  $\sigma_{app-soil}$  will indicate the specific impact of root segments on ERT measurements. We define a variable describing the relative change in  $\sigma_{app}$  due to the presence of root segments given by:

$$\delta\sigma_{app-rs} = \left| \frac{\sigma_{app-root} - \sigma_{app-soil}}{\sigma_{app-soil}} \right| \quad (3.6)$$

Our ERT injection scheme (comprising of 9742 quadrupoles from 50-point electrodes) consisted of a combination of various inbuilt options available ('mk\_stim\_patterns.m') in EIDORS software:

- a) op-op: opposite drive current injection and opposite drive potential measurement comprising of 2400 quadrupoles.
- b) op-ad: opposite drive current injection and adjacent drive potential measurement comprising of 2300 quadrupoles.
- c) ad-op: adjacent drive current injection and opposite drive potential measurement comprising of 2300 quadrupoles.
- d) ad-ad: adjacent drive current injection and adjacent drive potential measurement comprising of 2350 quadrupoles.
- e) dip-dip: dipole current injection and dipole potential measurement comprising of 392 quadrupoles.

Similarly,  $\sigma_{app}$  measured between the line electrodes at Y=0 plane (blue lines in Fig. 3.5) of each wall (top, bottom, left and right) gives effective electrical conductivity ( $\sigma_{eff}$ ) in the vertical and horizontal direction denoted by  $\sigma_{effZ}$  and  $\sigma_{effX}$ .

The computation of  $\sigma_{eff}$  ( $\sigma_{effZ}$  and  $\sigma_{effX}$ ) is repeated for two scenarios: 1) medium having soil and root system included denoted by  $\sigma_{eff-root}$ , and 2) medium having only the soil as if the roots had the same electrical conductivity than the surrounding soil, denoted by  $\sigma_{eff-soil}$ .

The difference in  $\sigma_{eff-root}$  and  $\sigma_{eff-soil}$  will indicate the specific impact of root segments on effective property. Similar to Equation 3.6 we define a parameter describing the relative change in  $\sigma_{eff}$  due to the presence of root segments given by:

$$\delta\sigma_{eff-rs} = \left| \frac{\sigma_{eff-root} - \sigma_{eff-soil}}{\sigma_{eff-soil}} \right| \quad (3.7)$$

### 2.2.6 Root electrical signature terms

The relative change terms are given in Equations 3.6 and 3.7, that is,  $\delta\sigma_{eff-rs}$  averaged over two perpendicular directions (denoted by  $\langle\delta\sigma_{eff-rs}\rangle$ ) and  $\delta\sigma_{app-rs}$  averaged over all the 9742 quadrupoles denoted by  $\langle\delta\sigma_{app-rs}\rangle$  are used as a parameter to assess the impact of roots in the ERT forward data. We also use  $\delta\sigma_{app-rs}$  computed for current injection between electrodes 1 and 9 and voltage measurement between 4 and 6 situated at the surface of rhizotron (Fig. 3.5) denoted by  $\delta\sigma_{app-rs} - S$ , due to its practical feasibility for an extension to field studies.

Hence, we will refer to  $\langle\delta\sigma_{eff-rs}\rangle$  and  $\langle\delta\sigma_{app-rs}\rangle$  as the root electrical signature term. We also define a term describing the electrical conductivity contrast between  $\sigma_{root}$  and  $\sigma_{bulk-soil}$ , denoted by C, computed by subtracting the mean of  $\sigma_{bulk-soil}$  from mean of  $\sigma_{root}$ . Here, C is a single number, which is a function of root age and soil type.

First, we generate additional synthetic data by increasing the mean root radius by a factor of two and three (increasing the root volume by four and nine). The original mean radius of root segments in the finite element mesh that matches with the experimental volume was shown in Figure 3.4-c (red squares). The thickening of root increases the root volume while keeping the root length intact. With seven different root ages (seven different root lengths, see Fig. 3.2) and three different root radii: actual (Fig. 3.4-c), double of actual and triple of actual denoted by r, 2r, and 3r, we have twenty-one different radii/volume.

We use these data to achieve the objectives of this paper, i.e. to find simulation-based answers to the specific questions as follows:

- 1) Does the root water uptake pattern have an impact on root electrical signature terms?

To answer the above question, we compute  $\langle \delta\sigma_{eff-rs} \rangle$  as a function of root age in two different mediums: a) A medium where soil electrical conductivity is dictated by root water uptake pattern (Fig. 3.7) and b) A medium having a homogeneous soil electrical conductivity (without root water uptake pattern) whose value is the spatial average of root water uptake scenario. The difference in these two scenarios will give us insight into the impact of root water uptake on electrical signatures of root segments.

- 2) How does root length density, root volume density, root age, and root radius relate to the root electrical signature terms?

We assess the dependency of root signature terms for each of the unique cases that correspond to different root variables such as length, ages, volume, surface area, electrical conductivity contrast, and radii. We investigate the multivariate dependency among these variables by correlation analysis.

### *2.2.7 Upscaled electrical properties*

To get an insight on how a rooted soil might differ from bare soil electrical properties, we divided the FFEM into smaller blocks having dimension: 2 cm x 1 cm x 2 cm, and compute the volume-weighted arithmetic and harmonic mean of electrical conductivity within each block:

$$\langle \sigma_{avg-am} \rangle = \frac{\sum V_i \sigma_i}{\sum V_i} \quad (3.8)$$

$$\langle \sigma_{avg-hm} \rangle = \left( \frac{\sum_i (V_i \sigma_i)^{-1}}{\sum_i V_i^{-1}} \right)^{-1} \quad (3.9)$$

where the  $V_i$  and  $\sigma_i$  are the volume and electrical conductivity of  $i$ th tetrahedron within an averaging block. We also computed the volume-weighted arithmetic mean of water content:

$$\langle \theta \rangle = \frac{\sum_i V_i \theta_i}{\sum_i V_i} \quad (3.10)$$

The  $\langle \sigma_{avg-am} \rangle$  assumes that the finite elements in each averaging block are electrically connected in series while the  $\langle \sigma_{avg-hm} \rangle$  assumes the elements to be in parallel. In reality, we expect the true  $\sigma_{bulk}$  to be in between the  $\langle \sigma_{avg-am} \rangle$  and  $\langle \sigma_{avg-hm} \rangle$ , depending on the structural properties of root and soil elements. The relation between the collection of averaged data points ( $\langle \theta \rangle$ ,  $\langle \sigma_{avg-am} \rangle$ ,  $\langle \sigma_{avg-hm} \rangle$ ) at every averaging block and at all time (day 5 to 21) will then approximately mimic the impact of roots at a block-scale on  $\sigma_{bulk}$ , when compared to Archie's law applied in soils only ( $\sigma_{bulk-soil}$ ). We also investigate the relation between effective properties ( $\sigma_{effZ}$  and  $\sigma_{effX}$ ) and volume-averaged (at rhizotron scale) water content at different times.

## 2.3 Results

In this section, we discuss the results obtained from the coupled water-flow and electrical model. First, we describe the outputs of root water uptake simulations in

terms of electrical conductivity. Then we discuss the impact of roots on petrophysical relation and root signatures in ERT forward simulations.

### *2.3.1 Electrical conductivity contrasts derived from root water uptake simulations*

Simulations show that the relative  $\theta$  distribution patterns depend on the soil type (Figs. 3.6-a, b). In loam, the normalized water saturation never drops below 0.2 even on day 21 whereas, in the sand, it reaches almost zero (0.00034) on day 21. On the same day, when the water depletion is the highest, there are still maximum water saturation values of 0.4 in sand and 0.6 in loam.

In the sand, the electrical conductivity of roots  $\sigma_{root}$  is always larger than the one of the soils  $\sigma_{bulk-sand}$  (Fig. 3.6-c). For loam, however, we see that the contrast changes with time (Fig. 3.6-d). Initially,  $\sigma_{bulk-loam}$  is larger than  $\sigma_{root}$ , at intermediate times (day 10, 12, 15), at top of rhizotron,  $\sigma_{bulk-loam}$  is equal to  $\sigma_{root}$  and at bottom of rhizotron,  $\sigma_{bulk-loam}$  is larger than  $\sigma_{root}$  and at the end final times (day 18 and 21), at some regions  $\sigma_{bulk-loam}$  is less than  $\sigma_{root}$ . On day 21, where the water depletion is highest, the water saturation varies from 3e-4 to 0.4 in sand and 0.2 to 0.6 in loam. When translated into electrical conductivity, in sand  $\sigma_{bulk-sand}$  varies from 5e-9 to 0.0087 S/m and in loam,  $\sigma_{bulk-loam}$  varies from 0.0057 to 0.0407 S/m. The extremely low value of conductivity in the sand ( $\sim 5e-9$  S/m) will need additional mesh refinement in the FFEM at regions where there are huge conductivity gradients to obtain an accurate result. To avoid that and to maintain accuracy, we find elements, which have conductivity lower than 0.0001 S/m and assign such

elements, the conductivity equal to 0.0001 S/m. Hence, in electrical simulation, the lowest possible conductivity is 0.0001 S/m. We show the minimum and maximum values of  $\sigma_{bulk-soil}$  for sand and loam simulation along with Maize root electrical conductivity range at different times in Figure 3.7.

Since electric current flow depends on the gradient of  $\sigma$ -distribution, the effect of roots in ERT experiments will be greater where there is higher  $\sigma_{root} - \sigma_{bulk-soil}$  contrasts and most importantly, it is time-dependent (Fig. 3.7). Besides, the density of roots plays a role in terms of  $\sigma_{root} - \sigma_{bulk-soil}$  contrasts, for instance at day 22, the upper part of the root system is more conductive than  $\sigma_{bulk-loam}$  in the upper part of the rhizotron and also reflects higher root volume than at initial times. Therefore, at later times (Fig. 3.6-d, day 22), the ERT estimate of water content in the upper region could be misleading due to a stronger root influence on  $\sigma_{bulk}$ .

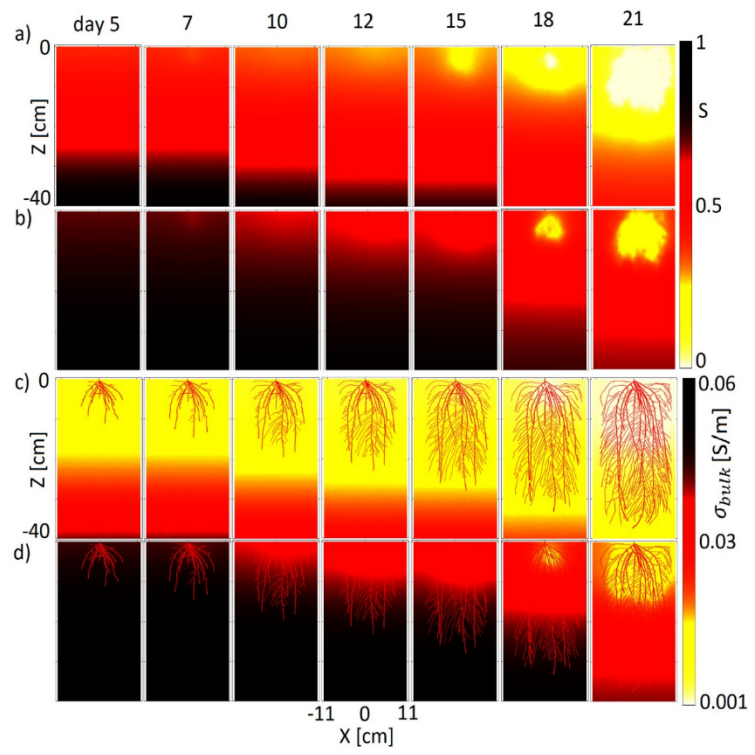


**Figure 3.6:** Volumetric water saturation distribution in a) sand and b) loam, and its corresponding  $\sigma$ -maps in c) sand and d) loam at  $Y = 0$  plane at different times.

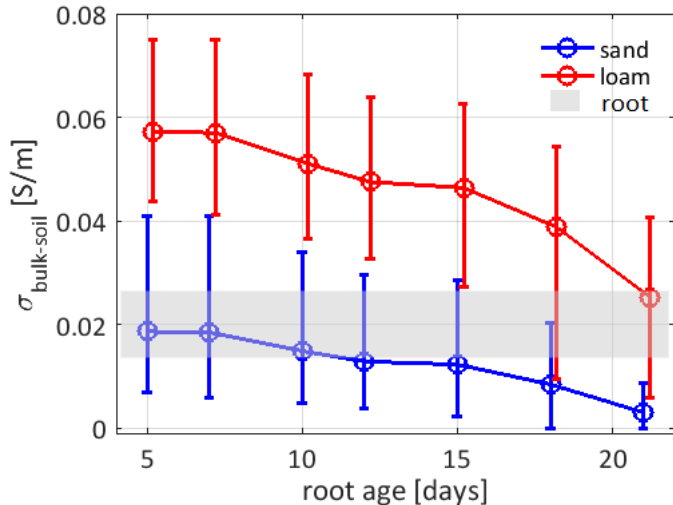


**Figure 3.7:** Variability of  $\sigma_{bulk-soil}$  in the rhizotron at different times for sand and loam. The vertical bars at various times represent the minimum and maximum values of  $\sigma_{bulk-soil}$ . The circle represents the arithmetic mean of  $\sigma_{bulk-soil}$  in the finite element mesh and is later used for homogeneous soil scenarios to compare with the root water uptake scenario. The gray shading represents  $\sigma_{root}$ .

### 2.3.2 The impact of roots on petrophysical relationships

The harmonic and arithmetic block-wise averaged electrical conductivity data points and their corresponding water content at various times are shown as vertical bars in Figure 3.8 (a and b) along with the Archie petrophysical relation. The upper limit of the vertical bar represents the maximum of  $\langle\sigma_{avg-hm}\rangle$  and  $\langle\sigma_{avg-am}\rangle$  while the lower limit represents their minimum. For each block ( $4 \text{ cm}^3$ ), the actual effective small scale (centimeter scale) conductivity is supposed to be located within this range.

At a larger rhizotron spatial scale, we illustrate the relationship between  $(\sigma_{effZ}, \sigma_{effX})$  and volume-averaged water content at various times in Figure 3.8 (a and b). Both effective properties at rhizotron scale and averaged properties at a small block scale deviate from Archie's curve and the deviation trend is different as seen from Figure 3.8 (a and b). Also, the difference between the horizontal and vertical effective properties  $\sigma_{effX}$  and  $\sigma_{effZ}$  indicate macro-scale anisotropy. For both soil types, the derived effective properties  $\sigma_{effX}$  and  $\sigma_{effZ}$  lies below Archie's curve defined at the lower scale due to the dry soil acting as a barrier to the electrical current flow, thereby decreasing the effective  $\sigma_{bulk}$ . The vertical effective property deviates more when compared to horizontal direction due to horizontal layering that develops in the electrical conductivity distribution due to root water uptake (see Figs. 3.8-a and b), which thereby affects current more in the vertical direction than in horizontal direction. For the loam medium, the anisotropic effect is less when compared to sand. ERT obtained electrical conductivity data are known to have a spread around the petrophysical model fitted curve as observed by Beff et al. (2013) and Garré et al. (2011). Our averaging results in Figure 3.8 (a and b) hints that this deviation of electrical conductivity data around the petrophysical model could be due to the presence of root segments.

In Figures 3.8-c and d, we show the deviations of  $\sigma_{effZ}$  from Archie's curve in sand and loam for three different scenarios: a) root water uptake with root segments (blue line), b) root water uptake without root segments (green line) and c) homogeneous soil (without root water uptake) with root segments (red line). For the homogeneous soil case (without root water uptake pattern), we use the mean of  $\sigma_{bulk-soil}$  for soil. As the root segment, electrical conductivity values

are generally higher than the dry soil, we see that deviation is positive when roots and not uptake are considered (red lines in Figs. 3.8-c and d) whereas, with root water uptake, the deviation is negative.

We find that the impact of root water uptake only is a bit bigger than the one of the root segment electrical conductivity (respectively green and red lines in Figs. 3.8-c and d). However, the additional impact of the presence of roots when water uptake is considered is negligible (blue line), demonstrating that the root water uptake pattern is then the main driver of these deviations. The presence of root inside of the depletion zone only marginally affects the electrical signature.

On a small scale, removing root segments results in a perfect agreement between block-wise averaged data and Archie's curve (not shown here) as the difference between the two averages in Figures 3.8 (a and b) is only due to root segments. This is because at block scale there is no significant water content heterogeneity present and thus averaged water content and averaged electrical conductivity (without roots) follow Archie's curve. At large scale though, the patterns generated by the water uptake generate more nonlinearities and the averaged water content does not relate anymore to effective properties dictated by Archie petrophysical relation.

The rhizotron scale, bulk electrical conductivity deviates from Archie's law quite differently when compared to the averaged data at a smaller scale (Fig. 3.9). This can be understood as the impact of soil heterogeneity playing a bigger role in influencing the bulk property at large scale whereas, at centimeter-scale (2 cm x 2 cm), the root density plays a major role in the deviating the bulk property from bare soil petrophysical relation ( $\sigma_{bulk-soil}$ ). This illustrates how the relationship between  $\theta$  and  $\sigma_{bulk}$  is scale dependent.

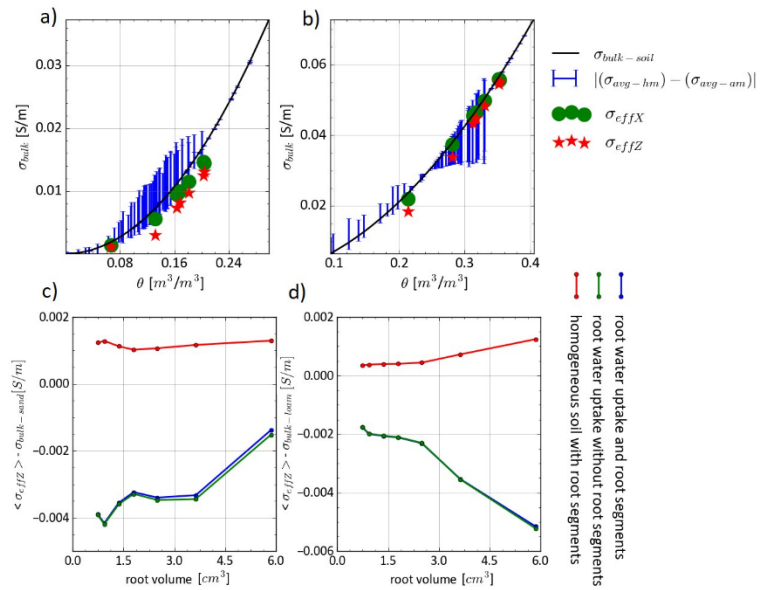


**Figure 3.8:** Comparison of Archie's law ( $\sigma_{\text{bulk-soil}}$ ) with block wise averaged electrical conductivity ( $\langle \theta \rangle$  vs  $\langle \sigma_{\text{avg-hm}} \rangle$ ,  $\langle \sigma_{\text{avg-am}} \rangle$ ) and rhizotron scale effective electrical conductivity in two perpendicular directions ( $\sigma_{\text{effX}}, \sigma_{\text{effZ}}$ ) in the sand (a) and loam (b). The error bar represents the difference between  $\langle \sigma_{\text{avg-am}} \rangle$  and  $\langle \sigma_{\text{avg-hm}} \rangle$ . The water content corresponding to  $\sigma_{\text{effX}}$  and  $\sigma_{\text{effZ}}$  were obtained by taking volumetric average of the whole rhizotron. The deviation of  $\sigma_{\text{effZ}}$  from  $\sigma_{\text{bulk-soil}}$  as a function of root volume for three different scenarios in c) sand and d) loam.

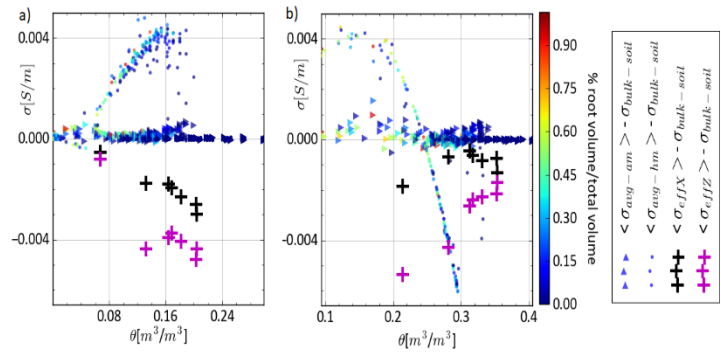


**Figure 3.9:** The deviation of effective and averaged conductivities from  $\sigma_{bulk-soil}$  as a function of water content in: a) sand and b) loam.

### 2.3.3 Root signatures in ERT forward simulations with point electrodes

In Figures 3.10 and 3.11, we show the dependence of  $\delta\sigma_{app-rs}$  on different stimulation schemes (rows) and root volume (columns). Generally, we see that  $\delta\sigma_{app-rs}$  is twice as large in the sand medium as compared to loam. Thus, under given conditions, root segments are expected to affect ERT measurements more in the sand medium. For the given mean radius,  $r \sim 0.025$  cm, most of the measurement in the sand have  $\delta\sigma_{app-rs}$  around 1 % but as we double the radius (i.e., increase the volume by 4 times) the no. of measurements having  $\delta\sigma_{app-rs}$  greater than 1% increases. Notice the shifting of histogram plots to the right side which is more clearly evident for op-op stimulation (first row of Fig. 3.10-b)

as we increase the radius from  $r$  to  $2r$  and  $3r$ . For tripling the radius (i.e. increasing the volume by 9 times) the  $\delta\sigma_{app-rs}$  can exceed 10% in sand medium, which is significant. By comparing Figures 3.10 and 3.11, we could say that in loam,  $\delta\sigma_{app-rs}$  is much lower and most measurements for  $r \sim 0.025$  cm lie below 1%. Only when we double or triple the radius, few measurements shift to 1 to 10%  $\delta\sigma_{app-rs}$  band (see Fig. 3.11-b). Among different stimulation schemes chosen, we see that op-op scheme is most sensitive to root presence having the largest  $\delta\sigma_{app-rs}$  signal. For sand, some measurements in the op-op scheme can reach up to 30% in  $\delta\sigma_{app-rs}$  for radius =  $r$  and up to 100% for radius =  $2r$  and 50% for radius =  $3r$  while in loam it never reaches above 20% (see Figs. 3.10-a and 3.11-a: column-wise).

For sand medium, except for op-op scheme, (see Fig. 3.10-b: rows 2 to 5) we observe that the histogram amplitudes at age 5 (red) has a negative slope (i.e. declining amplitude with increasing  $\delta\sigma_{app-rs}$ ) and notice the change in histogram shape as root system ages (red to green and green to blue). We see that histogram amplitudes start with a negative slope at age 5 and are nearly flat at age 15 and have a positive slope (rising histogram amplitude) at age 21 forming a U-shaped histogram amplitude pattern as we move from age 5 to 15 to 21. However, in loam (Fig. 3.11-b: rows 2 to 5), as root system ages, histogram amplitudes remain negatively sloped (declining histogram amplitude with increasing  $\delta\sigma_{app-rs}$ ).

The apparent conductivity measured from ERT has contributions not only from soil water content but also from root segments. We characterized the root contributions in Figures 3.10 and 3.11 by defining  $\delta\sigma_{app-rs}$ . To minimize the impact of roots on  $\sigma_{app}$ , we must carefully choose the stimulation scheme such that

it gives the lowest  $\delta\sigma_{app-rs}$  but they also mean lower sensitivity in the middle region of the rhizotron. Although for most measurement,  $\delta\sigma_{app-rs}$  is around 1 to 10%, they could get amplified in the final ERT inversion results due to the ill-posed nature of the ERT inversion problem (Günther et al. 2006). Thus an error in forward  $\sigma_{app}$  could get multiplied in the final water content estimate obtained by the inversion program and is dependent on inversion algorithm and regularization scheme used (Yang and LaBrecque 1998).

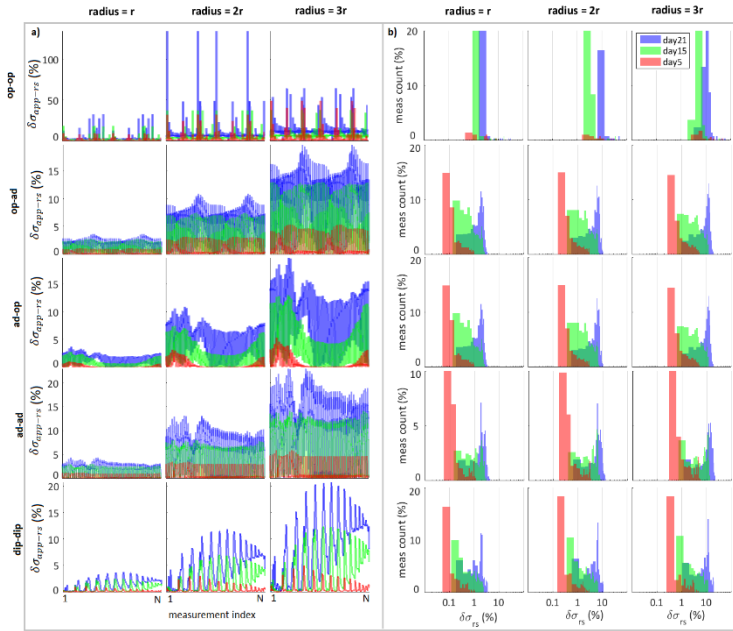


**Figure 3.10:** a)  $\delta\sigma_{app-rs}$  in the sand medium at age 5 (red), age 15 (green), and age 21 (blue) as a function of measurement index for different stimulation schemes (row-wise) and increasing root segment radius (column-wise). Here N is the total number of quadrupoles in a particular stimulation scheme as given in Table 4.2-b) Histogram of percentage  $\delta\sigma_{app-rs}$  in the sand medium for different stimulation schemes (row-wise) and increasing root

segment radius (column-wise). Here  $r$  is 0.025 cm (radius of root segment corresponding to original root volume).

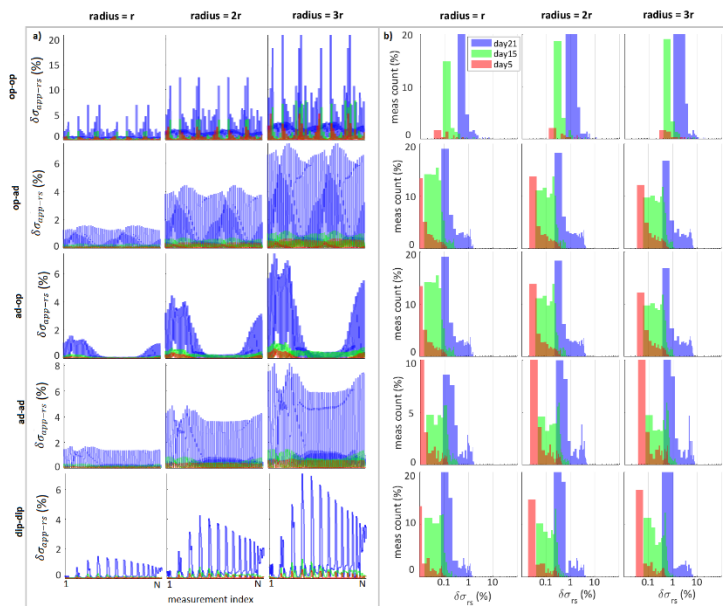


**Figure 3.11:** a)  $\delta\sigma_{app-rs}$  in loam medium at age 5 (red), age 15 (green), and age 21 (blue) as a function of measurement index for different stimulation schemes (row-wise) and increasing root segment radius (column-wise). Here N is the total number of quadrupoles in a particular stimulation scheme as given in Table 4.2-b) b) Histogram of percentage  $\delta\sigma_{app-rs}$  in loam medium for different stimulation scheme

(row-wise) and increasing root segment radius (column-wise). Here  $r$  is 0.025 cm (radius of root segment corresponding to original root volume).

### 2.3.4 Root signatures in ERT forward simulations

In Figure 3.12, we compare  $\langle \delta\sigma_{app-rs} \rangle$ , and  $\langle \delta\sigma_{eff-rs} \rangle$ , with the ratio of root to soil volume as a percentage. They show a very high correlation both in sand and loam ( $r > 0.8$ ). In general, the impact of roots in the sand was greater than in loam, as seen by its higher slope.

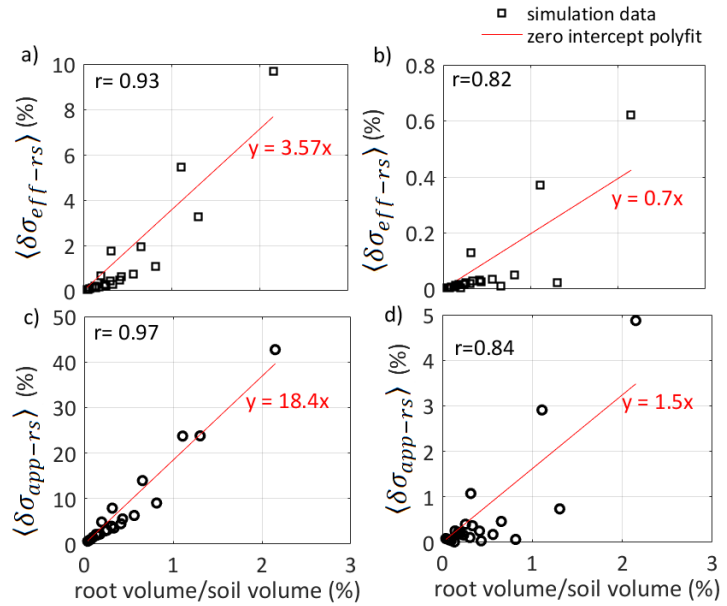


**Figure 3.12:** Relative change in effective conductivity resulting in root segments compared with soil only ( $\langle \delta\sigma_{app-rs} \rangle$ , in %) vs. root volume/soil volume ratio (%) (black squares) in a) sand and b) loam. Relative change in apparent conductivity from root segments compared with soil only ( $\delta\sigma_{app-rs}$ ) vs. root volume/soil volume ratio (%) (black squares) in c) sand and d) loam. The red line represents the zero-intercept-constrained polynomial fit.

In Figure 3.13, we examine the correlation of root electrical signature terms such as a)  $\delta\sigma_{app-rs}$ -S computed using surface point electrodes 1, 4, 6, and 9, b)  $\langle \delta\sigma_{app-rs} \rangle$  (quadrupole averaged apparent root electrical signature) and c)  $\langle \delta\sigma_{eff-rs} \rangle$  (directional average of effective root electrical signature) with the root geometrical properties such as radii, surface area, volume, age, and soil-root electrical contrast (C). The x-axis of these plots is arranged in increasing order of Pearson correlation coefficient ( $r^2$ ). The root electrical signature terms depend strongly on electrical contrast (C) which is the mean ( $\sigma_{root}$ ) – mean ( $\sigma_{bulk-soil}$ ) (last

column in Fig. 3.13) as compared to other parameters. Root length, surface, and volume correlate to the same extent to root electrical signature terms (correlation coefficient  $\sim 0.5$ ) while root radii and age correlate to the least extent comparatively. A positive correlation among different root variables with the root electrical signature suggests that it is a multivariate problem. It is interesting to see that the ranking of the correlation of electrical signature with different variables does not change when we have a point electrode signature, or quadrupole averaged signature or effective line electrode signature (different rows in Fig. 3.13). The magnitude of electrical signature is highest in the point electrode, intermediate in point quadrupole-averaged case, and lowest in line electrode effective case. By visual inspection of Figure 3.13, we find that age and length vary with root electrical signature terms correspondingly, while surface and volume form another group. The electrical contrast is an independent variable affecting the root electrical signature. Correlation analyses indicate that the root surface area and electrical contract are the two main drivers of the electrical signatures of root systems in the soils.

We did a principal component analysis only on  $\langle \delta\sigma_{eff-rs} \rangle$  which varies similarly as compared to  $\langle \delta\sigma_{app-rs} \rangle$  and  $\delta\sigma_{app-rs}$ -S concerning other root variables (Fig. 3.13). The results of principal component analysis (Fig. 3.14) confirmed the multivariate dependency among different variables relating to root geometrical and electrical properties. The principal component analysis revealed that the first three principal components explained about 92% of the variability (Fig. 3.14). Principal Component 1, with 58% of the total variance, captured the variability of root system size (volume, surface, radius, and age), which correlated with electrical contrast and the electrical signature. In other words, large root systems tend to increase their electrical signature.

Principal Component 2 separated the various drivers of variability into three groups. Age and length, which represent the extent of the root system, formed Group 1 and were negatively correlated with  $\langle \delta\sigma_{eff-rs} \rangle$ . Radius made up Group 2 and was weakly correlated with  $\langle \delta\sigma_{eff-rs} \rangle$ . Volume and surface, which represent a combination of extension and thickness, formed Group 3 and correlated with  $\langle \delta\sigma_{eff-rs} \rangle$ . Principal Component 3 captures a small part of the variation, where contrast and  $\langle \delta\sigma_{eff-rs} \rangle$  are correlated and are independent of the root system size.

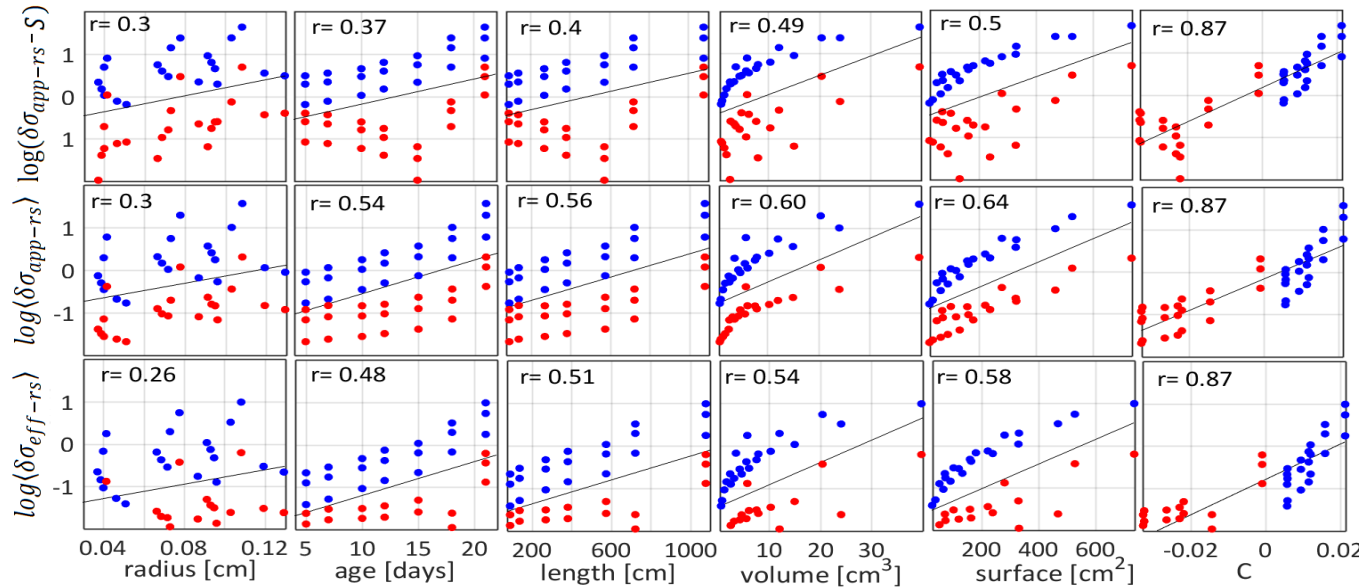


**Figure 3.13:** Correlation plots of different root variables: age, volume, surface area, length, electrical conductivity contrast between root and soil denoted by C, which is mean ( $\sigma_{root}$ ) – mean ( $\sigma_{bulk-soil}$ ) with the log10 of root electrical signature. The top row represents root signature  $\delta\sigma_{rs-app}-S$  computed using surface electrodes 1, 4, 6, 9. The middle row represents the  $\log\langle\delta\sigma_{app-rs}\rangle$  (quadrupole averaged  $\delta\sigma_{rs-app}$ ) vs root variables and the third row

represents the log of averaged effective root signature  $\langle \delta\sigma_{eff-rs} \rangle$  vs root variables. The red dots represent the loam medium while blue dots are sand. Here, r represents the Pearson correlation coefficient.

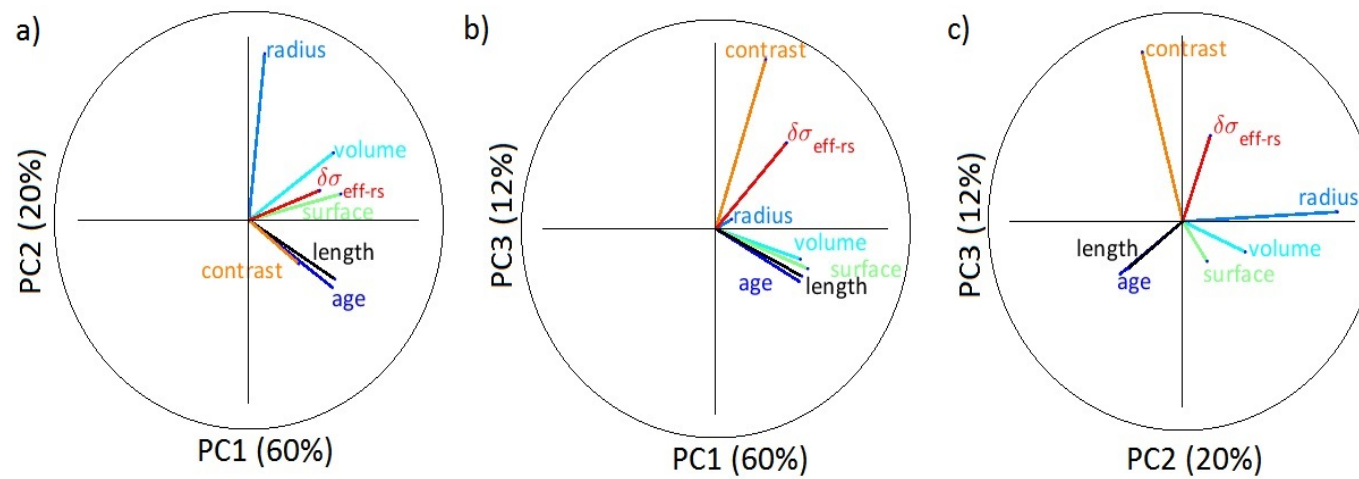


**Figure 3.14:** Principal component (PC) analysis of different root variables: (a) PC1 vs. PC2 decomposition, (b) PC1 vs. PC3 decomposition, and (c) PC2 vs. PC3 decomposition. The percentage values in the parentheses indicate the data variance explained by each PC. The circles have a unit radius going from  $-1$  to  $1$  on both axes.

## 2.4 Model Limitations

Here, we discuss the limitations of our modeling approach. First, we consider the limitations for the scenario where the process-based model described here is extended to model a real experiment. In agricultural fields as well as in the two-dimensional rhizotron, air-filled cracks can manifest in the soil, potentially influencing ERT measurements that our model does not account for; however, these could easily be integrated into the model. For future validation of the modeling results presented here in a real experiment, limitations in ERT such as bad electrode contact and other artifacts such as soil cracks can be combated through repeated measurements and adjustments during the experiment, which is simpler to implement in a rhizotron experiment than in the field (Huck and Taylor 1982).

Our model did not consider specific rhizosphere processes such as root exudation, which could also affect the water content estimates. In the model, we assumed that salt did not accumulate near the roots but assumed passive solute uptake only with no active uptake, exclusion, or exudation. Though this has been observed experimentally in field conditions by Beff et al. (2013) and corresponds to a situation where the nutrient solution exactly fits the plants' needs, the assumption is not necessarily always valid. Significant solute gradients may arise around roots through the processes mentioned above. If they were to occur, the forward conductivity map and hence the water content estimates could be impacted by such gradients.

Also, roots can swell and shrink, causing air gaps that change spatially and temporally between soil and roots under field conditions (Carminati et al. 2009). Studies have found that maize roots in sandy loam have a root-soil contact surface of 40 to 60% (Kooistra et al.

1992; Schmidt et al. 2012). These gaps could strongly influence the electrical signature by causing macroscopic anisotropy. Therefore, the inclusion of gap dynamics should be explored in future modeling studies. Finally, we also ignored the anisotropy of  $\sigma$  inside the root structure (stele–cortex variations), which may have a considerable effect on ERT measurements. Such structural variations may induce an even higher degree of anisotropy in electrical measurements.

## 2.5 Discussion

The modeling work described here is one of the first attempts to understand the impact of roots on ERT data by including processes such as root water uptake. Because of the nature of ERT inversion, a deviation in the forward data, as quantified here, could be amplified in the final inversion results. Thus, it is important to be aware of errors in water content estimates that can be caused by root segments. Hence, this model can serve as a tool to quantify errors in ERT-obtained water content estimates arising from the presence of root segments. It can also be used to optimize ERT measurement schemes for maximizing or minimizing root sensitivity to different root architectures and to shed light on whether ERT data provide information on root phenotyping and, if so, what can be done to maximize this information. Also, this modeling work could benefit the development of bio-petrophysical relationships in rooted soil that take the morphological features of roots and their electrical properties into account. Such bio-petrophysical models would minimize the error in  $\theta$  in the cropped field as estimated by the ERT method.

## 2.6 Conclusion

We presented here a coupled model of water flow in the soil-plant-continuum and electrical conduction able to represent ERT experiments applied to the actual field/laboratory conditions. This modeling framework aims at evaluating the impact of roots on the effective electrical conductivity of the soil-continuum. We illustrated the model's potential by simulating a growing and transpiring maize root system in a three-dimensional rhizotron and forward ERT measurements. The root system hydraulic architecture was derived from experimental data and root water uptake was simulated using a mechanistic water flow model in soil and roots. The impact of soil type and change of water content was evaluated using petrophysical relationships while the root electrical conductivity map was explicitly accounted for, based on measurements made on maize root segments.

Analysis of the  $\sigma$  distributions generated by simulated root water uptake and root system architecture showed a scale- and soil-dependent impact on the apparent petrophysical relationships. Upscaling the  $\sigma$  data (through averaging) showed a deviation or spread around Archie's curve with an uncertainty of approximately  $0.01 \text{ S m}^{-1}$  (at its peak) for given water content (Fig. 3.8-b). This deviation was caused by the presence of root segments. It is worth noting that uncertainty in the petrophysical relation of  $\sim 0.01 \text{ S m}^{-1}$  has been observed in some field ERT studies (Garré et al. 2011; Beff et al. 2013). In addition to measurement errors under field conditions, our model explains that the presence of root segments might also be an additional reason why ERT-obtained petrophysical data

sometimes have an uncertain spread around Archie's curve.

The difference between  $\sigma_{effX}$  and  $\sigma_{effZ}$  in Figure 3.8-a indicates macro-scale anisotropy in the soil-root system. Some studies show that electrical anisotropy could be used as a parameter to monitor soil–root systems (Furman et al. 2013; Rao et al. 2018, 2019). The feasibility of using electrical anisotropy at the field scale or pot scale for root phenotyping remains to be explored in a future study. Our model helps in predicting and quantifying the electrical anisotropy.

The forward ERT modeling results showed that the evolution of apparent conductivity measurements depended on root growth. The root electrical signature term in the effective electrical conductivity ( $\delta\sigma_{eff-rs}$ ), which is the relative change in effective conductivity caused by the presence of roots ranged from as low as 0.1% to as high as 10% in the sand; in loam, it ranged from 0.02 to 0.6% (negligible). For every 1% increase in root to sand volume ratio, the uncertainty in  $\sigma_{eff}$  was 4.5% in sand and 0.2% in loam (negligible) (Figs. 3.12-a, b). For surface electrode measurements, this uncertainty was even 18% in the sand and 1.5% in loam (Figs. 3.12-c, d).

Correlation analysis between root electrical signature terms and roots' geometrical properties and soil–root  $\sigma$  contrasts suggested that the impact of roots on electrical measurements has a multivariate dependency (Fig. 3.13). We cannot solely attribute the roots' impact on bulk electrical properties to root mass density or root length density, but they somehow affect the results in combination. However, the most important factors influencing the electrical signature were the soil–root electrical contrast, which showed a very high correlation of 0.89, and root surface area ( $r \sim 0.6$ ); the

root radius showed the lowest correlation. The principal component analysis biplots in Figure 3.14 revealed that length and age were always correlated, as well as surface and volume, demonstrating similar information content.

Hence, the coupled model described in this chapter can serve as a tool to optimize the ERT measurement scheme for maximizing/minimizing root sensitivity for different root architectures or to shed light on whether ERT data has information on root phenotyping and if so, what can be done to maximize the information. Also, this modeling work could benefit the development of the bio-petrophysical relationship in the rooted soil that takes root morphological features and its electrical properties into account. Such bio-petrophysical models will minimize the error in SWC estimates in the cropped field from the ERT method.

# **4 SIMULATION-BASED INVESTIGATION OF THE GEOMETRICAL INFORMATION CONTENT OF THE SOIL-ROOT CONTINUUM IN GEO-ELECTRIC MEASUREMENTS**

## **ABSTRACT**

Non-invasive characterization of root systems and their functioning is a challenging but important task in the pursuit of ideal root systems. We hypothesize that geo-electrical measurements (ERT/EIT) contain information on the geometrical features of root architecture and could, therefore, be used for root phenotyping. To test our hypothesis, we used the process-based model described in Chapter 3 to generate virtual electrical data of 75 root systems comprising of 3 species. Crootbox software was used to generate synthetic root architecture of different species. Our modeling results demonstrate a high correlation between geometrical parameters of root networks and simulated electrical anisotropy of effective conductivity of the soil-root continuum. Thus, electrical anisotropy is a very promising proxy for monitoring root topology.

### **3.1 Introduction**

Root architecture plays a key role in acquiring water and nutrients efficiently (Mi et al. 2010). For example, rice breeds that have deeper roots can access deeper water table, demonstrating thereby higher resistance against drought (Uga et al. 2013). However, a large root system also means higher metabolic costs for root growth (Lynch 2015) which can sometimes reduce above-ground yield as observed in Maize under drought (Bruce et al. 2002). Hence there is a trade-off between root system size and metabolic cost for developing the root system for an optimal yield. Shallow root growth is efficient in acquiring nutrients like phosphorous where water scarcity is not a problem while deep vertical growth is an important underwater deficit (Lynch and Brown 2008). In addition, models have been used to show how a combination of root architectural and hydraulic traits (or phenes) could yield optimal uptake strategies as a function of the environmental conditions (Leitner et al. 2014; Meunier et al. 2020). Hence, root architecture is an important property of a root system that can be tailored for soil and weather conditions for maximizing yield. Quantifying root architecture *in situ* to assess root system performances is therefore the key to select optimal plant roots and increase drought resistance and crop yields.

Usually measuring root architecture involves either expensive non-invasive techniques such as Magnetic resonance imaging (MRI) or X-ray tomography or labor-intensive manual extraction of the root system which is difficult *in-situ* on the fields. Yet, none of

these techniques is perfect. X-ray is limited to a small column, MRI has a low spatial resolution (Metzner et al. 2015) and field coring or trenches only provide a limited amount of information on the root system itself (Morandage et al. 2019). Therefore, different global indices have been proposed to characterize root system topology and architecture. For example, Popova et al. (2016) used the root tortuosity index on MRI-derived maize root architectures to investigate root elongation and root path formation processes in a pot experiment. They also used simpler indices such as depth vs root total length and horizontal vs vertical growth ratio to study gravitropism of root structures.

Grift et al. (2011) developed an imaging system to phenotype Maize root in a high throughput sense. First, they had to uproot the plants and place them on an imaging device, which then captured high-resolution digital images of the root architecture. They then computed parameters, assumed to be proxies for root complexity, such as fractal dimension (FD) and root top angle from these digital images taken. These parameters could differentiate different genomes in maize. They also proved that roots are fractal-like structures by demonstrating a high correlation between FD evaluated from digital images taken laterally and from the top.

Numerous other studies have also used FD for studying root system complexity (Yamauchi et al. 1989; Eghball et al. 1993; Nielsen et al. 1997; Masi and Maranville 1998; Wang et al. 2009; Bouda et al. 2016). Walk et al. (2004) related FD to nutrient acquisition and soil exploration efficiency of a root system. Wang et al. (2009) observed that root traits such as total root length related to FD with a correlation coefficient as high as 0.9. Using FD, they could also differentiate and quantify drought responses in different rice genotypes.

In addition, other indices have been used in the literature to characterize network topology. To study fracture networks in rocks, Zhang and Sanderson (1995) used the ratio of the sine of the angle between the fracture network and scan lines in the vertical and horizontal direction. The scan lines were vertical or horizontal lines and this ratio of sine intersection angle or the geometrical anisotropic factor (*GAF*) captured permeability of rocks (Figure 7 in (Zhang and Sanderson 1995)). Vertical and horizontal root extents have been used to study gravitropism in roots (Popova et al. 2016). Recently, Meunier et al. (2020) used a convex hull of root system architectures for sensitivity analysis of synthetic root architectures for crop breeding applications.

Non-invasive techniques such as the electrical resistivity tomography (ERT) (Rao et al. 2020) and electrical impedance tomography (EIT) (Weigand 2016) method might offer promising features for the root system phenotyping. However, it is not clear whether the electrical properties of the soil-root domain derived from ERT/EIT contain relevant information on root architectural features for phenotyping.

In this chapter, we hypothesize that anisotropy in the frequency-dependent electrical signature of a vegetated soil pot is a function of the root system architecture. Anisotropy could arise due to root processes such as root water uptake, root architectural evolution (growth), exudation, soil gaps generated by swelling and shrinking of roots, and solute uptake. In this study though, we only take root architecture and root water uptake as the possible factors leading to electrical anisotropy. We also expect that this electrical anisotropy of soil-root medium could contain information on root geometrical features such as root

architecture and water uptake patterns. Therefore, the objectives are three fold:

1. To investigate whether frequency-dependent electrical properties of the soil-root continuum contain information on root system architecture?
2. To assess which electrical properties of the soil-root continuum can be related to root parameters such as root length, root fractal dimension, root extent or root volume, etc.?
3. To define optimal experimental conditions for root phenotyping (in terms of root radius, EC contrast, etc.).

Here in this chapter, we use process-based numerical experiments of Chapter 3 in a cuboid pot geometry for a series of simulated root systems to achieve our objectives.

## 3.2 Materials and Methods

The methodology of the current chapter is presented as a flowchart in Figure 4.1. First, the complex electrical signatures of soil and roots were characterized. The second step consisted of generating 25 different replicates of root system architectures of three different species grown in pots using the root architectural software CRootbox (Schnepp et al. 2018). The three species were chosen to represent contrasted root system topology. In the third step, root water uptake for these seventy-five root systems in pots was simulated using R-SWMS (Javaux et al. 2008). The water content distribution of soil was transformed into soil complex electrical conductivity distribution using the measured petrophysical relation. Electrical anisotropy in electrical conductivity in the horizontal and vertical

direction was computed on the generated electrical conductivity map with explicit root representation using EIDORS (Adler and Lionheart 2006) as described in Chapter 3. In the next subsections, each step is described briefly.

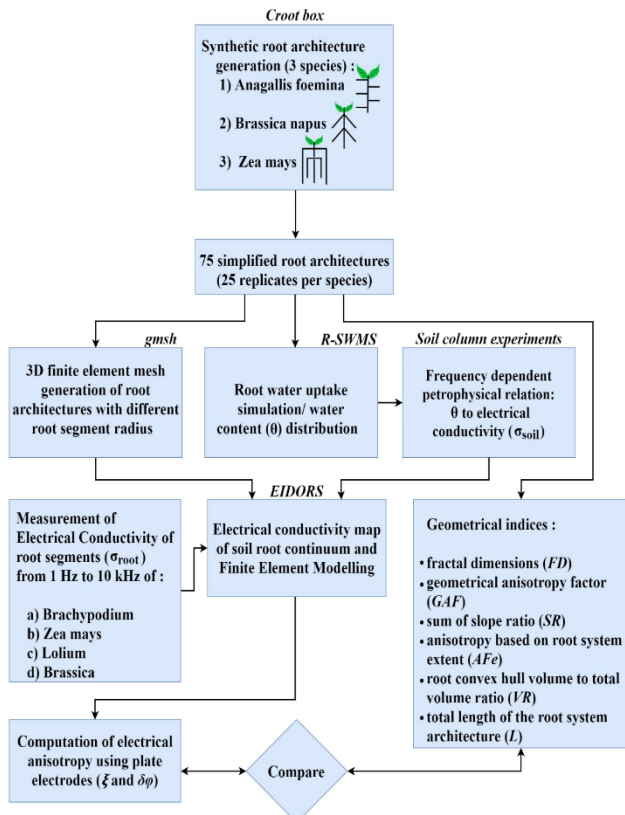


**Figure 4.1:** Methodology for comparing soil-root electrical properties with the geometrical indices of root architecture.

### 3.2.1 Silty Soil Petrophysical Relation

The frequency-dependent impedance response of silty soil was determined using soil column experiments at different moisture levels (van Treeck 2019). The following empirical equation was used to fit the measurement data:

$$\sigma = \exp \exp (a\phi^c + b) \quad (4.1)$$

where,  $\sigma [S m^{-1}]$  is the electrical conductivity (inverse of resistivity) decomposed into real and imaginary part ( $\sigma_{real}$  and  $\sigma_{imag}$ ),  $\phi [-]$  are the soil water content saturation and  $a$ ,  $b$  and  $c$  are the fitting parameters. The empirical fitting parameters along with the data are shown in Figure 4.2.

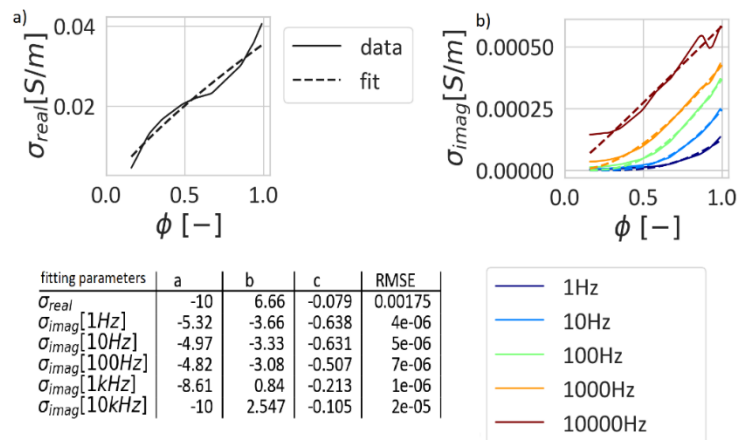


**Figure 4.2:** Measured and empirical fits to silt electrical conductivity at different moisture levels. a) real part of  $\sigma$ , and b) imaginary part of  $\sigma$ . The fitting parameters are shown as a table.

### 3.2.2 Root Electrical properties

The objective of this experiment was to obtain a range of electrical properties for different types of roots. Root electrical properties were measured for Maize (*Zea Mays*), Ryegrass (*Lolium perenne*), Rapeseed (*Brassica napus*), and Stiff brome (*Brachypodium distachyon L.*). The impedance of root segments belonging to these

species was measured at different frequencies ranging from 1 to 10 kHz as described in section 2.8.3. These measurements were part of the Ph.D. thesis of Solomon Ehosioka (under publication 2020). The measurement was repeated on four replicates on the collar segment of primary roots. The distance between the four-point electrode was 1.5 cm. At the time of measurements, roots were 4 weeks old from the date of germination. The results along with mean and standard deviation are shown in Figure 4.3. The real part of conductivity increases approximately three times between 10 and 10KHz while the imaginary part increases by a factor six showing a very strong polarization signature. We chose the lower limit of *Brachypodium* and upper limit of *Brassica* (black dashed lines in Fig. 4.3) denoted by  $\sigma_l$  and  $\sigma_u$  at 10 Hz and 10 KHz (black circles and squares in Fig. 4.3) for parameterizing our different species. The parameters  $\sigma_{root} = \sigma_l$  and  $\sigma_{root} = \sigma_u$  envelops realistic ranges of electrical properties for roots. These will be used in the rest of this study to represent the electrical signal for other plant species.

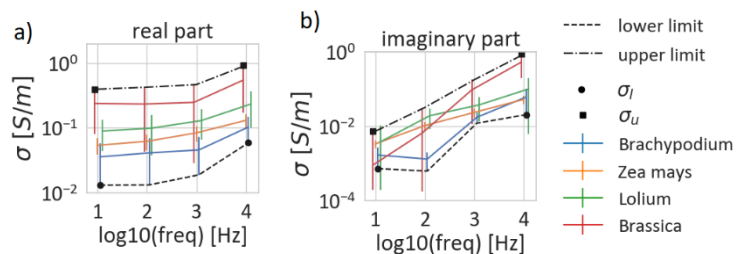


**Figure 4.3:** Measured electrical conductivity of different root segments as a function of frequency. The vertical lines represent the standard deviation of four plants. Black circles and squares indicate the upper and lower limit of root electrical conductivity range at 10 Hz and 10 KHz.

### 3.2.3 Root Architecture Simulation

We generated synthetic three-dimensional root system architectures constrained to grow in cuboid pots of size 20 cm x 20 cm x 30 cm. We chose three different plant species with very contrasted root system architectural features: *Anagallis Foemina*, which produces nearly horizontal secondary roots, *Brassica napus*, which produce tilted secondary roots and *Zea mays* having nearly vertical roots as shown in Figure 4.4. C-Rootbox software (Schnepf et al. 2018) was used for the generation of these root architectures. Each plant species is characterized C-Rootbox by a set of parameters that describe the root geometrical and growth properties, whose values are picked up from a distribution defined by the parameter mean and standard deviation. The root architectural parameters for each category of root architecture were referred from (Schnepf et al. 2017). Further, we generated 25 replicates or realizations for each plant species comprising a total of 75 root systems for our study. Replicates of a given species share the same mean and standard deviation values for their parameterization. The first three replicates are shown in Figure 4.4.

We modified the original values of the species' parameters in C-Rootbox such that it produced root systems with only two root orders: primary and secondary roots. We do not simulate higher-order roots due to computational constraints in finite element mesh generation. In addition, the number of secondary roots was randomly reduced by 25% to have a manageable computational load while meshing. This simplification, though not perfectly representative of a real plant (higher-order removed), still preserves the main topological features of the different species.

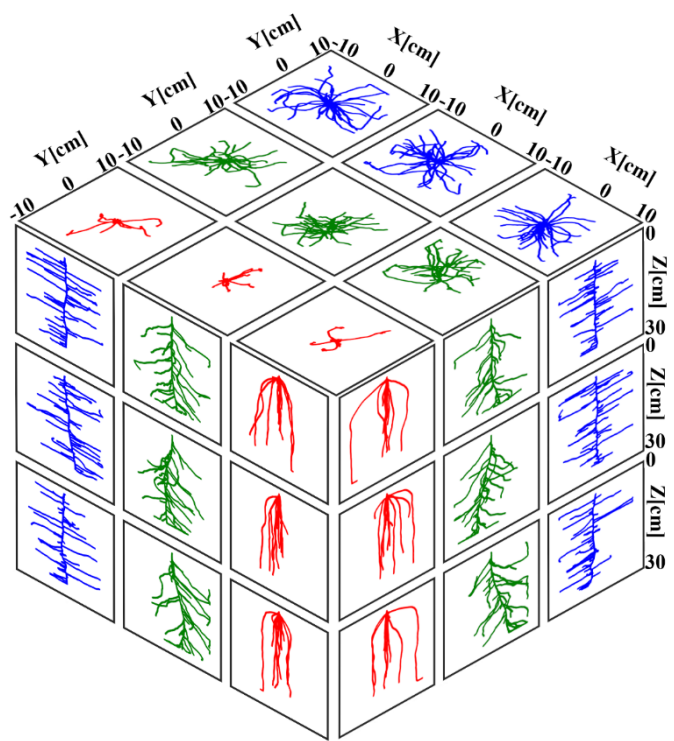


**Figure 4.4:** The First three realization (rows) of different root architectures (columns) generated using C-Rootbox.

The cube represents the top, front, and side view of the root architectures. Colors indicate plant species: blue = Anagallis, green = Brassica, and red = Zea mays.

### 3.2.4 Geometrical Indices for Soil-Root System

In order to quantify the geometrical and topological differences species, we reviewed a series of indices found in the literature.

#### *Root extent and slope ratio*

We define the following indices based on the root system architecture (see Fig. 4.5):

- Anisotropy based on root system extent:

$$AF_e = \frac{Z_{\text{extent}}}{\sqrt{X_{\text{extent}}^2 + Y_{\text{extent}}^2}}$$

where  $Z_{\text{extent}}$  is the vertical distance between the soil surface and the deepest root segment,  $X_{\text{extent}}$  and  $Y_{\text{extent}}$  are horizontal distances between the most distant root segments along X and Y, respectively as shown in Figure 4.5 (Popova et al. 2016).

- Average slope ratio ( $SR$ ) of root segments (see Fig. 4.5):

$$SR = \frac{\sum_{i=1}^n dz}{\sum_{i=1}^n \sqrt{dx^2 + dy^2}}$$

where  $dx$ ,  $dy$  and  $dz$  are incremental distance within a root segment in x, y, and z directions as shown in Figure 4.6. The summation is over all the root segments.

- Root architecture convex hull volume (yellow box in Fig. 4.5) to the total pot volume ratio (Leitner et al. 2014):

$$VR = \frac{\text{vol. of convex hull of root system}}{\text{total volume of pot}}$$

- The total length of the root system denoted by L (Schnepp et al. 2018).

$$L = \sum_{i=1}^n dl$$

where  $dl$  is the length of a particular root segment and summation is over all the root segment.

### *Fractal Dimension (FD)*

We first convert a given root architecture generated from Crootbox into a 2-D binary image in front view (XZ plane) and then apply the traditional box-counting method to compute the underlying Fractal dimension as described for Maize roots by Grift et al. (2011). In the box-counting method (Landis 2005; Grift et al. 2011), we discretize the 2-D binary image of the root projection in XZ plane with a square grid or boxes of different sizes as shown in Figure 4.5 (a-d) and count the no. of boxes (N) that completely cover the 2-D root

architecture for a given box or grid size ( $s$ ) (grey boxes in Fig. 4.5-a). Then we may vary the box size ( $s$ ) and recompute  $N$  as a function of  $s$ . The slope of the plot of the logarithm of  $N$  vs logarithm of the inverse of  $s$  is the fractal dimension (Landis 2005). Mathematically,  $FD$  can be written as (Bouda et al. 2016):

$$FD = \frac{-\log(N(s))}{\log(s)}.$$

The procedure of converting root architecture into a 2-D binary image and then computing its  $FD$  is achieved using custom made MATLAB functions. Fractal dimension is computed for three possibilities each for the front, lateral, and top view of the root architecture denoted by  $FD_x$ ,  $FD_y$  and  $FD_z$ .

#### *Geometrical Anisotropic Factor (GAF)*

We modified the 2-D *GAF* indices used in their study to capture the 3-D geometry of the root system architecture.

We compute *GAF* index for our synthetic root systems only in two coordinates (XZ) ignoring the Y-variations. First, we have parallel scanlines with a spacing of 2 cm in the horizontal or vertical direction. Two such scan lines (red dashed lines) along with the point of intersection between scanline and root segments (black dots) are shown in Figure 4.5-e. The *GAF* is the ratio of the sine of intersection angle between root segments and scan lines in the vertical and horizontal direction:

$$GAF = \frac{\frac{1}{Lz} \sum \sin \sin (\gamma_z)}{0.5 * \left( \frac{1}{Lx} \sum \sin \sin (\gamma_x) + \frac{1}{Ly} \sum \sin \sin (\gamma_y) \right)}$$

where,  $\gamma_x$ ,  $\gamma_y$  and  $\gamma_z$  are the angles between a scan line and root segments in different directions, the summation is on the number of intersections between

scan lines and root segments,  $L_x$ ,  $L_y$ , and  $L_z$  are the length of scan lines in X, Y and Z directions (Zhang and Sanderson 1995). Because of the ratio,  $GAF$  is independent of total root length but only depends on root architecture.

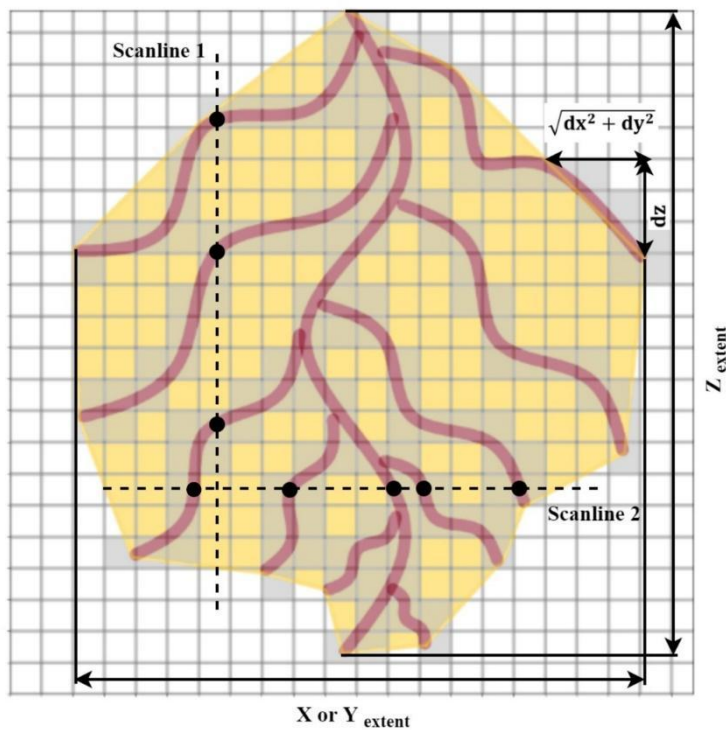


**Figure 4.5:** Geometrical indices on root system architecture. The shaded grey boxes are traversed by root segments used for the box-counting method while white and yellow boxes are untouched by roots. The yellow region represents the convex hull of the root system architecture. Scanlines for computing geometrical anisotropic factor ( $GAF$ ) are shown (dashed lines) along with the point of intersection (dots).

### 3.2.5 Root water uptake simulation

We used the soil-plant water flow model R-SWMS (Javaux et al. 2008) to simulate the evolution of soil water content distributions affected by root water uptake. The soil domain had the following dimension: 20 [cm] x 20 [cm] x 30[cm] (the corresponding reference axis are  $-10 < x < 10$  [cm],  $-10 < y < 10$  [cm],  $-30$  [cm]  $< z < 0$ ) corresponding to a cuboid pot. The initial time (or root age) was 25 days and the initial soil condition was a homogeneous water content corresponding to a pressure head of -50 [cm]. We simulated water uptake for 6 days, with an imposed transpiration flow of 20 cm<sup>3</sup>/d, which allowed the root system to generate soil water depletion patterns as shown in Figure 4.6. The other boundary conditions for the soil domain were no flow (no drainage and no evaporation).

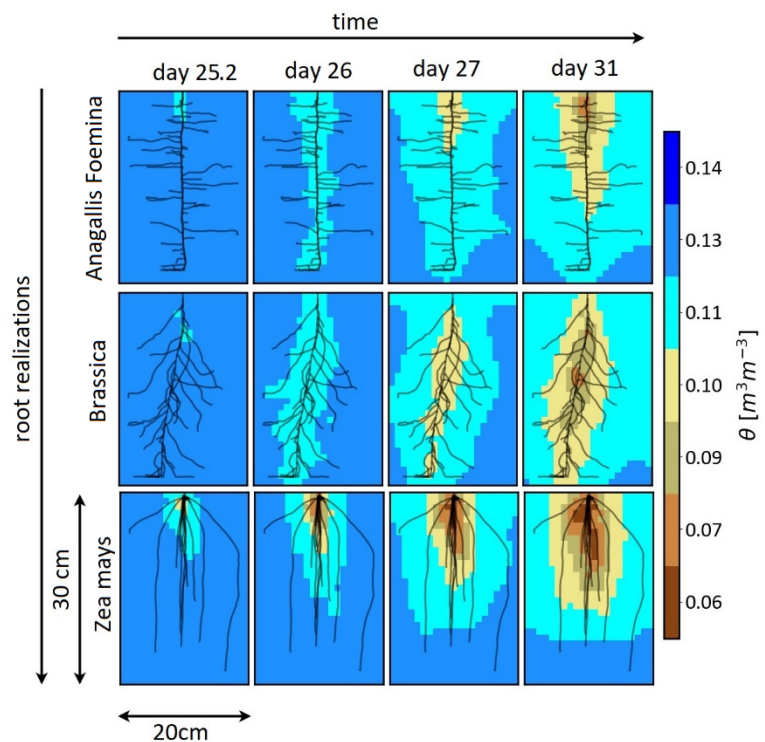


**Figure 4.6:** Root water uptake simulation at Y = 0 plane for one of the 25 realizations of each different species in R-SWMS: a) day 25, b) day 26, c) day 27 and d) day 31.

For soil hydraulic parameters, we chose the van-Genuchten model of a Silty loam. For root radial and axial hydraulic conductivity values, we chose parameters from the study of (Koch et al. 2019).

**Table 4.1:**

Residual water content $\theta_r$ [cm <sup>3</sup> /cm <sup>-3</sup> ]	Saturation water content $\theta_s$ [cm <sup>3</sup> /cm <sup>-3</sup> ]	Shape parameters of VGM model				Hydraulic conductivity of soil $K_s$ [cm/day]
		$a$ [1/cm]	$n$	$m$ [ $1 - \frac{1}{1 + \lambda}$ ]	$\lambda$	
0.06	0.41	0.03	2.5	0.6	0.5	10.24

### 3.2.6 Finite element mesh generation and the finite element model

In order to solve the Poisson equation, a detailed finite element meshing representing explicitly the root system had to be produced. The 3-D root structures were meshed using Gmsh (Geuzaine and Remacle 2009) to create a finite element electrical simulation model in a cuboid pot geometry. The tetrahedrons generated were of good quality (mesh quality factor > 0.7 for 90% of elements while none had quality factor less than 0.2) with zero ill-shaped elements in the mesh. The finite element model for one of the realizations of Anagallis in a pot geometry for different root radii is shown in Figure 4.7. Due to the small root

radius ( $r \sim 1$  mm), mesh refinement near root segments was achieved using distance and attractor features in Gmsh. The root radius in the final finite element mesh is back computed using a known volume of root tetrahedrons and total root length in C-Rootbox generated root systems. Similar to chapter 3, we created finite element models with three cases of root segment radii ( $r_1 \sim 1$  mm,  $r_2 \sim 1.5$  mm,  $r_3 \sim 2.5$  mm as shown in Fig. 4.7-d) in the finite element mesh to understand the scaling of electrical properties with the increasing root volume/radii. The number of tetrahedrons in the finite element mesh ranged from  $2e5$  to  $6e5$ . The simulated root systems are less than 1% in volume for all the scenarios considered as shown in Figure 4.7-d.

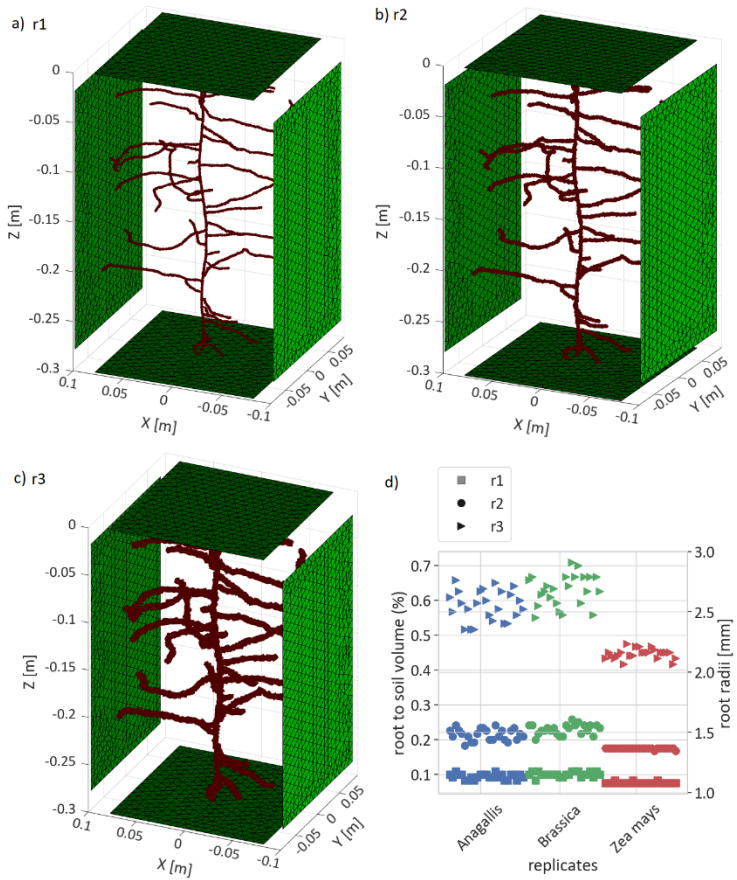


**Figure 4.7:** Finite element model in a pot geometry for a root architecture for a) radius = r1, b) r2 and c) r3. The green rectangles at the boundary represent the six-plate electrode on each face of the cuboid and d) root to soil volume ratio in percentage for r1 (square), r2 (circle), and r3 (triangle) scenarios for 75 different root systems in the finite element mesh. Colors indicate plant species: blue = Anagallis, green = Brassica, and red = Zea mays.

### 3.2.7 Electrical anisotropic factor

After the mesh generation, we assigned each finite element with appropriate electrical property similar to the procedure explained in Chapter 3. Furthermore, we generate additional simulation data by assuming the electrical properties of 4 different species as shown in Figure 4.3.

First, we computed effective electrical conductivity ( $\sigma_{eff}$ ) in the two perpendicular directions (X) and (Z) using four plate electrodes located on four faces of the cuboid (Figs. 4.7-a, b, and c). For example, effective electrical conductivity between the plate electrode located in the top and the bottom face (XZ-plane) in Figure 4.8 gives the effective property in Z-direction denoted by  $\sigma_{effZ}$ . Similarly, we get effective electrical conductivity  $\sigma_{effX}$  using the left and right plate electrodes. Due to the rotational symmetry of root systems and for simplicity, we do not consider the effective properties in the Y direction. For computing effective properties between plate electrodes, we solve Poisson's equation using EIDORS software in MATLAB (Adler and Lionheart 2006) as described in Chapter 3.

The computed quantities,  $\sigma_{effX}$  and  $\sigma_{effZ}$  are complex quantities having magnitude and phase ( $\varphi$ ). We define

the effective percentage anisotropic factor in magnitude as:

$$\xi = 100 * \left( \frac{|\sigma_{effX}|}{|\sigma_{effZ}|} - 1 \right)$$

Similarly, in phase, we define it as  $\delta\varphi = \varphi_X - \varphi_Z$ . These quantities quantify heterogeneity in electrical conductivity in two principal directions. The magnitude part quantifies the DC properties while the phase part represents the polarizing property as described in Chapter 2.

### 3.2.8 *The testing discriminatory power of Indices*

To test if a root index sufficiently discriminates a particular species from others, we do the following tests:

1. Check for the statistical significance of particular indices between three different species using ANOVA.
2. Compare means of particular indices between three different species pairwise and perform Tukey mean honestly significant difference test for statistical significance (Tukey 1949).
3. Perform the K-nearest neighbor classification algorithm to check If the algorithm correctly classifies a particular species based on a particular index (Peterson 2009).

## 3.3 Results and Discussions

### 3.3.1 Characterization of geometrical and topological differences between root systems

The various geometrical and topological indices described in section 4.2.4 were applied to each replicate of each species to characterize the variation of geometry within and between species. We performed linear correlation analysis pairwise and the results are shown in Figure 4.8.

From the probability density functions (pdf) (diagonal of Fig. 4.8), we see that  $GAF$ ,  $SR$ , and  $AF_e$  discriminates different root architectures (fewer overlaps between red, green and blue curves) better than the  $VR$ ,  $L$ ,  $FD_x$ ,  $FD_y$  and  $FD_z$  indices. In addition, we observe an overlap between blue and green pdf for indices  $AF_e$ ,  $VR$ ,  $L$ ,  $FD_x$ ,  $FD_y$  and  $FD_z$ , which demonstrates that these are not suitable for discriminating root system architectures of *Zea mays* and *Brassica*. On the other hand, well-separated pdf can be seen in  $GAF$  and  $SR$  showing their superiority in discriminating against the three species root system architectures. The anisotropy in root extent ( $AF_e$ ) also nicely differentiates different species but in an opposite trend (red dots below the blue dots) as compared to  $GAF$ ,  $SR$ ,  $FD_x$ ,  $FD_y$  and  $FD_z$  and is also well correlated to other variables including the length with Pearson coefficient ranging from 0.72 to 0.91 ( $p < 0.0001$ ).

We observe a strong correlation ( $r \sim 0.9$ ) that are highly significant ( $P < 0.0001$ ) between fractal dimensions obtained from a different cross-sectional view of the synthetic root architectures ( $FD_x$ ,  $FD_y$  and  $FD_z$ ). This is consistent with the experimental observations made by Grift et al. (2010) who observed correlation ranging from 0.77 to 0.88 ( $P < 0.001$ ) between fractal dimensions of lateral and top root images. We also observe that  $GAF$  is nicely correlated with all other

indices except total root length ( $L$ ) and structurally appears similar to the slope ratio ( $SR$ ) and fractal dimension ( $FD_x$ ,  $FD_y$  and  $FD_z$ ). Hence these indices essentially capture the same information of the root topology.

Our next step is to relate each of these geometrical indices to the electrical anisotropy index ( $\xi$  and  $\delta\varphi$ ) defined in section 4.2.7 and assess which of the geometrical features can be retrieved from electrical anisotropy.

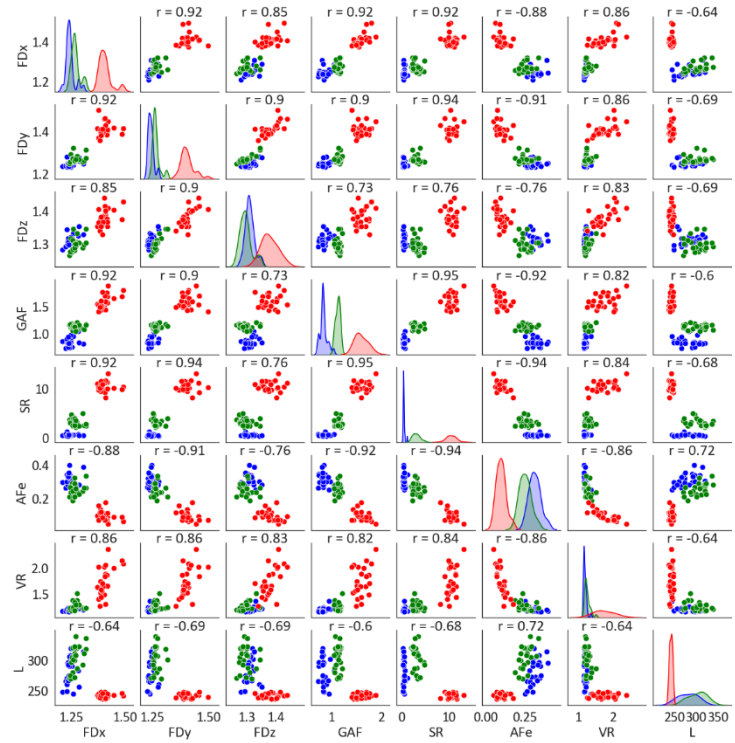


**Figure 4.8:** Correlation analysis and scatter plot of root geometrical indices. Colors indicate plant species: blue = Anagallis, green = Brassica, and red = Zea mays. The distributions on the diagonal represent the probability density functions of each index.

### 3.3.2 Electrical anisotropy signatures of roots

Figure 4.9 shows simulated  $\xi$  vs  $\delta\varphi$  for the different radius ( $r_1, r_2, r_3$ ), frequency (10 Hz and 10 kHz), root electrical conductivity ( $\sigma_{root} = \sigma_l$  and  $\sigma_{root} = \sigma_u$ ) and time (day 25.2 and 31).

At low frequency or DC and at initial time 25.2, we do not see any anisotropy both in magnitude and phase due to the absence of root polarization as well as soil water uptake pattern (first row of Fig. 4.9-a). On day 31, as root takes up water, we see some anisotropy in magnitude (second row of Fig. 4.9-b) which is mainly the response of the soil. The phase anisotropy remains negligible for frequency = 10 Hz and  $\sigma_{root} = \sigma_l$ . Interestingly, the impact of the radius is also negligible. Hence, under these circumstances, anisotropy cannot be used for phenotyping root systems.

In Figure 4.9b, we kept the frequency same (10 Hz) but changed root electrical properties to the upper limit ( $\sigma_{root} = \sigma_u$ ). We not only observe the impact of radius as opposed to Figure 4.10-a but also observe the phase anisotropy ( $\delta\varphi$ ). Larger the root radius, higher the  $\xi$  and  $\delta\varphi$ . Interestingly, we do not observe the impact of time or the soil water uptake so much. Hence, for a high contrast roots ( $\sigma_{root} = \sigma_u$ ), anisotropy is driven by root presence, at least for the assumed parameters.

At high frequency (10 kHz), when roots have low contrast with soil ( $\sigma_{root} = \sigma_l$ ), the radius has an impact on  $\delta\varphi$  but not on  $\xi$  both when soil is homogeneous (day 25.2 in Fig. 4.9-c) and when the soil has uptake

patterns (day 31 in Fig. 4.9-c). We see a linear increase of magnitude in  $\delta\varphi$  with an increasing radius. When roots have higher contrast than soil ( $\sigma_{root} = \sigma_u$ ), we see an increase in both  $\xi$  and  $\delta\varphi$  in a linear fashion with increasing radii.

From Figure 4.9, we learn that discrimination between species in terms of electrical anisotropy is poorer for thinner roots ( $r = r1$ ) than for thicker roots ( $r = r3$ ). For low frequency or DC measurements, only for radius =  $r3$  and  $\sigma_{root} = \sigma_u$ , we see nice discrimination of different species (Fig. 4.9-b). Hence for low-frequency measurements, the ideal situation for electrical imaging of root is when roots are thicker, have good electrical contrast with soil, and contains soil water uptake patterns. At high frequency, we see a nice separation among species both in magnitude and phase for both  $\sigma_{root} = \sigma_l$  and  $\sigma_{root} = \sigma_u$  due to polarizability of roots (Figs. 4.9-c and d). Hence, high frequency should be favorable for imaging root systems, at least for the assumed parameters.

Another interesting feature to be observed in Figure 4.9 is the slope ( $m$ ) between  $\xi$  and  $\delta\varphi$  which varies as a function of time, frequency, radius, and root electrical properties. The slope signifies the dominance of the phase part of anisotropy ( $\delta\varphi$ ) over magnitude ( $\xi$ ). A large slope implies high polarizability (Fig. 4.9-c) while zero slopes (Fig. 4.9-a) implies no polarization. The slope is quite horizontal when soil is homogeneous, freq=10 Hz and  $\sigma_{root} = \sigma_l$  (Fig. 4.9-a) and becomes positive for  $\sigma_{root} = \sigma_u$  or freq=10 kHz as a function of radius, time, and frequency (Figs. 4.9-b, c, and d).

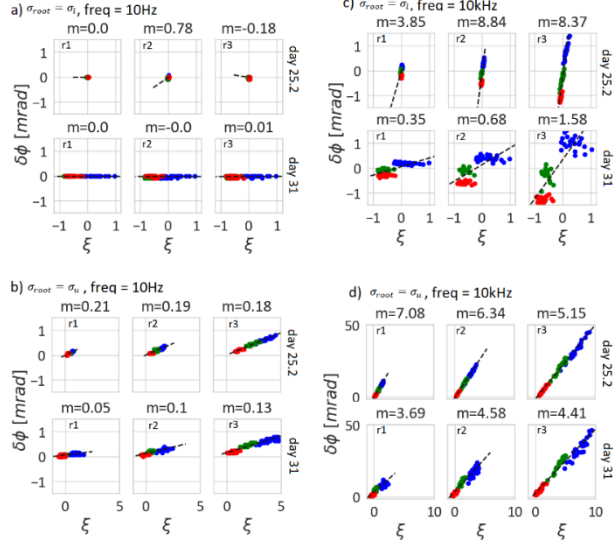


**Figure 4.9:**  $\xi$  versus  $\delta\phi$  for different root radii (columns) and time (rows) for a)  $\sigma_{root} = \sigma_l$  and frequency = 10 Hz, b)  $\sigma_{root} = \sigma_u$  and frequency = 10 Hz, c)  $\sigma_{root} = \sigma_l$  and frequency = 10 kHz, and d)  $\sigma_{root} = \sigma_u$  and frequency = 10 kHz. Colors indicate plant species: blue = Anagallis, green = Brassica, and red = Zea mays.  $m$  is the slope of the correlation line.

### 3.3.3 The relation between electrical anisotropy and geometrical indices at low frequency

Figure 4.10 relates  $\xi$  for different root electrical properties ( $\sigma_l$  and  $\sigma_u$ ), radii (r1, r2, and r3) and water uptake patterns (at day 25.2 and 31) with different geometrical indices. We do not relate  $\delta\phi$  to geometrical indices at low frequency due to low polarization of roots as observed in Figure 4.10.

First, we observe that the correlation between  $\xi$  and other geometrical indices is always higher than 0.6 in absolute value when the soil water content is

homogeneous (day 25.2) as seen in Figure 4.10-a and c. This demonstrates that information on root geometrical information is present in electrical anisotropy. However, the magnitude of anisotropy is very small at day 25.2 (in Fig. 4.10-a) as the soil is homogeneous with little uptake near the collar and low contrast between soil and roots. On the opposite, on day 31 (Fig. 4.10-b), soil water content is more heterogeneous due to water uptake, and it translates into a broader range of  $\xi$ . This means that, for less contrasted soil-root properties, the electrical anisotropy is enhanced by uptake patterns induced by roots rather than by the presence of roots only.

It is also interesting to note that the slope reverses direction in Figure 4.10-c as compared to Figure 4.10-a. This might be due to the preferential flow of electric current in Figure 4.10-c due to the higher conductivity of roots ( $\sigma_{root} = \sigma_u$ ) as compared to Figure 4.10-a where roots had lower conductivity ( $\sigma_{root} = \sigma_l$ ). Figure 4.10-c further shows that  $\xi$  can be related to  $L$ ,  $FD_x$ ,  $GAF$ , and  $SR$  with a correlation as high as 0.9 when soil is homogeneous and root electrical conductivity ( $\sigma_u$ ) has sufficient contrast as compared to soil electrical conductivity.

We also observed that increasing radius had no impact in  $\xi$  (results not shown) and hence the variations we observe in Figure 4.10-a are predominantly due to root architecture and root electrical properties at day 25.2. At a later time, the root water uptake pattern distorts the linear relation of anisotropy with geometrical indices as evident from the lower correlation on day 31.

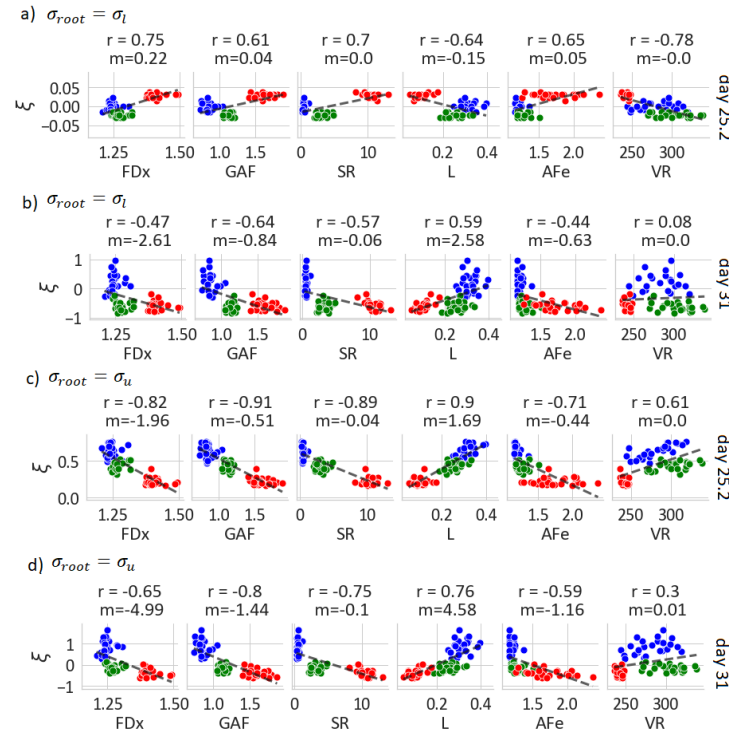


**Figure 4.10:**  $\xi$  as a function of various geometrical indices for a) electrical conductivity of root =  $\sigma_l$  and at day 25.2, a) electrical conductivity of root =  $\sigma_l$  and at day 25.2, b) electrical conductivity of root =  $\sigma_l$  and at day 31, c) electrical conductivity of root =  $\sigma_u$  and at day 25.2 and d) electrical conductivity of root =  $\sigma_u$  and on day 31. Colors indicate plant species: blue = Anagallis, green = Brassica, and red = Zea mays.  $m$  is the slope of the correlation line.

### 3.3.4 Electrical anisotropy phase at high frequency

Simulations at 10 KHz and day 25.2 (homogeneous soil) show that for  $\sigma_{root} = \sigma_l$ ,  $\delta\varphi$  has a good correlation with  $L$ ,  $SR$ ,  $GAF$ , and  $FDx$  while the correlation is weaker in  $\xi$  (Fig. 4.11-a). With the onset

of water depletion pattern at day 31 in Figure 4.11-b, improvement of the correlation coefficient between  $\xi$  and some geometrical indices can be observed while the general trend of  $\delta\varphi$  remains the same. Thus, we can conclude that  $\xi$  mainly depends on soil water uptake patterns when roots are less conductive ( $\sigma_{root} = \sigma_l$ ) while  $\delta\varphi$  is essentially due to root presence.

For  $\sigma_{root} = \sigma_u$ , we see that both  $\xi$  and  $\delta\varphi$  show good correlation with geometrical indices irrespective of the water uptake patterns (Figs. 4.11-c and d). Thus, when soil-root electrical contrast is high enough, electrical anisotropy in both magnitude and phase can be related to root geometrical features such as  $L, SR, GAF$ , and  $FDx$ .

We also observe in Figure 4.11 that the slope between electrical anisotropy and geometrical indices (black dashed line) varies as a function of root electrical contrast and uptake. The slope ( $m$ ) increases from Figure 4.11-a to Figure 4.11-d eight times in  $\xi$  and forty times in  $\delta\varphi$ . This might open the possibility of using these correlations to have a quantitative index for root activity and properties.

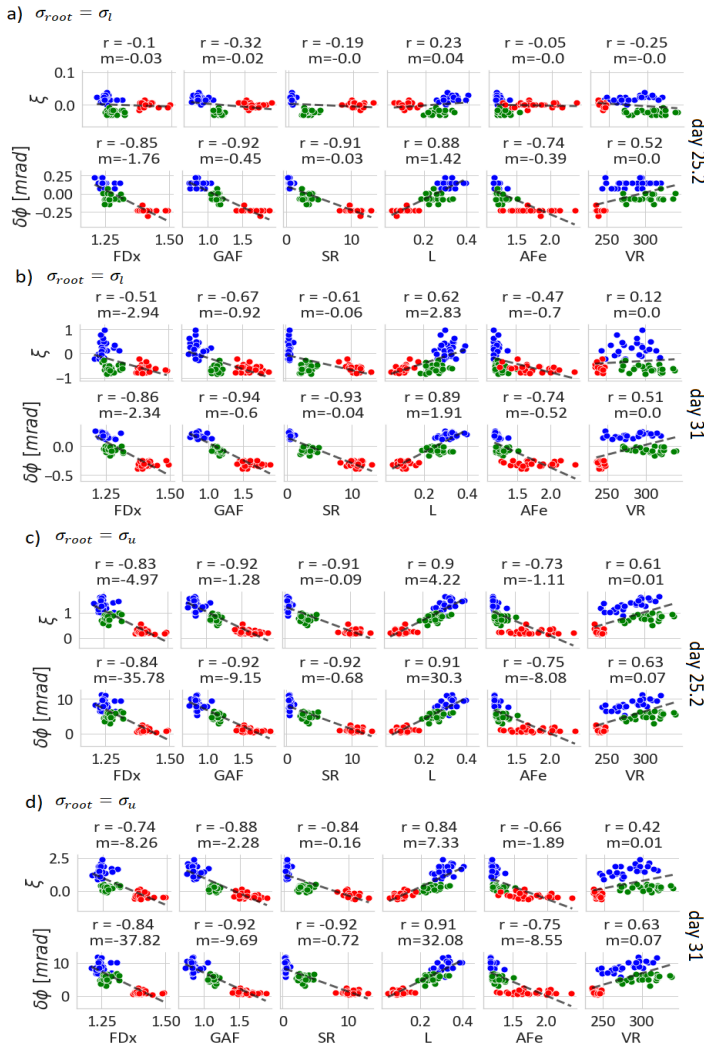


**Figure 4.11:**  $\xi$  and  $\delta\phi$  as a function of various geometrical indices for a) electrical conductivity of root =  $\sigma_l$  and at day 25.2, b) electrical conductivity of root =  $\sigma_l$  and at day 31, c) electrical conductivity of root =  $\sigma_u$  and at day 25.2 and d) electrical conductivity of root =  $\sigma_u$  and on day 31. Different colors indicate plant species: blue = Anagallis, green = Brassica, and red = Zea mays.  $m$  is the slope of the correlation line.

### 3.3.5 The discriminatory power of electrical anisotropy

Figure 4.12 shows the probability density functions of  $GAF$ ,  $SR$ ,  $\xi$ ,  $\delta\phi$ ,  $FDx$ ,  $L$ ,  $AFe$ , and  $VR$ . We can observe that electrical quantities  $\xi$  and  $\delta\phi$  (shown for frequency = 10 kHz, radius =  $r_1$ , and day 25.2) discriminates (less overlap between different colors) the different root architectures as good as  $GAF$  or  $SR$  and better than most other variables considered. Both one-way ANOVA and pairwise Tukey mean HSD statistics show differences between different species (red, blue, and green in Fig. 4.12) of both geometrical indices and electrical anisotropy are statistically significant ( $p = 0.001$ ). This shows that  $\xi$  and  $\delta\phi$  can be used for root phenotyping purposes at higher frequency (10 kHz).

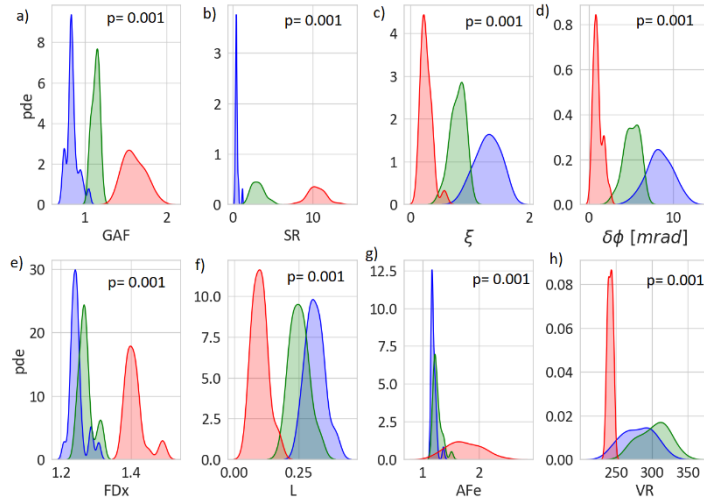


**Figure 4.12:** Probability density function of different variables (xlables). Different colors indicate blue = Anagallis, green = Brassica, and red = Zea mays.

To further highlight the discriminatory power of each index, we did a K-nearest neighbor classification ( $k = 3$ ) and the resulting classification accuracy scores are shown in Figure 4.13. In this machine-learning

approach, we observe that both magnitude (Fig. 4.13-a) and phase parts (Fig. 4.13-b) of electrical anisotropy perform better than the geometrical indices (Fig. 4.13-c). On average, the algorithm classifies the root architecture correctly 80% of the time. In k-means, the number of neighbor's "k" is the points to be considered while computing the value of a given point. For a test point, say  $p_0$ , three nearest neighbor points  $p_1, p_2, p_3$  will be computed. The optimal integer value of  $k$  ( $> 0$ ) varies with the application. In our case, since we have a small dataset, it is logical to have a smaller number of neighbors. We have chosen  $k = 3$  as it is the smallest and the accuracy is consistent up to  $k = 5$ . The classification accuracy with the High Frequency (10 kHz) signal is excellent for both the plants 1 and 2, with both magnitude and phase parts. But the low frequency has a lesser accuracy to classify plant1.

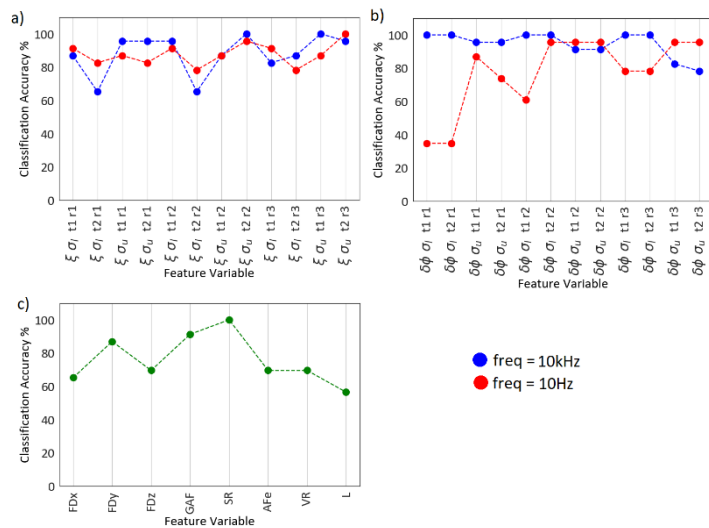


**Figure 4.13:** K-nearest neighbor classification of root species based on a)  $\xi$ , b)  $\delta\phi$  and c) various geometrical indices of the root system architecture. In a and b,  $\sigma_u$  and  $\sigma_l$  represents upper and lower bounds of root electrical properties, t1 and t2 represent day 25.2 and 31, red and blue represent the frequency of 10 Hz and 10 kHz, and r1, r2, and r3 represent different root radii.

### 3.4 Conclusion

In this chapter, we extended the coupled model presented in Chapter 3 to a pot scale in 3-D to investigate the geometrical information contained in the electrical signatures of the soil-root continuum of 3 contrasted root architectures (horizontal *Anagallis Foemina*, tilted *Brassica*, vertical *Zeae mays*).

To quantify the differences in terms of topology and geometry between species, we computed different indices for synthetic root architectures such as fractal dimension ( $FD_x$ ,  $FD_y$  and  $FD_z$ ), geometrical anisotropy (*GAF*), slope ratio (*SR*), anisotropy in root extent ( $AF_e$ ), root convex hull volume ratio (*VR*), and total length (*L*). We observed that fractal dimensions obtained from different views of the root system were highly correlated confirming that roots are fractal-like structures as observed by Grift et al. (2010). We also observed that *GAF* and *SR* were more suitable to discriminate species as compared to other indices.

From the synthetic pot experiment performed in this study, we observe that computed magnitude and phase part of the electrical anisotropy depend on root architecture and are discriminated among three categories of roots considered. While the magnitude part  $\xi$  is both dependent on root uptake pattern as well as root architecture, phase part  $\xi$  is dependent only on the root architecture at least for the assumed parameters of this study.

We found that  $\xi$  and  $\delta\varphi$  were highly correlated to geometrical indices with the correlation coefficient as high as 0.9. We also observed that electrical anisotropy quantities  $\delta\varphi$  and  $\xi$  contain similar information as *FD*, *GAF*, or *SR*. While *GAF* has not been attempted to root

systems (to the best of our knowledge),  $FDx$  has been thoroughly established index for studying root systems. For example,  $FDx$  is an indicator of root system complexity, soil exploration efficiency, plant response to soil saturation, drought response and salinity, water use efficiency, and root phenotyping (Bouda et al. 2016). However, the FD index for the root system can only be obtained invasively and labor-intensive (Grift et al. 2011). In our study, we show that  $\delta\varphi$  and  $\xi$  virtually contains similar information as  $FDx$  and is even more discriminatory between different root systems than  $FDx$ . This shows the rich root geometrical information contained within the electrical properties of soil-root continuum. Within the scope of the simulations run in this study, we conclude that electrical anisotropy ( $\delta\varphi$  and  $\xi$ ) is a very promising proxy for monitoring root topology.

The practical extensions of ideas developed in this chapter to the real-world require the design of electrodes capable of measuring effective properties in at least two different directions. However, designing plate electrodes is not easy and hence an easy approach would be to have several point electrodes operate to deduce effective properties as in the study of (Al-Hazaimay et al. 2016).

With a huge dataset of anisotropy measurements for each plant species and the different conditions, it is possible to classify the root architectures non-invasively with a good level of accuracy using machine learning algorithms such as K-nearest neighbor. As a logical extension of this electrical sensing method, we can combine the multi-frequency probing approach and machine learning to push the classification accuracy even further. The next step would be to test this methodology in real experiments with plants in pots.





PART IV

ROOT  
PHENOTYPING AT  
FIELD-SCALE



In this section we will present a new methodology for phenotyping grass root systems in drought conditios using electrical resistivity tomography experiments.

*Uṛdwam jigātu bheṣhaṇam*

*Taitīryāranyakamopniṣad*

Meaning: Let trees having medicinal properties grow skywards

Taitirya Aranyakam Upanishad





# **5 IMAGING PLANT RESPONSES TO WATER DEFICIT USING ELECTRICAL RESISTIVITY TOMOGRAPHY**

Chapter adapted from:

Rao S, Lesparre N, Orozco A. F., Wagner F, Javaux M.  
Imaging plant responses to water deficit using  
electrical resistivity tomography. Accepted for  
publication in Plant and Soil. 2020 June.

---

## **ABSTRACT**

Monitoring root water uptake dynamics under water deficit (WD) conditions in fields is crucial to assess plant drought tolerance. In this study, we investigate the ability of Electrical Resistivity Tomography (ERT) to capture specific soil water depletion induced by root water uptake. A combination of surface and depth electrodes with high spatial resolution (10 cm) was used to map 2-D changes of soil EC changes in an agronomic trial with different grass and forb species. A synthetic experiment with a mechanistic model was performed to assess the ability of the electrode configuration to discriminate root water uptake patterns. The synthetic analysis allowed us to define two synthetic indices (depletion averaged depth and extent), which statistically discriminate between species specific depletion patterns.

The time-lapse analysis of the ERT imaging shows that different root water uptake patterns can be delineated for measurements collected under WD conditions but that patterns are not so easily recovered from data collected under well irrigated conditions. ERT seems to be able to discriminate root water uptake dynamics between species, in WD conditions. Yet, only changes of ERT-retrieved water content or electrical resistivity in two weeks were able to adequately delineate water depletion peak and extent with an accuracy of around 5 cm. We show that Cockstfoot and Ryegrass had shallower soil water depletion zones than white clover and white clover combined with Ryegrass. ERT is a well-suited method for phenotyping root water uptake ability in field trials under WD conditions.

## 4.1 Introduction

Developing and characterizing crops tolerant to drought and able to keep high yields under limited soil water resources are key challenges to face increasing global food demand in a changing environment. Root systems control plant access to soil water and are thus key organs for drought tolerance. Plant breeders are interested to optimize plant performances by understanding the soil exploration dynamics of roots, their reaction to soil water spatial distribution and distribution of root hydraulic properties between root orders and root age (Meunier et al. 2020). Yet, the ability to easily, accurately, and extensively characterize root traits or phenes (i.e. characteristic features) is a major challenge in the field of root biology (Meister et al. 2014). Novel root phenotyping techniques, i.e., tools to characterize root system properties and functions *in situ* (Atkinson et al. 2019) are instrumental to develop these new genotypes. Typically, most of the current root phenotyping is performed on young plants grown in aeroponics, or small containers filled with non-natural substrates.

Plant's ability to deal with the heterogeneous environment is therefore difficult to assess. Recognizing the limiting interest of root phenotyping in pots, Passioura (2012) suggested that field phenotyping is needed to ensure that plant genotypes can deal with the natural temporal and spatial variability of the environment.

Root water uptake distribution is a key factor to assess plant tolerance and adaptation to WD conditions. Root water uptake is not the only function of root system architecture and soil water availability, but also of root hydraulics (Leitner et al. 2014; Meunier et al. 2017). Hence, the dynamics of root water uptake reveals plant functioning, in particular under WD. Yet, root water fluxes are impossible to monitor in the field, and often soil water depletion resulting from root uptake is measured instead. However, soil water depletion patterns cannot always be linked to root water uptake distribution due to soil water movements (Vandoorne et al. 2012). In wet conductive soils, water uptake can take place without a change of soil moisture, for instance. To associate water depletion to uptake patterns, soil water fluxes must be limited.

Recently Cimpoiașu et al. (2020) reviewed specific advantages and limitations of geoelectrical methods to monitor root zone processes and structure and showed that Electrical Resistivity Tomography (ERT) is well suited to monitor soil water content evolution and thus soil water depletion patterns *in situ*. High-resolution root-zone soil moisture monitoring can reveal the differences between the root system of different species under varying climatic conditions. For example, ERT imaging conducted on a transition zone from forest to grassland showed that soil moisture dynamics at different seasons were significantly different for forest and grassland (Jayawickreme et al. 2008). In their study, the forest showed higher sub-surface resistivity changes as compared to grasslands.

Monitoring soil water depletion patterns via ERT has shown to provide useful information on root density (Amato et al. 2008; Paglis 2013), soil compaction due to tillage (Besson et al. 2004), soil water content (Michot et al. 2003; Garré et al. 2011; Beff et al. 2013; Dahlin et al. 2014) thereby promising itself as a valuable tool to monitor soil-root system. Because of its larger monitoring depth and its nonlinear relation to water content, ERT seems to be promising in characterizing deep changes of soil matric potentials, more directly related to plant WD than water content (Whalley et al. 2017). Several studies have investigated the potential of ERT to characterize soil water abstraction patterns. Panissod et al. (2008) demonstrated that 2D ERT could be used to investigate soil water patterns in maize fields. Srayeddin and Doussan (2009) used ERT to compare soil water depletion patterns of maize and Sorghum and found Sorghum to be more efficient in water extraction as compared to Maize. However, in water stress treatment, the water uptake front could not be quantified beyond 50-60cm depth due to poor sensitivity of surface electrode configuration (Srayeddin and Doussan 2009). Brillante et al. (2015) applied ERT to vineyards. Ain-Lhout et al. (2016) monitored soil moisture in the root zone system of a tree. Other studies focused on characterizing soil moisture differences between contrasted vegetation and/or soil types (Jayawickreme et al. 2008; Nijland et al. 2010; Garré et al. 2013), also based on 2D-ERT. All these studies used surface electrodes to estimate 2D soil moisture space-time distribution in open ecosystems or for crops with large interrow distance, which facilitates the observation of water abstraction patterns. More recently, Whalley et al. (2017) successfully used surface ERT at field scale to distinguish wheat genotypes based on their soil water profile evolution.

However, ERT faces several challenges when used for field phenotyping. Small differences in rooting or water

uptake depths between genotypes might result in large differences in terms of tolerance (Manschadi et al. 2006), which means that high spatial resolution is needed. Therefore, contrast between uptake patterns of different genotypes is not always visible with ERT (Whalley et al. 2017). Also, the sensitivity of ERT measurements to root and soil water depletion is not always sufficient (Rao et al. 2019), and can even be decreased by additional processes such as solute distribution or too wet soil conditions. Furthermore, commonly used surface electrode configuration may not be suitable for phenotyping roots that need higher spatial resolution in the sub-meter scale where differences between different root systems occur (Sravyedin et al. 2009). Because of ill-posed nature of ERT inversion, it is necessary to differentiate the changes observed in ERT inversions in terms of artifacts and physiology of plants to have meaningful results.

In this study, our general objective is to investigate the ability of ERT to detect slight differences in depletion depths between plant species in a quantitative way. Our specific questions were (i) how to analyze ERT field data to detect slight changes in water depletion? (ii) what is the spatial resolution that is needed and that can be achieved to discriminate plant uptake behaviors? To answer these questions, we develop a new quantitative approach to discriminate soil water abstraction depths and extent based on a synthetic experiment with process-based model. This methodology was used to interpret 2-D ERT field data in an agronomic field trial comparing different forbs and grass species, with potentially different root functioning as a test for our method.

## 4.2 Materials and Methods

#### 4.2.1 Field Trial Description

The experimental field is located in Corroy-le-Grand (Belgium), in the De Marbais University farm. A random-block field trial was established in 2012 for comparing combinations of grass and forb species under two contrasted treatments: control (normal weather conditions) and water deficit conditions (WD through a shelter preventing rainfall for six week). The whole field trial was organized in blocks (7.2 m x 7 m) made of four plots (1.5 m width x 7 m length each) with a separation of 30 cm between plots (Fig. 5.1). In this study, we focused on four plots with the following species: cocksfoot (C), ryegrass+white clover mixture (R+WC), white clover (WC) and ryegrass (R). Cocksfoot (*Dactylis Glomerata*) and ryegrass (*Lolium Perenne*) are both deep-rooted perennial grasses. White clover (*Trifolium repense*) is a perennial legume plant commonly grown in mixture with ryegrass in pastures. It is typically described as a shallow-rooted plant but its root system can reach 1m-depth (Nichols et al. 2016).

The soil type is a luvisol (loamy soil developed on loess) with 6 different soil horizons: Ap1, Ap2, Ap3, Bt1, Bt2 and C in WD treatment and 5 soil horizons in control (all except Bt2) as shown in Fig. 5.1-b. Due to natural heterogeneity, the WD and control treatment zones had slightly different soil horizons as revealed by soil trenches (Fig. 5.1-b). Soil trenches were dug to estimate root distribution profiles for each species in each plot using the Tardieu profile method (Tardieu 1988). We used a grid of 5 cm x 5 cm to count the root numbers to obtain a 2-D distribution of Root Number Density (RND) at the end of the season.

The soil hydraulic properties were characterized using the evaporation method (Bezerra-Coelho et al. 2018) on 250 cm<sup>3</sup> undisturbed soil cores sampled from the different horizon and the Hyprop-fit software

(Pertassek et al. 2015) to fit the experimental data with the Van-Genuchten-Mualem (VGM) soil hydraulic model. A nearby weather station provided the evapotranspiration (ET<sub>0</sub>) and precipitation information. The evapotranspiration, precipitation and root number density are shown in Fig. 5.2.

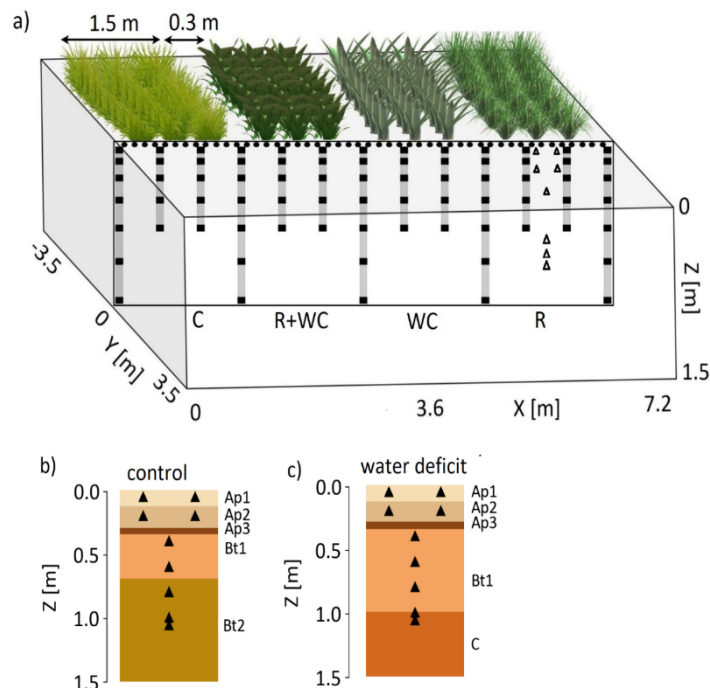


**Figure 5.1:** a) A schematic view of an individual block showing the ERT electrodes at the center plane ( $y = 0$ ) used for two-dimensional ERT imaging. The black dots represent the surface point electrodes while the black squares are the borehole ring electrodes. Inside the ERT block, one binary mixture (R+WC: ryegrass+white clover) and three monocultures (C: cocksfoot; WC: white clover; R: ryegrass) are present. Location of TDR probes (triangles) installed at different depths in the ryegrass plot. Different soil-horizons are indicated along with TDR locations (triangles) for: b) control and c) water deficit treatments.

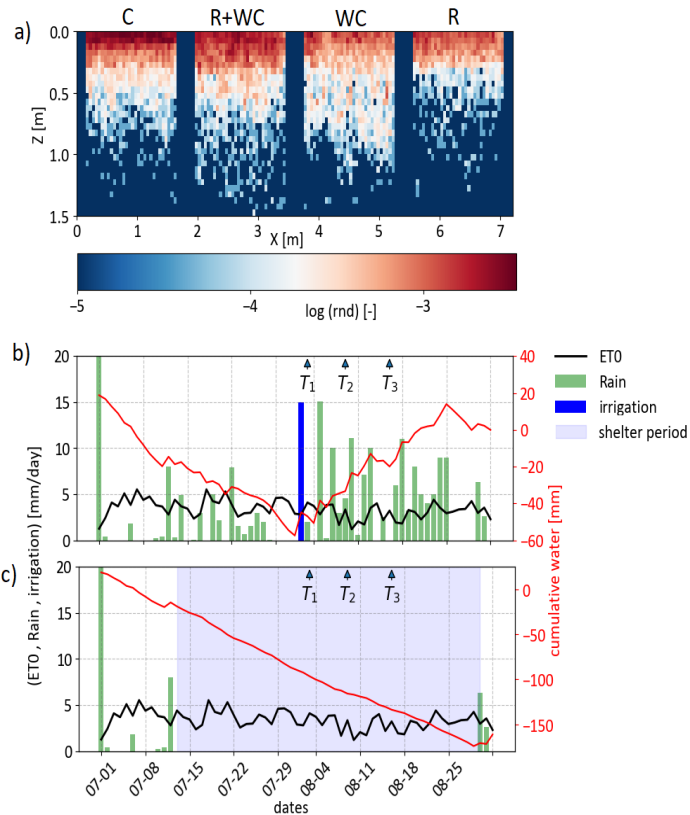


**Figure 5.2:** a) Log of root number density measured in the field, b) weather condition in the control plot and c) weather condition in water deficit plot.

#### 4.2.2 Field ERT

##### ERT data acquisition

In 2016, surface and depth ERT electrodes were installed regularly along 2-D planes, each of them crossing the middle of four plots (see Fig. 5.1-a): one in WD, the other one in control conditions.

For ERT data acquisition, we used 123 electrodes, including 48 surface electrodes (with a separation of 0.15 m) and 75 electrodes distributed along 13 boreholes (Fig. 5.3). Boreholes were made of PVC

sticks, with embedded stainless-steel rings used as electrodes, with a diameter of 46 mm for each ring (same as Beff et al. 2013), the separation between electrodes increases with depth (Fig. 5.1-a). There are four surface electrodes between each pair of borehole sticks.

The ERT data was collected using an ARES II 10-channel automatic resistivity system (from GF instruments®). ERT monitoring data set consisted of three-time stamps (denoted by t1 to t3), with data collected along the experimental block every week along three consecutive weeks. The exact dates of measurements were t1: 03/08/2017, t2: 09/08/2017 and t3: 16/08/2017. For the ERT measurements, we used current injections with 100% duty cycle, with a pulse length of 300 ms, and stacking varying between 3 and 4 repetitions.

The injection scheme comprised of 3084 quadrupoles, out of which 450 quadrupoles were reciprocal readings (collection of the same quadrupole after interchanging the current and potential dipoles). To describe the configuration in the injection scheme, we denote current injecting electrodes as AB and potential measuring electrodes as MN. The injection scheme used in the experiment is categorized into:

- a) Scheme 1 (Surface measurements only): Gradient (Schlumberger) and dipole-dipole configuration (Dahlin and Zhou 2006) among the 48 surface electrodes spanning 7.2 m representing 20% of total quadrupoles. The dipole-dipole scheme consisted of skip-0 (dipole spacing of one electrode or 15 cm), skip-1 (dipole spacing of two electrodes or 30 cm) and skip-2 (dipole spacing of three electrodes or 45 cm) protocols. Each current injection consisted of five potential measurements with a separation varying from 15 to 45 cm. Gradient configuration had a maximum current electrode separation distance of 60cm and each current injection had 5

- simultaneous potential measurements with a dipole spacing of 1 to 3 electrodes (15 to 45 cm).
- b) Scheme 2 (Boreholes only): (i) AB on a given borehole and MN on its adjacent borehole, and (ii) AM on a given borehole and BN on its adjacent borehole. Only two adjacent boreholes were used in the injection scheme, i.e., there was no measurement or injection between the first and third borehole. This scheme represented about 20% of the total quadrupoles.
  - c) Scheme 3 (Surface-borehole interacting scheme): AB (or MN) on surface electrodes located between any two borehole sticks and MN (or AB) on boreholes situated directly below surface electrodes with a dipole spacing of one or two for current injection and for each AB we had five to seven MN's with skip-0 and skip-1 spacing. This scheme represented the remaining 60% of the total quadrupoles.

#### *ERT inversion theory*

The pyGIMLi software (Rücker et al. 2017) was used for ERT inversions, where the Gauss-Newton scheme is used to iteratively minimize the following objective function ( $\phi$ ):

$$\phi = \phi_d + \lambda \phi_m = \left\| \frac{d' - f(m')}{\log(1+E_{model})} \right\|_2^2 + \lambda \|W(m' - m'_0)\|_2^2 \quad (5.1)$$

$\phi_d$  corresponds to the data misfit between the measured data vector ( $d'$ ) and the data estimated by the model ( $f(m')$ ) down-weighted by the error model ( $E_{model}$ ).  $\phi_m$  represents the model misfit and is multiplied by the regularization parameter  $\lambda$  determining the weighting of the model versus data misfits.  $d'$  stands for the log of measured apparent

resistivities from real/numerical experiments,  $m'_0$  is a homogeneous starting model vector,  $W$  is a first-order smoothness regularization matrix used to stabilize the inverse problem that is inherently ill-posed. An L2-norm is adopted as smoothed shapes of the subsurface properties are inferred. The regularization is made anisotropic by having a smaller value for smoothness in the vertical direction as compared to the horizontal direction for resolving horizontal layering of soil horizons.

We quantified field data error using the analysis of normal-reciprocal misfit, first described by LaBrecque et al. (LaBrecque et al. 1996). In our measurements, we computed an absolute error of  $0.04 \Omega$  and a relative error of 12% (see supplement Appendix B for details).

The optimum regularization constant  $\lambda$  was determined using L-curve analysis (Hansen 1992; Bergmann et al. 2017). For different values of  $\lambda$  ranging from 5 to 1000, we computed  $\phi_d$  and  $\phi_m$ . The  $\lambda$  value for which the  $\phi_d$  vs  $\phi_m$  curve has a minimum distance to the origin is chosen as the optimum value (see supplement Appendix C for details).

The ratio by which  $\lambda$  is reduced for vertical contrast is determined by  $Z_w$  that is fixed to 0.5 meaning that the smoothness regularization strength in the vertical direction is half of the horizontal one. We chose  $Z_w$  of 0.5 and a  $\lambda$  of 150 for the inversion of synthetic data. We found that the choice of  $Z_w$  played an important role in reducing inversion artifacts and the chosen value of 0.5 produced least artifacts when visually as well as quantitatively compared with the original model (see supplement Appendix D for details).

We used the relative root mean square error (rrms) and chi-square  $\chi^2$  value to assess the quality of inversion:

$$(5.2) \quad rrms = \sqrt{\frac{\sum \left[ \frac{d' - f(m)}{d'} \right]^2}{N}} \cdot 100\%$$

$$(5.3) \quad \chi^2 = \frac{\sum \left[ \frac{d' - f(m)}{E_{model}} \right]^2}{N}$$

where N is the length of the data vector ( $d'$ ). Here the inversion is stopped when the rrms value reaches 2% or  $\chi^2$  is around 5 to 8 (Günther and Rücker 2006).

Optimized resistivity fields were then temperature-corrected at 25°C (Luo et al. 2019) based on field thermometers (see next section) assuming homogeneous lateral temperature distribution and linear depth interpolation.

#### 4.2.3 Time Domain Reflectometry (TDR) and Pedophysical Model

Besides ERT, we installed nine TDR probes along the ryegrass plant plot at different depths (i.e., soil horizons) for monitoring on an hourly basis soil water content ( $\theta_{TDR}$ ) and electrical resistivity ( $\rho_{TDR}$ ) from 29/05/2018 to 26/10/2018. Temperature sensors were installed at the same depths as the TDR for electrical resistivity temperature correction. We followed a 2% decrease in electrical resistivity per degree centigrade (Whalley et al. 2017; Luo et al. 2019).

A median filter with a window size of 3 hours was used to filter out the outliers in  $\rho_{TDR}$  and  $\theta_{TDR}$ . The filtered data were combined per groups of the pedological horizon (Ap and Bt) for WD and control conditions and used to characterize soil petrophysical functions per horizon, by fitting the following model:

$$\theta = a \log_{10}(\rho)^b + \theta_r \quad (5.4)$$

where  $a$  and  $b$  are the fitting parameters,  $\theta_r$  is the residual water content. The fitting parameters for each soil horizons along with RMSE of fits are given in Table 5.1, and  $\theta_r$  is 0 except for the C layer (Table 5.2). The fits along with the TDR data are shown in Figure 5.3.

**Table 5.1:** Empirical fitting parameters found using non-linear optimization presented in Equation 5.4 for different soil horizon and their corresponding RMSE.

Horizon	$a$	$b$	$\theta_r$	RMSE
Ap (Ap1, Ap2, Ap3)	0 .4528	-1.7 299		0.01 7
Bt (Bt1, Bt2)	1 .107	-3.6 19		0.02 5
C	1 8.8792	-9.0 224	.1	0.01 2

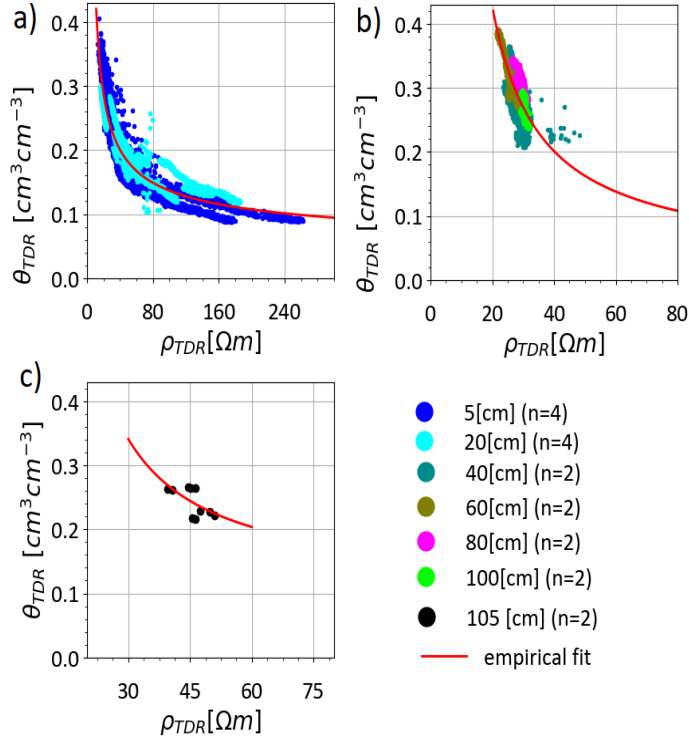


**Figure 5.3:** Combined TDR measurements in 2018 for water deficit and control conditions (electrical conductivity ( $\sigma_{TDR}$ ) versus water content  $\theta$ ) at different soil horizons: a) Ap layer, b) Bt layer, and c) C layer. The color in the scatter plot indicates the depth of the TDR probes and  $n$  is the no. of probes. The red line represents the empirical model fit (Eq. 5.4) to the data..

#### 4.2.4 Numerical Experiments

We conducted a numerical experiment with the following objectives: (1) test the reliability of the ERT injection scheme to capture the variability of subsurface resistivity and to investigate the sensitivity of ERT to the evolution of root water uptake patterns; (2) improve the interpretation of field ERT results through the comparison of synthetic data, and (3)

formulate indices quantifying the uptake behavior of plants.

Figure 5.4 describes the detailed workflow for the numerical experiment and its connection to real field data interpretation. We combined water-flow simulations (blue in Fig. 5.4) with forward and inverse ERT simulations (red in Fig. 5.4) to generate synthetic experiments representing potential ERT field observations to later compare with real field data.

#### *Water flow simulations*

We used a mechanistic soil-plant water flow model R-SWMS (Javaux et al. 2008) to simulate the evolution of soil water content distributions in the field trial for 3 weeks (between 03/08/2017 and 16/08/2017). The simulation domain is a block of 7.2 m x 0.1 m x 1.5 m crossing the middle of the 4 plots corresponding to the location of the vertical ERT electrode plane. Two simulations were run: one for the control and one for the WD conditions, with the corresponding, observed rainfall, irrigation and evapotranspiration times series.

The soil domain consisted of five layers corresponding to the observed soil horizons shown in Fig. 5.1-b and Fig. 5.1-c (control and WD treatments have a slightly different horizon distribution). Soil hydraulic properties of each layer were parameterized with the VGM model (see Table 5.2 in the supplement Appendix E).

The soil boundary conditions for the control treatment consisted of the precipitation time series from weather station complemented by manual irrigation (Fig. 5.2-c). Free drainage was used as soil bottom boundary condition. For WD treatment, a no-flux soil top boundary condition was used as neither rainfall nor irrigation happened during the simulation period. Evaporation fluxes between plots were neglected. To generate realistic 3-D initial conditions at the beginning of our experimental period, we ran the warm-up for 30 days. The initial soil condition at time -30 days was

hydrostatic equilibrium with a saturated soil at the depth of -316 cm.

Root water uptake of the different plant species was simulated using the macroscopic parameterization proposed by Couvreur et al. (2012). We normalized the measured RND of the 4 plots as a proxy for soil uptake fraction (*SUF*) distribution (Fig. 5.2-b). We assumed that the equivalent conductance of the root system (*Krs*) equals the compensatory root water uptake conductance (*Kcomp*) (see Table 5.3 of supplementary material). With this assumption, differences between root water uptake patterns will only be due to the difference between *RND* distributions and to available water in the soil. This means that no differencee between root hydraulic properties of the different species were considered. The ET0 estimated from the weather station data was used as a plant flux boundary condition.

#### *ERT simulations - Generation of synthetic resistivity distributions*

Modeled water content maps were transformed to electrical resistivity fields using Equation 5.4. The pyGIMLi software was used for ERT forward simulations on the synthetic resistivity model, which solves Poisson's equation in 2.5-D to compute the modeled ERT data with the same injection scheme than in reality. An error was added to these modeled ERT data, which followed the field error model. Inversion of the modeled ERT data was performed using the same methodology as in the field.

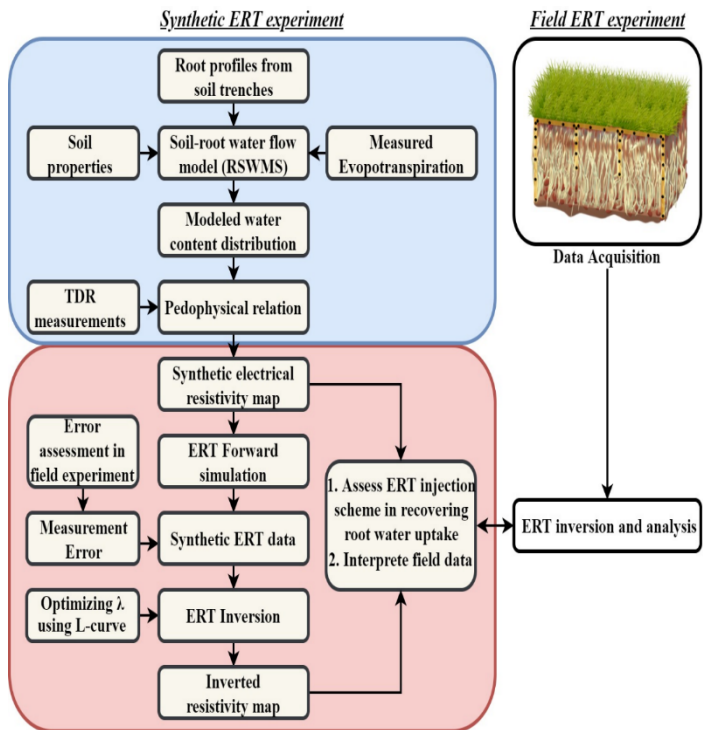


**Figure 5.4:** Methodology for synthetic experiment and its relation to the field experiment, the blue area corresponds to water-flow simulations and the red area shows the ERT simulations. The region outside the red and blue areas corresponds to real field experiments.

#### 4.2.5 Gaussian fits

In WD treatment, any increase in electrical resistivity is supposed to be due to a water content decreased generated by plant water uptake. The 2-D distributions of water content at  $t_3$  and  $t_1$  denoted by  $\theta(t_3)$  and  $\theta(t_1)$  are obtained by applying petrophysical relation (Eq. 5.4) to 2-D distributions of electrical resistivity at  $t_3$  and  $t_1$  denoted by  $\rho(t_3)$  and  $\rho(t_1)$ . To characterize plant-specific depletion patterns, we compute the 2-D time difference of resistivity and water content defined as:

$$\delta\rho = \log(\rho(t_3)) - \log(\rho(t_1))$$

and the change of water content between t1 and t3 is defined as:

$$\delta\theta = \theta(t3) - \theta(t1)$$

The 1-D medians at each depth from 2-D distributions of  $\delta\rho$  and  $\delta\theta$  was computed for each plant and a Gaussian curve was fitted to the 1-D medians of  $\delta\rho$  and  $\delta\theta$  profiles ( $\delta\rho_{fit}$  and  $\delta\theta_{fit}$ ):

$$\delta\rho_{fit} = A_{\delta\rho} * \exp\left(\frac{-(\delta\rho - \mu_{Z,\delta\rho})^2}{2*\sigma_{Z,\delta\rho}^2}\right)$$

$$\delta\theta_{fit} = A_{\delta\theta} * \exp\left(\frac{-(\delta\theta - \mu_{Z,\delta\theta})^2}{2*\sigma_{Z,\delta\theta}^2}\right)$$

From the fitted Gaussian function, the six parameters of a Gaussian function were then optimized to fit these 1-D profiles:  $A_{\delta\rho}$ ,  $A_{\delta\theta}$ ,  $\mu_{Z,\delta\rho}$ ,  $\mu_{Z,\delta\theta}$ ,  $\sigma_{Z,\delta\rho}$  and  $\sigma_{Z,\delta\theta}$ . The mean parameter  $\mu_{Z,\delta\rho}$  or  $\mu_{Z,\delta\theta}$  represents the depth at which depletion is the largest (maximum depletion depth) while  $\sigma_{Z,\delta\rho}$  or  $\sigma_{Z,\delta\theta}$  represents the extent of the depletion as illustrated in Figure 5.5. The amplitude parameters ( $A_{\delta\rho}$ ,  $A_{\delta\theta}$ ) denotes the magnitude of change in water content or resistivity.

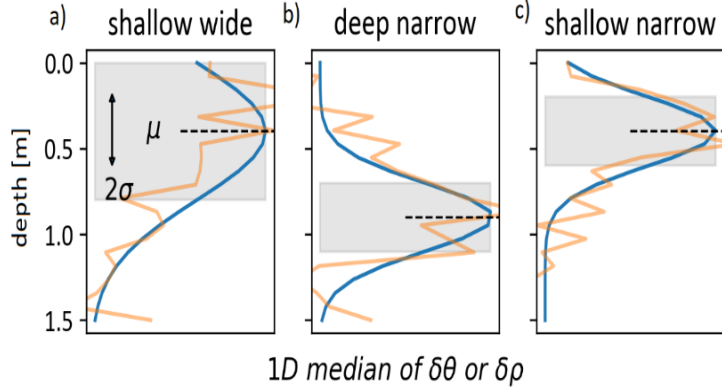


**Figure 5.5:** Illustration of Gaussian fits for discriminating plant uptake behavior: a) plant uptake region is shallow, but the extent is wide, b) uptake region is deeper while extent is narrow, and c) uptake is shallow and extent is narrow. The yellow line indicates possible ERT observation while the blue line is the Gaussian fit. The gray shade indicates the uptake extent ( $\sigma_{z,\delta\rho}$  or  $\sigma_{z,\delta\theta}$ ) while dotted line indicates maximum depletion depth ( $\mu_{z,\delta\rho}$  or  $\mu_{z,\delta\theta}$ ).

### 4.3 Results

#### *ERT Field Experiment results: Qualitative comparison between WD and control conditions*

In Figures 5.6-a and b, we show the inversion results of field data under control and WD conditions, respectively. The inversion converged after 3 to 5 iterations with  $\text{rrms} < 2$  and  $\chi^2 < 8$  (see the textbox to the right of Fig. 5-a). Since we had higher measurement errors in the WD treatment, the inversion has higher  $\chi^2$  values as compared to the control treatment. Since only small regions show the log of resistivity higher than 2.2 or lower than 1.2 in both WD and control treatments, we cut our color scale from 1.2

to 2.2 in Figs. 5.6-a and b to compare both treatments simultaneously.

Conspicuously, the impact of treatments WD versus control is well captured by the ERT imaging. WD plots are increasingly resistive from t1 to t3 whereas the opposite scenario happens for the control treatment. In the controlled plots, rainfall and soil infiltration decrease the electrical resistivity of the surface layer as shown by the fading red region in the top horizon ( $Z < 0.3$  m) from t1 to t3. On the contrary, in WD treatment, the root water uptake is the main driver of electrical resistivity changes. Indeed, such a process is highlighted by the widening drying front of the light green region (corresponding to  $\log(\rho) = 1.75 \Omega \cdot m$ ) from t1 to t3 in Fig. 5.6-b indicating a deeper root water uptake ( $Z < -1$  m).

Some differences between plants (plots) are visible in both control and WD conditions. In control, the region corresponding to  $\log \log(\rho) = 1.56$  to  $1.65 \Omega \cdot m$  goes deeper ( $Z > 0.5$  m) for plants R+WC and WC as compared to the plants C and R (Fig. 5.5a). Similarly, in WD, the region corresponding to  $\log \log(\rho) = 1.75 \Omega \cdot m$  goes deeper ( $Z > 0.5$  m) for the first three plants (C, R+WC and WC) compared to R (Fig. 5.6-b).

The inversion results in both treatments show a slightly shallower depletion zone of R as compared to the first three plants (C, R+WC, and WC). However, large variability in electrical resistivity is also visible within plots, which makes the proper quantification of the depletion depth difficult to assess.

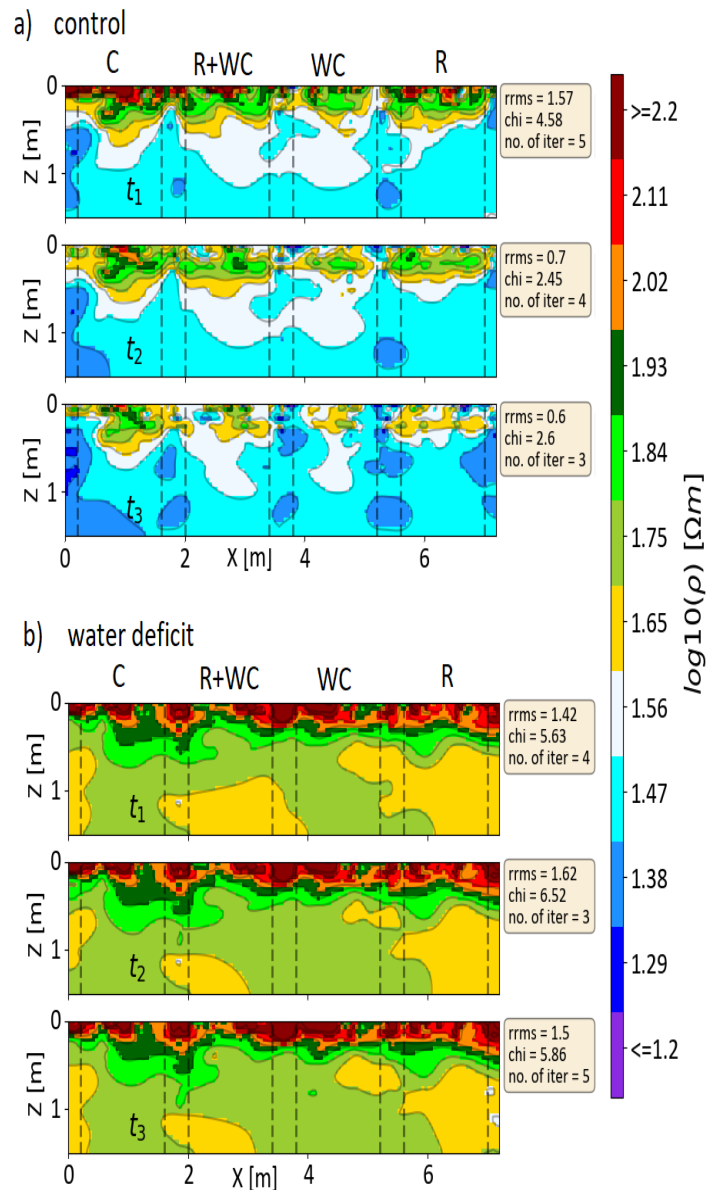


**Figure 5.6:** Inversion results of field data at different times for a) control and b) water deficit treatments. Inversion quality parameters are shown to the right. The black dotted line represents the positions of different plants.

### 4.3.1 Synthetic Experiments

#### *Forward simulations*

In Figures 5.7-a and b, R-SWMS simulations show contrasted soil water content patterns for control and WD treatments. In both control and WD treatments, we observe the effect of root water uptake on soil water content (dark brown patches in Figs. 5.7-a and b). The water content distribution in control treatment is quite homogeneous below 0.75 m (Fig. 5.6-a) while it is the opposite in WD treatment (Fig. 5.7-b). We see the impact of root water uptake in WD treatment up to 1.5 m in depth (dark brown patches in Fig. 5.7-b at  $Z > 1$  m). In control treatment (Fig. 5.7-a), regular rainfall events between  $t_1$  and  $t_3$  (see Fig. 5.2-b) fade out the soil water depletion pattern in the top 25 cm of the soil (increasing blue front in top 25 cm of Fig. 5.7-a). In WD treatment, we see the impact of root water uptake in the form of a deepening drying front between  $t_1$  and  $t_3$  (expansion of dark brown patches in Fig. 5.7-b).

The differences between (C, R+WC, and WC) and R are evident in both treatments. The plant R does not go deeper than 30 cm while other plants influence the soil water content much below 30 cm (Fig. 5.7-a). Although slight differences between species can be observed for the control treatment (Fig. 5.7-b), the soil water content pattern evolution is mainly controlled by rain and not root characteristics.

Figures 5.6-c and d show the corresponding electrical resistivity fields for control and WD treatments, respectively obtained with the petrophysical relations (Fig. 5.3). Similar to field data in Fig. 5.5, only small regions in our synthetic experiment showed the log of resistivity higher than 2.2 or lower than 1.2 in both treatments. Therefore, we cut our color scale from 1.2 to 2.2 in Figs. 5.7-c and d to compare both treatments simultaneously. Although the objective of the synthetic

experiment was not to fit the field observations, we can still make a qualitative comparison of the observed patterns. The fading of the high resistive region ( $\log(\rho) >= 2.2$ ) in the top horizon of the control condition in Fig. 5.7-c closely resembles the experimental results of Fig. 5.6-a. However, in WD condition, comparing Figs. 5.7-d and 5.6-b show that field data are more resistive especially at depth  $0.5 \text{ m} < Z < 1 \text{ m}$  and structurally more heterogeneous in terms of uptake front. These differences in resistivity magnitude in simulations and experiments can arise due to uncertainty in the petrophysical function used to convert R-SWMS water content to electrical resistivity.

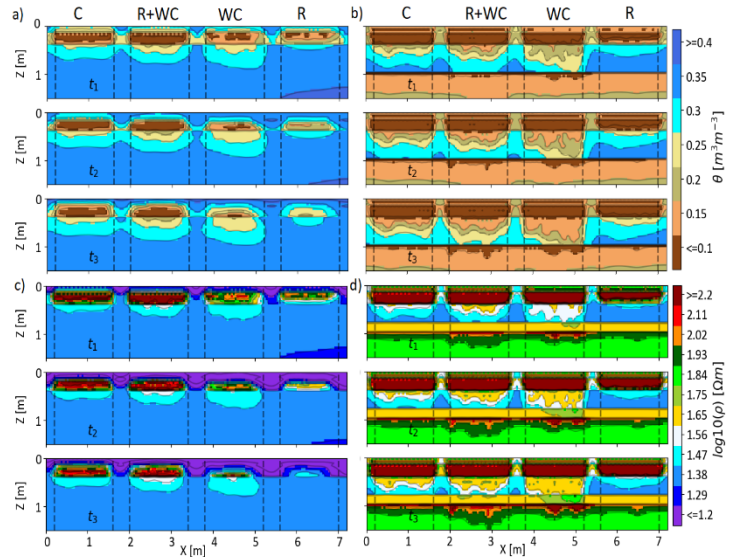


**Figure 5.7:** Simulated evolution of water content ( $\theta$ ) distribution from  $t_1$  to  $t_3$ : a) control treatment and b) water deficit treatment and its corresponding evolution of electrical resistivity ( $\rho$ ): c) control treatment and d) water deficit treatment. The black dotted line represents the positions of different plants.

### *ERT inversion*

Figures 5.8-a and b show the forward and inverted  $\log(\rho)$  at t3 for control and WD treatments. We focused only on the first-meter depth, where the sensitivity is higher (see supplement material section C). It is observed that the inverted  $\log(\rho)$  field generally keeps the main features than the forward simulations. In general, the high-resistivity zones are retrieved for both treatments and all (combinations of) plant species. However, while the difference between species is clearly in the control treatment, no obvious difference between patterns seems to appear in the WD treatment.

Figures 5.8-c and d show the time difference or the change of log resistivity between t1 and t3 ( $\delta\rho$ ) of the forward and inverted datasets. Areas with positive  $\delta\rho$  correspond to the zone from which soil water was extracted. Forward simulations for the control treatment show no increase in electrical resistivity (Fig. 5.8-c), probably due to the rainfall events. Even if, in general, the inversion recovered well the main patterns, no information on root water uptake depths can be inferred from the control treatment.

In the WD treatment, differences between species are much clearer in  $\delta\rho$  (Fig. 5.8-d) than in  $\log(\rho)$  (Fig. 5.8-b). Interestingly, not only the magnitude of  $\delta\rho$  but also its spatial distribution are affected by plant species. Although the sharp boundary of depleted zones is blurred in the inversion results in Figure 5.8-d, possibly due to the smoothness constraint in the ERT inversion, the ranking of plants uptake depth seems to remain. For example, notice the differences between (C, R+WC, and WC) and R in Figure 5.8-d.

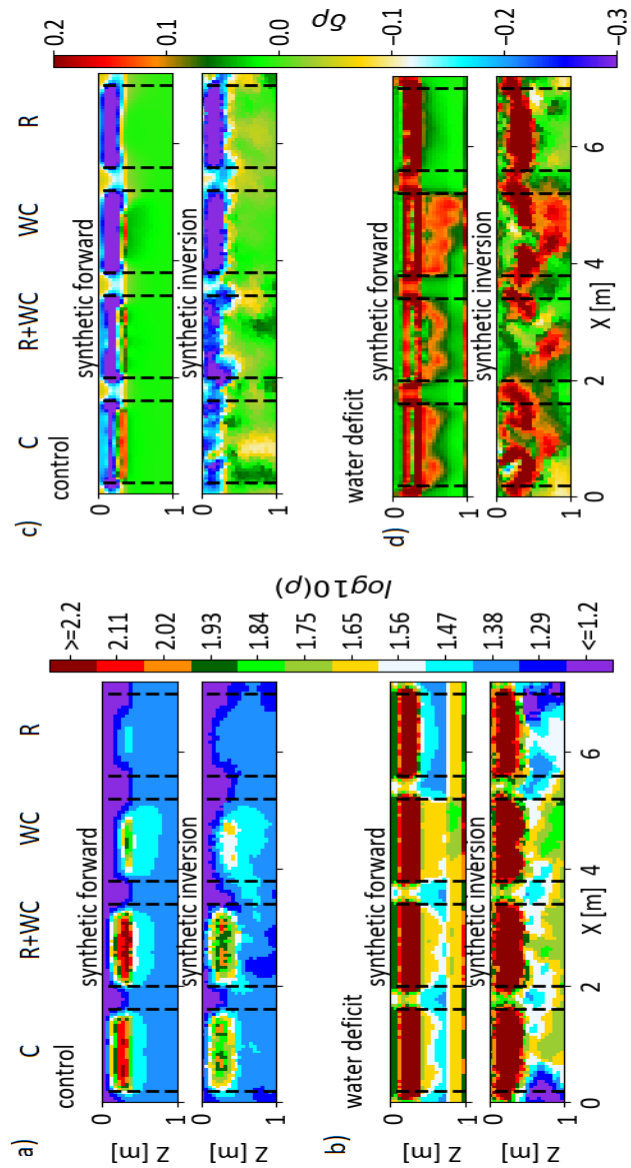


**Figure 5.8:** Comparison of R-SWMS simulated forward data (first row) and ERT inversion of R-SWMS simulated data (second row). a)  $\log(\rho)$  at  $t_3$  in the control treatment, b)  $\log(\rho)$  at  $t_3$  in water deficit treatment, c) The change of  $\log$  resistivity between  $t_1$  and  $t_3$  ( $\delta\rho$ ) in control treatment, d) The change of  $\log$  resistivity between  $t_1$  and  $t_3$  ( $\delta\rho$ ) in water deficit treatment. The color bar in Figs. (a) and (b) has been

cut at a specified scale for visualization purposes. The black dotted line represents the positions of different plants.

#### 4.3.2 Using ERT to recover plant-specific depletion zones

##### *Synthetic Experiments*

To better visualize differences between plant behaviors under water-limited conditions, plant-specific median profiles of several variables related to water depletion are shown in Figure 5.9-a. The water depletion  $\delta\theta$  profiles of the forward simulations (dashed black lines) is compared to inverted  $\delta\rho$  profiles (dashed red profile) and to water depletion profile  $\delta\theta$  obtained from inverted ERT (dashed blue line). Besides, the fits of a Gaussian distribution function on ERT-inverted  $\delta\theta$  and  $\delta\rho$  profiles are shown in the same colors (solid lines).

The use of a Gaussian function seems to be adequate to fit the depletion profiles, as observed in Figure 5.9-a. In general, the fitted Gaussian distributions match pretty well the inverse  $\delta\theta$  and  $\delta\rho$  profiles, which support its use for further statistics.

The comparison between forwarding  $\delta\theta$  and inverse  $\delta\rho$  profiles (black and red dashed lines) show some discrepancies. However, when petrophysical relations are used to retrieve  $\delta\theta$  profiles (blue lines), the match to forward  $\delta\theta$  (dashed black lines) improve significantly especially for WC and R. We observe that in general, inversely retrieved  $\delta\theta$  are more dispersed than direct  $\delta\theta$  profiles, with lower peaks.

We used the Gaussian function parameters ( $\mu_{z,\delta\rho}$ ,  $\mu_{z,\delta\theta}$ ,  $\sigma_{z,\delta\rho}$  and  $\sigma_{z,\delta\theta}$ ) to compare the 1-D profiles in terms of maximum depletion depth and depletion zone extent, respectively. These statistics are shown in Figures 5.9-b and c for each (combination of) species and compared to the forward  $\delta\theta$  statistics. Our forward

simulations show a maximum depletion depth generally below 0.5 m with the following ranking: R < C < R+WC < WC. If we compare  $\mu_{z,\theta}$  to  $\mu_{z,\delta\rho}$  obtained by inversion, we observe that the ranking between species is retrieved for all species except for R+WC and WC, which are inverted. For C and R+WC, we observe ERT-retrieved  $\mu_{z,\delta\rho}$  is usually closer to the forward  $\mu_{z,\theta}$  (less than 5 cm difference) than the inverted  $\mu_{z,\theta}$ . For C and R+WC, the forward simulation lies between inverted  $\mu_{z,\delta\rho}$  and  $\mu_{z,\theta}$  and for WC, we observe ERT-retrieved  $\mu_{z,\delta\rho}$  is usually closer to the forward  $\mu_{z,\theta}$  (less than 5 cm difference) than the inverted  $\mu_{z,\theta}$  and for R, this is the opposite. In general, the difference between forward and inverted maximum depletion depth is always lower than 10 cm. In terms of depletion extent, it is observed that ERT-retrieved  $\sigma_{z,\delta\rho}$  always overestimate forward  $\sigma_{z,\theta}$ . On the opposite, the match between forward and inverse  $\sigma_{z,\theta}$  is remarkably good (less than 5 cm difference). The nonlinearity of the petrophysical relation explains why sometimes the use of  $\delta\rho$  leads to the wrong estimate of  $\mu_{z,\theta}$  or  $\sigma_{z,\theta}$ .

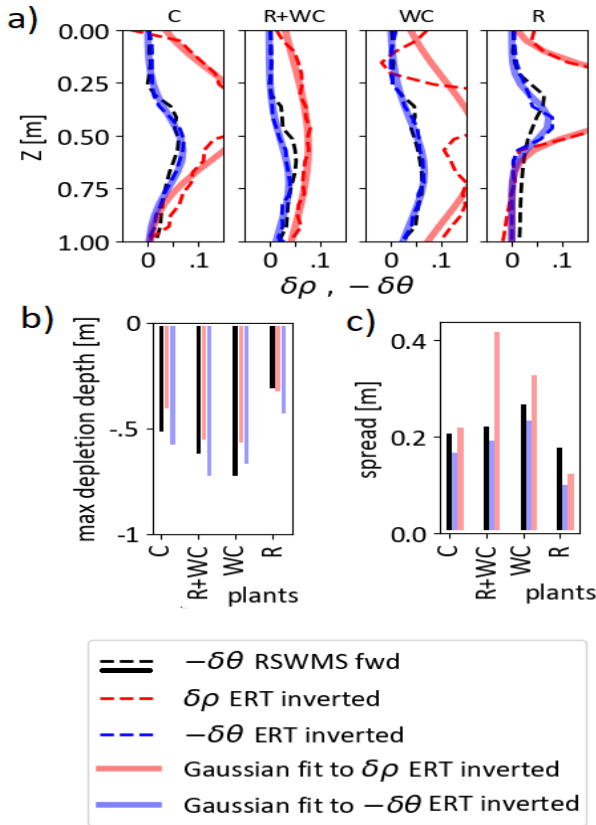


**Figure 5.9:** a) The 1-D median of the change of log resistivity between t1 and t3 ( $\delta\rho$ ) and negative of the change of water content between t1 and t3 ( $-\delta\theta$ ) for different plants in water deficit condition (dashed lines) and the Gaussian fit (solid line). The blue dotted lines represent  $-\delta\theta$  derived from ERT inversion while the black dashed line represents the R-SWMS forward modeled  $-\delta\theta$  (ground truth). b) maximum depletion depth of 1-D median of  $\delta\rho$  and  $-\delta\theta$  as a function of plant species. The red solid lines represent  $\mu_{Z,\delta\rho}$  derived from Gaussian fit to ERT derived  $\delta\rho$ , the blue solid lines represent  $\mu_{Z,-\delta\theta}$  derived from Gaussian fit to ERT derived  $-\delta\theta$ , while black dashed line represents the maximum depletion depth of 1-D median of R-SWMS forward modeled  $-\delta\theta$ . c) depletion extent of 1-D median of  $\delta\rho$  and  $-\delta\theta$  as a function of plant species. The red solid lines represent  $\sigma_{Z,\delta\rho}$  derived from Gaussian fit to ERT derived  $\delta\rho$ , the blue solid lines represent  $\sigma_{Z,-\delta\theta}$  derived from Gaussian fit to ERT derived  $-\delta\theta$ .

, while black dashed line represent  $\sigma_{z,\delta\theta}$  derived from Gaussian fit to R-SWMS forward modeled  $-\delta\theta$ .

#### *Field data*

Figures 5.10-a and b show the retrieved  $\delta\rho$  distributions of the field data for control and water deficit conditions. Like in the synthetic experiment, depletion zones are hardly visible in the control treatment. Root water uptake depletion zones are compensated by water infiltration and hide thereby plant-specific uptake patterns (Fig. 5.10-a). We will, therefore, focus on the WD treatment data.

When we compare Figures 5.10-b to Fig. 5.8-d, resistivity change patterns in the real field are much patchier than in the synthetic experiment. This can partly be associated with the inversion, which already generated patches in the synthetic experiment (see bottom subplot in Fig. 5.8-d). Also, variability in the actual soil hydraulic and petrophysical properties might have further increased the variability in  $\delta\rho$  spatial field due to their nonlinearity.

Our synthetic experiments demonstrated that a 1-D profile of temporal changes helps visualize differences between species. We applied this method here to the  $\delta\rho$  and  $\delta\theta$  fields per plant (after using petrophysical relations). Figure 5.10-c shows the  $\delta\rho$  and  $\delta\theta$  1-D median profiles, together with the corresponding Gaussian fits. Large changes of resistivity are observed in the upper soil horizon (between 0 and 25 cm depth) of all plant plots. Yet, when we use the petrophysical relations to transform  $\rho$  to  $\theta$ , these large  $\delta\rho$  changes translate into much lower changes in terms of  $\delta\theta$  (blue dashed lines in Fig. 5.10-c). These large changes in resistivity observed in experiments (not observed in model) are probably due to evaporation, which was not included in our synthetic experiment. To discriminate water uptake from evaporation impact on water depletion, we fitted the Gaussian relations on the  $\delta\rho$

and  $\delta\theta$  profiles only below 25 cm depth (horizontal dashed lines in Fig. 5.10-c).

Figures 5.10-d and e show the parameters of the Gaussian fits:  $\mu_{z,\delta\rho}$ ,  $\mu_{z,\delta\theta}$ ,  $\sigma_{z,\delta\rho}$  and  $\sigma_{z,\delta\theta}$ . The depths of maximum uptake zone  $\mu_z$  differ of maximum 5 cm between  $\delta\rho$  and  $\delta\theta$ . Two groups of maximum uptake depths can be seen in Figure 5.10-d: shallower uptake for C and deeper uptake for R, WC, and R+WC. These maxima all occur below 0.5 m depth, where the root density (green curve in Fig. 5.10-c) is the lowest. This is expected as, in WD condition, root water uptake not only depends on root density but also on soil water availability, which is larger below the dry root zone. We can conclude from this trial that Ryegrass, White clover (WC) and their combination (WC+R) have deeper depletion zones than cocksfoot. In the synthetic example, the ranking was slightly different: the maximum uptake depth was similar for C, R+WC, and WC, while R had a shallower  $\mu_z$ . In the synthetic study though, the only difference between simulated species was their root distribution. In reality, there are a lot of other plant characteristics, which might affect their water uptake distribution, like plant root conductance, distribution of their hydraulic properties between root types, or their stomatal regulation.

In terms of uptake extent  $\sigma_z$ , it is observed that R has a much higher extent than WC, WC+R, and C both in  $\delta\rho$  and  $\delta\theta$ . On the opposite of the synthetic experiment, we see that in general  $\sigma_{z,\delta\theta}$  is larger than  $\sigma_{z,\delta\rho}$  except for R. We conclude that Ryegrass has a much smoother and uniform uptake depth range than the other species. This is in agreement with the early field observations of Volaire et al. (1998), who found C to be less efficient in terms of water extraction as compared to R

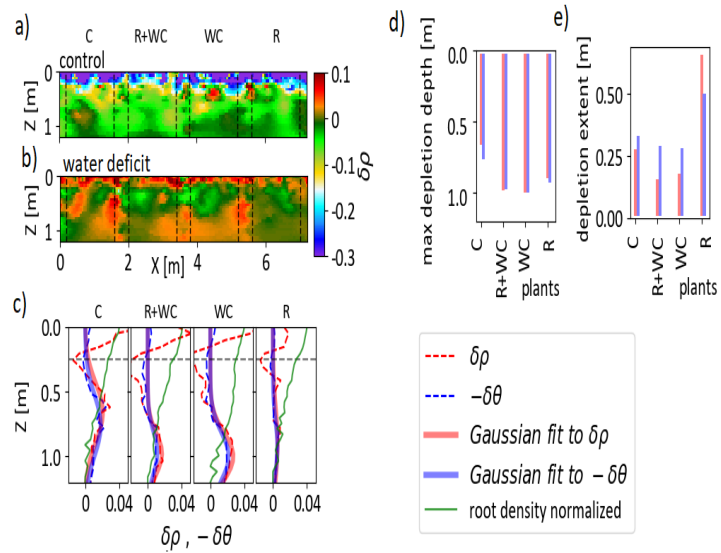


**Figure 5.10:** The change of log resistivity between t1 and t3 of field inverted data ( $\delta\rho$ ) for control and water deficit treatments. a)  $\delta\rho$  in the control treatment, b)  $\delta\rho$  in water deficit treatment. The black dotted line represents the positions of different plants. c) The 1-D median of  $\delta\rho$  and  $-\delta\theta$  for different plants in water deficit condition (dotted lines) and the Gaussian fit (solid line) and normalized root length densities (green line). The black dotted line represents the depth ( $Z=0.25$ ) above which data is discarded for Gaussian fit. d) maximum depletion depth of 1-D median of  $\delta\rho$  and  $-\delta\theta$  as a function of plant species. The red solid lines represent  $\mu_{Z,\delta\rho}$  derived from Gaussian fit to ERT derived  $\delta\rho$ , the blue solid lines represent  $\mu_{Z,-\delta\theta}$  derived from Gaussian fit to ERT derived  $-\delta\theta$ . e) depletion extent of 1-D median of  $\delta\rho$  and  $-\delta\theta$  as a function of plant species. The red solid lines represent  $\sigma_{Z,\delta\rho}$  derived from Gaussian fit to ERT derived  $\delta\rho$ , the blue solid lines represent  $\sigma_{Z,-\delta\theta}$  derived from Gaussian fit to ERT derived  $-\delta\theta$ .

## 4.4 Discussion

We conducted a high-resolution ERT study on an intercropped field trial with 3 different herbaceous species and one mixture subject to two different treatments (control and water deficit). The main aim of the study was to map the plant uptake response to drought and investigate the sensitivity of ERT in capturing differences in water depletion patterns between species.

The synthetic analysis demonstrated that, despite higher smoothness due to inversion, the forward and inverse dry zones were relatively well retrieved in terms of  $\log(\rho)$ . However, differences between species were hardly visible. One-dimensional profiles of temporal changes in median  $\rho$  or  $\theta$  made the difference in depletion zones between species clearer. The ERT-retrieved  $\delta\theta$  1-D profiles were shown to match relatively well the actual depletion profiles. We fitted a Gaussian function to the 1-D profiles under WD conditions to retrieve four parameters:  $\mu_{z,\delta\rho}$ ,  $\mu_{z,\delta\theta}$ ,  $\sigma_{z,\delta\rho}$  and  $\sigma_{z,\delta\theta}$ . While the maximum depletion depths ( $\mu_{z,\delta\theta}$ ) were generally well retrieved in terms of  $\delta\theta$  or  $\delta\rho$ , the extent of the depletion zone ( $\sigma_z$ ) was much better recovered using  $\delta\theta$  than  $\delta\rho$ , demonstrating the importance of using petrophysical relations. These mean and standard deviations parameters in  $\delta\theta$  were proved to adequately represent respectively the maximum depletion depth and the extent of the depletion zone. They could be used as root phenotyping parameters in quantifying the water uptake ability of a plant in drought conditions. However, extending this approach to diverse crops, soils, and environments are needed to establish the methodology presented here.

Large changes of resistivity observed in the upper soil horizon (between 0 and 25 cm depth) of all plant plots in the stress condition of the real field is not observed in the synthetic experiments. A possible reason could be surface evaporation which was ignored in the

model. Hence, future modeling studies should include surface evaporation as an additional topsoil boundary condition.

Although studies show that root segments could affect petrophysical relation (Rao et al. 2019), we did not account for the impact of roots in the petrophysical relation due to following reason: a) First, roots were static (no growth) in the species (perennial) under the study time frame, b) Second, we examine changes of water content which eliminates the impact of roots in the petrophysical relation as there was no change in the root system and only change in the soil electrical resistivity that occurred comes from root water uptake. During uptake process or evaporation at the surface, a decrease in water content would increase the salinity of the pore water and its electrical conductivity causing uncertainty in petrophysical relation. Future study should focus on the variability of the petrophysical relation due to changing pore water salinity.

When we use Gaussian fit indices for our real field data, we conclude that white clover (WC) (alone or in combination with Ryegrass) takes up water in deeper regions than the two other plants (Ryegrass and Cocksfoot). We also observe that Ryegrass has a more uniform water depletion (and hence uptake) profile. This methodology should be tested on more plant species and at different scales.

The synthetic studies also showed that differences between plant uptake dynamics could better be characterized in WD conditions. Hence, plant phenotyping with ERT should ideally be realized under WD conditions. Yet, this study was performed for a relatively short (but realistic) WD period of three weeks. We expect that longer WD periods will enhance even more differences between species. Despite depth electrodes we observe that the coverage is still low below 1m depth. More depth electrodes are potentially needed to see deep root water uptake. In the near future, we will use these Gaussian fit indices to assess

their application on the whole field trial that includes additional species and their replicates.

## 4.5 Appendices

### Appendix A: Soil Layer Description

The description of soil layers for water deficit condition from the observation is as follows:

- a) Ap1 (0-10 cm): the moist color of the horizon is brown. The horizon has a moderate fine to a medium granular structure. This horizon contains many very fine to coarse roots.
- b) Ap2 (10-25cm): the moist color of the horizon is brown. The horizon has a weak fine to a medium platy structure. This horizon is less porous than the Ap1 horizon. However, many fine to medium roots was still present.
- c) Ap3 (25-35cm): the plough sole. The horizon has a strong thick platy structure. The roots were growing horizontally along the boundary between Ap2 and Ap3 horizon.
- d) Bt (35-95 cm): the horizon has a brownish color. The horizon has a moderate to strong coarse/thick blocky structure. The horizon contains few roots. Earthworm's channels were present in the horizon
- e) C (95cm +): Bruxellien sand. The horizon has a yellowish-brown color. The horizon has a strong coarse/thick blocky structure. The horizon contains very few fine roots. Little rocks were also present on this horizon.

The description of soil layers for control condition from the observation is as follows:

- a) Ap1(0-10 cm): the moist color of the horizon is brown. The horizon has a moderate fine to a medium granular structure. This horizon contains many very fine to

coarse roots. Some remaining vegetation still also present. This horizon is highly porous.

- b) Ap2(10-25cm): the moist color of the horizon is brown. The horizon has a weak fine to a medium granular structure. This horizon is less porous than the Ap1 horizon. However, many very fine to coarse roots still present.
- c) Ap3(25-38cm): the plough sole. The horizon has a strong thick platy structure. Many very fine to coarse roots are present. The roots are growing horizontally belong to the boundary between Ap2 and Ap3 horizon.
- d) Bt1(38-78 cm): the horizon has a brownish color. The horizon has a moderate to strong coarse/thick blocky structure. The horizon contains few very fine to fine roots. Earthworms channels are also present on the horizon.
- e) Bt2 (78cm +): the loess layer. The horizon has a greyish color. The horizon has a strong very coarse/thick blocky structure.

## **Appendix B: ERT data processing**

The detailed workflow for processing raw ERT data and assessment of measurement error prior to the inversion procedure is shown in Figure 5.11-a. In this section, we describe in detail each step, namely: preliminary filtering, normal-reciprocal analysis and error model. Figure 5.11-b shows the number of quadrupoles remaining at each stage of the data processing described below.

### *Preliminary Filtering: identification and removal of outliers*

A filter is applied to remove ERT data having the following criteria:

- a) Geometric factor > 50000
- b) Apparent resistivity outside [5 – 2000] [ $\Omega \cdot m$ ]. Such bounds include the TDR values measured on the field and vary in [25 – 200] [ $\Omega \cdot m$ ].
- c) Data having stacking error greater than 50% (Beff et al. 2013).

### *Normal-Reciprocal Analysis: detailed filtering of the data*

We look at the resistance measured in normal ( $R_n$ ) and reciprocal ( $R_r$ ) readings to characterize the error as shown in Figure 5.12-a. The number of quadrupoles having reciprocals was 450 out of 3084 quadrupoles in the raw data. In the normal-reciprocal filtering, we have the following steps:

a) Compute error and fractional error ( $FE$ ) as:

$$E = |R_n - R_r| \quad (B.1)$$

$$FE = \frac{E}{R_{mean}} \quad (B.2)$$

- b) Remove quadrupoles having  $FE > 0.5$
- c) For remaining normal-reciprocal pairs, we replace  $R_n$  and  $R_r$  by their arithmetic mean ( $R_{mean}$ ):

$$R_{mean} = \frac{R_n + R_r}{2} \quad (B.3)$$

### *Quantification of the data-error*

The data-error in ERT can be described by a linear model (e.g., LaBrecque et al. 1996; Slater et al. 2000) that depends on the magnitude of measured resistances and expressed in terms of two parameters, which can be written as:

$$E_{model} = a + bR \quad (B.4)$$

where  $R$  is the magnitude of the resistance,  $a$  is the absolute error and  $b$  is the relative error. As described in LaBrecque et al. (1996), the absolute error is mainly dominating for low resistance values (e.g. above  $1 \Omega$ ); whereas the relative error is mainly describing the error for high resistance readings.

After the removal of clear outliers, we assume that the measurements are only affected by random error, which can be quantified by the model expressed in Equation 5.4.

In Figure 5.12-b, we compare the histograms of  $R_{mean}$  with that of resistances of all data (quadrupoles that did not have reciprocals included) concatenated for all three-time stamps. The available normal-reciprocal data represents only about one-fifth of the total data as seen from their histograms. We see that the cumulative reciprocals are representing the total data for a large range of resistances.

Among the different methods allowing the quantification of the error parameters, we used the log-binning method (described in detail in Koestel et al. 2008). We find the absolute error ( $a = 0.04$ ) and the relative error ( $b = 0.12$ ) as shown in Figure 5.12-c. These values were used for ERT inversion of all-time series.

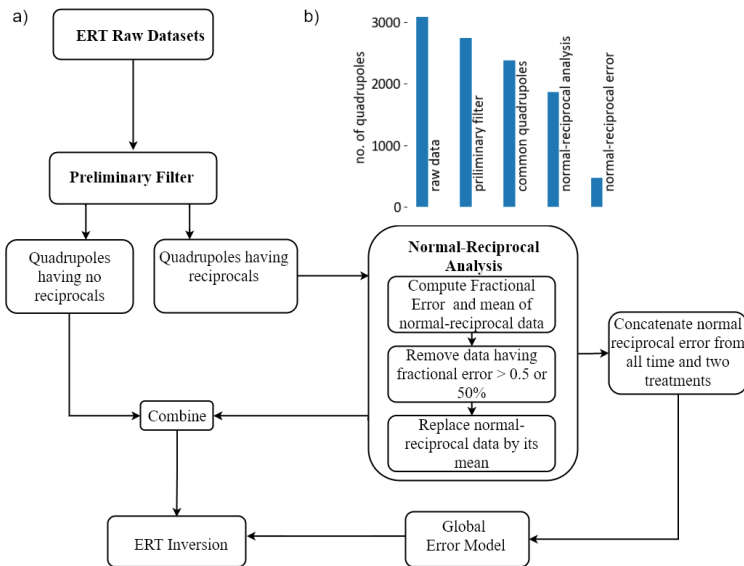


**Figure 5.11:** a) Methodology workflow chart for ERT data processing of field data and b) no. of quadrupoles per dataset remaining at various stages of the filtering process.

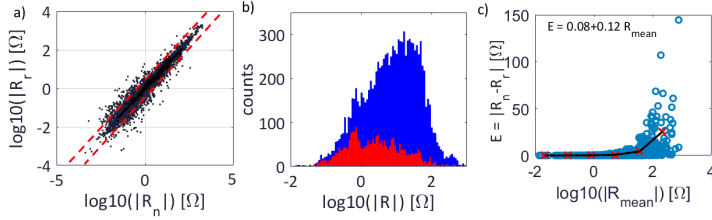


**Figure 5.12:** a) Normal and reciprocal resistances of cumulative data from t1 to t3. The dashed line indicates the range considered in the error model ( $FE < 0.5$  while data points outside the dashed lines are discarded, b) Histograms of cumulative resistances of all data from t1 to t3 in blue, and normal-reciprocal resistances averaged in red, c) Error vs resistance plot (blue circles) with log binned values: standard deviation of error vs mean resistance (red crosses) and a fit to log binned values (black line). The fit is  $E = 0.04 + 0.12 R$ .

## Appendix C: Optimizing $\lambda$ and $Z_w$

Figure 5.13 shows the L-curve computed for the control condition at t1 for different  $Z_w$  (other times are not shown although we computed optimal lambda for each time separately). The optimal  $\lambda$  or the corner of L-curve varied between 150 and 200 for most of our synthetic and experimental data. Hence, we chose the value of 175 to be optimal for our further studies. We provide the inversion quality and images in section E.

To optimize  $Z_w$ , we looked at two indices: a) Mean Square Error ( $mse$ ) between original synthetic model and inverted model interpolated on the same mesh and b) Structural Similarity Index ( $ssim$ ) (Wang et al. 2004) which measured the structural similarity (0 to 1 scale) between original synthetic model and the inverted model. Optimized  $Z_w$  is assumed to be the one for which  $mse$  is lowest and  $ssim$  is highest between inverted and original model. For  $Z_w$  optimization, we compare  $mse$  and  $ssim$  indices for the following

quantities between the original model and inverted model:

- Electrical resistivity distribution at a given time denoted by  $\rho(t_1)$ ,  $\rho(t_2)$ , and  $\rho(t_3)$ .
- Water content distribution at a given time denoted by  $\theta(t_1)$ ,  $\theta(t_2)$ , and  $\theta(t_3)$ .
- Log difference of electrical resistivity at  $t_3$  and  $t_1$ :  

$$\delta\rho = \log(\rho(t_3)) - \log(\rho(t_1)).$$
- A difference of water content between  $t_3$  and  $t_1$ :  

$$\delta\theta = \theta(t_3) - \theta(t_1).$$

The optimal  $Z_w$  for which *ssim* was maximum and *mse* was minimum varied for different quantities, time and treatments ( $\rho$ ,  $\theta$ ,  $\delta\theta$  and  $\delta\rho$ ) and ranged from 0.1 to 0.8. To have a common  $Z_w$  for all the data, we took the mean value which was around  $Z_w = 0.5$ . Also, this choice of  $Z_w = 0.5$  produced minimal artifacts when inspected visually (See section D).

Up to 1m in-depth, we have good uniform coverage below which the sensitivity of electrodes becomes non-uniform mainly due to greater electrode separation and lesser electrodes (See Fig. 5.13). Hence, we can expect that inversion results below 1m depth may contain artifacts and should not be interpreted. However, at depths greater than 1m, TDR measurements showed fewer variations in the resistivity and hence lower coverage of ERT electrodes was sufficient.

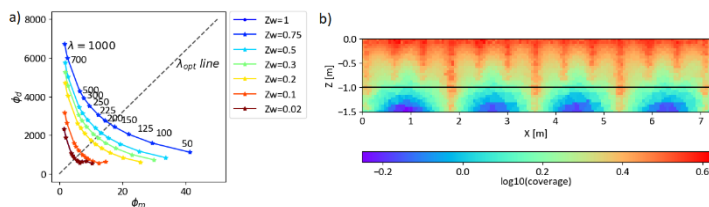


**Figure 5.13:** a) L-curves computed for electrical resistivity at  $t_3$  of Figure 5.7-c for different  $Z_w$ . The optimal lambda is

at the corner of the L-curve indicated by a diagonal line, b) Logarithm of electrode coverage of the ERT injection scheme.

## Appendix D: Impact of Zw on Inversion

The optimal  $Z_w$  as predicted by mse and ssim indices differed for each data, quantity, and treatments. We compared the inversion with a forward synthetic map of  $\rho(t_3)$ ,  $\theta(t_3)$ ,  $\delta\theta$  and  $\delta\rho$  for different values of  $Z_w$ . First, we can see that our injection scheme recovers the most important features in the soil-root zone. Note that the injection scheme is able to recover the uptake patterns of different plants up to 1m in depth. Second, we find that  $Z_w = 0.5$  performs better than other choices in terms of reduced artifacts.

The  $rrms$  was within 2% and  $\chi^2$  within 5% for all inversions results involving both synthetic and real data showing the good quality of ERT inversion fits at  $Z_w =$

0.5. The *ssim* index between synthetic forward and ERT inverted varied between 0.55 to 0.62 for synthetic studies while *mse* index ranged from 34 to 74 [ $\Omega^2 m^2$ ].

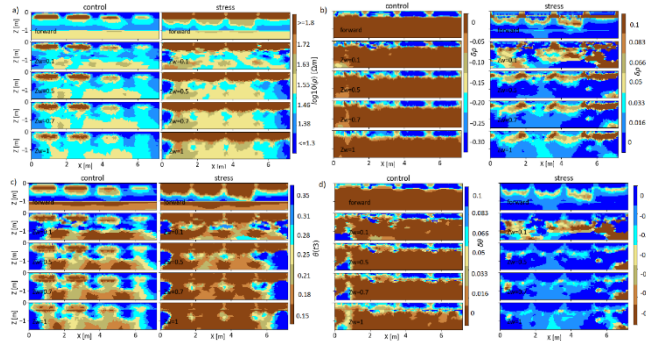


**Figure 5.14:** a) Comparison of Synthetic forward resistivity distribution at  $\rho(t_3)$  with ERT inversion at different  $Z_w$  for control treatment and stress treatment, b) Comparison of forward log ratio of resistivity at time 3 and time1 ( $\delta\rho$ ) with ERT inversion at different  $Z_w$  for control treatment and stress treatment, c) Comparison of transformed forward water content distribution at  $\theta(t_3)$  with ERT inversion at different  $Z_w$  for control treatment and stress treatment, and d) Comparison of a forward difference of water content at time 3 and time1 ( $\delta\theta$ ) with ERT inversion at different  $Z_w$  for control treatment and stress treatment.

## Appendix E: Plant and Soil boundary condition

**Table 5.2:** Soil hydraulic properties per horizon.  $\theta_r$ : Residual water content,  $\theta_s$ : Saturated water content,  $a$ ,  $n$ ,  $m$  and  $\lambda$ : shape parameters in Van Genuchten-Mualem equations,  $K_s$ : saturated soil hydraulic conductivity.

H orizon		$\theta_r$ $[m^3 cm^{-3}]$	$\theta_s$ $[m^3 cm^{-3}]$	$a$ $[1/cm]$	$n$	$= 1-1/n$	$n$ $[cm/day]$	$K_s$	$\lambda$
A p1		0	0.	0	.174	.1482	0	44.	.1
A p2		0.	0.	0	.521	.3425	0	0.7	.340

p3	A	0. 039	0. 404	0 .00416	.521	0 .3425	0.7 32	.340
1	Bt	0	0. 4	0 .00421	.214	0 .1762	1.5	.731
2	Bt	0	0. 4	0 .00421	.214	0 .1762	1.5	.731
C	1	0. 357	0. .0148	0 .056	.5136	0 5		.155

**Table 5.3:** Plant parameters used in R-SWMS simulation

Equivalent conductance of the whole root system	1 [cm <sup>3</sup> /hPa/day]
Compensatory RWU conductance of the root system	1 [cm <sup>3</sup> /hPa/day]
Limiting collar water potential (isohydric plant)	-15000 hPa

## **6** FIELD PHENOTYPING OF GRASS WATER UPTAKE UNDER WATER DEFICIT BY ERT

## ABSTRACT

Grasslands are potentially sensitive to shift in precipitations induced by climate changes. Combinations of grass and forbs species with different ability to extract deep soil water might increase the resilience of grasslands against water deficit conditions and help keep the same forage quality and quantity in adverse conditions. In this study, a field trial with imposed water deficit was set up to compare grassland productivity of different compositions. It consisted of 4 replicate plots (7.2 m x 1.5 m) of different grasses and forbs under 2 treatments: water deficit (no rainfall) and control (normal weather).

Surface and depth electrodes were installed on a vertical transect across replicate plots to monitor soil electrical resistivity using Electrical Resistivity Tomography (ERT) for both treatments. We hypothesize that different plant water uptake strategies would result in different distributions of soil water depletion and thus, of electrical resistivity evolution.

By computing the 1-D averaged profiles of electrical resistivity changes, different depletion patterns could be discriminated for different plant species. The differences in the uptake pattern were then linked to plant physiology and root characteristics.

### 5.1 Introduction

More than 25% of the world land area and 70% of the world agricultural area are covered with grasslands and support crop-livestock farming systems that contribute to the livelihoods of more than 800 million people worldwide (Rojas-Briales 2015). Beyond forage production, grasslands provide numerous ecosystem

services including carbon sequestration, water erosion control, flood mitigation, protection and enrichment of the soil and maintenance of biodiversity (Zhao et al. 2020). Globally, 5.5Gt of carbon are estimated to be stored in the top 30 cm of grassland soils, which represent 40% of agricultural area of the world (Gibson 2009; Kipling et al. 2016; Scurlock and Hall 1998; Suttie et al. 2005).

However, global change deeply affects grasslands and threatens their ecosystem services (Hopkins and Del Prado 2007). Despite the fertilization effects of increased atmospheric CO<sub>2</sub>, change of precipitation patterns, increased drought frequency and heat waves will affect grassland vegetation (Ergon et al. 2018; Haddad et al. 2002; Tilman and El Haddi 1992) and might reduce biomass production in grasslands if soil moisture becomes limiting (Gilgen and Buchmann 2009). Therefore, adaptation strategies need to be found to increase grassland resilience and productivity and maintain the ecosystem services they currently deliver. Amongst them, it has been proposed to diversify and combine different forage crop species and investigate within-species diversity in response to drought (Hanna et al. 2018). It is therefore crucial to develop techniques to assess the ability of specific plants or combinations of plants to cope with drought and take up water in adverse conditions.

Water and nutrient uptake efficiency in grasses and clovers have been linked to root traits (Jackman and Mouat 1972). For instance, early pot studies by Evans (1977) found that grasses such as *Lolium perenne L.* and *Dactylis glomerata L.* were more efficient in terms of nutrient and water uptake than clovers such as *Trifolium pratense L.* and *Trifolium repens L.* This efficiency was linked to the superior root traits of grasses such as higher no. of root hairs or greater root length per unit volume as compared to clovers (Evans 1977). In an another early study, manual removal of root system in pot experiment reduced water uptake but

not the nitrogen uptake (Andrews and Newman 1970). A more recent study by (Zhang et al. 2009) on winter wheat suggests that under water deficit condition, root water uptake is not affected by root system size. This contrasting conclusion suggests our incomplete understanding of soil-plant-environment interactions.

Some studies indicate that drought stress could affect root growth rate, root architecture and root biomass production (Hoogenboom et al. 1987; Rodrigues et al. 1995). However, a study on grasslands in Switzerland showed that drought did not have an effect on root biomass production and only affected above ground bio-mass (Gilgen and Buchmann 2009). Another study by Dickin and Wright (2008) showed that stressors such as waterlogging and droughts could decrease the total root length but not the rooting depth in winter wheat. Field studies on Ryegrass and Cocksfoot show that tolerance to droughts could be linked to deeper roots or deeper uptake depths and their quick ability to take up nitrogen upon availability of water (Volaire et al. 1998). In their study, Cocksfoot (Lutetia breed) was unable to extract water at deeper soil horizons due to fewer roots at depths below 70 cm as compared to Ryegrass. However, in both species no uptake was found below 1m depth when subjected to a drought of 80 days.

According to (Blum 2011) studying phenotyping traits in plants such as water uptake ability is the key solution to drought resistance as compared to finding drought tolerant genes through genomics method. Various studies target phenotyping the aerial part of the plant. They include field scale optical imaging techniques such as the use of thermal camera, laser scanning and hyperspectral cameras (Fiorani and Schurr 2013; Golzarian et al. 2011; Yang et al. 2013). The estimated key parameter, such as shoot biomass, plant growth, and photosynthesis, then helps in identifying efficient phenotypes within a plant species. For example, structural traits such as leaf angle distribution are

linked to light interception (Ford et al. 2008) and canopy temperatures are linked to leaf transpiration (Wasson et al. 2012).

Since roots are the plant organs, that first detect agricultural stresses such as water deficit or high salinity and sends appropriate chemical stress signals to the shoot, in turn, reducing the crop yields (Jenks et al. 2007), it is very important to understand them. However, compared to the aerial part, there are not many studies on direct root phenotyping at field scale. Some studies use certain above ground traits such as leaf transpiration, leaf area index, shoot biomass and canopy temperatures as an indirect proxy for measuring root system performance but are not always accurate and useful (Wasson et al. 2012). Direct root phenotyping is at the frontier of plant phenotyping research but is still challenging due to lack of accessibility (Fiorani and Schurr 2013).

Traditional root phenotyping methods involve manual digging of soil to expose roots or specialized rhizotrons equipped with cameras. There is also the use of tractors attached with soil coring equipment that can take large no. of soil core samples in less time as compared to manual digging (Wasson et al. 2012). However, these techniques only samples small portion of root systems leaving the rest unexplored (Cendrero-Mateo et al. 2017). In addition, pot experiments aimed at selecting superior genotypes by excavating and analyzing entire root traits are unrealistic due to time consuming nature (Norris and Thomas 1982).

For a long time, measuring water depletion in soils is used as a good proxy for root phenotyping (Horn 1971; Kiniry et al. 1983). Water depletion is easier to measure as compared to root counting through the use of sensors and has been widely used in different plant species (Dardanelli et al. 1997; Dick et al. 2018; Gordon et al. 1989; Hattendorf et al. 1988; Merrill et al. 2004; Moroke et al. 2011; Pepe and Welsh 1979; Robinson et al. 2006; Stone et al. 2002; Volaire et al.

1998; Wang et al. 2009). For example, Kirkham et al. (1998) used neutron probe method to compare water depletion in Maize and Soybean and could relate it to root density. Stone et al. (2002) used neutron probe to quantify water depletion depths in sunflower and sorghum and found sunflower to be more efficient in uptake than sorghum due to its deeper root. Similarly, Wang et al. (2009) used soil moisture sensor to differentiate water depletion depths in alfalfa, caragana brush and pine species and was able to relate these differences to root density. On the other hand, Pepe and Welsh (1979) monitored water depletion in winter wheat cultivars using gravimetric sensors at a resolution of 30cm and could not relate water depletion to root activity. The commonly used methods such as neutron probe or gravimetry lacks depth resolution (Schmugge et al. 1980) and hence better methods are needed to quantify depletion depths of plants.

Monitoring root water depletion signatures via the electrical resistivity tomography (ERT) method has recently been found to be useful in retrieving root phenotyping information such as depth and extent of water depletion (Rao et al. 2020). Many ERT studies on cropped soil uses surface electrodes, most commonly the Wenner array. Jayawickreme et al. (2008) and Dick et al. (2018) investigated contrasting root systems such as that of forests and grasslands by ERT. Jayawickreme et al. (2008) used a Wenner configuration (surface electrodes) with an electrode spacing of more than one meter while Dick et al. (2018) used an electrode spacing of 1m for forest and 0.5 m for heather. Srayeddin and Doussan (2009) used an ERT Wenner array configuration with relatively less electrode spacing of 0.3 m to study root water uptake depths in Maize and Sorghum field. They observed water depletion in both Maize and Sorghum for depths up to 160 cm and found that Sorghum extracted more water than Maize. However, in water stress treatment, the water uptake could not be quantified beyond 50 - 60 cm depth due to poor sensitivity of surface electrode

configuration. Therefore, surface configuration may not be suitable for phenotyping roots that need higher resolution in the sub-meter scale where differences between different grass root systems occur. Even for larger trees, ERT experiments show that the root activity takes place at the decimeter scale (0.1 m) (Vanella et al. 2018). In Table 6.1, we summarize some of the studies that used water depletion as a proxy for root activity.

**Table 6.1:** Studies using water depletion depths in cropped soils

Author	Scale	Method	Species	Maximum depletion depth (m)
Brown (1971)	Field	Neutron probe	Winter wheat	0.91

Pepe and Welsh (1979)	Fieldd	Gravimetry	Red winter wheat	-
Hattendorf et al. (1988)	Fieldd	Neutron probe	Sunflower	0.99-1.6
Kirkham (1998)	Rhizontron	Neutron probe	Maize Soybean	0.45-0.9 0.3-0.6
Stone et al. (2002)	Fieldd	Neutron probe	Sunflower Sorghum	3.1 2.5
Merill et al. (2004)	Fieldd	Neutron probe	Sunflower Canola Spring wheat Dry pea	> 0.6 > 0.6 < 0.6 < 0.6
Moroke (2005)	Fieldd	Neutron probe	Cowpea Sorghum Sunflower	0.5-1.7 1-1.8 1-1.8
Robinson et al. (2006)	Fieldd	Gravimetry	Eucalyptus	8-10
Wang et al. (2009)	Fieldd	Gravimetry	Alfalfa Caragana brush Pine forest	15.5 22.4 21.5
Srayeddin and Doussan (2009)	Fieldd	ERT	Maize Sorghum	1.6 1.6
Rao et al. (2020)	Fieldd	ERT	Rye grass White clover Cocksfoot	0.5-1 0.5-1 0.5-1

Therefore, the main objective of this study to investigate the ability of ERT to differentiate water

depletion patterns in plants when subjected to water deficit in situ. We used 2-D ERT in an agronomic field trial comparing combination of forage crop genotypes and extended the previous high-resolution ERT study of Rao et al. (2020) to derive response to drought of 5 different crop forage species and their combinations.

## 5.2 Materials and Methods

### 5.2.1 Field Trial Description

The experimental field is located in Corroy-le-Grand (Belgium), at the De Marbais University farm, in the agricultural Loess region.

A random-block field trial was established for comparing combinations of grass and forb species under water deficit conditions (through a shelter preventing rainfall for six weeks) as shown in Fig. 6.1-a.

The experimental field is organized in four blocks of 7.2 m by 7 m (B1 to B4). Each block contains eight plots sown homogeneously with a given (combination) of species as shown in Fig. 6.1-b. For ERT measurements, each block is split organized into two panels of four plots (dimension 1.2 m x 7 m) separated by a layer of 30 cm (Figure 6.1-c).

The trial consisted of five monocultures: *Lolium perenne L.*, *Medicago sativa L.*, *Dactylis glomerata L.*, *Trifolium pratense L.*, *Trifolium repens L.* and three binary mixtures: (*Lolium perenne L./Trifolium repens L.*, *Dactylis glomerata L./Medicago sativa L.*, *Lolium perenne L./Trifolium pratense L.*) subjected to water deficit treatment. Each crop monoculture or combination of crops had four replicates, totalizing 32 plots. The abbreviation used for each species along with English names and sowing density are shown in Table 6.2.

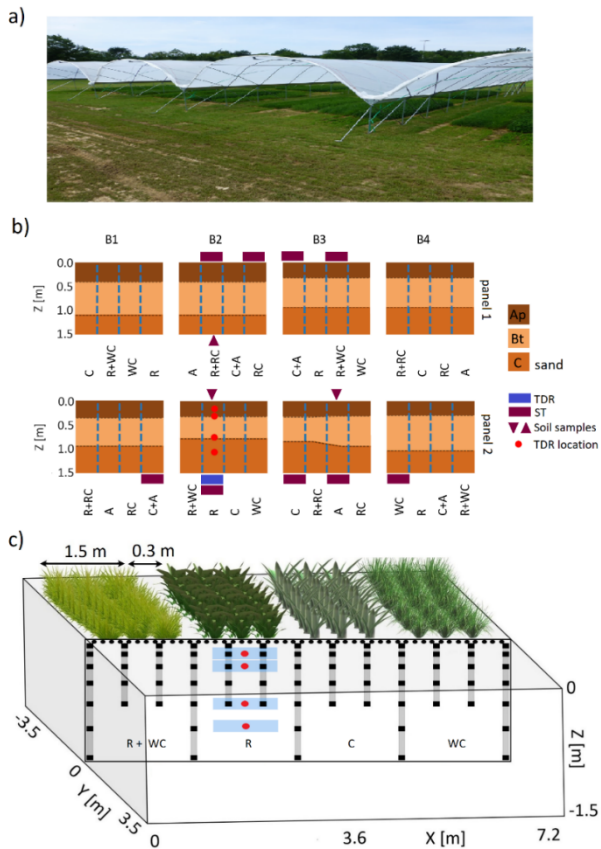


**Figure 6.1:** a) Picture of an experimental site with water deficit treatment. b) Sketch of the vertical cross-section for each plot of the experimental field in Corroy-le-Grand. TDR probes and thermometers are located under ryegrass plots of block2 (red circles). Different soil-horizons are indicated by the corresponding brown color scale. ST represents the sampling trenches. Letters below each plot indicate the (combination of) species of the plot: three binary mixtures (R+WC: ryegrass+white clover; R+RC: ryegrass+red clover; C+A: cocksfoot+alfalfa) and five monocultures (A: alfalfa; C: cocksfoot; R: ryegrass; RC: red clover; WC: white clover) is present; and c) A schematic view of a panel (here block 2, panel2) showing the ERT electrodes at the center plane ( $y = 0$ ) used for two-dimensional ERT imaging. The black dots represent the surface point electrodes while the black squares are the borehole ring electrodes. Location

of TDR probes (red circles) installed at different depth in ryegrass strip. Blue rectangles around TDR probes represent

Species	English name	A bbrev.	Sowing density (kg/ha)
<i>Lolium perenne L.</i>	Ryegrass	R	25
<i>Medicago sativa L.</i>	Alfalfa	A	30
<i>Dactylis glomerata L.</i>	Cocksfoot	C	30
<i>Trifolium pratense L.</i>	Red clover	R C	25
<i>Trifolium repens L.</i>	White clover	W C	12
<i>Lolium perenne L. + Trifolium repens L.</i>	Ryegrass + White clover	R + WC	20 + 2
<i>Dactylis glomerata L. + Medicago sativa L.</i>	Cocksfoot + Alfalfa	C + A	15 + 18
<i>Lolium perenne L. + Trifolium pratense L.</i>	Ryegrass + Red clover	R + RC	20 + 8

the region for averaging ERT data for comparison against TDR values.

**Table 6.2:** Details of plant species in the study

Soil is classified as a Haplic Luvisol (Soil Atlas of Europe, 2005) according to the FAO classification system and considered a well-drained loam (Aba(1)), according to the Belgian soil classification. Three to four soil horizons were identified with trenches dug out around the field trial, depending on the location in the field trial (Fig. 6.1). The soil layers were characterized as follow:

- a) Ap: brown horizon with moderate fine to medium granular structure. This horizon contains many very fine to coarse roots.

- b) Bt: brownish horizon with a moderate to strong coarse/thick blocky structure. The horizon contains few roots. Earthworm's channels were present in the horizon
- c) C: Brusselian sand. The horizon has yellowish brown color. The horizon has strong coarse/thick blocky structure. The horizon contains very few fine roots. Little rocks were also present in this horizon.

### *5.2.2 ERT Acquisition*

ERT data were acquired independently within each panel through 2-D cross sections. ERT monitoring data set consisted of four-time stamps (denoted by t1 to t4), with data collected along the experimental panel every week along four consecutive weeks. The exact dates of measurements were t1: 03/08/2017, t2: 09/08/2017, t3:16/08/2017 and t4:24/08/2017. A rainout shelter was placed to prevent precipitation between 1/07/2017 to 29/08/2017. In addition, during this period no irrigation was added as shown in Figure 6.2.

Each panel was equipped with 123 electrodes, including 48 surface electrodes (with a separation of 0.15 m, circles in Fig. 6.1-c) and 75 electrodes distributed along 13 boreholes (separated of 50 cm), crossing the middle of each panel. The electrode layout, injection scheme, data processing and ERT inversion in this study are described in Rao et al. (2020). For the first three weeks (t1 to t3), we used the same measurement protocol and for the fourth week (t4), we changed the measurement scheme to include more reciprocals for error assessment and optimize the injection scheme for faster data acquisition. From t1 to t3, panel 1 and 2 contained 3054 and 2734 quadrupoles and at time 4, panel 1 and 2 contained 2051 and 1877 quadrupoles.

The raw data was filtered for outliers as described in Rao et al. (2020). We used python based pyGIMLI software (Rücker et al. 2017) for the inversion of ERT filtered data. We assume that measurement error in the filtered follows a linear model that depends on the magnitude of measured resistances and characterized by two parameter: absolute term and relative term (Günther et al. 2006; Koestel et al. 2008; Uduphay et al. 2011). The absolute and relative term was found using the approach of Koestel et al. (2008). Finally, to assess the ERT inverted results, we made use of the relative root mean square error and chi-square value (Beff et al. 2013).

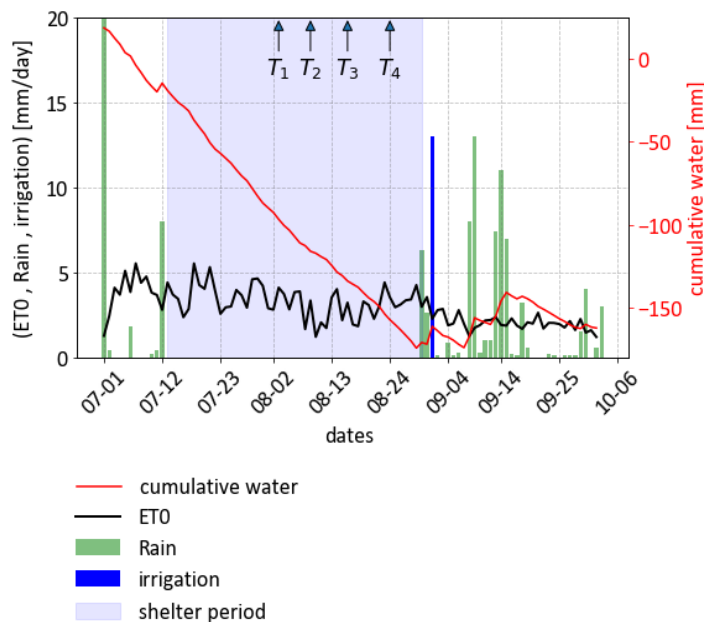


**Figure 6.2:** Boundary treatments in the field during the ERT/TDR data acquisition time. Rainfall, irrigation, evapotranspiration and cumulative water. Cumulative water is the cumulative sum of precipitation and irrigation subtracted with a cumulative sum of evapotranspiration.

### 5.2.3 Time Domain Reflectometry

Four Time domain reflectometry (TDR) probes were inserted horizontally at different soil depths below one single plot (sown with Ryegrass), which measured soil water content every week from t1 and electrical resistivity from t3 (red dots in Fig. 6.1-c). The TDR probes were installed at depths:  $Z = 0.15$  m, 0.3 m, 0.75 m and 1.05 m and  $Y = -0.35$  m. The TDR data was collected manually during the same duration as that of ERT and calibrated with a TDR probe cell constant of  $K_p = 1.57$  [ $m^{-1}$ ] along with temperature correction as described in Beff et al. (2013). Topp equation was used to convert permittivity to water content (Topp et al. 1984). Comparison with soil coring moisture content provided a  $r^2$  of 0.99 with a RMSE in water content of  $0.04 \text{ cm}^3/\text{cm}^3$ .

The pedophysical relation between EC and water content used for ERT was realized with a new set of TDR probes (Campbell, Logan, USA) installed in the year 2018 in the same field as described in Rao et al. (2020), which simultaneously monitored water content ( $\theta$ ) and electrical conductivity (EC). The TDR data was grouped into three soil horizons: Ap, Bt and C for pedophysical characterization (See Appendix A).

To compare ERT and TDR water content, we averaged the ERT derived water content on a rectangle surrounding the TDR probe (+/- 5 cm) with a height of 10 cm and width of 1.5 m (blue rectangles in Fig. 6.2). Comparing ERT results with TDR will not only allow us to conclude on the accuracy of ERT inversion but also on the optimal pedophysical characterization of soils from 2018 TDRs (Huisman et al. 2008; Koestel et al. 2008).

#### 5.2.4 Root characteristics measurements

Nine trenches (2 m x 2 m x 1.8 m) were dug on the edge of the plots for soil horizon characterization and root counting on October 31<sup>st</sup>, 2018 (Fig. 6.1-b). A grid (1.5 m x 1.5 m) composed of 900 cells (5 cm x 5 cm)

was fixed vertically against the soil wall. Then, the number of roots present in each cell was counted for each plant plots. The resulting root number density showed species dependent variations as shown in Figure 6.3. We will compare the root density profiles of Figure 6.3 with the water depletion patterns derived from ERT in the following sections.

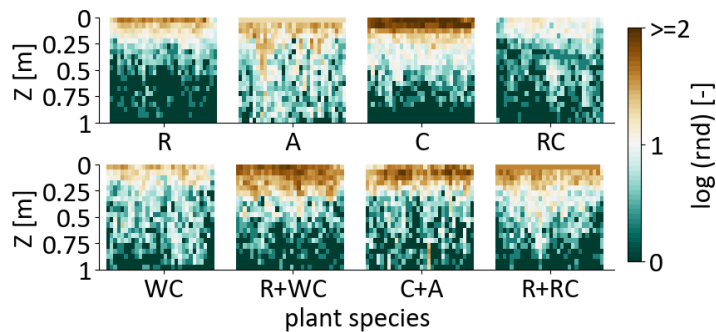


**Figure 6.3:** Root number density as a function of plant species. The units are normalized.

### 5.2.5 Analyses of plant depletion patterns

We follow the Gaussian fit method from Rao et al. (2020) to characterize plant-specific depletion patterns. First, we compute the 2-D time difference of water content defined as:

$$\delta\theta = \theta(t1) - \theta(t4)$$

The 1-D medians at each depth from 2-D distributions of  $\delta\theta$  was computed for each plot and a Gaussian curve was fitted to the 1-D medians of  $\delta\theta$  profiles. From the fitted Gaussian function, the two parameters of a Gaussian function were then optimized to fit these 1-D profiles:  $\mu_{z,\delta\theta}$  and  $\sigma_{z,\delta\theta}$ . The mean parameter  $\mu_{z,\delta\theta}$  represents the depth at which depletion is the largest (maximum depletion depth) while  $\sigma_{z,\delta\theta}$  represents the extent of the depleted zone.

In addition, we also perform one-way ANOVA (Weckesser and Haberland 2019) and kruskal-wallis h-tests (Kruskal and Wallis 1952) on Gaussian fit parameters for different replicates grouped by plant species to analyze the statistical significance of the differences observed in species. Finally, as post-hoc test, we also performed Tukey honestly significant difference test pairwise between two species to determine which groups were significantly different in terms of Gaussian fits (Tukey 1949). These tests were performed using SciPy library (Virtanen et al. 2020).

## 5.3 Results

### 5.3.1 Comparison between soil water content measured by TDR and ERT

Figure 6.4 compares the ERT averaged water content along with standard deviation with the TDR derived water content combined for different time and depths. We observe higher lateral variations of ERT water content (vertical bars in Fig. 6.4) at depths 75 cm and 105 cm as compared to shallow depths of 15 cm and 30 cm which is opposite to what Beff et al. (2013) observed. In general, we observe a very high 1:1 correlation ( $r^2 = 0.99$ ) of TDR and ERT with a rmse 0.03 [ $m^3 m^{-3}$ ] showing reasonable accuracy of the used pedophysical relation and the accuracy of ERT inversion in quantifying soil water content variability.

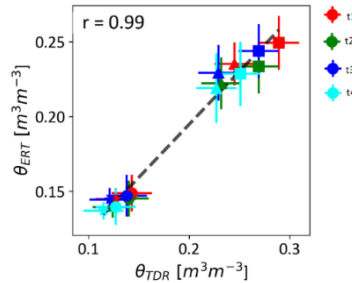


**Figure 6.4:** Mean soil water content measured by ERT and TDR at different depths. The vertical bar represents the standard deviation of ERT data corresponding to the lateral variability of the ERT values at the depth of the TDR +/- 5 cm. The TDR error bar corresponds to the rmse of the TDR calibration. The dotted line corresponds to 1:1 correlation line. Color represents different time: red: t1, green: t2, blue: t3 and cyan: t4. Different markers represent depths: circle: 15cm, star: 30 cm, square: 75 cm and triangle: 105 cm.

### 5.3.2 Water content evolution

Figure 6.5 shows the 2-D water content distribution evolution of the 4 replicates for each (combination of) plant species. As plots were spread between different blocks with different layering, differences in the depth of the sand layer (blue region below 0.8 m) can be observed between replicates of the same species. In general, we see a consistent drying pattern progressing between t1 to t4 (increasing brown patches) except for some panels such as RC in B3, WC in B2 and R+RC in B3. In these plots (RC in B3, WC in B2 and R+RC in B3), inconsistent patterns appear such as t2 being drier than t4 which is not possible. One possible explanation could be the lower ERT sensitivity of some of these plots. Hence when we inspected the sensitivity map as a function of plant species (Appendix A2), we clearly see that these panels where we see earlier times drier than final time, the sensitivity was poorer. In general, the sensitivity below 1m depth drops below 1.5 but for some plot's sensitivity is lower even above 1m. The plots for which sensitivity is below a threshold value of

1.5 (Fig. A2) at shallow depths ( $Z < 0.8$  m) is marked with red diamond to the left in Figure 6.5.

As the water deficit increases with time, we expect to see more changes between t4 and t1 than between t3 and t1 or t2 and t1. Hence, in the next section we analyze  $\delta\theta$  between time 1 and time 4 only.

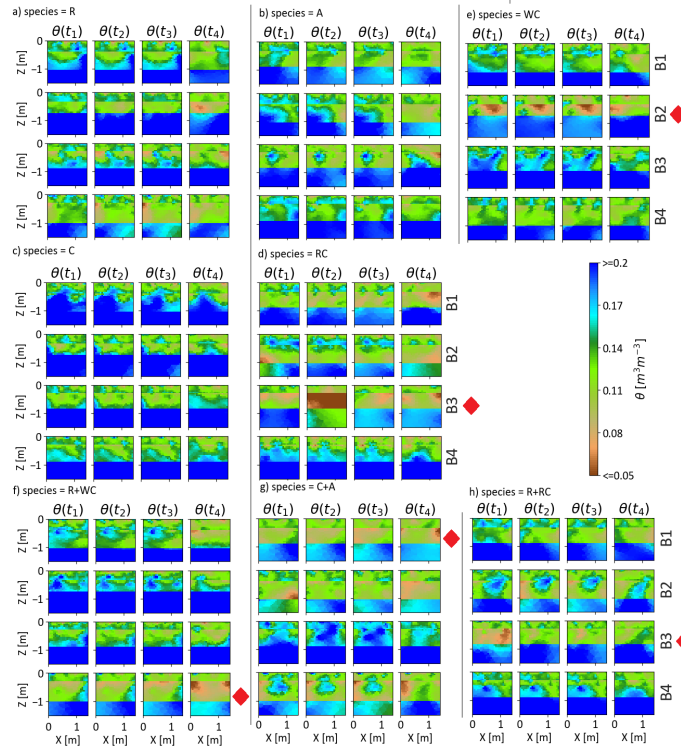


**Figure 6.5:** ERT inverted water content at different times (columns) for different replicates or blocks within a species (rows) for: a) ryegrass (R), b) red clover (RC), c) alfalfa (A), d) cocksfoot (C), e) white clover (WC), f) ryegrass and white clover mixture (R+WC), g) cocksfoot and alfalfa mixture (C+A), h) ryegrass and red clover mixture (R+RC). Red diamonds show replicates for which coverage was low.

### 5.3.3 Depletion depth and root and available water distributions

In Figure 6.6 the 2-D distribution of  $\delta\theta$  is computed for all replicates and combinations of species. In the second column of Figure 6.6, we fitted Gaussian curves to positive change of  $\delta\theta$  medians (representing water depletion) to quantify maximum depletion depth and depletion zone extent of each replicate. In general, despite high variability between 2-D  $\delta\theta$ , we see consistency in the shape of  $\delta\theta$  medians between replicates, which is a good indication that ERT was able to capture a representative signature of the depletion pattern. It means that local water content changes are probably not able to characterize species-specific signature and that (at least) a 2-D coverage is needed to acquire a representative picture of the uptake patterns.

In Figure 6.7-a, we compare the Gaussian fitting parameters, namely maximum depletion depth (black dots) and depletion zone extent (vertical bar) for each replicate within a species. We observe that there exists some difference among different species. In general depletion profiles between replicates is very similar except for red and blue sticks, where more variation is observed. The red sticks are the ones with low coverage while the blue are outliers based on interquartile ranges. Figure 6.7-b and c shows the box plot (Williamson et al. 1989) characterizing minimum, maximum, median ( $50^{\text{th}}$  percentile), first quartile ( $25^{\text{th}}$  percentile) and third quartile ( $75^{\text{th}}$  percentile) of depletion depth and extent of different replicates within a given species. Clearly the blue sticks in Fig. 6.7-a appear outside the quartile range (blue diamonds) in the box plots of Figs. 6.7-c and d.

Both one-way Anova and Kruskal-Wallis h-test confirms the statistical significance of differences observed in different species corresponding to a very low p-value ( $p < 0.05$ ). Hence, water depletion patterns are captured by the Gaussian fits parameters that are statistically significant.

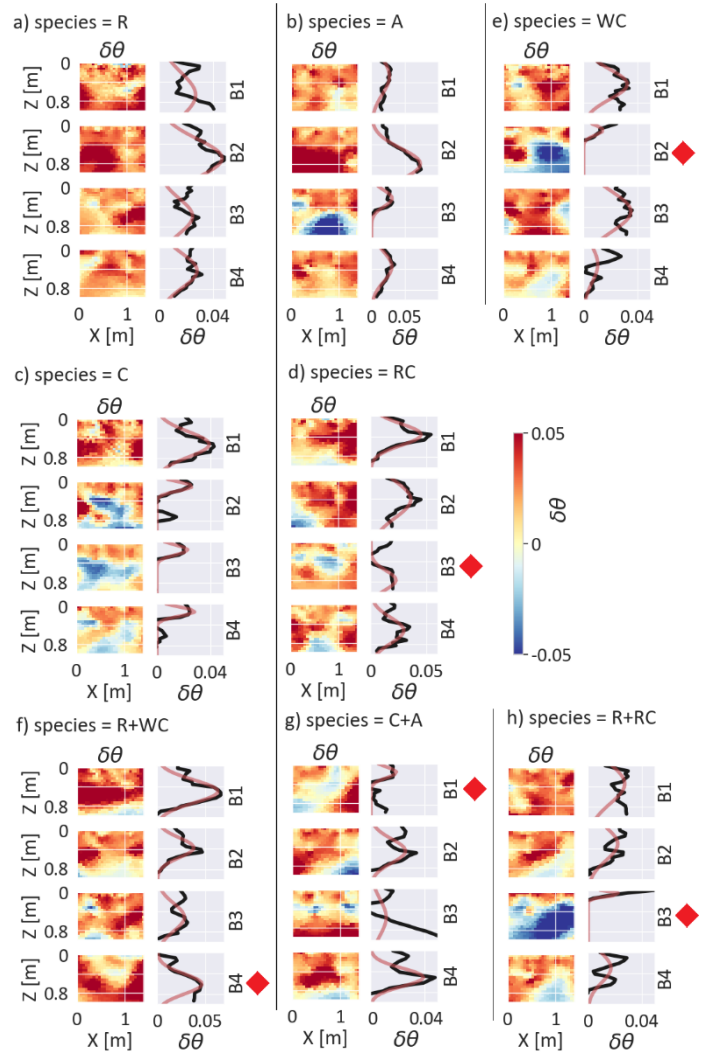


**Figure 6.6:** ERT inverted change of water content ( $\delta\theta$ ) between t1 and t4 in the first column and 1-D profile of  $\delta\theta$  (black) in the second column for different replicates or blocks within a species (rows) for: a) ryegrass (R), b) red clover (RC), c) alfalfa (A), d) cocksfoot (C), e) white clover (WC), f) ryegrass and white clover mixture (R+WC), g) cocksfoot and alfalfa mixture (C+A), h) ryegrass and red clover mixture (R+RC). The black solid lines are 1-D  $\delta\theta$  median as a function of depth and red lines are Gaussian fits to positive changes of  $\delta\theta$ .

Looking at Figure 6.7-a and Table 6.3, we can observe that R and C have specific and contrasted behaviors as compared to the other species. R has a deep depletion depth, which is significantly different from all other species but C+A. On the opposite, C has a shallow depletion depth (Fig. 6.7-b), which discriminates from all other species except from A and R+RC (Table 6.3). When mixing is considered, we see that the depletion depth of R+WC cannot be differentiated from the depletion depths of its two contributing species R and WC. On the opposite, C+A, A and C are from different distributions, as if competition between species in the mix plot would differentiate the uptake depth of both species. In addition, root density profile in Figure 6.3 shows that C is shallow ( $Z < 50$  cm) while A is uniformly distributed at depths below 50 cm and hence their combination (C+A) might complement each other for water acquisition. The situation is different for the mix R+RC, which is not significantly different from RC but significantly different from R. It might reflect different species strategies under drought and competition.

In terms of depletion extent, C and R have also contrasting behaviors while all the other species have relatively homogeneous depletion extents. C has a very narrow extent (Fig. 6.7-c), which differs from all other species but R+WC and RC. On the opposite R has a broad extent (Fig. 6.7-c) significantly different than A, RC and R+WC. In terms of mixed crops, we could have expected that the extent of the combination differs from its contributing species but it is only the case between R and R+WC and between C and C+A.

In Figure 6.7-d, we compare root percentiles, maximum rooting depth, replicates averaged mean depletion depth and maximum depletion extent of Gaussian fits. In general, the mean depletion depth takes place below or close to the 25th percentile of root distribution. We can hypothesize that plant transpiration in this condition is ensured by less than

25% of the root system. On the opposite, plants like A and C seem to be less able to use their deepest roots to extract water. Interestingly, we also observe that under combinations of crops, the uptake is systematically deeper than the root 25<sup>th</sup> percentile.

**Table 6.3:** Tukey HSD statistics for Gaussian fit parameters. True means that the medians are significantly different.

Group1	Group2	P-value for $\sigma_{z,\theta}$	Reject $\sigma_{z,\theta}$	P-value for $\mu_{z,\theta}$	Reject $\mu_{z,\theta}$
A	C	0.001	TRUE	0.1369	FALSE
A	C+A	0.742	FALSE	0.0074	TRUE
A	R	0.6633	FALSE	0.001	TRUE
A	R+RC	0.9	FALSE	0.9	FALSE
A	R+WC	0.4146	FALSE	0.053	FALSE
A	RC	0.2536	FALSE	0.1447	FALSE
A	WC	0.9	FALSE	0.3009	FALSE
C	C+A	0.0158	TRUE	0.001	TRUE
C	R	0.001	TRUE	0.001	TRUE
C	R+RC	0.001	TRUE	0.0581	FALSE
C	R+WC	0.0514	FALSE	0.001	TRUE
C	RC	0.0967	FALSE	0.001	TRUE
C	WC	0.001	TRUE	0.0014	TRUE
C+A	R	0.0715	FALSE	0.2631	FALSE
C+A	R+RC	0.549	FALSE	0.0188	TRUE
C+A	R+WC	0.9	FALSE	0.9	FALSE
C+A	RC	0.9	FALSE	0.7294	FALSE
C+A	WC	0.3921	FALSE	0.4846	FALSE
R	R+RC	0.8563	FALSE	0.001	TRUE
R	R+WC	0.0223	TRUE	0.0448	TRUE
R	RC	0.0114	TRUE	0.0152	TRUE
R	WC	0.9	FALSE	0.0062	TRUE
R+RC	R+WC	0.2462	FALSE	0.1258	FALSE
R+RC	RC	0.1405	FALSE	0.3088	FALSE
R+RC	WC	0.9	FALSE	0.548	FALSE
R+WC	RC	0.9	FALSE	0.9	FALSE
R+WC	WC	0.1535	FALSE	0.9	FALSE
RC	WC	0.0841	FALSE	0.9	FALSE

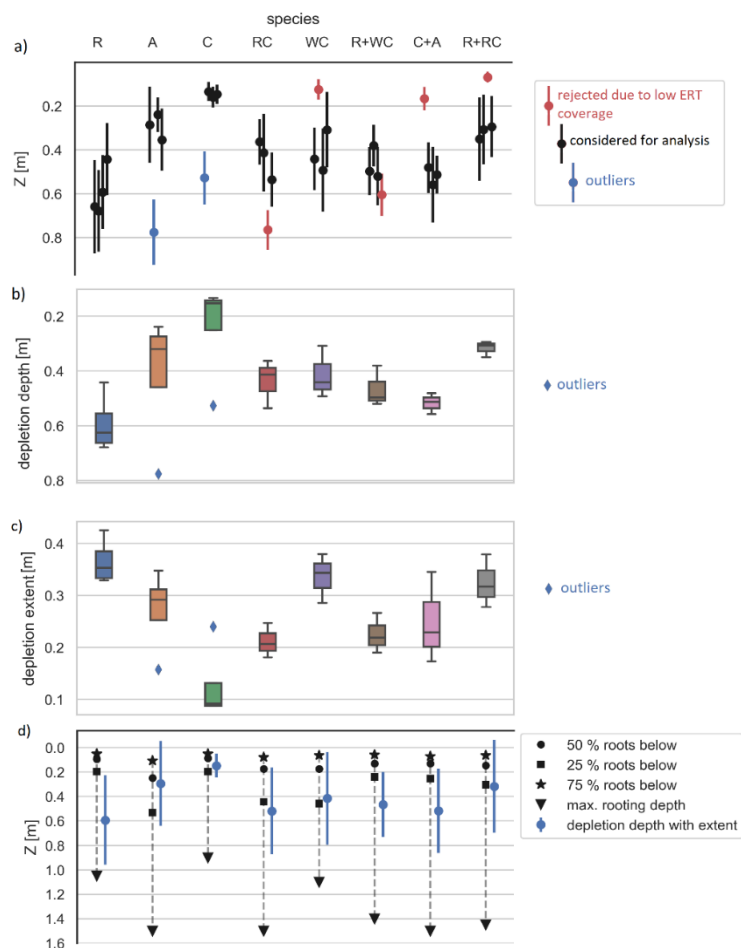


**Figure 6.7:** a) maximum depletion depth ( $\mu_{Z,\delta\theta}$  derived from Gaussian fit to negative changes of  $\delta\theta$ ) of a 1-D median of  $\delta\theta$  as a function of plant species and depletion extent ( $\sigma_{Z,\delta\theta}$  derived from Gaussian fit to negative changes of  $\delta\theta$ ) of a 1-D median of  $\delta\theta$  as a function of plant species. Box plot statistics of Gaussian fits: b) maximum depletion depth ( $\mu_{Z,\delta\theta}$  derived from Gaussian fit to changes of  $\delta\theta$ ) of a 1-D median of  $\delta\theta$  and c) depletion extent ( $\sigma_{Z,\delta\theta}$  derived from Gaussian fit to changes of  $\delta\theta$ ) of a 1-D median of  $\delta\theta$ . d) Percentile root profile for different species from soil trench data along with Gaussian fit parameters.

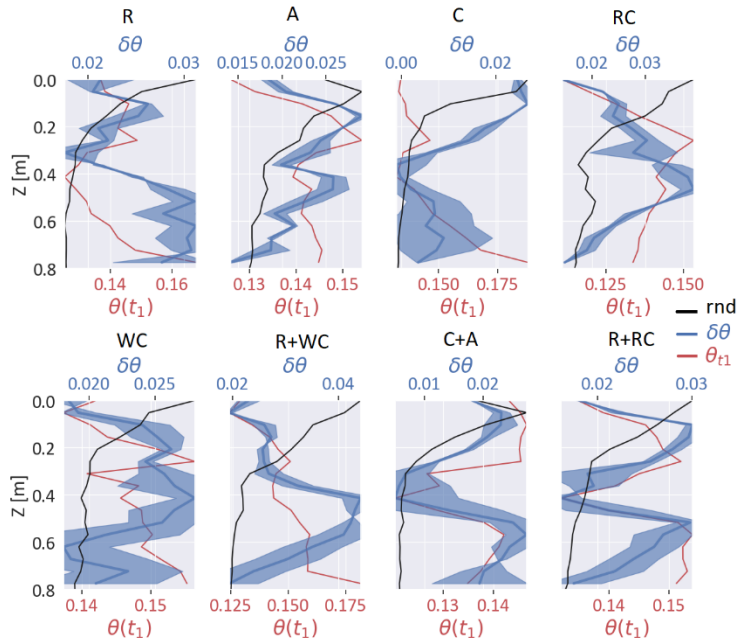


**Figure 6.8:** 1-D profile of  $\delta\theta$  in blue, normalized root number density ( $rnd$ ) in black normalized to min/max of the blue curve and water content at time 1 (red). The different plot indicates plant species.

In Figure 6.8, we compare 1-D median profile of temporal difference of water content ( $\delta\theta$ ) with water availability at initial time ( $\theta(t_1)$ ) and root distribution profiles. We observe that the depletion pattern (in blue) is affected by both water content distribution (water availability) and root length distribution (root conductance), as predicted by physically based uptake models (Javaux et al. 2008; Couvreur et al. 2013). In general, the maximum uptake is not located at the surface where most roots are but were the water availability is low due to the uptake from the beginning of the season. Most of the uptake takes place below 30 cm depth except for plants like Alfalfa A, ryegrass+red clover R+RC and cocksfoot C. We also observe striking differences of depletion patterns between species with similar root distribution profiles, like between rye grass (R) and cocksfoot (C). While rye

grass (R) seems to be able to extract deeper soil water, C only takes up surface water. This might be due to the role of root conductance's which allows rye grass (R) to be more efficient than cocksfoot (C). Interestingly, we observe multimodal (double-peak) uptake profiles for combination of species (C+A and R+RC), potentially showing a niche distribution of water uptake.

## 5.4 Summary and Conclusion

The aim of the study was to demonstrate that ERT was able to discriminate plant ability to extract water under water deficit conditions. For this, we extended the previous high resolution ERT study of Rao et al. (2020) to include 5 different herbaceous species and combinations of them, and check whether intra species water depletion variability was lower than differences between species.

One-dimensional profile of temporal changes of water content over 4 weeks ( $\delta\theta$ ) was fitted with Gaussian function to retrieve maximum depletion depths ( $\mu_{z,\delta\theta}$ ) and depletion zone extent ( $\sigma_{z,\delta\theta}$ ). Outliers in fitting parameters were removed based on ERT coverage and statistics. The filtered parameters showed good agreement within replicates and the differences between species was statistically significant ( $p < 0.001$ ).

Based on the Gaussian fit parameters, we conclude that Ryegrass (R) is an efficient species in terms of combatting water deficit soil conditions as compared to Cocksfoot (C) despite having similar root density profile. While Cocksfoot (C) has mostly shallow roots, alfalfa (A) has comparatively deeper roots and hence there is less competition for water when C+A is combined. Therefore, Cocksfoot when mixed with

alfalfa (C+A) performs better in terms of water depletion as compared to Cocksfoot (C) alone. This is in consistent with multimodal uptake patterns observed in C+A and yield analysis (Koch et al. unpublished) where mixed cultivation resulted in better yield compared to monocultures. From 1-D profiles of  $\theta(t_1)$ ,  $r_{nd}$  and  $\delta\theta$  indicates that uptake phenomenon in plants depends both on soil water availability and root density under drought condition.

## 5.5 Appendices

### Appendix A1: Coverage/ Sensitivity analysis

In Figure 6.9, we show the 2-D sensitivity or coverage of the ERT measurement scheme (after data filtering) as a function of plant species and replicates or blocks. Below 1m depth, the sensitivity is quite poor (red dashed line) and up to 80 cm sensitivity is quite good (above 1.5). For some plots as indicated by red rhombus in Figure 6.5, the sensitivity drops below 1.5 at depths as shallow as 50 cm due to fewer quadrupoles in the injection scheme and data filtering process.

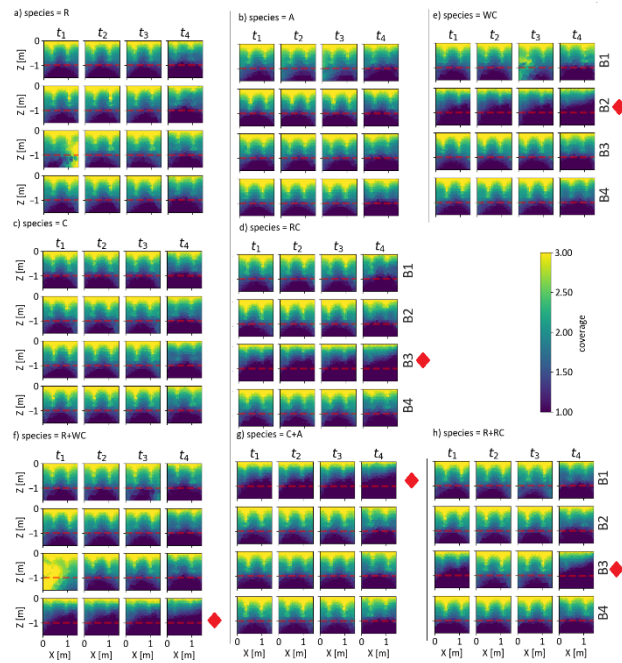


**Figure 6.9:** Spatial distribution of ERT injection scheme sensitivity or coverage map (after filtering) for different replicates or blocks within a species (rows) for: a) ryegrass (R), b) red clover (RC), c) alfalfa (A), d) cocksfoot (C), e) white clover (WC), f) ryegrass and white clover mixture (R+WC), g) cocksfoot and alfalfa mixture (C+A), h) ryegrass and red clover mixture (R+RC).

## Appendix A2: ERT Inversion parameters

**Table 6.4:** ERT inversion quality parameters (frms and chi<sup>2</sup>), no. of iterations in inversion, no. of quadrupoles in raw data (Nq<sub>raw</sub>), and in filtered data (Nq<sub>f</sub>) as a function of the block, panel and time.

lock	B	ime	T	anel	P	Plants	R	hi <sup>2</sup>	Iterations	N	q <sub>raw</sub>	q <sub>f</sub>
							rms		ns			
1	B	1	t		1	{C, R+WC, WC, R}	.67	1	4	054	3	617
1	B	1	t		2	{R+RC, A, RC, C+A}	.86	1	3	734	2	567
1	B	2	t		1	{C, R+WC, WC, R}	.75	1	5	054	3	617
1	B	2	t		2	{R+RC, A, RC, C+A}	.84	1	3	734	2	546
1	B	3	t		1	{C, R+WC, WC, R}	.71	1	4	054	3	645
1	B	3	t		2	{R+RC, A, RC, C+A}	.88	1	3	734	2	555
1	B	4	t		1	{C, R+WC, WC, R}	.78	1	4	051	2	60
1	B	4	t		2	{R+RC, A, RC, C+A}	.01	2	3	877	1	18
2	B	1	t		1	{A, R+RC, C+A, RC}	.98	1	3	054	3	956

	B	t			{R+WC, R, C, WC}	.01	2	.51	4	4	734	2	565
2	B	t		2	{A, R+RC, C+A, RC}	.00	2	.53	1	3	054	3	973
2	B	t		2	{R+WC, R, C, WC}	.01	2	.11	1	5	734	2	564
2	B	t		1	{A, R+RC, C+A, RC}	.96	1	.35	3	3	054	3	944
2	B	t		2	{R+WC, R, C, WC}	.02	2	.92	1	4	734	2	560
2	B	t		1	{A, R+RC, C+A, RC}	.90	1	.74	3	3	051	2	02
2	B	t		2	{R+WC, R, C, WC}	.04	2	.60	1	3	877	1	42
3	B	t		1	{C+A, R, R+WC, WC}	.66	1	.85	1	4	054	3	880
3	B	t		2	{C, R+RC, A, RC}	.94	1	.60	0	4	734	2	494
3	B	t		1	{C+A, R, R+WC, WC}	.72	1	.47	4	4	054	3	889
lock	B	T	P		Plants	rms	R	hi <sup>2</sup>		Iterations	N	q <sub>raw</sub>	q <sub>f</sub>
	ime	anel			{C, R+RC, A, RC}	.80	1	.32	4	5	734	2	614
3	B	t		1	{C+A, R, R+WC, WC}	.72	1	.69	4	4	054	3	899

3	B	3	t	2	{C, R+RC, A, RC}	.70	1	.09	4	734	2	635
3	B	4	t	1	{C+A, R, R+WC, WC}	.76	1	.19	3	051	2	20
3	B	4	t	2	{C, R+RC, A, RC}	.92	1	.44	3	877	1	84
4	B	1	t	1	{R+RC, C, RC, A}	.43	1	.50	3	054	3	914
4	B	1	t	2	{WC, R, C+A, R+WC}	.01	2	.78	3	734	2	586
4	B	2	t	1	{R+RC, C, RC, A}	.57	1	.23	4	054	3	946
4	B	2	t	2	{WC, R, C+A, R+WC}	.02	2	.77	3	734	2	605
4	B	3	t	1	{R+RC, C, RC, A}	.49	1	.57	3	054	3	954
4	B	3	t	2	{WC, R, C+A, R+WC}	.03	2	.04	4	734	2	622
4	B	4	t	1	{R+RC, C, RC, A}	.60	1	.63	3	051	2	13
4	B	4	t	2	{WC, R, C+A, R+WC}	.82	1	.08	3	877	1	40



## PART V

### CONCLUSION AND PERSPECTIVES



In this final section we will discuss the summary of the thesis, achievements, concluding remarks and future perspectives.

*Kadvamlalavayaistikspairdrayairatrtha  
secilailb  
Bhavanti pittajā rogā grīsmakāle ghanātpaye*

Vrikṣayurveda

Meaning: Diseases in plants occur in summer/ drought, and when the plants are watered with bitter, sour, strong and salty solutions

Vriksha Ayurveda







## 7 CONCLUSIONS AND PERSPECTIVES

Root zone monitoring is a crucial tool for developing more resilient and sustainable agriculture. Characterizing root functions *in situ* are instrumental to understand nutrient and water absorption by plants and to develop efficient and reliable field root phenotyping supports for crop breeding. Recently, electrical imaging of root zone soil has been gaining wide attention among agronomists and soil scientists (Zhao et al. 2019) because of its sensitivity to soil moisture and soil solution concentration, which are key elements for plant developments. However, a quantitative understanding of electrical signatures of roots in electrical imaging is still somewhat missing as described in Chapter 1.

Plant root systems have direct and indirect impacts on the electrical signature of vegetated soils. First, through its distinct electrical properties, roots directly affect the bulk electrical properties of the soil-root domain by its presence within the soil. Second, roots indirectly impact the electrical properties of soil through water depletion, nutrient uptake, and exudation, which all change the electrical signature of the soil/rhizosphere matrix. The main objective of this Ph.D. thesis was to quantify both the direct and indirect impact (with a focus on water) of the root system in geo-electric methods such as ERT or EIT.

A first emphasis of the thesis was put on understanding the impact of roots in small scale rhizotron and pots by numerical experiments. Chapter 3 dealt with quantifying the impact of roots on pedophysical relations while incorporating both direct (root explicit electrical properties) and indirect (root water uptake patterns) in the forward calculation. Thanks to a unique process-based soil-plant numerical model, we could

simulate the water uptake in a realistic way and improve thereby our understanding of electrical signatures of root systems in soils. While in Chapter 4, we proved that bulk electrical properties at pot scale (under realistic conditions) contains root geometrical information.

The second emphasis of the thesis was put on using ERT experiments to quantify plant root traits. We proposed a new methodology for quantifying root water uptake from a high-resolution ERT study on a field trial with 3 different herbaceous species and one mixture subject to two different treatments (control and water deficit) in Chapter 5. The methodology included numerical model to interpret field datasets in quantifying slight changes in water content due to root water uptake.

The summary of the thesis along with perspective is shown as a flowchart in Figure 7.1. The implication of first emphasis leads to development of bio-petrophysical relation while the second emphasis leads to novel root phenotyping indices via geo-electric method (Fig. 7.1).

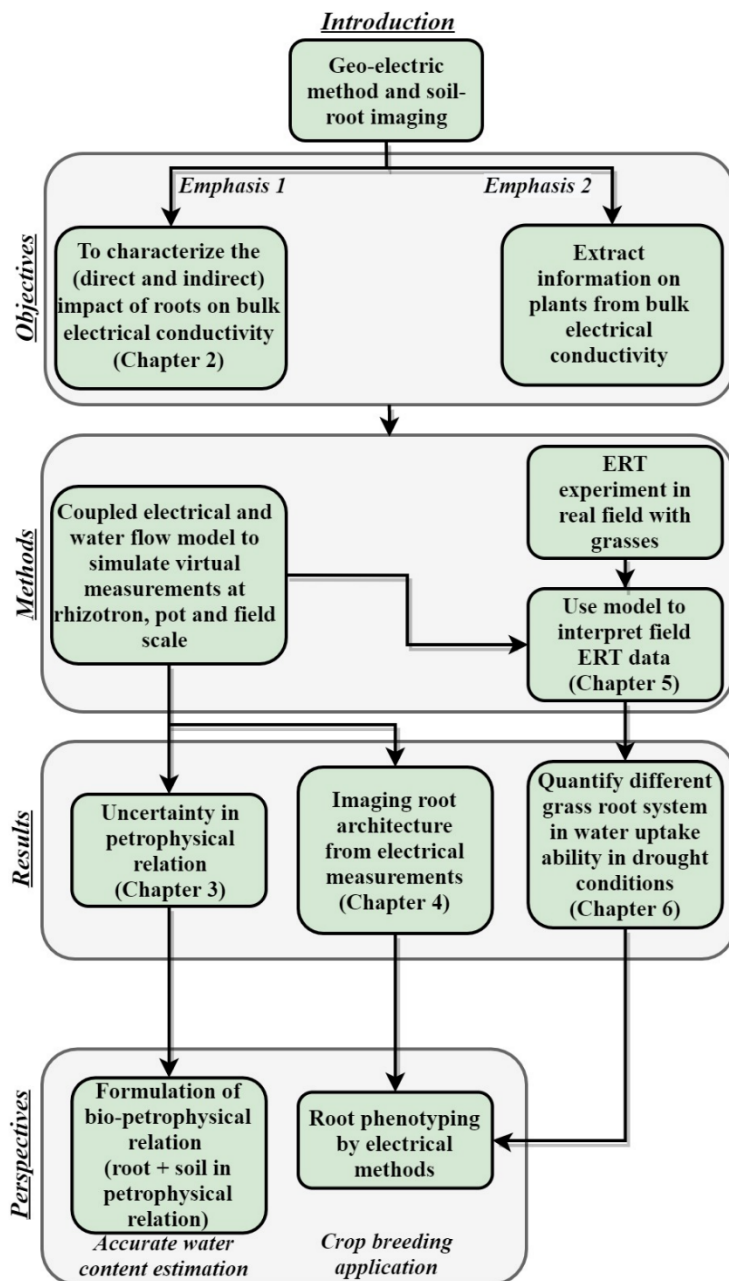


**Figure 7.1:** Flowchart for conclusion and perspective of the thesis

## **6.1 Bulk soil electrical properties vs root electrical properties**

Root electrical properties change with plant species, root type, and age. When roots invade soils, they affect the bulk soil electrical properties. Soil-root electrical contrast needs to be high enough to have a detectable root signature for root imaging applications using ERT/EIT. Our review in Chapter 2 shows that roots have good contrast with soils in magnitude part of conductivity below 15% of water content. Also we saw in Chapter 2 that compared to soils and earth materials, whose phase part of electrical conductivity (polarization) range from 0 to 20 milliradians (Vanhala and Soininen 1995; Vanderborght et al. 2013), root segment exhibits a very large phase or polarization signature (0.2 to 0.6 radians). Although roots possess stronger polarization response than soil, at higher soil water content, they become unobservable due to soil dominance in magnitude part (Mary et al. 2016). We hypothesize from the literature review of Chapter 2 that lower water content (around 15%) in soil should be better for root imaging although too low water content translates to very dry soil where electrode contact issues might arise.

Many studies reviewed in Chapter 2 show that root properties such as its mass can be derived from measuring electrical properties of a soil-root continuum such as electrical capacitance or resistivity. This also means roots can impact soil petrophysical relation leading to the wrong estimation of water content if they are no accounted for.

The numerical model can help us in understanding the impact of roots in electrical measurements. To quantify the electrical response of roots in soils, a widely used circuit model is inadequate in capturing the complex geometry of root architecture and its electrical connection to the soil matrix. Further, electrical measurements on root segments (Section 2.8) indicate

that electrical properties of roots are root type, species, age, and radius dependent. Thus, we concluded in Chapter 2 that process-based explicit modeling of root structures is important to quantify and understand the electrical response of roots in the soil.

Our next focus in Chapter 3 was to establish a process-based numerical model of a soil root continuum. For this, we had to couple of existing electrical flow and water flow models to simulate a growing and transpiring maize root system in a three-dimensional thin rhizotron and forward ERT measurements. This is the first attempt in the scientific community to rigorously model a growing root system aimed at evaluating the impact of roots on the effective electrical conductivity of the soil-continuum.

Thin rhizotron geometry allowed a higher density of roots within the soil medium maximizing root signatures and hence ideal condition to understand the impact of roots on petrophysical relations. Analysis of the  $\sigma$  distributions generated by simulated root water uptake and root system architecture showed a scale- and soil-dependent impact on the apparent petrophysical relationships. The uncertainty in the petrophysical relation of  $\sim 0.01 \text{ S m}^{-1}$  predicted by the model has also been observed in some field ERT studies (Garré et al. 2011; Beff et al. 2013). In addition to measurement errors under field conditions, analysis of the  $\sigma$  distributions generated by simulated root water uptake and root system architecture shows that the presence of root segments might also be an additional reason why ERT-obtained petrophysical data sometimes have an uncertain spread around Archie's curve.

Even though we find that root water uptake has the main influence on effective electrical properties of soil, our 3-D ERT forward modeling demonstrated that for every 1% increase in root to sand volume ratio, there can be 13 % increase in uncertainty of effective electrical conductivity. This uncertainty is caused by

the presence of root segments while such uncertainty in loam medium is 0.7%. Understanding uncertainty in forward measurements is important as they can get amplified in the ERT inversion due to the ill-posed nature of the inverse problem. Hence quantification of forward uncertainty is important for estimation of uncertainty in ERT inversion. Further, we showed that root signatures in ERT measurements are stimulation scheme dependent with some quadrupoles being more sensitive to roots than others. To minimize the impact of roots on ERT measurements, we must carefully choose the stimulation scheme such that it gives the lowest root signature but they also mean lower sensitivity in the root region. However, for root imaging applications, we must choose quadrupoles that are most sensitive to root presence. Hence our model can serve as a tool for root imaging community for optimization of measurement scheme. Another interesting observation made in Chapter 3 was macroscopic electrical anisotropy observed in effective electrical conductivity in vertical and horizontal directions. This observation led us to the work of Chapter 4 where we investigated anisotropy of different root architectures to great detail using a similar modeling approach of Chapter 3.

In Chapter 4, we tested the hypothesis that the frequency-dependent electrical signature of a vegetated soil pot is a function of the root system architecture and that electrical anisotropy was an appropriate index to capture root difference in topology. In terms of methodology, we extended the work of Chapter 3 by working on 3-D pots rather than in thin rhizotron and by including polarization aspects. To quantify the differences in terms of root topology and geometry between root systems of different species, we established geometrical indices. For the first time, we show that the magnitude and phase part of electrical anisotropy ( $\xi$  and  $\delta\varphi$ ) are highly correlated to various geometrical indices of root systems with the correlation coefficient as high as 0.9. Within the scope of the

simulations run in Chapter 4, we conclude that electrical anisotropy ( $\delta\varphi$  and  $\xi$ ) is a very promising proxy for imaging root topology that can be measured non-invasively.

## 6.2 Root properties

Root water uptake is not the only function of root system architecture and soil water availability, but also of root hydraulics (Leitner et al. 2014; Meunier et al. 2017). Hence, the dynamics of root water uptake is an indirect way of measuring plant functioning, in particular under drought. Since changes in water content due to root water uptake translates to changes in electrical properties of soil, Electrical Resistivity Tomography (ERT) is well suited to monitor soil water content evolution and thus soil water depletion patterns *in situ*.

In chapter 5, we propose a new methodology for quantifying root functioning from a high-resolution ERT study on an intercropped field trial with 3 different herbaceous species and one mixture subject to two different treatments (control and water deficit). The main aim of the study was to image the drought response and investigate the sensitivity of ERT in capturing root water uptake variability between species. For this purpose, we also conducted a mechanistic synthetic study that mimicked the actual experimental conditions. The synthetic and field studies showed that differences between plant uptake dynamics could better be characterized in water deficit conditions. Hence, plant phenotyping with ERT should ideally be realized under water deficit conditions. Also, changes in water content could be used as root phenotyping parameters in quantifying the water uptake ability of a plant in drought conditions.

In chapter 6, we used the methodology developed in chapter 5 to systematically analyze the response to the drought of 6 different crop forage species and their combinations in water deficit conditions. We analyzed the results of a 2-D ERT temporal dataset in an agronomic field trial comparing the combination of forage crop species. The ERT derived changes in water content were fitted with Gaussian function to retrieve maximum depletion depths and depletion zone extent. The fitted parameters showed good agreement within replicates and the differences between inter-species were statistically significant ( $p < 0.001$ ).

We found Ryegrass (R) to be an efficient species in terms of combatting water deficit soil conditions as compared to Cocksfoot (C) despite having similar root density profile. Cocksfoot when mixed with alfalfa (C+A) performs better in terms of water depletion as compared to Cocksfoot (C) alone. This is consistent with yield analysis (Koch et al., unpublished) where mixed cultivation resulted in better yield compared to monocultures. From 1-D profiles of initial water content, root density and evolution of water depletion indicate that uptake phenomenon in plants depends both on soil water availability and root density under water-limited condition. Thus, it is possible to compare species and perform root phenotyping using the method proposed in Chapter 6.

### 6.3 Perspectives

Due to the complexity of the root system architecture (RSA) embedded in the soil matrix, upscaling electrical properties measured at root segment scale to plant scale or to field scale is a challenging task (Mary et al. 2016; Weigand and Kemna 2017). Process-based multi-scale numerical modeling of a soil root continuum that we achieved in Chapter 3 and 4 upscales electrical properties from the root segment to a single plant scale

(rhizotron and pot). However, to further move from plant to field scale, explicitly representing root architecture (as in Chapter 3 or 4) in the computational domain demands a very high spatial resolution in the numerical grid, thus increasing computational time and memory consumption. Further research on upscaling mechanistic models of Chapter 3 to field-scale without explicit root representation is required. For instance, one subdomain in the field scale model could derive its electrical properties from plant scale models of Chapter 4 eliminating the need for field-scale explicit root representation. The development of such a field-scale soil-root model will pave the way towards the development of bio-petrophysical relation in the rooted soil that takes root morphological features and its electrical properties into account. Such field-scale models will also help in understanding the electrical response of roots and optimizing geo-electric measurement scheme for maximizing root signatures. Further, the experimental validation of numerical results observed in Chapters 3 and 4 is yet to be achieved and hence the next step would be to perform several rhizotron and pot experiments to validate the model in terms of electrical response. Such experimental validation in rhizotron or pot scale will shed light on the importance of ignored parameters in the model such as soil cracks, root exudation, rhizosphere specific electrical properties, swelling and shrinking of roots leading to air gaps, and bad electrode contacts. We hypothesize that phenomena such as air gaps due to swelling and shrinking of roots will strongly influence the electrical signature by causing macroscopic anisotropy and provide an avenue to study gap dynamics around roots using the approach of Chapter 4 experimentally. Studying gap dynamics is important in terms of nutrient and water uptake in roots. The experimental extensions of ideas developed in Chapter 4 however require the design of suitable non-polarizing electrodes (Schwartz and Furman 2014) capable of measuring effective properties in at least two different directions and at low and high frequency.

The work contained in Chapters 5 and 6 could be extended to include EIT or polarization measurement at the field scale. Such an extension could allow us to differentiate root response from soil response at the field scale. Further, a machine learning algorithm should be used to extract plant-specific signatures in field data which could be more complex than just Gaussian fit parameters as characterized in Chapters 5 and 6. Although, we got some success in using the K-nearest neighbor algorithm in Chapter 4 in classifying different root architecture, extending it to a real field-scale experiment is a very important logical extension.

## GENERAL BIBLIOGRAPHY

- (1) Ackerson JP (2013) Monitoring Cracking of a Smectitic Vertisol using Three-dimensional Electrical Resistivity Tomography (cit. on p. 40).
- (2) Adler A, Lionheart WRB (2006a) Uses and abuses of EIDORS: an extensible software base for EIT. Physiological Measurement 27:S25 (cit. on pp. 66, 89).
- (3) Adler A, Lionheart WRB (2006b) Uses and abuses of EIDORS: an extensible software base for EIT. Physiol Meas 27:S25. DOI: 10.1088/0967-3334/27/5/S03 (cit. on p. 101).
- (4) Ahmed MA, Zarebanadkouki M, Meunier F, et al (2018) Root type matters: measurement of water uptake by seminal, crown, and lateral roots in maize. J Exp Bot 69:1199–1206. DOI: 10.1093/jxb/erx439 (cit. on p. 57).
- (5) Al Hagrey SA (2007) Geophysical imaging of root-zone, trunk, and moisture heterogeneity. Journal of Experimental Botany 58:839–854. <https://doi.org/10.1093/jxb/erl237> (cit. on pp. 40, 57).
- (6) Al Hagrey SA, Petersen T (2011) Numerical and experimental mapping of small root zones using optimized surface and borehole resistivity tomography. Geophysics 76:G25–G35. DOI: 10.1190/1.3545067 (cit. on p. 57).
- (7) Al-Hazaimay S, Huisman JA, Zimmermann E, Vereecken H (2016) Using electrical anisotropy for structural characterization of sediments: an

experimental validation study. *Near Surface Geophysics* 14:357–369 (cit. on p. 112).

- (8) Allred B, Daniels JJ, Ehsani MR (2008) *Handbook of agricultural geophysics*. CRC Press (cit. on p. 9).
- (9) Amato M, Basso B, Celano G, et al (2008a) In situ detection of tree root distribution and biomass by multi-electrode resistivity imaging. *Tree Physiol* 28:1441–1448 (cit. on pp. 10, 11, 24, 35, 36).
- (10) Amato M, Basso B, Celano G, et al (2008b) In situ detection of tree root distribution and biomass by multi-electrode resistivity imaging. *Tree Physiol* 28:1441–1448 (cit. on pp. 10, 35, 36, 120).
- (11) Amato M, Bitella G, Rossi R, et al (2009a) Multi-electrode 3-D resistivity imaging of alfalfa root zone. *European Journal of Agronomy* 31:213–222. DOI: 10.1016/j.eja.2009.08.005 (cit. on pp. 24, 35, 36, 57).
- (12) Amato M, Bitella G, Rossi R, et al (2009b) Multi-electrode 3-D resistivity imaging of alfalfa root zone. *European Journal of Agronomy* 31:213–222 (cit. on pp. 24, 35, 36, 119).
- (13) Anderson WP, Higinbotham N (1976a) Electrical resistances of corn root segments. *Plant physiology* 57:137–141 (cit. on pp. 27, 30, 31, 33, 46, 56).
- (14) Anderson WP, Higinbotham N (1976b) Electrical Resistances of Corn Root Segments. *Plant Physiology* 57:137–141 (cit. on pp. 31, 33, 46, 56).
- (15) André F, van Leeuwen C, Saussez S, et al (2012) High-resolution imaging of a vineyard in south of France using ground-penetrating radar, electromagnetic induction and electrical resistivity tomography. *Journal of Applied Geophysics* 78:113–122. DOI: 10.1016/j.jappgeo.2011.08.002 (cit. on p. 11).

- (16) Andrenelli MC, Magini S, Pellegrini S, et al (2013) The use of the ARP© system to reduce the costs of soil survey for precision viticulture. *Journal of Applied Geophysics* 99:24–34 (cit. on p. 9).
- (17) Archie GE (1942) The electrical resistivity log as an aid in determining some reservoir characteristics. *Transactions of the AIME* 146:54–62 (cit. on p. 39).
- (18) Atkinson JA, Pound MP, Bennett MJ, Wells DM (2019a) Uncovering the hidden half of plants using new advances in root phenotyping. *Current Opinion in Biotechnology* 55:1–8. DOI: 10.1016/j.copbio.2018.06.002 (cit. on p. 13).
- (19) Atkinson JA, Pound MP, Bennett MJ, Wells DM (2019b) Uncovering the hidden half of plants using new advances in root phenotyping. *Current Opinion in Biotechnology* 55:1–8. DOI: 10.1016/j.copbio.2018.06.002 (cit. on p. 119).
- (20) Aubrecht L, Staněk Z, Koller J (2006) Electrical measurement of the absorption surfaces of tree roots by the earth impedance method: 1. Theory. *Tree Physiology* 26:1105–1112 (cit. on pp. 30, 33, 41).
- (21) Bai G, Ge Y, Hussain W, et al (2016) A multi-sensor system for high throughput field phenotyping in soybean and wheat breeding. *Computers and Electronics in Agriculture* 128:181–192. DOI: 10.1016/j.compag.2016.08.021 (cit. on p. 13).
- (22) Bauke SL, Landl M, Koch M, et al (2017) Macropore effects on phosphorus acquisition by wheat roots – a rhizotron study. *Plant Soil* 416:67–82. DOI: 10.1007/s11104-017-3194-0 (cit. on p. 57).
- (23) Beff L, Günther T, Vandoorne B, et al (2013a) Three-dimensional monitoring of soil water content in a maize field using Electrical Resistivity Tomography. *Hydrology and Earth System Sciences* 17:595–609.

DOI: 10.5194/hess-17-595-2013 (cit. on pp. 10, 11, 36, 40, 72, 83, 84, 120, 123, 141, 154, 156, 177).

- (24) Beff L, Günther T, Vandoorne B, et al (2013b) Three-dimensional monitoring of soil water content in a maize field using Electrical Resistivity Tomography. *Hydrol Earth Syst Sci* 17:595–609. DOI: 10.5194/hess-17-595-2013 (cit. on pp. 10, 11, 56, 72, 83, 84, 123, 154, 156, 177).
- (25) Beff L, Günther T, Vandoorne B, et al (2013c) Three-dimensional monitoring of soil water content in a maize field using Electrical Resistivity Tomography. *Hydrology and Earth System Sciences* 17:595–609. DOI: 10.5194/hess-17-595-2013 (cit. on pp. 10, 11, 72, 77, 83, 84, 123, 153, 154, 156).
- (26) Behrens HM, Gradmann D (1985) Electrical properties of the vertically growing root tip of *Lepidium sativum* L. *Planta* 163:453–462 (cit. on p. 31).
- (27) Bera TK, Bera S, Kar K, Mondal S (2016) Studying the variations of complex electrical bio-impedance of plant tissues during boiling. *Procedia Technology* 23:248–255 (cit. on p. 28).
- (28) Bergmann P, Schmidt-Hattenberger C, Labitzke T, et al (2017) Fluid injection monitoring using electrical resistivity tomography—five years of CO<sub>2</sub> injection at Ketzin, Germany. *Geophysical Prospecting* 65:859–875 (cit. on p. 125).
- (29) Besson A, Cousin I, Samouëlian A, et al (2004) Structural heterogeneity of the soil tilled layer as characterized by 2-D electrical resistivity surveying. *Soil and Tillage Research* 79:239–249 (cit. on p. 9).
- (30) Bezerra-Coelho CR, Zhuang L, Barbosa MC, et al (2018) Further tests of the HYPROP evaporation method for estimating the unsaturated soil hydraulic properties. *Journal of Hydrology and Hydromechanics* 66:161–169 (cit. on p. 121).

- (31) Binley A, Kemna A (2005) DC resistivity and induced polarization methods. In: Hydrogeophysics. Springer, pp 129–156 (cit. on pp. 37, 38).
- (32) Bodner G, Leitner D, Kaul H-P (2014) Coarse and fine root plants affect pore size distributions differently. *Plant and soil* 380:133–151 (cit. on p. 41).
- (33) Bouda M, Caplan JS, Saiers JE (2016) Box-Counting Dimension Revisited: Presenting an Efficient Method of Minimizing Quantization Error and an Assessment of the Self-Similarity of Structural Root Systems. *Frontiers in Plant Science* 7:149. DOI: 10.3389/fpls.2016.00149 (cit. on pp. 88, 96, 112).
- (34) Brillante L, Bois B, Lévêque J, Mathieu O (2016) Variations in soil-water use by grapevine according to plant water status and soil physical-chemical characteristics-A 3-D spatio-temporal analysis. *European Journal of Agronomy* 77:122–135. DOI: 10.1016/j.eja.2016.04.004 (cit. on p. 56).
- (35) Brovelli A, Cassiani G (2011) Combined estimation of effective electrical conductivity and permittivity for soil monitoring. *Water Resour Res* 47:W08510. DOI: 10.1029/2011WR010487 (cit. on p. 62).
- (36) Bruce WB, Edmeades GO, Barker TC (2002) Molecular and physiological approaches to maize improvement for drought tolerance. *Journal of experimental botany* 53:13–25 (cit. on pp. 8, 87).
- (37) Cai G, Vanderborght J, Klotzsche A, et al (2016) Construction of Minirhizotron Facilities for Investigating Root Zone Processes. *Vadose Zone Journal* 15:. DOI: 10.2136/vzj2016.05.0043 (cit. on p. 8).
- (38) Cairns JE, Sanchez C, Vargas M, et al (2012) Dissecting maize productivity: ideotypes associated with grain yield under drought stress and well-watered

conditions. *J Integr Plant Biol* 54:1007–1020. DOI: 10.1111/j.1744-7909.2012.01156.x (cit. on p. 8).

- (39) Cao Y, Repo T, Silvennoinen R, et al (2010) Analysis of the willow root system by electrical impedance spectroscopy. *Journal of experimental botany* 62:351–358 (cit. on pp. 31, 33, 45, 46, 47, 56).
- (40) Carminati A, Vetterlein D, Weller U, et al (2009) When Roots Lose Contact. *Vadose Zone Journal* 8:805–809. DOI: 10.2136/vzj2008.0147 (cit. on pp. 41, 83).
- (41) Carsel RF, Parrish RS (1988) Developing joint probability distributions of soil water retention characteristics. *Water resources research* 24:755–769 (cit. on p. 60).
- (42) Chen B, Garré S, Liu H, et al (2019) Two-dimensional monitoring of soil water content in fields with plastic mulching using electrical resistivity tomography. *Computers and Electronics in Agriculture* 159:84–91 (cit. on p. 40).
- (43) Chloupek O (1972) The relationship between electric capacitance and some other parameters of plant roots. *Biologia Plantarum* 14:227–230 (cit. on pp. 34, 35).
- (44) Chloupek O (1977) Evaluation of the size of a plant's root system using its electrical capacitance. *Plant and Soil* 48:525–532 (cit. on p. 34).
- (45) Chowdhury S (2011) Employment in India: What does the latest data show? *Economic and political weekly* 46:23–26 (cit. on p. 5).
- (46) Cimpoiaşu MO, Kuras O, Pridmore T, Mooney SJ (2020) Potential of geoelectrical methods to monitor root zone processes and structure: A review. *Geoderma* 365:114232 (cit. on p. 9).
- (47) Corona-Lopez DD, Sommer S, Rolfe SA, et al (2019a) Electrical impedance tomography as a tool for

phenotyping plant roots. *Plant methods* 15:49 (cit. on p. 13).

- (48) Corona-Lopez DD, Sommer S, Rolfe SA, et al (2019b) Electrical impedance tomography as a tool for phenotyping plant roots. *Plant methods* 15:49 (cit. on p. 120).
- (49) Corwin DL, Lesch SM (2005) Apparent soil electrical conductivity measurements in agriculture. *Computers and electronics in agriculture* 46:11–43 (cit. on p. 11).
- (50) Costa C, Schurr U, Loreto F, et al (2019) Plant phenotyping research trends, a science mapping approach. *Frontiers in plant science* 9:1933 (cit. on p. 5).
- (51) Couvreur V, Vanderborght J, Javaux M (2012a) A simple three-dimensional macroscopic root water uptake model based on the hydraulic architecture approach. *Hydrol Earth Syst Sci* 16:2957–2971. DOI: 10.5194/hess-16-2957-2012 (cit. on pp. 60, 128, 164).
- (52) Couvreur V, Vanderborght J, Javaux M (2012b) A simple three-dimensional macroscopic root water uptake model based on the hydraulic architecture approach. *Hydrology & Earth System Sciences* 16: (cit. on pp. 128, 164).
- (53) Dahlin T, Aronsson P, Thörnelöf M (2014) Soil resistivity monitoring of an irrigation experiment. *Near Surface Geophysics* 12:35–44 (cit. on p. 120).
- (54) Dahlin T, Zhou B (2006) Multiple-gradient array measurements for multichannel 2-D resistivity imaging. *Near Surface Geophysics* 4:113–123 (cit. on p. 124).
- (55) Dainty J, Hope AB (1959) Ionic Relations of Cells of *Ohara Australis* I. Ion Exchange in the Cell Wall. *Australian Journal of Biological Sciences* 12:395–411 (cit. on pp. 31, 33).

- (56) Dalton FN (1995) In-situ root extent measurements by electrical capacitance methods. *Plant and soil* 173:157–165 (cit. on pp. 33, 44).
- (57) De Carlo L, Battilani A, Solimando D, et al (2015) Monitoring different irrigation strategies using surface ERT. pp 71–75 (cit. on p.56 ).
- (58) de Dorlodot S, Forster B, Pagès L, et al (2007) Root system architecture: opportunities and constraints for genetic improvement of crops. *Trends in Plant Science* 12:474–481. DOI: 10.1016/j.tplants.2007.08.012 (cit. on p. 56).
- (59) Dickin E, Wright D (2008) The effects of winter waterlogging and summer drought on the growth and yield of winter wheat (*Triticum aestivum* L.). *European Journal of Agronomy* 28:234–244 (cit. on p. 149).
- (60) Doussan C, Pierret A, Garrigues E, Pagès L (2006) Water Uptake by Plant Roots: II – Modelling of Water Transfer in the Soil Root-system with Explicit Account of Flow within the Root System – Comparison with Experiments. *Plant Soil* 283:99–117. DOI: 10.1007/s11104-004-7904-z (cit. on p. 60).
- (61) Dvořák M, Černohorská J, Janáček K (1981) Characteristics of current passage through plant tissue. *Biologia Plantarum* 23:306 (cit. on p. 25).
- (62) Eghball B, Settimi JR, Maranville JW, Parkhurst AM (1993) Fractal analysis for morphological description of corn roots under nitrogen stress. *Agronomy Journal* 85:287–289 (cit. on p. 88).
- (63) Ehsoioke S, Sarah Garré, Kremer T, et al (2018) A New Method For Characterizing The Complex Electrical Properties of Root Segments. conference paper, 10th Symposium of the International Society of Root Research,July 2018, Israel (cit. on pp. 31, 45).

- (64) Ergon Å, Seddaiu G, Korhonen P, et al (2018) How can forage production in Nordic and Mediterranean Europe adapt to the challenges and opportunities arising from climate change? *European Journal of Agronomy* 92:97–106 (cit. on p. 149).
- (65) Evans LT, Evans LT, Evans LT (1998) Feeding the ten billion: plants and population growth. Cambridge University Press (cit. on p. 7).
- (66) Fahlgren N, Gehan MA, Baxter I (2015) Lights, camera, action: high-throughput plant phenotyping is ready for a close-up. *Current Opinion in Plant Biology* 24:93–99. DOI: 10.1016/j.pbi.2015.02.006 (cit. on p. 13).
- (67) Faurès J-M, Hoogeveen J, Bruinsma J (2002) The FAO irrigated area forecast for 2030. FAO, Rome, Italy (cit. on p. 6).
- (68) Fensom DS (1966) On measuring electrical resistance in situ in higher plants. *Canadian Journal of Plant Science* 46:169–175 (cit. on pp. 30, 33).
- (69) Fensom DS (1960) A note on electrical resistance measurements in *Acer saccharum*. *Canadian Journal of Botany* 38:263–265 (cit. on p. 31).
- (70) Fensom DS, Meylan S, Pilet P-E (1965) Induced electro-osmosis in root tissues. *Canadian Journal of Botany* 43:453–467 (cit. on p. 31).
- (71) Friedman SP (2005a) Soil properties influencing apparent electrical conductivity: a review. *Computers and Electronics in Agriculture* 46:45–70. DOI: 10.1016/j.compag.2004.11.001 (cit. on pp. 24, 39, 41, 56).
- (72) Friedman SP (2005b) Soil properties influencing apparent electrical conductivity: a review. *Computers and electronics in agriculture* 46:45–70 (cit. on pp. 24, 39, 41, 56).

- (73) Gadgil S, Kumar KR (2006) The Asian monsoon—agriculture and economy. In: The Asian Monsoon. Springer, pp 651–683 (cit. on p. 6).
- (74) Gao Y, Duan A, Qiu X, et al (2010) Distribution of roots and root length density in a maize/soybean strip intercropping system. Agricultural Water Management 98:199–212. DOI: 10.1016/j.agwat.2010.08.021 (cit. on p. 60).
- (75) Garré S, Coteur I, Wongleecharoen C, et al (2013a) Noninvasive Monitoring of Soil Water Dynamics in Mixed Cropping Systems: A Case Study in Ratchaburi Province, Thailand. Vadose Zone Journal 12:. DOI: 10.2136/vzj2012.0129 (cit. on pp. 14, 40, 120).
- (76) Garré S, Coteur I, Wongleecharoen C, et al (2013b) Noninvasive Monitoring of Soil Water Dynamics in Mixed Cropping Systems: A Case Study in Ratchaburi Province, Thailand. Vadose Zone Journal 12:. DOI: 10.2136/vzj2012.0129 (cit. on pp. 14, 120).
- (77) Garré S, Coteur I, Wongleecharoen C, et al (2013c) Can we use electrical resistivity tomography to measure root zone dynamics in fields with multiple crops? Procedia Environmental Sciences 19:403–410 (cit. on p. 36).
- (78) Garré S, Coteur I, Wongleecharoen C, et al (2012) Can we use Electrical Resistivity Tomography to measure root zone moisture dynamics in fields with multiple crops? In: AGU Fall Meeting Abstracts (cit. on pp. 10, 11, 72, 84, 177).
- (79) Garré S, Javaux M, Vanderborght J, et al (2011a) Three-Dimensional Electrical Resistivity Tomography to Monitor Root Zone Water Dynamics. Vadose Zone Journal 10:412–424. DOI: 10.2136/vzj2010.0079 (cit. on pp. 10, 11, 72, 84, 120, 177).
- (80) Garré S, Javaux M, Vanderborght J, et al (2011b) Three-Dimensional Electrical Resistivity Tomography

to Monitor Root Zone Water Dynamics. *Vadose Zone Journal* 10:412–424. DOI: 10.2136/vzj2010.0079 (cit. on pp. 10, 11, 56, 72, 84, 177).

- (81) Garré S, Javaux M, Vanderborght J, et al (2011c) Three-Dimensional Electrical Resistivity Tomography to Monitor Root Zone Water Dynamics. *Vadose Zone Journal* 10:412–424. DOI: 10.2136/vzj2010.0079 (cit. on p. 9).
- (82) Garrigues E, Doussan C, Pierret A (2006a) Water Uptake by Plant Roots: I – Formation and Propagation of a Water Extraction Front in Mature Root Systems as Evidenced by 2-D Light Transmission Imaging. *Plant and Soil* 283:83. DOI: 10.1007/s11104-004-7903-0 (cit. on pp. 9, 57).
- (83) Garrigues E, Doussan C, Pierret A (2006b) Water Uptake by Plant Roots: I – Formation and Propagation of a Water Extraction Front in Mature Root Systems as Evidenced by 2-D Light Transmission Imaging. *Plant Soil* 283:83. DOI: 10.1007/s11104-004-7903-0 (cit. on p. 63).
- (84) Geuzaine C, Remacle J-F (2009a) Gmsh: A 3-D finite element mesh generator with built-in pre- and post-processing facilities. *International Journal for Numerical Methods in Engineering* 79:1309–1331. DOI: 10.1002/nme.2579 (cit. on p. 99).
- (85) Geuzaine C, Remacle J-F (2009b) Gmsh: A 3-D finite element mesh generator with built-in pre- and post-processing facilities. *International Journal for Numerical Methods in Engineering* 79:1309–1331. DOI: 10.1002/nme.2579 (cit. on p. 149).
- (86) Gilgen AK, Buchmann N (2009) Response of temperate grasslands at different altitudes to simulated summer drought differed but scaled with annual precipitation. *Biogeosciences Discussions* 6:5217–5250 (cit. on p. 33).

- (87) Ginsburg H, Laties GG (1973) Longitudinal electrical resistance of maize roots. *Journal of Experimental Botany* 24:1035–1040 (cit. on p. 30).
- (88) Glerum C (1969) The influence of temperature on the electrical impedance of woody tissue. Oxford University Press (cit. on p. 149).
- (89) Golzarian MR, Frick RA, Rajendran K, et al (2011) Accurate inference of shoot biomass from high-throughput images of cereal plants. *Plant Methods* 7:2. DOI: 10.1186/1746-4811-7-2 (cit. on p. 149).
- (90) Gora EM, Yanoviak SP (2014) Electrical properties of temperate forest trees: a review and quantitative comparison with vines. *Canadian Journal of Forest Research* 45:236–245 (cit. on pp. 25, 31).
- (91) Grift TE, Novais J, Bohn M (2011) High-throughput phenotyping technology for maize roots. *Biosystems Engineering* 110:40–48. DOI: 10.1016/j.biosystemseng.2011.06.004 (cit. on pp. 87, 187).
- (92) Grisso R, Alley M, Holshouser D, Thomason W (2009) Precision Farming Tools: Soil Electrical Conductivity. Virginia Cooperative Extension 442–508: (cit. on p. 10).
- (93) Günther T, Rücker C (2006) A general approach for introducing information into inversion and examples from dc resistivity inversion. In: Near Surface 2006-12th EAGE European Meeting of Environmental and Engineering Geophysics. European Association of Geoscientists & Engineers, p cp-14-00060 (cit. on p. 126).
- (94) Günther T, Rücker C, Spitzer K (2006a) Three-dimensional modelling and inversion of DC resistivity data incorporating topography—II. Inversion. *Geophysical Journal International* 166:506–517 (cit. on p. 76).

- (95) Günther T, Rücker C, Spitzer K (2006b) Three-dimensional modelling and inversion of DC resistivity data incorporating topography—II. Inversion. *Geophysical Journal International* 166:506–517 (cit. on p. 153).
- (96) Haddad NM, Tilman D, Knops JM (2002) Long-term oscillations in grassland productivity induced by drought. *Ecology Letters* 5:110–120 (cit. on p. 149).
- (97) Hammer GL, Dong Z, McLean G, et al (2009) Can changes in canopy and/or root system architecture explain historical maize yield trends in the US corn belt? *Crop Science* 49:299–312 (cit. on p. 8).
- (98) Hanke M, Harrach B, Hyvönen N (2011) Justification of point electrode models in electrical impedance tomography. *Math Models Methods Appl Sci* 21:1395–1413. DOI: 10.1142/S0218202511005362 (cit. on p. 67).
- (99) Hanna M, Janne K, Perttu V, Helena K (2018) Gaps in the capacity of modern forage crops to adapt to the changing climate in northern Europe. *Mitigation and adaptation strategies for global change* 23:81–100 (cit. on p. 149).
- (100) Hansen PC (1992) Analysis of discrete ill-posed problems by means of the L-curve. *SIAM review* 34:561–580 (cit. on p. 125).
- (101) Harold K (2015) Population, Resources and Food Production. GMO School (cit. on pp. 5 , 6, 7).
- (102) Hayden RI, Moyse CA, Calder FW, et al (1969) Electrical impedance studies on potato and alfalfa tissue. *Journal of Experimental Botany* 20:177–200 (cit. on p. 31).
- (103) Hill HJ, Milburn JD (1956) Effect of clay and water salinity on electrochemical behavior of reservoir rocks (cit. on p. 40).

- (104) Holtham DA, Matthews GP, Scholefield DS (2007) Measurement and simulation of void structure and hydraulic changes caused by root-induced soil structuring under white clover compared to ryegrass. *Geoderma* 142:142–151 (cit. on p. 41).
- (105) Hoogenboom G, Huck MG, Peterson CM (1987) Root growth rate of soybean as affected by drought stress 1. *Agronomy Journal* 79:607–614 (cit. on p. 149).
- (106) Hopkins A, Del Prado A (2007) Implications of climate change for grassland in Europe: impacts, adaptations and mitigation options: a review. *Grass and Forage Science* 62:118–126 (cit. on p. 149).
- (107) Hopmans JW, Bristow KL (2002) Current capabilities and future needs of root water and nutrient uptake modeling. In: *Advances in agronomy*. Elsevier, pp 103–183 (cit. on p. 61).
- (108) Huisman JA, Lin CP, Weihermüller L, Vereecken H (2008) Accuracy of bulk electrical conductivity measurements with time domain reflectometry. *Vadose Zone Journal* 7:426–433 (cit. on p. 155).
- (109) Huisman JA, Snepvangers J, Bouting W, Heuvelink GBM (2002) Mapping spatial variation in surface soil water content: comparison of ground-penetrating radar and time domain reflectometry. *Journal of Hydrology* 269:194–207 (cit. on p. 9).
- (110) Iguldun JR, Streck DA, Pender JW (1989) Smart irrigation sprinklers. Google Patents (cit. on p. 9).
- (111) Javaux M, Couvreur V, Vanderborght J, Vereecken H (2013) Root water uptake: From three-dimensional biophysical processes to macroscopic modeling approaches. *Vadose Zone Journal* 12:
- (112) Javaux M, Schröder T, Vanderborght J, Vereecken H (2008) Use of a Three-Dimensional Detailed Modeling Approach for Predicting Root Water Uptake. *Vadose*

- Zone Journal 7:1079–1088. DOI: 10.2136/vzj2007.0115 (cit. on pp. 58, 60, 89, 98, 128, 164).
- (113) Jayawickreme DH, Jobbágy EG, Jackson RB (2014) Geophysical subsurface imaging for ecological applications. *New Phytologist* 201:1170–1175 (cit. on p. 24).
- (114) Jayawickreme DH, Van Dam RL, Hyndman DW (2008a) Subsurface imaging of vegetation, climate, and root-zone moisture interactions. *Geophysical research letters* 35: (cit. on pp. 14, 36, 119, 154).
- (115) Jayawickreme DH, Van Dam RL, Hyndman DW (2008b) Subsurface imaging of vegetation, climate, and root-zone moisture interactions. *Geophysical research letters* 35: (cit. on pp. 36, 150).
- (116) Jenks MA, Hasegawa PM, Jain SM (eds) (2007) Advances in Molecular Breeding Toward Drought and Salt Tolerant Crops. Springer Netherlands (cit. on p. 150).
- (117) Jones HG (2006) Monitoring plant and soil water status: established and novel methods revisited and their relevance to studies of drought tolerance. *Journal of experimental botany* 58:119–130 (cit. on p. 11).
- (118) Kemna A (2000) Tomographic inversion of complex resistivity: Theory and application. Der Andere Verlag (cit. on p. 29).
- (119) Kemna A, Vanderborght J, Kulessa B, Vereecken H (2002) Imaging and characterisation of subsurface solute transport using electrical resistivity tomography (ERT) and equivalent transport models. *Journal of Hydrology* 267:125–146. DOI: 10.1016/S0022-1694(02)00145-2 (cit. on p. 9).
- (120) Kinraide TB, Ryan PR, Kochian LV (1992) Interactive effects of Al<sup>3+</sup>, H<sup>+</sup>, and other cations on root

- elongation considered in terms of cell-surface electrical potential. *Plant Physiology* 99:1461–1468 (cit. on p. 30).
- (121) Kipling RP, Virkajärvi P, Breitsameter L, et al (2016) Key challenges and priorities for modelling European grasslands under climate change. *Science of the Total Environment* 566:851–864 (cit. on p. 150).
- (122) Koch A, Meunier F, Vanderborght J, et al (2019) Functional-structural root-system model validation using a soil MRI experiment. *Journal of experimental botany* 70:2797–2809 (cit. on p. 99).
- (123) Kodešová R, Kodeš V, Žigová A, Šimůnek J (2006) Impact of plant roots and soil organisms on soil micromorphology and hydraulic properties. *Biologia* 61:S339–S343 (cit. on p. 41).
- (124) Koestel J, Kemna A, Javaux M, et al (2008) Quantitative imaging of solute transport in an unsaturated and undisturbed soil monolith with 3-D ERT and TDR. *Water Resources Research* 44: (cit. on pp. 143, 154, 156).
- (125) Kruskal WH, Wallis WA (1952) Use of ranks in one-criterion variance analysis. *Journal of the American statistical Association* 47:583–621 (cit. on p. 157).
- (126) Ksenzhek O, Petrova S, Kolodyazhny M (2004) Electrical properties of plant tissues: resistance of a maize leaf. *Bulgarian Journal of Plant Physiology* 30:61–67 (cit. on p. 31).
- (127) Kuang W, Nelson SO (1998) Low-frequency dielectric properties of biological tissues: a review with some new insights. *Transactions of the ASAE-American Society of Agricultural Engineers* 41:173–184 (cit. on p. 25).

- (128) Kulkarni AG, Satyanarayana KG, Rohatgi PK (1981) Electrical resistivity and dielectric strength of plant fibres. *Journal of Materials Science* 16:1719–1726 (cit. on p. 31).
- (129) LaBrecque DJ, Miletto M, Daily W, et al (1996) The effects of noise on Occam's inversion of resistivity tomography data. *Geophysics* 61:538–548 (cit. on pp. 126, 142, 143).
- (130) Landis EN (2005) Damage variables based on three-dimensional measurements of crack geometry. *Strength, fracture and complexity* 3:163–173 (cit. on p. 97).
- (131) Leitner D, Meunier F, Bodner G, et al (2014a) Impact of contrasted maize root traits at flowering on water stress tolerance - A simulation study. *Field Crops Research* 165:125–137 (cit. on pp. 120, 179).
- (132) Leitner D, Meunier F, Bodner G, et al (2014b) Impact of contrasted maize root traits at flowering on water stress tolerance—a simulation study. *Field crops research* 165:125–137 (cit. on pp. 8, 88, 96).
- (133) Li Z, Liu Y, Zheng Y, Xu R (2015) Zeta potential at the root surfaces of rice characterized by streaming potential measurements. *Plant and soil* 386:237–250
- (134) Lipper L, Thornton P, Campbell BM, et al (2014) Climate-smart agriculture for food security. *Nature climate change* 4:1068–1072 (cit. on p. 6).
- (135) Lobet G, Pagès L, Draye X (2011) A Novel Image-Analysis Toolbox Enabling Quantitative Analysis of Root System Architecture. *Plant Physiol* 157:29–39. DOI: 10.1104/pp.111.179895 (cit. on pp. 60, 61).
- (136) Lu Z, Hickey CJ, Sabatier JM (2004) Effects of compaction on the acoustic velocity in soils. *Soil Science Society of America Journal* 68:7–16

- (137) Luo Z, Guan H, Zhang X (2019) The temperature effect and correction models for using electrical resistivity to estimate wood moisture variations. *Journal of Hydrology* 578:124022
- (138) Lynch JP (2007) Roots of the second green revolution. *Australian Journal of Botany* 55:493–512 (cit. on pp. 5, 8).
- (139) Lynch JP (2015) Root phenes that reduce the metabolic costs of soil exploration: opportunities for 21st century agriculture. *Plant, Cell & Environment* 38:1775–1784 (cit. on pp. 8, 88).
- (140) Lynch JP, Brown KM (2012) New roots for agriculture: exploiting the root phenome. *Philosophical Transactions of the Royal Society B: Biological Sciences* 367:1598–1604 (cit. on p. 5).
- (141) Lynch JP, Brown KM (2008) Root strategies for phosphorus acquisition. In: *The ecophysiology of plant-phosphorus interactions*. Springer, pp 83–116 (cit. on pp. 8, 88).
- (142) Mancuso S (2011) Measuring roots: an updated approach. Springer Science & Business Media (cit. on pp. 31, 33, 36).
- (143) Mary B, Abdulsamad F, Saracco G, et al (2017) Improvement of coarse root detection using time and frequency induced polarization: from laboratory to field experiments. *Plant and Soil* 417:243–259 (cit. on pp. 10, 37, 38, 42).
- (144) Mary B, Peruzzo L, Boaga J, et al (2018) Small-scale characterization of vine plant root water uptake via 3-D electrical resistivity tomography and mise-à-la-masse method. *Hydrol Earth Syst Sci* 22:5427–5444. DOI: 10.5194/hess-22-5427-2018 (cit. on pp. 10, 36).
- (145) Mary B, Saracco G, Peyras L, et al (2016) Mapping tree root system in dikes using induced polarization:

- Focus on the influence of soil water content. *Journal of Applied Geophysics* 135:387–396. DOI: 10.1016/j.jappgeo.2016.05.005 (cit. on pp. 10, 11, 13, 36, 37, 38, 40, 42, 49, 50, 177, 180).
- (146) MASI CEA, MARANVILLE JW (1998) Evaluation of sorghum root branching using fractals. *The Journal of Agricultural Science* 131:259–265 (cit. on p. 89).
  - (147) McCready MS, Dukes MD, Miller GL (2009) Water conservation potential of smart irrigation controllers on St. Augustinegrass. *Agricultural Water Management* 96:1623–1632. DOI: 10.1016/j.agwat.2009.06.007 (cit. on p. 9).
  - (148) Meister R, Rajani MS, Ruzicka D, Schachtman DP (2014) Challenges of modifying root traits in crops for agriculture. *Trends in Plant Science* 19:779–788. DOI: 10.1016/j.tplants.2014.08.005 (cit. on pp. 13, 120).
  - (149) Metzner R, Eggert A, Van Dusschoten D, et al (2015) Direct comparison of MRI and X-ray CT technologies for 3-D imaging of root systems in soil: potential and challenges for root trait quantification. *Plant methods* 11:17 (cit. on p. 88).
  - (150) Meunier F, Couvreur V, Draye X, et al (2017) Water movement through plant roots—exact solutions of the water flow equation in roots with linear or exponential piecewise hydraulic properties. *Hydrology and Earth System Sciences* 21:6519–6540 (cit. on pp. 120, 179).
  - (151) Meunier F, Heymans A, Draye X, et al (2020) MARSHAL, a novel tool for virtual phenotyping of maize root system hydraulic architectures. *in silico Plants* 2:diz012 (cit. on pp. 88, 89, 120).
  - (152) Mi G, Chen F, Wu Q, et al (2010) Ideotype root architecture for efficient nitrogen acquisition by maize in intensive cropping systems. *Science China Life Sciences* 53:1369–1373

- (153) Michot D, Benderitter Y, Dorigny A, et al (2003a) Spatial and temporal monitoring of soil water content with an irrigated corn crop cover using surface electrical resistivity tomography. *Water Resources Research* 39:SBH141–SBH1420 (cit. on pp. 10, 36, 56).
- (154) Michot D, Benderitter Y, Dorigny A, et al (2003b) Spatial and temporal monitoring of soil water content with an irrigated corn crop cover using surface electrical resistivity tomography. *Water Resources Research* 39:. DOI: 10.1029/2002WR001581 (cit. on pp. 9, 10, 36, 121).
- (155) Michot D, Benderitter Y, Dorigny A, et al (2003c) Spatial and temporal monitoring of soil water content with an irrigated corn crop cover using surface electrical resistivity tomography. *Water Resources Research* 39:. DOI: 10.1029/2002WR001581 (cit. on pp. 10, 36).
- (156) Michot D, Thomas Z, Adam I (2016) Nonstationarity of the electrical resistivity and soil moisture relationship in a heterogeneous soil system: a case study. *SOIL* 2:241–255. DOI: 10.5194/soil-2-241-2016 (cit. on pp. 10, 11, 56).
- (157) Morais R, Valente A, Serôdio C (2005) A wireless sensor network for smart irrigation and environmental monitoring: A position article. In: 5th European federation for information technology in agriculture, food and environement and 3rd world congress on computers in agriculture and natural resources (EFITA/WCCA). pp 845–850 (cit. on p. 9).
- (158) Morandage S, Schnepf A, Leitner D, et al (2019) Parameter sensitivity analysis of a root system architecture model based on virtual field sampling. *Plant and soil* 438:101–126 (cit. on p. 88).
- (159) Ni J-J, Cheng Y-F, Bordoloi S, et al (2018) Investigating plant root effects on soil electrical

conductivity: An integrated field monitoring and statistical modelling approach. *Earth Surface Processes and Landforms*. DOI: 10.1002/esp.4533

- (160) Nichols SN, Hofmann RW, Williams WM, van Koten C (2016) Rooting depth and root depth distribution of *Trifolium repens* × *T. uniflorum* interspecific hybrids. *Ann Bot* 118:699–710. DOI: 10.1093/aob/mcw067 (cit. on p. 122).
- (161) Nielsen KL, Lynch JP, Weiss HN (1997) Fractal geometry of bean root systems: correlations between spatial and fractal dimension. *American Journal of Botany* 84:26–33 (cit. on p. 89).
- (162) Ozier-Lafontaine H, Bajazet T (2005) Analysis of root growth by impedance spectroscopy (EIS). *Plant and Soil* 277:299–313 (cit. on p. 44).
- (163) Paglis CM (2013a) Application of Electrical Resistivity Tomography for Detecting Root Biomass in Coffee Trees. In: *International Journal of Geophysics*. <https://www.hindawi.com/journals/ijge/2013/383261/>. Accessed 26 May 2018 (cit. on p. 11).
- (164) Paglis CM (2013b) Application of Electrical Resistivity Tomography for Detecting Root Biomass in Coffee Trees. In: *International Journal of Geophysics*. <https://www.hindawi.com/journals/ijge/2013/383261/>. Accessed 26 May 2018 (cit. on p. 121).
- (165) Passioura JB (2002) “Soil conditions and plant growth.” *Plant, Cell and Environment* 25:311–318. DOI: 10.1046/j.0016-8025.2001.00802.x (cit. on p. 14).
- (166) Passioura JB (2012) Phenotyping for drought tolerance in grain crops: when is it useful to breeders? *Functional Plant Biol* 39:851–859. DOI: 10.1071/FP12079 (cit. on pp. 14, 120).

- (167) Pertassek T, Peters A, Durner W (2015) HYPROP-FIT software user's manual, V. 3.0. UMS GmbH, Munich, Germany (cit. on p. 122).
- (168) Peruzzo L, Chou C, Wu Y, et al (2020) Imaging of plant current pathways for non-invasive root Phenotyping using a newly developed electrical current source density approach. *PLANT AND SOIL* (cit. on pp. 13, 27).
- (169) Peterson LE (2009) K-nearest neighbor. *Scholarpedia* 4:1883 (cit. on p. 102).
- (170) Popova L, van Dusschoten D, Nagel KA, et al (2016) Plant root tortuosity: an indicator of root path formation in soil with different composition and density. *Annals of Botany* 118:685–698. DOI: 10.1093/aob/mcw057 (cit. on pp. 88, 89, 96).
- (171) Rao S, Meunier F, Ehosioke S, et al (2018) A mechanistic model for electrical conduction in soil&ndash;root continuum: a virtual rhizotron study. *Biogeosciences Discussions* 1–28. DOI: 10.5194/bg-2018-280
- (172) Rao S, Meunier F, Ehosioke S, et al (2019) Impact of Maize Roots on Soil–Root Electrical Conductivity: A Simulation Study. *Vadose Zone Journal* 18:
- (173) Rasse DP, Smucker AJ, Santos D (2000) Alfalfa root and shoot mulching effects on soil hydraulic properties and aggregation. *Soil Science Society of America Journal* 64:725–731 (cit. on p. 41).
- (174) Raven PH, Evert RF, Eichhorn SE (2005) Biology of plants. Macmillan (cit. on p. 27).
- (175) Repo T, Cao Y, Silvennoinen R, Ozier-Lafontaine H (2012) Electrical impedance spectroscopy and roots. In: *Measuring roots*. Springer, pp 25–49

- (176) Repo T, Laukkanen J, Silvennoinen R (2005) Measurement of the tree root growth using electrical impedance spectroscopy
- (177) Repo T, Zhang MIN (1993) Modelling woody plant tissues using a distributed electrical circuit. *Journal of experimental botany* 977–982
- (178) Rhoades JD, Manteghi NA, Shouse PJ, Alves WJ (1989) Soil electrical conductivity and soil salinity: New formulations and calibrations. *Soil Science Society of America Journal* 53:433–439 (cit. on p. 27).
- (179) Robinson JL, Slater LD, Schäfer KV (2012) Evidence for spatial variability in hydraulic redistribution within an oak–pine forest from resistivity imaging. *Journal of Hydrology* 430:69–79 (cit. on p. 35).
- (180) Rodrigues ML, Pacheco CMA, Chaves MM (1995) Soil-plant water relations, root distribution and biomass partitioning in *Lupinus albus* L. under drought conditions. *Journal of Experimental Botany* 46:947–956 (cit. on p. 150).
- (181) Rojas-Briales E (2015) Sparing grasslands: FAO’s active role. *Science* 347:1211–1211 (cit. on p. 150).
- (182) Rossi R, Amato M, Bitella G, et al (2011) Electrical resistivity tomography as a non-destructive method for mapping root biomass in an orchard. *European Journal of Soil Science* 62:206–215. DOI: 10.1111/j.1365-2389.2010.01329.x (cit. on pp. 11, 13, 15, 35, 57).
- (183) Rücker C, Gün T, Wagner FM (2017) pyGIMLi: An open-source library for modelling and inversion in geophysics. *Computers & Geosciences* 109:106–123 (cit. on pp. 126, 154).
- (184) Samouëlian A, Cousin I, Tabbagh A, et al (2005) Electrical resistivity survey in soil science: a review. *Soil and Tillage research* 83:173–193 (cit. on p. 11).

- (185) Satriani A, Loperte A, Proto M, Bavusi M (2010) Building damage caused by tree roots: laboratory experiments of GPR and ERT surveys. *Advances in Geosciences* 24:133–137 (cit. on p. 36).
- (186) Schnepf A, Leitner D, Landl M, et al (2018) CRootBox: a structural-functional modelling framework for root systems. *Annals of botany* 121:1033–1053 (cit. on pp. 90, 94, 96).
- (187) Schnepf A, Leitner D, Lobet G, et al (2017) CRootBox parameter files. DOI: 10.6084/m9.figshare.c.3745478.v1 (cit. on p. 94).
- (188) Schwan HP (1992) Linear and nonlinear electrode polarization and biological materials. *Annals of biomedical engineering* 20:269–288 (cit. on p. 28).
- (189) Schwartz N, Furman A (2014) On the spectral induced polarization signature of soil organic matter. *Geophysical Journal International* 200:589–595 (cit. on p. 180).
- (190) Sekhon GS (1995) Fertilizer-N use efficiency and nitrate pollution of groundwater in developing countries. *Journal of Contaminant Hydrology* 20:167–184 (cit. on p. 5).
- (191) Singh A, Ganapathysubramanian B, Singh AK, Sarkar S (2016) Machine Learning for High-Throughput Stress Phenotyping in Plants. *Trends in Plant Science* 21:110–124. DOI: 10.1016/j.tplants.2015.10.015 (cit. on p. 13).
- (192) Slater L, Binley AM, Daily W, Johnson R (2000) Cross-hole electrical imaging of a controlled saline tracer injection. *Journal of applied geophysics* 44:85–102 (cit. on p. 142).
- (193) Sposito G (2013) Green water and global food security. *Vadose Zone Journal* 12: (cit. on p. 6).

- (194) Srayeddin I, Doussan C (2009a) Estimation of the spatial variability of root water uptake of maize and sorghum at the field scale by electrical resistivity tomography. *Plant and soil* 319:185–207 (cit. on p. 11).
- (195) Srayeddin I, Doussan C (2009b) Estimation of the spatial variability of root water uptake of maize and sorghum at the field scale by electrical resistivity tomography. *Plant Soil* 319:185–207. DOI: 10.1007/s11104-008-9860-5 (cit. on p. 56).
- (196) Stiles W (1994) Principles of plant physiology. Discovery Publishing House (cit. on p. 33).
- (197) Stout DG (1988) Effect of cold acclimation on bulk tissue electrical impedance: I. Measurements with birdsfoot trefoil at subfreezing temperatures. *Plant physiology* 86:275–282 (cit. on p. 30).
- (198) Sudduth KA, Kitchen NR, Wiebold WJ, et al (2005) Relating apparent electrical conductivity to soil properties across the north-central USA. *Computers and electronics in agriculture* 46:263–283 (cit. on p. 40).
- (199) Svane SF, Jensen CS, Thorup-Kristensen K (2019) Construction of a large-scale semi-field facility to study genotypic differences in deep root growth and resources acquisition. *Plant Methods* 15:26. DOI: 10.1186/s13007-019-0409-9 (cit. on p. 8).
- (200) Tardieu F (1988) Analysis of the spatial variability of maize root density. *Plant and Soil* 107:259–266 (cit. on p. 122).
- (201) Tilman D, El Haddi A (1992) Drought and biodiversity in grasslands. *Oecologia* 89:257–264 (cit. on p. 150).
- (202) Topp GC, Zebchuk WD, Davis JL, Bailey WG (1984) The measurement of soil water content using a portable TDR hand probe. *Canadian Journal of Soil Science* 64:313–321 (cit. on p. 155).

- (203) Tournier P-H, Hecht F, Comte M (2015) Finite Element Model of Soil Water and Nutrient Transport with Root Uptake: Explicit Geometry and Unstructured Adaptive Meshing. *Transport in Porous Media* 106:487–504. DOI: 10.1007/s11242-014-0411-7 (cit. on p. 57).
- (204) Trenberth KE, Dai A, Van Der Schrier G, et al (2014) Global warming and changes in drought. *Nature Climate Change* 4:17–22 (cit. on p. 6).
- (205) Tresoldi G, Arosio D, Hojat A, et al (2019) Long-term hydrogeophysical monitoring of the internal conditions of river levees. *Engineering Geology* 259:105139 (cit. on p. 9).
- (206) Tukey JW (1949) Comparing individual means in the analysis of variance. *Biometrics* 99–114 (cit. on pp. 102, 157).
- (207) Udphuay S, Günther T, Everett ME, et al (2011) Three-dimensional resistivity tomography in extreme coastal terrain amidst dense cultural signals: application to cliff stability assessment at the historic D-Day site. *Geophysical Journal International* 185:201–220 (cit. on p. 154).
- (208) Uga Y, Sugimoto K, Ogawa S, et al (2013) Control of root system architecture by DEEPER ROOTING 1 increases rice yield under drought conditions. *Nature genetics* 45:1097 (cit. on pp. 8, 88).
- (209) Urban J, Bequet R, Mainiero R (2011) Assessing the applicability of the earth impedance method for in situ studies of tree root systems. *Journal of experimental botany* 62:1857–1869 (cit. on pp. 33, 36, 41).
- (210) van Genuchten MTh (1980) CLOSED-FORM EQUATION FOR PREDICTING THE HYDRAULIC CONDUCTIVITY OF UNSATURATED SOILS. *Soil Science Society of America Journal* 44:892–898 (cit. on p. 60).

- (211) van Treeck S (2019) personal communication Shari van Treeck, 2019, unpublished data, measurements conducted by Valentin Michels and Shari van Treeck at the Section Geophysics, Institute of Geosciences, University of Bonn (cit. on p. 92).
- (212) Vanderborght J, Huisman JA, Kruk J, Vereecken H (2013) Geophysical methods for field-scale imaging of root zone properties and processes. *Soil–water–root processes: Advances in tomography and imaging* 247–282 (cit. on pp. 9, 15, 33, 36, 37, 39, 40, 50, 177).
- (213) Vandoorne B, Beff L, Lutts S, Javaux M (2012) Root Water Uptake Dynamics of *Cichorium intybus* var. *sativum* Under Water-Limited Conditions. *Vadose Zone Journal* 11:. DOI: 10.2136/vzj2012.0005 (cit. on p. 120).
- (214) Vanella D, Cassiani G, Busato L, et al (2018a) Use of small scale electrical resistivity tomography to identify soil-root interactions during deficit irrigation. *Journal of Hydrology* 556:310–324. DOI: 10.1016/j.jhydrol.2017.11.025 (cit. on pp. 56, 57).
- (215) Vanella D, Cassiani G, Busato L, et al (2018b) Use of small scale electrical resistivity tomography to identify soil-root interactions during deficit irrigation. *Journal of Hydrology* 556:310–324. DOI: 10.1016/j.jhydrol.2017.11.025 (cit. on pp. 57, 151).
- (216) Vanhala H, Soininen H (1995) Laboratory technique for measurement of spectral induced polarization response of soil samples. *Geophysical prospecting* 43:655–676 (cit. on pp. 50, 177).
- (217) Vereecken H, Binley A, Cassiani G, et al (2006) Applied hydrogeophysics. In: *Applied Hydrogeophysics*. Springer, pp 1–8 (cit. on p. 9).
- (218) Virtanen P, Gommers R, Oliphant TE, et al (2020) SciPy 1.0: fundamental algorithms for scientific

computing in Python. *Nature methods* 17:261–272 (cit. on p. 157).

- (219) Walk TC, Van Erp E, Lynch JP (2004) Modelling applicability of fractal analysis to efficiency of soil exploration by roots. *Annals of Botany* 94:119–128 (cit. on p. 89).
- (220) Wang H, Siopongco J, Wade LJ, Yamauchi A (2009) Fractal analysis on root systems of rice plants in response to drought stress. *Environmental and Experimental Botany* 65:338–344 (cit. on p. 89).
- (221) Wang Z, Bovik AC, Sheikh HR, Simoncelli EP (2004) Image quality assessment: from error visibility to structural similarity. *IEEE transactions on image processing* 13:600–612 (cit. on p. 145).
- (222) Wasson AP, Richards RA, Chatrath R, et al (2012) Traits and selection strategies to improve root systems and water uptake in water-limited wheat crops. *Journal of experimental botany* 63:3485–3498 (cit. on p. 8).
- (223) Waxman MH, Smits LJM (1968) Electrical conductivities in oil-bearing shaly sands. *Society of Petroleum Engineers Journal* 8:107–122 (cit. on p. 40)
- (224) Weckesser W, Haberland M (2019) A Solid Foundation for Statistics in Python with SciPy (cit. on p. 157).
- (225) Weigand M (2016) Monitoring structural and physiological properties of crop roots using spectral electrical impedance tomography. Universitäts-und Landesbibliothek Bonn (cit. on p. 89).
- (226) Weigand M, Kemna A (2017a) Multi-frequency electrical impedance tomography as a non-invasive tool to characterize and monitor crop root systems. *Biogeosciences* 14:921–939. DOI: 10.5194/bg-14-921-2017 (cit. on pp. 10, 27, 37, 50, 67, 180).

- (227) Weigand M, Kemna A (2017b) Multi-frequency electrical impedance tomography as a non-invasive tool to characterize and monitor crop root systems. *Biogeosciences* 14:921–939 (cit. on pp. 10, 27, 37, 50, 67, 180).
- (228) Werban U, Al Hagrey SA, Rabbel W (2008) Monitoring of root-zone water content in the laboratory by 2-D geoelectrical tomography. *Journal of Plant Nutrition and Soil Science* 171:927–935. DOI: 10.1002/jpln.200700145 (cit. on pp. 11, 12, 36, 41, 42, 56, 62).
- (229) Whalley WR, Binley A, Watts CW, et al (2017a) Methods to estimate changes in soil water for phenotyping root activity in the field. *Plant and Soil* 415:407–422. DOI: 10.1007/s11104-016-3161-1 (cit. on pp. 10, 121).
- (230) Whalley WR, Binley A, Watts CW, et al (2017b) Methods to estimate changes in soil water for phenotyping root activity in the field (cit. on pp. 10, 13, 56, 121).
- (231) Whalley WR, Binley A, Watts CW, et al (2017c) Methods to estimate changes in soil water for phenotyping root activity in the field. *Plant and Soil* 415:407–422. DOI: 10.1007/s11104-016-3161-1 (cit. on pp. 10, 121, 127).
- (232) Wheeler T, Von Braun J (2013) Climate change impacts on global food security. *Science* 341:508–513 (cit. on p. 5).
- (233) Wilderotter O (2003a) An adaptive numerical method for the Richards equation with root growth. *Plant and Soil* 251:255–267. DOI: 10.1023/A:1023031924963 (cit. on p. 57).
- (234) Wilderotter O (2003b) An adaptive numerical method for the Richards equation with root growth. *Plant and Soil* 251:255–267 (cit. on p. 13).

- (235) Williamson DF, Parker RA, Kendrick JS (1989) The box plot: a simple visual method to interpret data. *Annals of internal medicine* 110:916–921 (cit. on p. 160).
- (236) Wilner J (1964) Seasonal changes in electrical resistance of apple shoots as a criterion of their maturity. *Canadian Journal of Plant Science* 44:329–331 (cit. on p. 31).
- (237) Winchen T, Kemna A, Vereecken H, Huisman J (2009) Characterization of bimodal facies distributions using effective anisotropic complex resistivity: A 2-D numerical study based on Cole-Cole models. *GEOPHYSICS* 74:A19–A22. DOI: 10.1190/1.3113986 (cit. on p. 43).
- (238) YAMAUCHI A, TATSUMI J, KONO Y (1989) Fractal Analysis of Plant Root Systems. *Annals of Botany* 64:499–503. doi: 10.1093/oxfordjournals.aob.a087871 (cit. on p. 89).
- (239) Yan N, Marschner P (2012) Response of microbial activity and biomass to increasing salinity depends on the final salinity, not the original salinity. *Soil Biology and Biochemistry* 53:50–55 (cit. on p. 24).
- (240) Yang W, Duan L, Chen G, et al (2013) Plant phenomics and high-throughput phenotyping: accelerating rice functional genomics using multidisciplinary technologies. *Current Opinion in Plant Biology* 16:180–187. DOI: 10.1016/j.pbi.2013.03.005 (cit. on p. 150).
- (241) Yang W, Guo Z, Huang C, et al (2014) Combining high-throughput phenotyping and genome-wide association studies to reveal natural genetic variation in rice. *Nature communications* 5:5087 (cit. on p. 5).
- (242) Yang X, LaBrecque DJ (1998) Stochastic inversion of 3-D ERT data. In: *Symposium on the Application of Geophysics to Engineering and Environmental*

Problems 1998. Society of Exploration Geophysicists, pp 221–228 (cit. on p. 76).

- (243) Young IM (1998) Biophysical interactions at the root–soil interface: a review. *The Journal of Agricultural Science* 130:1–7 (cit. on p. 41).
- (244) Zenone T, Morelli G, Teobaldelli M, et al (2008a) Preliminary use of ground-penetrating radar and electrical resistivity tomography to study tree roots in pine forests and poplar plantations. *Functional Plant Biology* 35:1047–1058 (cit. on pp. 10, 11, 13, 35, 47).
- (245) Zenone T, Morelli G, Teobaldelli M, et al (2008b) Preliminary use of ground-penetrating radar and electrical resistivity tomography to study tree roots in pine forests and poplar plantations. *Functional Plant Biology* 35:1047–1058 (cit. on pp. 10, 11, 13, 35).
- (246) Zenone T, Morelli G, Teobaldelli M, et al (2008c) Preliminary use of ground-penetrating radar and electrical resistivity tomography to study tree roots in pine forests and poplar plantations. *Functional plant biology FPB* (cit. on pp. 10, 11, 13, 35, 57).
- (247) Zhang MIN, Willison JHM (1993) Electrical impedance analysis in plant tissues8. *Journal of Experimental Botany* 44:1369–1375 (cit. on pp. 31, 44).
- (248) Zhang X, Sanderson DJ (1995) Anisotropic features of geometry and permeability in fractured rock masses. *Engineering Geology* 40:65–75. DOI: 10.1016/0013-7952(95)00040-2 (cit. on pp. 89, 97).
- (249) Zhao P-F, Wang Y-Q, Yan S-X, et al (2019) Electrical imaging of plant root zone: A review. *Computers and Electronics in Agriculture* 105:058 (cit. on pp. ix, 38, 175).
- (250) Zhao Y, Liu Z, Wu J (2020) Grassland ecosystem services: A systematic review of research advances and

future directions. *Landscape Ecology* 1–22 (cit. on p. 150).

- (251) Zhou QY, Shimada J, Sato A (2001) Three-dimensional spatial and temporal monitoring of soil water content using electrical resistivity tomography. *Water Resources Research* 37:273–285 (cit. on p. 10).
- (252) Zimmermann E, Kemna A, Berwix J, et al (2008) A high-accuracy impedance spectrometer for measuring sediments with low polarizability. *Measurement Science and Technology* 19:105603 (cit. on p. 47).